Decoherence and correlations in systems of trapped ultra-cold quantum gases

Christian Schroll

aus Tübingen (Deutschland)

Basel, 2005

Genehmigt von der Philosophisch-Naturwissenschaftlichen Fakultät
auf Antrag von

Prof. Dr. C. Bruder
Prof. Dr. W. Belzig
Prof. Dr. W. Zwerger

Basel, den 7. Juni 2005

Prof. Dr. Hans-Jakob Wirz
Dekan

Acknowledgments

I am indebted to many people for all the help and support during my time in Basel. First I would like to thank Prof. Christoph Bruder for accepting me as a PhD student and for all the continuous support during my work. Furthermore I would like to thank Prof. Wilhelm Zwerger for co-refereeing my thesis.

I am especially indebted to Prof. Wolfgang Belzig for the collaboration on the atom-chip project and the help and guidance during the work on density correlations in ultra-cold gases. To Florian Marquardt I owe many thanks for the support in the project on the superfluid Mott-insulator transition in optical lattices. I am grateful to Simon Gardiner for all the stimulating discussions and the hospitality during my visit at the University of Oxford.

I would like to thank Bill Coish for giving me a hand whenever I encountered a problem with the English language. In addition I would like to acknowledge all those people who made my life in Basel much more enjoyable. The condensed matter theory group for the fascinating and instructive discussions during coffee breaks. Leo Merz for the numerous Tichu evenings. Verónica Cerletti and Hanno Gassmann for all the undertakings and fun we had.

Finally, I want to thank Senta Karotke with all my heart for all her love and for always being a source of happiness.

Summary

Since the achievement of Bose-Einstein condensation (BEC), the progress in matter-wave physics has been immense. Among the many recent achievements there is the miniaturization of atom traps, demonstration of the superfluid-Mott insulator quantum-phase transition in optical lattices and the experimental demonstration of the BEC-BCS crossover in ultra-cold gases.

Miniaturization of atom traps using micro-structured wires on a chip is one important step towards an on-chip cold-atom device. These so-called "atom chips" provide high control and versatility for trapping and guiding the ultra-cold atomic clouds. Particularly interesting is the use of these microchips to build mesoscopic devices for cold atomic clouds as, for instance, in the case of an atom-cloud interferometer. However, these mesoscopic devices require coherent transport of the atom cloud. A general method to treat decoherence due to current fluctuations in multi-wire atom-chip traps is presented in the first part of this thesis. The decoherence rate Γ shows a strong dependence on the distance between the wire and the atom cloud, r_0, scaling as $\Gamma \sim r_0^{-4}$ for a single atom waveguide. Considering an interferometer device, a strong dependence of the decoherence rate on the trap geometry is found.

Studying many-body effects in ultra-cold quantum gases is another important research field. Experiments using ultra-cold quantum gases in optical lattices have demonstrated the superfluid-Mott insulator quantum phase transition and many-body entanglement. Optical lattices are based on a periodic modulation of the light intensity, generated by retro-reflected laser beams. Correlations of the atomic cloud between different lattice sites of the optical lattice play a central role in these many-body experiments. The different phases of the superfluid-Mott insulator system can be characterized by the different behavior of the inter-lattice site correlations. There are several numerical methods such as Quantum Monte Carlo (QMC) simulations, Density Matrix Renormalization Group (DMRG) simulations, exact-diagonalization, or the Gutzwiller ansatz, to investigate the dynamics of an ultra-cold gas in an optical lattice theoretically. The Gutzwiller method, corresponding to the mean-field solution, allows for the treatment of large lattice sizes. Mean-field approaches have proven to be very useful to describe many-body physics. However, difficulties arise in the correct description of the behavior of the decay of inter-lattice site correlations. Based on the Gutzwiller approach, we have developed a method which allows the successive inclusion of inter-lattice site correlations. Comparing the results for the particle-number fluctuations and the correlation function obtained from pure Gutzwiller calculations, to calculations which perturbatively include short-range correlations and calculations

using "quasi-exact methods", showed a considerable improvement relative to the pure Gutzwiller results due to the inclusion of short-range correlations.

Many-body effects do not only arise in periodic potentials, but become increasingly important at ultra-low temperatures. The formation of Bose-Einstein condensates requires an overlap of the atom wavefunctions and, hence, the formation of a single condensate wavefunction. Another example of a many-body state is the superfluid-BCS state, commonly used as a description of superconductivity. Here, fermions in different hyperfine states form Cooper pairs. Experiments with ultracold quantum gases enable a variation of the interparticle interaction, e.g. , by using a Feshbach resonance. Using Feshbach resonances to tune the interaction strength has enabled the experimental observation of the crossover from a superfluid-BCS state to a Bose-Einstein condensate of molecules. A useful way to characterize the different states of ultra-cold quantum gases is to investigate the particle-number fluctuations. In this thesis we suggest to divide the atomic cloud into bins and consider the atom-number fluctuations in these bins. We calculate the full counting statistics for different physical systems of ultra-cold gases (e.g. bosonic gases, fermionic gases, and spin mixtures). In particular, we consider the BCS-state as a first trial example to show that there is a strong variation in the particle-number statistics at the crossover from a superfluid-BCS state to a Bose-Einstein condensate of molecules.

Contents

Chapter 1

Introduction

"Decoherence and correlations in systems of trapped ultra-cold quantum gases"! — Scientist not familiar with the term "ultra-cold quantum gases", which are also called matter waves, might wonder what is meant by "ultra-cold quantum gases". Trying to classify matter-wave physics leads to the realization, that it is neither purely atomic physics nor is it purely condensed matter physics. The physics of ultra-cold gases seems to be rather something in between.

On the one hand, atomic physics is interested in the description of single isolated atoms. Quantum mechanics was developed and intensively expanded, based on these isolated systems. On the other hand, we are very familiar with the concept of a large number of atoms tightly packed in a lattice. Condensed matter physics dominates our everyday life as, for example, in computers, mobile phones and many other electronic devices. Solids are much more complex systems than isolated atoms and many-body effects lead to additional physical phenomena. However, what happens if we take a few atoms and form a cold dilute cloud? Quantum mechanics will play an important role in these cold-dilute gases. However, in contrast to the isolated atom, ultra-cold quantum gases will also show many-body effects. In fact, dilute atomic gases give rise to physical systems, which show phenomena from atomic and solid-state physics.

Trapped ultra-cold quantum gases can be thought of as very dilute many-body systems. These ultra-cold atom clouds consist in general of about 10^5 to 10^7 atoms which can be fermions, bosons or fermion-boson mixtures. The densities of the ultra-cold quantum gases vary from 10^{13}cm^{-3} to 10^{15}cm^{-3}. Hence, matter waves have densities which are about eight to ten orders in magnitude smaller than in a solid. The dilute gases are collected in ultra-high vacuum chambers. Laser-cooling [1–3] and evaporative-cooling [4] techniques enable the cooling of the dilute-atomic quantum gases to temperatures of a few microkelvin. In fact, the low densities and the low temperatures achievable by evaporative-cooling made the formation of a Bose-Einstein condensate (BEC) in a ultra-cold atom clouds possible [5,6]. Creating almost pure Bose-Einstein condensates is probably the most striking experimental achievement in matter-wave physics. Dilute fermionic gases can be cooled to a fraction of the Fermi temperature $T_F = \epsilon_F/k_B$, where the fermionic atom cloud forms a degenerate Fermi gas. Particularly interesting are fermionic spin-mixtures. Cooled below the critical

temperature T_C^{BCS}, one expects the formation of a superfluid BCS state similar to the many-body state known from conventional superconductivity. The dilute-atomic clouds are usually trapped in magnetic or optical traps which offer a large variety of possibilities to manipulate and transport the atomic cloud. The atomic cloud can be guided along waveguides, rotated or put in a periodic lattice, to name only a few examples.

Matter waves offer a world of many-body physics from Bose-Einstein condensation to Cooper pairing combined with the great versatility and control provided by quantum-optical techniques. Indeed, matter-wave physics has become a field where atomic physics, quantum optics and condensed matter physics meet. With the input of these numerous different backgrounds, matter-wave physics quickly developed into a new innovative field. An array of research ideas were put forward, successfully combining condensed matter and atomic physics. It is the aim of this chapter to give a few examples of research done with ultra-cold quantum gases. Each example will stress a different combination of quantum-optical, atomic and solid-state physics.

1.1   The atom chip

The name "atom chip" already summarizes the idea behind the device very nicely. Atom chips use the concepts of chip technology to construct traps and guides for clouds of neutral atoms. The breakthrough of electronic devices came only with the successful downsizing from large devices like vacuum tubes to what is known today as chip technology, with transistor sizes of a few hundred nanometers. If applications using ultra-cold atomic gases, like atomic clocks [7] or ultra-sensitive gyroscopes [8,9], are to become everyday devices, they need to be sized down to the same dimensions. Usual atom traps use huge coils to produce the magnetic trapping fields. Downsizing of the trap can be achieved if the magnetic field is produced by currents in thin wires. Chip technology provides a tool to microstructure the wires and to reduce the trap to the size of a chip. Thus, atom chips provide strongly confined traps for atomic clouds which can be used to guide and manipulate the ultra-cold gases. In fact, first experiments with atom chips have been very successful (see [10–12] for a review). Ultra-cold atomic clouds have been transported along waveguides, split into two clouds at a beam splitter [13] or stored in a ring waveguide [14].

However, atom-chip traps offer far more than simply a miniaturization of known physics. The huge versatility of the atom waveguides opens the door to a new world of mesoscopic transport of matter waves. Atom-chip waveguides are expected to be very good candidates for coherent transport of ultra-cold atomic clouds. This makes chip traps an interesting means to study quantum phenomena in the transport of bosonic and fermionic ultra-cold gases or Bose-Einstein condensates.

A further step towards an atom-chip device is the combination of optical elements with atom-chip traps [9,15]. Integrated optical elements offer a huge toolbox for the manipulation and control of the atomic cloud. Additionally, optical elements can be used as interfaces between the atomic cloud and the environment. These elements

allow the exchange of information between different matter waves or serve as an interface to an outside user. An example would be the interface for a quantum information processor on an atom chip [16]. The use of on-chip micro cavities can then be used as single-atom detectors for the readout procedure [17].

1.2 Optical lattices

The name "optical lattice" is again a strong hint to a combination of quantum optics, atomic and condensed matter physics. Optical lattices are based on a concept which is very different from the atom chip. This time, the technology known from quantum optics provides the technical support to trap the dilute atomic cloud. Atoms have been trapped in laser fields for a long time. The new idea behind optical lattices is the formation of an array of atom traps, i.e., a lattice. Retro-reflecting a laser beam leads to a standing wave with intensity maxima and minima, forming an array of atom traps. Using one, two or three laser beams allows the formation of a one-, two- or three-dimensional lattice. Trapping ultra-cold atoms in these optical lattices leads to a physical system reminiscent of a solid body.

In the case of optical lattices, it is the great versatility of the trapping potential for the matter-wave system that makes experiments particularly attractive. The lattice spacing and the lattice structure can easily be changed by adjusting frequency, intensity and orientation of the laser beams. Moreover, optical lattices form ideal lattices without lattice defects like dislocations, grain boundaries or impurities. Noise sources perturbing the optical lattice remain in fluctuations of the intensity or of the shape of the laser beam, to name only a few examples. Disorder, in form of irregularities of the lattice-site trapping potentials, can be added in a controlled way, using two-color superlattices or speckle patterns [18]. Hence, optical lattices provide also an ideal testing ground to investigate phenomena in disordered lattices, as for example, the Bose-glass transition [19]. Changing the laser intensity gives control over the potential depth of each lattice side. Varying the potential depth corresponds to a variation in the tunneling barrier between neighboring lattice sites. Hence, the control over the potential depth provides a tool to tune the dynamical properties of the atomic gas in the optical lattice. In contrast to their solid-state relatives, optical lattices offer the possibility to load the periodic potential with bosons, fermions, molecules or mixtures giving rise to a huge diversity of different systems.

Being something like a copy of a solid-state crystal, optical lattices show all the phenomena known from their solid state relatives, which have their origin in the periodicity of potential. Starting from demonstrations of Bloch Oscillations [20], to direct visualization of the Brillouin zones [21] and Fermi surfaces [22], optical lattices are an ideal testing ground for lattice-induced effects known from condensed matter physics. Several many-body effects, known from solid-state physics, have also been observed in optical lattices. The most prominent example is the Mott-insulator quantum phase transition in optical lattices [23,24]. Being theoretically investigated for many years, the experimental demonstration and the ability to tune the potential

shape in optical lattices, rekindled the interest in this field. A further example for the versatility of experiments with optical lattices is the creation of a Tonks-Girardeau gas [25]. The realization of strongly interacting Bose gases in one-dimensional optical lattices [25–27] provides a testing ground to investigate the Tonks-Girardeau regime, which has been discussed theoretically for a long time [28, 29]. The investigation of a Bose-glass phase in disordered optical lattices or the exploration of a superfluid state of Cooper pairs, anti-ferromagnetic or d-wave pairing states of fermionic gases in optical lattices [30] are only a few possible future applications for systems which are reminiscent of problems in solid-state physics. Furthermore, optical lattice offer the possibility to study the dynamics of bosons, fermions, boson-fermion mixtures, spin-mixtures, spin-polarized gases and molecules in lattice potentials . This gives rise to many new physical systems which have no counterpart in the solid-state world.

Still, the concept of an optical lattice provides far more possibilities. The ideal lattice and the perfect control over the trapped atoms allows the preparation of a state consisting of an array of isolated atoms. These atom arrays form the perfect prerequisite for many-body quantum entanglement [31, 32]. In fact, each atom in the array can be thought of as a two-level quantum system forming a qubit. The scalability and the good control of the system thus provide a good candidate for a quantum computer with neutral atoms [33–35].

1.3 Bose-Einstein condensation and the BEC-BCS crossover

The last example for research done with ultra-cold quantum gases combines atomic physics and condensed matter physics in yet a different manner. This time, both, atomic and solid state physics provide systems which allow an investigation of a similar underlying physical mechanism. Matter waves behave neither as a system of isolated atoms, nor like a complex solid body. In fact, matter waves provide the unique possibility to investigate many-body physics in a very dilute environment. Ultra-cold dilute atom clouds have densities of typically $10^{13}\mathrm{cm}^{-3}$ – $10^{15}\mathrm{cm}^{-3}$ [36] and have, thus, densities roughly eight to ten orders of magnitude smaller than those of a solid.

The most famous example of a many-body phenomenom, which finally has been accessible in a dilute-atomic gas, is Bose-Einstein condensation. Bose-Einstein condensates form in bosonic gases at a critical temperature[1] T_C^{BEC} when the thermal wavelength reaches the same order of magnitude as the interparticle spacing [37]. Even though Bose-Einstein condensation was intensively studied in superfluid ^{4}He experiments [39], it was not until dilute atomic gases reached sufficiently low temperatures and sufficiently low densities that Bose-Einstein condensates with high condensate fractions were observed experimentally [5,6]. Since the first experimental

---

[1]The critical temperature in an ideal gas is [37]: $k_B T_C^{\mathrm{BEC}} = 2\pi\hbar^2/m(Vg_{3/2}(1)/N)^{2/3}$, where $g_n(z) = \sum_{l=0}^{\infty} z^l/l^n$. For a more detailed discussion of the critical temperature, considering finite size effects or trapping geometries, see Ref. [38].

observation, there has been an immense increase in research activity, investigating the physics of Bose-Einstein condensates. The many-body nature of the Bose-Einstein condensate exhibits a number exciting properties, as for instance, interference effects [40–43], the formation of solitons [44,45] and vortex formation [46,47].

One other very exciting example which has drawn a lot of recent attention is the crossover from a state of Bose-Einstein condensed molecules to a superfluid of Cooper-paired fermions. The ultra-cold gas is prepared in a mixture of fermions in two different spin states. The advantage of BEC-BCS crossover experiments in ultra-cold quantum gases lies in the high controllability of the interaction strength between the particles. The interaction between the fermions in different spin states can be tuned between a negative scattering length and a positive scattering length using a Feshbach resonance. On the side of the Feshbach resonance with negative scattering length, fermions in different spin states perceive an attractive interaction. Tuning the magnetic field adiabatically from negativ to the positive scattering length changes the two-fermion scattering state into a bound state. Hence the fermions pair up and form molecules. Fermions in different spin states which are unpaired perceive a repulisve interaction due to the positive scattering length. If the temperature is below T_C^{BEC}, a molecular Bose-Einstein condensate emerges. Attractive interaction between the fermions, however, leads to the formation of a superfluid BCS state as known from conventional superconductivity. Tuning the interaction strength from repulsive to attractive interactions leads to a crossover from a Bose-Einstein condensate of molecules to a BCS state of Cooper-paired fermions. The BEC-BCS crossover has been of physical interest for many years. Originally discussed as a theoretical model in the context of high-temperature superconductivity [48] it was difficult to investigate the BEC-BCS crossover experimentally. The low densities achievable in ultra-cold gases finally made the BEC-BCS crossover regime experimentally reachable. Thus, matter-wave physics provides a way to experimentally investigate the interesting many-body physics, occurring at the crossover from a Bose-Einstein condensate of molecules to a superfluid BCS state. Even though a high-temperature superconductor, with its rather complicated lattice structure, is very different from an ultra-cold atomic gas composed of fermions in two different spin states, the basic underlying many-body physics remains the same. Both systems are expected to access the BEC-BCS crossover region. It is primarily the simplification of the system and the large number of adjustable parameters which makes the BEC-BCS crossover experiment in ultra-cold dilute gases so attractive.

1.4 Correlation and coherence

The previous sections have shown that matter-wave physics is a very versatile field to study quantum effects in a many-body system. The use of tools and techniques from solid-state physics, atomic physics and quantum optics created a whole range of new ways to study dilute many-body systems. As in most quantum systems, correlations and coherence between the particles play a key role in matter-wave experiments. Atom chips are expected to serve as waveguides for coherent transport. Many-body

effects observed in optical lattices and dilute many-body systems are based on corre-lations and entanglement between the atoms. It is therefore the issue of decoherence, correlations and noise in matter-wave systems which will be the central topic of this thesis.

As we have already introduced some ideas about matter-wave physics in the last three sections, let us use those same examples to get a better idea of the importance which coherence and correlations play in matter-wave systems. This section is in-tended not only to serve as an introduction to the basic principles, but also to give a taste of what is to come in the following chapters.

Atom chips were previously introduced as waveguides for matter waves. How-ever, if mesoscopic quantum devices are to be built from atom-chip waveguides, then sufficiently long coherence times are needed. Hence, guiding matter waves requires coherent transport. The investigation of possible sources of decoherence are therefore a key issue for the realization of coherent transport on atom chips. Atom-chip traps are composed of a microstructured wire layout on a chip put in a vacuum chamber. Atoms are cooled down to several microkelvin and then trapped by the magnetic fields formed by the currents flowing through microwires on the chip. The cold atomic cloud is finally trapped in the close vicinity of the chip surface. As a consequence, there will be interactions between the substrate and the trapped atomic cloud, and the cold gas can no longer be considered an isolated system. Figure 1.1 shows a sketch of the system. Recent experiments reported a fragmentation of cold atomic clouds or Bose-Einstein condensates in a microwire waveguide [49–55] on reducing the distance between the wavepackets and the chip surface. The fragmentation of atom clouds, emerging if the cloud is approached to the chip surface, shows that atomic gases in wire traps are very sensitive to the environment. Current noise in the wires is an obvious source of decoherence. As the trap is formed by the current passing through the wires, any current fluctuation will directly translate into a fluctuation of the trapping potential and consequently lead to decoherence of the atomic cloud. On the one hand, there is spatial decoherence along the cloud, as atoms located at different positions will in general perceive different potential fluctuations. On the other hand, transitions between different trap states give rise to decoherence. Fluctuations in the trap potential cause the atoms to jump back and forth from the ground state into excited states. As the particles undergo different time evolution in the different states and as the time between jumps is stochastic, atoms start to pick up different phases. Including the discrete spectrum of the trapping potential gives rise to a decoherence mechanism with a decoherence rate Γ that scales like $\Gamma \sim 1/r_0^4$ with the distance r_0 from the trap minimum to the wire. Loss of particles during transport along the wire is also caused by the noisy environment. However, these particle losses, due to spin flips into untrapped states, do not limit the coherence time. The contents of Chapter 2 will look more closely at the impact of current noise on the coherent transport in multi-waveguide atom-chip traps.

The second example of matter-wave physics discussed an ultra-cold quantum gas trapped in a periodic potential. Considering optical lattices, we will focus on the
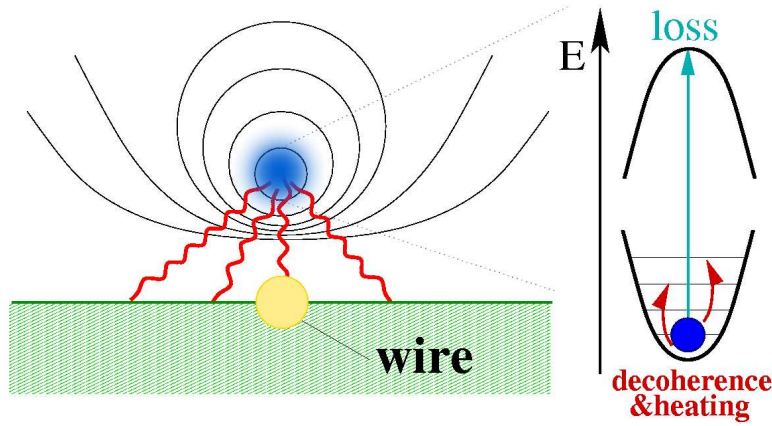
Figure 1.1: *Left:* Sketch of an atomic cloud trapped in the magnetic field of a chip trap. The red wiggled lines suggest the coupling of the environment to the atomic cloud. *Right:* Sketch of the energy spectrum of a trapped atom. Heating, decoherence and loss processes as a consequence of the coupling to the substrate lead to transitions into excited states.

importance of correlations between the atoms in different lattice sites. The optical-lattice traps are formed by standing waves from a set of laser beams. Imperfections of the lattice and fluctuations in the laser intensities play a very minor role in these systems. Optical lattices are thus perfect for physical processes which require long coherence times, as for example coherent states [56] or the entanglement of atoms [31]. Coherence or correlations between atoms in optical lattices manifest themselves in a way which is different from the previously discussed decoherence of matter waves trapped in an atom-chip trap. Instead of simply loosing the phase coherence there can be a reversible transition from a state with long spatial phase coherence into a state with short or even zero coherence length. This is the case in the so called Mott-insulator transition. The Mott-insulator transition is observable in optical lattices if the number of bosons N is an integer multiple of the number of lattice sites M i.e $N = i \times M$. In this situation, bosons, which are trapped in the lowest Bloch band of an optical lattice, can be found in two different phases: the superfluid phase and the Mott-insulator phase. The transition is driven by the ratio of the tunneling rate of the bosons from one lattice site to the next, J, and the on-site repulsion energy U. If the hopping energy dominates, then the bosons are in the superfluid phase. The atoms form a coherent state which is delocalized and thus correlated over many lattice sites. The situation, where the on-site repulsion dominates, is very different. Now, it is favorable for the system to minimize the number of bosons per lattice site. The bosonic gas forms a Mott-insulator phase. In the Mott-insulator phase, every lattice site is occupied by exactly the same number of bosons $i = N/M$. Hence, the bosons are localized and the state can be described as a product of Fock states. The Mott-insulator state, however, shows large fluctuations between the phases on different lattice sites. Phase correlations between different lattice sites are practically zero. The correlation length is, however, not strictly zero for the complete parameter range of the Mott-insulator phase [57–61]. Here, short-range correlations play an important

role. The impact of short-range correlations on the different physical observables will be studied in Chapter 3 by extending the mean-field treatment of the Mott-Hubbard model perturbatively.

The third and last example discussed the new field of dilute many-body systems which matter waves provide. Bose-Einstein condensation and the superfluid BCS state are two examples of systems which are accessible in dilute quantum gases. Coherence and correlations among the atoms again play a central role in the formation of these many-body states. Correlations, however, also provide another very different aspect. Correlations in noise measurements can be used to extract information about the state of the system. Recent experimental work [62, 63] has confirmed the applicability of noise measurements as a useful tool to characterize the state of the matter-wave system. Letting the trapped atomic cloud expand and taking an absorption picture after a short waiting period can expose information about the initial state. Correlation measurements in the noise of absorption pictures have been made using a fermionic spin mixture [62]. In this experiment, density correlations with point inversion symmetry to the center of the cloud have been found for attractive interactions between the fermions in different spin states. These correlations are a strong indication for a state of $(\mathbf{k}, -\mathbf{k})$ momentum pairs as expected for a BCS superfluid [62, 64]. The measurement of density correlations for the BEC-BCS crossover is particularly interesting [65]. Crossing over from a system of bosonic molecules, forming a Bose-Einstein condensate, to a superfluid BCS state of fermions, paired in momentum space, gives rise to a drastic change in the statistical behavior. Measuring the number statistics of a small subsystem allows one to track down the change from the BEC to the BCS state. The detailed discussion of the statistical behavior of atom-number fluctuations for the BEC-BCS crossover will be the subject of Chapter 4.

1.5   Outline of this thesis

The thesis is divided into three main chapters. Following the ideas presented in the introduction, each chapter will discuss an example, which demonstrates the close connection between quantum optics, atomic physics and condensed matter physics in matter-wave systems. However, each example will emphasize a different aspect of the versatility of matter-wave physics.

Each chapter is presented in a closed form and can thus be read separately. As the examples discussed in this thesis are not based on a common theory, there will be an introduction to each chapter. Additionally, each chapter starts with an abstract (written in italics) bringing each example into the common context of the thesis.

The first example, presented in Chapter 2, discusses decoherence in atom-chip waveguides. A general method for the treatment of an arbitrary multi-wire waveguide is presented and applied to the specific example of the single- and double-wire waveguides. In contrast to earlier work [66], the theory presented in Chapter 2 takes the excited states of the trapping potential into account. Consequences to the de-

coherence due to transitions between the transverse levels are discussed. Chapter 3 addresses the Mott-insulator transition in optical lattices. Special focus is placed on short-range correlations. Short-range correlations are discussed within the scope of the Gutzwiller approach. A method to successively include short-range correlations perturbatively is introduced and applied to calculate the expansion pictures. Results with and without a harmonic trapping potential are presented and compared to different numerical approaches. Finally, Chapter 4 presents a new approach to measure atom-number correlations in atomic clouds in order to obtain information about the state of the matter-wave system. The full counting statistics (FCS) for the BEC-BCS crossover at zero temperature is calculated and discussed as a possible application of the method. A qualitative discussion of the extension to the finite-temperature regime is given.

Chapter 2

Decoherence of ultra-cold atoms in atom-chip traps

Atom chips provide a nice example of the combination of atomic and condensed matter physics. On the one hand, miniaturization and the possibility for mass production is the key to the successful application of atomic devices in the future. On the other hand, atom chips give rise to a variety of trap configurations enabling the investigation of mesoscopic transport of matter waves. Yet, this new field of coherent transport experiments with ultra-cold bosonic, fermionic or Bose-Einstein condensed gases is reminiscent of mesoscopic transport in condensed matter devices.

Guiding of atomic clouds has been experimentally demonstrated in many experiments [67–70]. In addition, a huge number of experiments have shown the versatility in atom-chip traps can be used. Atomic clouds have been guided along spirals [71] and transported from one reservoir to another reservoir using a conveyor belt for cold atomic gases [72]. Bose-Einstein condensates have been successfully trapped and guided using atom chips [49, 55, 73–75] (see [11] for a review). Storage rings have been loaded with atomic clouds which remained in the ring for several cycles before the atoms were lost [14]. Furthermore, plans to use atom chips for quantum information processing have been put forward [16]. A first step in this direction would be given by the successful demonstration of single-atom detection, for instance, by using an on-chip micro cavity [17]. However, if atom-chip traps are to be used for mesoscopic quantum experiments or quantum information processing then the atomic clouds must be coherently transported along the waveguide. Decoherence due to the coupling of the cloud to its environment is therefore one of the key issues for atom-chip traps.

It is the aim of this chapter to consider the impact of current fluctuations in atom-chip traps. A general model will be derived, describing the decoherence of atomic clouds in atom-chip traps, taking the excited states of the trapping potential into account. Including the discrete spectrum of the trapping potential gives rise to a decoherence mechanism with a decoherence rate Γ that scales like $\Gamma \sim 1/r_0^4$ with the distance r_0 from the trap minimum to the wire. Eventually, the model will be applied to different examples, the single-wire and the double-wire trap. The most important example will be the double-wire trap which will be considered in the context of an

atomic interferometer. Decoherence in an interferometer is particularly interesting, as it provides the basic tool to test the coherence of an atomic cloud. Many different suggestions have been put forward [76–78] and the experimental demonstration of a beam splitter [13] shows that an experimental realization of such an interferometer is very likely in the near future. In fact, in a recent experiment, a Michelson interferometer for Bose-Einstein condensates was built on an atom chip using on-chip mirrors [9].

2.1   Atom-chip traps

There are many different approaches for on-chip atomic traps. A first distinction can be made between permanently magnetized structures and those magnetic-field traps, which are formed by current carrying wires.

Permanent-magnet traps use common video tape or a floppy disk which is glued to the chip (see [10] for a review). Choosing an appropriate structure of permanent magnets allows the guiding of atomic clouds [79–81]. Experiments lately demonstrated the creation of a Bose-Einstein condensate in a permanent-magnet atom-chip trap [82]. Furthermore, permanently magnetized traps have been used as magnetic mirrors for ultra-cold atom clouds [83–85]. Recently, a technique was suggested which allowed the structuring of the magnetic material using a laser beam [86]. The magnetic material was first fully magnetized and then areas with flipped magnetization were created by heating with a laser beam.

The experimentally most common way to trap atoms on a chip are wire-based traps. The magnetic field is created by the currents in the wires and by additional external bias fields[1]. The wires are microfabricated on the chip with the techniques known from chip technology. Even microstructuring using a CNC-milling machine allows small enough structures to trap a Bose-Einstein condensate [55]. There is a large number of possible wire configurations leading to a wire-based chip trap (see [69] for a review). However, as the main part of this chapter considers decoherence of atomic clouds in wire-based atomic chip traps, we will postpone the detailed description of the setup to the next section.

Finally, it must be mentioned, that magnetic fields are not the only way to trap neutral atoms. Using the Stark effect, $V_S = -\alpha|E|^2/2$, neutral atoms can be trapped and manipulated by electrostatic fields [87].

2.1.1   Wire traps

Wire traps are commonly used to trap neutral atoms in a magnetic potential. The magnetic moment of the atoms couples to the magnetic field. Supposing that the

---

[1]There are trap configurations which allow trapping of neutral atoms without any external magnetic bias fields.

Larmor frequency $\omega_L = \mu_B B/\hbar$ is much faster than the spatial motion of the atom, the magnetic moment can be assumed to follow the magnetic trapping field adiabatically. As the frequency of the trapping potential, characterizing the atomic motion, is in all relevant cases much smaller than the Larmor frequency, this approximation is well applicable. Consequently, the magnetic moment of the atom $\boldsymbol{\mu}$ can be replaced by its mean value $\langle F, m_F | \boldsymbol{\mu} | F, m_F \rangle$. Here F denotes the hyperfine spin and m_F the magnetic quantum number. The interaction Hamiltonian for the atom in the magnetic field is

$$V(\mathbf{x}) = -\langle F, m_F | \boldsymbol{\mu} | F, m_F \rangle \mathbf{B}(\mathbf{x}) . \tag{2.1}$$

Depending on the magnetic spin quantum number m_F and the applied magnetic field $\mathbf{B}(\mathbf{x})$, the atomic states can be distinguished into two classes [10]: the low-field seeking states and the high-field seeking states. As their names already suggest, atoms prepared in low-field seeking states favor regions of low magnetic fields in order to minimize their energy. High-field seeking states lower their energy in high magnetic field regions, respectively. As magnetic field maxima are not allowed by Maxwell theory, neutral-atom traps require a magnetic-field minimum, in which atoms in low-field seeking states are trapped. The exception is given by Keppler waveguides [88], where atoms orbit around a current-carrying wire. Atoms are trapped in the high-field seeking state and stabilized due to the conservation of angular momentum.

In the following several special wire-trap configurations are discussed. As the special focus is on atom-chip traps, it will always be assumed that the wires are microstructured on a substrate (see [12] for a review of fabrication techniques). Figures 2.1 and 2.2 show the single-wire and double-wire setup, respectively. The substrate is forming the $\hat{x} - \hat{z}$ plane and the atomic cloud is assumed to be trapped in the positive half space above this plane. There are many experiments, however, which choose to trap the cold-atomic cloud below the wires. This case can be easily taken into account by simply rotating the previously discussed geometry by π about the $\hat{x}$ axis. The only difference between the top and bottom configuration is due to the influence of gravity on the trapping potential. Gravitational forces acting on the atoms lead to an additional term $V_g = -mgy$ in the Hamiltonian. Assuming strong magnetic confinement of the atomic cloud, the gravitational force will be neglected. Finally, the wires are assumed to run along the $\hat{z}$ direction and to be infinitely long.

Single-wire trap

The single-wire trap is the simplest trapping configuration. There are numerous experiments demonstrating the successful trapping of cold-atomic clouds in these single-wire micro traps [67–69, 89, 90]. The setup of the single-wire atom-chip trap, consisting of a single wire and a homogeneous-magnetic bias field parallel to the chip surface, is shown on the right hand side of Fig. 2.1. The bias field $B_{\text{bias}}^{(x)}$ and the circular magnetic field, generated by the current through the wire, form a potential minimum with $\mathbf{B} = 0$ at the point, where the two fields cancel. Atoms, which are prepared in a low-field seeking hyperfine state, can be trapped in this local field minimum. The number of spin flips into untrapped states is, however, very large in zero magnetic field. In order to avoid heavy losses of atoms, a further magnetic-bias

Figure 2.1: *Left:* Contour plot of the magnetic field of the single-wire trap for $B_{\text{bias}}^{(x)} = 10\text{G}$, $B_{\text{bias}}^{(z)} = 5\text{G}$, and $I = 0.1\text{A}$. The upper (right) plot shows a horizontal (vertical) cut through the potential minimum. The dashed lines in the upper and the right plot show the harmonic approximation of the trapping field. *Right:* Setup of the single-wire trap. Bias fields $B_{\text{bias}}^{(x)}$ and $B_{\text{bias}}^{(z)}$ are applied parallel to the substrate surface. The current carrying wire is running along the $\hat{z}$ axis.

field parallel to the wire, $B_{\text{bias}}^{(z)}$, is applied. The longitudinal-magnetic bias field can be generated by bending the end caps of the wire into a "U" or "Z" shape. The most common configuration is the "Z" or Ioffe-Pritchard trap [67, 90, 91]. The less common "U"-configuration has the disadvantage, that the magnetic field vanishes in the center of the trap, as can be seen from symmetry arguments. Finally, assuming $B_{\text{bias}}^{(x)}$ and $B_{\text{bias}}^{(z)}$ to be constant, the resulting magnetic field is

$$\mathbf{B}(\mathbf{x}) = \frac{\mu_0 I}{2\pi} \frac{1}{x^2 + y^2} \begin{pmatrix} -y \\ x \\ 0 \end{pmatrix} + \begin{pmatrix} B_{\text{bias}}^{(x)} \\ 0 \\ B_{\text{bias}}^{(z)} \end{pmatrix}. \tag{2.2}$$

The minimum of the trapping potential is located above the wire at $x_0 = 0$ and has a wire to trap distance of $r_0 = y_0 = \mu_0 I/(2\pi B_{\text{bias}}^{(x)})$. Figure 2.1 shows in the left graph the magnetic trapping potential of a single-wire trap. As a further consequence of the longitudinal bias field $B_{\text{bias}}^{(z)}$, the trapping potential changes in the close surrounding of the minimum from a linear into a harmonic trap (see Fig. 2.1 on the left).

The main disadvantage of the single-wire trap configuration is immediately obvious if more complicated structures are considered, as for example, curved wires. The single-wire trap allows only small deviations from the perpendicular configuration of the bias field $B_{\text{bias}}^{(x)}$ and the wire. The tilting angle is constrained by the requirement that the potential depth must always be larger than the thermal energy $k_B T$ of the atoms. Consequently, the single-wire trap is only convenient for uni-directional guiding.
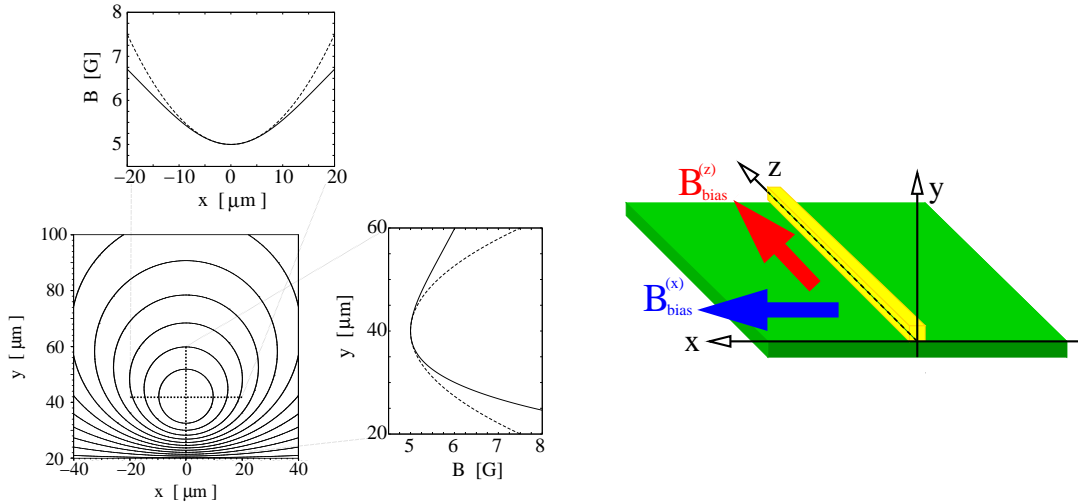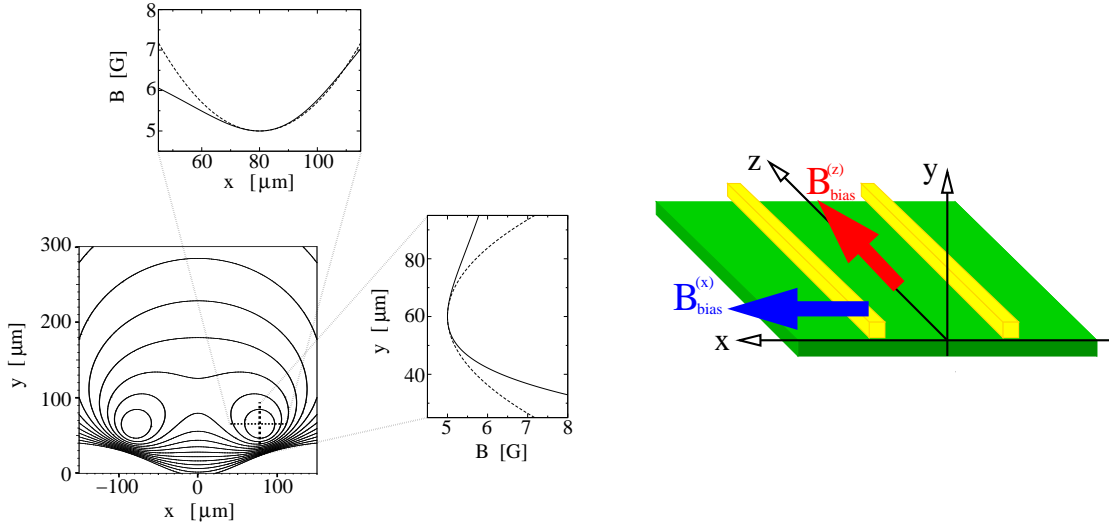
Figure 2.2: *Left:* Contour plot of the magnetic field in the double-wire geometry for $B_{\text{bias}}^{(x)} = 10$G, $B_{\text{bias}}^{(z)} = 5$G, and $I = 0.3$A. The wires are located at $x = \pm 100\mu$m and $y = 0$. Two potential minima are located roughly above the current-carrying wires. The upper (right) plot shows a horizontal (vertical) cut through the right potential minimum. The dashed lines in the upper and the right plot show the harmonic approximation of the trapping field. *Right:* Setup of the double-wire trap. Bias fields $B_{\text{bias}}^{(x)}$ and $B_{\text{bias}}^{(z)}$ are applied parallel to the substrate surface. The current-carrying wire is running along the $\hat{z}$ axis.

Double-wire trap

A more sophisticated trap is provided by the double-wire trap. The double-wire trap has essentially the same setup as the single-wire trap, but with two parallel wires (Fig. 2.2 right). The magnetic field of the double-wire trap is

$$\mathbf{B}(\mathbf{x}) = \frac{\mu_0 I}{2\pi} \left[\frac{1}{\left(x + \frac{d}{2}\right)^2 + y^2} \begin{pmatrix} -y \\ x + \frac{d}{2} \\ 0 \end{pmatrix} + \frac{1}{\left(x - \frac{d}{2}\right)^2 + y^2} \begin{pmatrix} -y \\ x - \frac{d}{2} \\ 0 \end{pmatrix} \right] + \begin{pmatrix} B_{\text{bias}}^{(x)} \\ 0 \\ B_{\text{bias}}^{(z)} \end{pmatrix}, \tag{2.3}$$

where the wires are assumed to be located at $\pm d/2$. The magnetic field of the double-wire trap is shown in Fig. 2.2 on the left.

The main advantages of the double-wire trap lie in its versatility as a single waveguide and a double waveguide. In general, a double-wire trap has two field minima. Depending on the applied currents, bias fields and wire separation two different regimes can be distinguished. Let us consider the situation, where the current in the wires is kept constant and the wire separation d is varied. Defining a critical wire separation $\bar{y}_0 = \mu_0 I/(2\pi B_{\text{bias}}^{(x)})$ we can distinguish two situations. The first case is $d > 2\bar{y}_0$, where the trap minima are located on a horizontal line at $x_0^{L/R} = \mp\sqrt{d^2/4 - \bar{y}_0^2}$ and $y_0 = \bar{y}_0$. Both potential minima lie above the substrate and are suitable as atom traps. This configuration is therefore used as a double waveguide. The second situation is $d < 2\bar{y}_0$, where the trap minima are positioned on a

vertical line at $x_0 = 0$ and $y_0^\pm = \bar{y}_0 \pm \sqrt{\bar{y}_0^2 - d^2/4}$. Again, both minima are above the substrate, but the lower one is very close to the chip surface. The lower potential minimum is unsuitable as an atom trap as the close vicinity of the substrate leads to large losses of atoms. Thus, the latter configuration and the special case, $d = 2\bar{y}_0$, where the minima overlap and form a single minimum, are used as single waveguides. The versatility as a single and double waveguide makes the double-wire trap an ideal configuration for beam splitters [13, 92] and for interferometers [77, 78].

The future analysis of decoherence in the double-wire trap, Sec. 2.4.2, will concentrate on the configuration shown on the left of Fig. 2.2. It should be mentioned that there are further possible double-wire configurations which are suitable as trapping potentials. The most convenient setup is given by two counter-propagating currents in the wires and a magnetic bias field perpendicular to the substrate. This configuration enables multi-directional guiding as has been demonstrated in many experiments [70,71,93,94]. However, this field configuration would also need a magnetic bias field along the waveguide in order to avoid spin flips. Instead of the magnetic bias field along the waveguide an oscillating magnetic field in the vertical direction is proposed [71]. If the oscillation of the vertical magnetic field is slower than the Larmor frequency and faster than the trap frequency, the atoms perceive a time-averaged, non-vanishing potential. This non-vanishing potential avoids the spin flips.

Multi-wire traps

Single- and double-wire configurations are not the only way of creating trapping potentials for neutral atoms. In fact, there is a huge variety of wire traps based on three, four or even more parallel wires with and without additional magnetic bias fields. A set of examples for these multi-wire traps is discussed in references [12,13,93].

2.2   Limiting processes for atom-chip experiments

Microchip traps exploit the huge versatility to design guiding wires on a chip. Consequently, the cold-atomic clouds are guided in the close vicinity of the substrate and the wires. Distances from a few hundred micrometers down to a few micrometers [95] have been achieved in experiments. For distances in this range, the question of how strongly the substrate and wires couple to the atoms immediately arises. Current fluctuations, thermal near fields, technical noise and inhomogeneities in the microstructures impose limitations to the usability of the trapping potentials for cold-neutral atoms. The main obstacles are heating, decoherence and loss processes, which will be briefly discussed now.

2.2.1   Heating

Cold-atomic clouds are commonly cooled down to a few microkelvin and below before they are transfered into the the atom-chip trap. The aim is an atomic cloud, which is frozen out in its transverse states. The cold-atomic cloud is therefore assumed to be in the transverse ground state of the trap. However, coupling to the chip surface

and the wires can heat the atomic cloud. Heating leads either to a broadening of the momentum distribution or even to excitations into higher transverse states as shown schematically in Fig. 1.1. The transition rate between different trap states follows the power law of $\Gamma \sim r_0^{-3}$ as calculated for an atomic cloud above a metallic half space [12] or even $\Gamma \sim r_0^{-4}$ depending on the noise source [96, 97].

Heating of the atomic cloud cannot only occur due to the coupling to its environment. Non-adiabatic changes in the magnetic trapping potential also excite the atoms to higher trap states. Particularly for devices like interferometers, the splitting of the cloud must be done in a suitable i.e. adiabatic way, to avoid the heating of the atomic cloud [76].

2.2.2 Atom losses

Most of the limiting processes for the trapping of atoms in atom-chip traps are difficult to investigate in experiments. Measurements of atom losses, however, are experimentally well accessible [51, 53, 90, 95, 98]. Taking absorption pictures of the cloud before and after a certain hold time at a distance h above the chip surface, gives a direct measure for the number of atoms which got lost from the trap.

From the theoretical point of view, the origin of the losses relies on spin-flip processes. Current fluctuations, or thermal near fields for instance, lead to spin flips from the trapped low-field seeking state, $|F, m_F^i\rangle$, to a high-field seeking state $|F, m_F^f\rangle$. Consequently, the atom sees after the spin flip no longer a potential minimum in the trap center, but a potential maximum. Thus, the atom is expelled from the trap (see Fig. 1.1). Using Fermi's Golden rule, the spin-flip rate for trapped atoms has been calculated as [96]

$$\Gamma_{i\to f} = \frac{1}{\hbar^2} \sum_{\alpha,\beta=x,y,z} \langle F, m_F^i|\mu_\alpha|F, m_F^f\rangle\langle F, m_F^f|\mu_\beta|F, m_F^i\rangle S_{\alpha\beta}(\mathbf{r}, -\omega_{fi})\,, \qquad (2.4)$$

where $m_F^{i/f}$ are the initial/final magnetic spin quantum number of the atom and $S_{\alpha\beta}(\mathbf{r}, -\omega_{fi})$ is the noise power at position $\mathbf{r}$ and transition frequency ω_{fi} between the two atomic hyperfine states. Effects as current fluctuations in the guiding wire or evanescent near fields of the metallic surface are acting as noise sources $S_{\alpha\beta}$. Near-field noise above a planar substrate leads in the low-frequency regime [96, 99] to spin-flip rates of

$$\Gamma_{i\to f} \sim \frac{1}{r_0}\left(1 + \frac{2r_0^3}{3\delta(|\omega|)^3}\right)^{-1}. \qquad (2.5)$$

For wire to atom cloud distances r_0 much larger than the skin depth δ of the metal surface i.e. $r_0 \gg \delta$, the spin-flip rate scales with the power law $1/r_0^4$. In the opposite limit, $r_0 \ll \delta$, the scaling with the wire to atom-cloud distance is proportional to $1/r_0$. Theoretical analysis of the spin-flip rate for different skin depths has shown that the loss of atoms is maximal at distances r_0 comparable to the skin depth δ [100]. The spin-flip rate depends also on the layer thickness and can exhibit a different behavior, depending on the ratio of skin depth, layer thickness and atom-cloud to chip-surface

distance [101]. Experimental findings are in agreement with the theoretically predicted loss rates [53, 95, 98]. Yet, the exact behavior of the loss rate depends very strongly on the geometry of the setup. Recent experiments [53], using a wire with a copper core and and an outer layer of aluminum, have measured loss rates which show a strong dependence on the skin depths and layer thicknesses of both metals. Taking the specific geometry of this experiment [53] into account, the theoretical prediction for the loss rates agrees well with the experimental measurements [100].

2.2.3   Inhomogeneous trapping potentials

With the improvement of the atom-chip trapping technique, it was possible to trap cold-atom clouds closer and closer to the guiding wire. Approaching a thermal-atom cloud or a Bose-Einstein condensate to the chip surface led to a fragmentation of the cloud along the wire axis [49,51–55]. Surprisingly, most of the experiments have shown a fragmentation of the atomic cloud on the same length scale of $200\mu m - 300\mu m$. The fragmentation was only visible if the thermal cloud or Bose-Einstein condensate was approached close to the substrate. This fragmentation of the condensate has not been observed in optical traps, even if the condensate was brought close to an atom-chip surface [50]. The absence of the condensate fragmentation in optical traps is therefore a strong indication that the fragmentation is due to the currents in the wires.

Inhomogeneities of the wires are assumed to be the source of the condensate fragmentation [102]. As the microstructured wires are not perfectly smooth, fluctuations in the width or the central position lead also to an inhomogeneous-magnetic trapping field [2]. Changes in the center position of the wire lead to currents perpendicular to the wire axis. These perpendicular currents generate an unwanted additional potential along the guiding direction. Studies of the potential, generated by a wire with fluctuating width and center position has shown potential fluctuations on the same length scale as observed in the experiments [49,51–55]. Since the wire-width and wire-center position fluctuations depend neither on the material nor on the specific geometry of the trap, similar length scales of the condensate fragmentation have been found in different experiments [49, 51–55]. Recent experimental investigations confirmed the theory of wire-width and central-position fluctuations [103]. The exact shape of a wire was obtained by taking a scanning electron microscope picture. From the detailed knowledge of the wire structure the guiding potential was computed. Comparison of this result with the potential landscape extracted from the condensate fragmentation above the wire, has shown good agreement, corroborating the theory.

Additionally to the fluctuating central position of the wires, there are impurities in the wires. These impurities lead also to a transversal component of the current and thus lead to a distortion of the trapping potential.

---

[2]The model investigated in [102] ascribe the potential fluctuations to the fluctuations of the central position of the wire. In their model the results were unaffected by fluctuations of the wire width.

2.2.4 Decoherence

The existence of coherent states is one of the most important peculiarity of quantum mechanics. However, due to the coupling of the system to its environment, decoherence restricts the lifetime of coherent states considerably. Hence, systems are needed which are only weakly coupled to their environment. For this reason, trapped neutral atoms seem to be ideal candidates for coherent transport. The expected long coherence times and the huge versatility of the micro traps suggested the use of cold atoms on atom chips for quantum information processing [16, 17]. A further application arises from atomic clouds which are prepared in a coherent superposition of two internal spin states. These atomic ensembles are promising candidates for a miniature atomic clock on a microchip [7].

The main advantage of neutral atoms is the absence of charge, that eliminates the strong Coulomb coupling. Any decoherence mechanism can only arise via magnetic fields which have a much weaker interaction strength. Moreover, atom chips provide highly confined trapping potentials which should prevent the decoherence of the atoms via transverse states (Fig. 1.1). These tight traps are, however, only obtained in the close vicinity to the current-carrying wires. Theoretical studies show that, if the atom cloud is approached to the wire, the increase of decoherence due to the current noise is larger than the decrease of decoherence due to the increase of the transverse level spacing [97]. In fact, the decoherence rate increases with the wire to trap distance r_0 as $\Gamma \sim 1/r_0^4$. However, there is not only decoherence due to transitions to higher transverse trap states. In addition, decoherence along the trapping axis of the atomic cloud can occur. Theoretical studies for an atom cloud in the vicinity of a metallic plane [66] has shown that the decoherence length is of the order of surface to trap distance r_0. In this work, the transverse states were assumed to be frozen out. Thus all atoms were assumed to be confined to the ground state of the trap. Nevertheless, similar decoherence lengths are obtained if the lowest transversal states are included [97].

So far only decoherence in non-interacting thermal clouds has been discussed. Recent theoretical work on decoherence of Bose-Einstein condensation in micro traps indicates a suppression of decoherence due to the presence of interactions [104]. However, interacting atomic clouds are not discussed within the scope of this thesis.

Applications for quantum information and metrology requires the coherent superposition between different spin states of the cold atoms. Here, the concern lies in the maintaince of the coherence within the internal states of each atom. The atoms do not have to conserve a coherent state in their spatial degrees of freedom. First experimental results using Ramsey spectroscopy gave decoherence times of a few seconds [7]. Furthermore, the decoherence times were independent of the distance of the atoms to the surface and to the wire[3]. In fact, the decoherence times are similar to those for atoms trapped in macroscopic magnetic traps and an additional decoher-

---

[3]Measurement of [7] covered trap-surface and trap-wire distances of 4μm - 130μm and 34μm - 160μm, respectively.

ence effect could not be attributed to the presence of the atom chip.

In contrast, coherent transport requires that the atomic cloud conserves its spatial coherence. The successful implementation of an interference experiment would be essential to measure the coherence properties of the atom-chip waveguides. There are several suggestions of microchip interferometers based on different approaches. Present proposals for atom-chip interferometers either suggest to split the atom cloud in a time-dependent potential [76, 77] or split and recombine the matter wave spatially [78].

2.3   Decoherence in multi-wire configurations

Motivated by the promising ways which atom-chip traps offer for transport and manipulation of coherent matter waves, we will focus on decoherence of thermal-atom clouds[4] in microwire atom-chip traps in the following sections. First, a general formalism to treat the influence of current fluctuations on the decoherence properties of the trapped-atom cloud will be developed. The formalism will be designed to take multi-wire trapping configurations into account. This general approach enables us not only to consider decoherence in the huge variety of single waveguides, but will also include multi-waveguide configurations. Hence, the theoretical approach allows us to examine decoherence effects in particularly interesting multi-waveguide configurations such as the double waveguide. The double waveguide forms the basic building block for an interference experiment required to demonstrate the coherent transport of cold-atom clouds.

2.3.1   Current-noise correlation function

Considering atom-chip traps based on current-carrying wires, it is evident to investigate the impact of current noise as a source of decoherence. Fluctuations of the magnetic bias fields $B_{\text{bias}}^{(x)}$ and $B_{\text{bias}}^{(z)}$, required to form the trapping potential, will be neglected. The current noise couples to the atoms through the magnetic field, which is generated by the current. Thus, the current fluctuations lead to a fluctuating magnetic field. The field fluctuations $\delta\mathbf{B}$ are linked to the current fluctuations via the Biot-Savart law

$$\mathbf{B}(\mathbf{x}) = \frac{\mu_0}{4\pi} \int d^3x \, \mathbf{j}(\mathbf{x}') \times \frac{\mathbf{x} - \mathbf{x}'}{|\mathbf{x} - \mathbf{x}'|^3} \,, \tag{2.6}$$

where $\mu_0 = 0.4\pi \cdot 10^{-6} N/A^2$ is the vacuum permeability. The atoms in turn couple to the magnetic-field fluctuations through their magnetic moment, Eq. (2.1). Appendix A shows a detailed derivation of the potential-noise correlator $\langle \delta V(\mathbf{x}) \delta V(\mathbf{x}') \rangle$ derived from the current-noise correlations. Current noise, thus, is directly translated into a potential fluctuation leading to decoherence of the atomic cloud.

---

[4]The term "thermal-atom cloud" is used to distinguish a non-condensed atom cloud from an atom cloud with a finite condensate fraction. The term "thermal" will be neglected in the following sections.
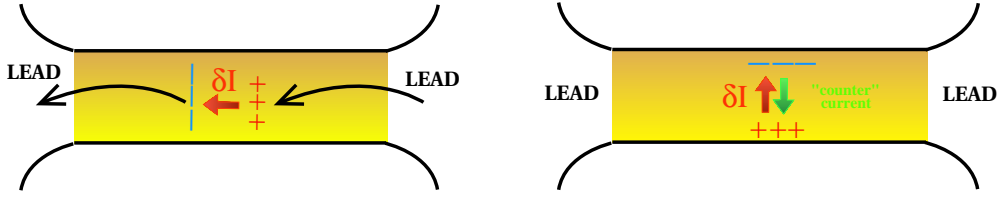
Figure 2.3: Sketch of transversal and longitudinal current fluctuations in a wire on the atom chip. *Left:* Longitudinal fluctuations. The leads act as reservoirs and hence no charging effects occur. *Right:* Transversal fluctuations. Charging effects at the wire surfaces yield to a counteracting electrical field which suppresses the current fluctuations.

In the following, the wire, generating the potential fluctuations, is assumed to be one dimensional. This is a reasonable assumption for wire to trap distances r_0 which are much larger than the wire cross section. Typically, wires heights l_h are about 1μm and wire widths are 10μm to 50μm [12]. Recently, microstructuring techniques were reported that enable atom-chip trap fabrication with wire widths below 1μm [105]. As a consequence of the restriction to one-dimensional wires, current fluctuations are assumed to occur only along the wire. Hence, the current density is approximated as

$$\mathbf{j}(\mathbf{x}, t) = I(z, t)\delta(x)\delta(y)\hat{\mathbf{z}} ,\tag{2.7}$$

where $\hat{\mathbf{z}}$ is the unit vector in $\hat{z}$-direction. The fluctuations of the current density are defined by $\delta\mathbf{j}(\mathbf{x}, t) \equiv \mathbf{j}(\mathbf{x}, t) - \langle\mathbf{j}(\mathbf{x})\rangle$. Average currents will be included as a static potential $V_t(\mathbf{r}_\perp)$. Transversal current fluctuations lead to surface charging and thus to an electrical field which points in opposite direction to the current fluctuation (Fig. 2.3). This surface charging effect will suppress transversal fluctuations which are slow compared to RC-frequency, $\omega_{RC} = \sigma\Lambda/\epsilon_0 l_w$. Here, σ is the conductivity of the wire, ϵ_0 the (vacuum) dielectric constant, and $\Lambda \approx 1\text{\AA}$ is the screening length of the metal. This leads to RC-frequencies of $\omega_{RC} \approx 10^{13}$Hz for wire widths of $l_w = 10\mu$m and for typical values for the conductivity in a metal. The characteristic time scale for the atomic motion in the trap is given by the frequency of the trapping potential $\omega \approx 10^4$Hz. Thus, considering atom-chip traps with $\omega \ll \omega_{RC}$ the current fluctuations can be taken along $\hat{\mathbf{z}}$ as a direct consequence of the quasi-one dimensionality of the wire.

Finally, we have to be more specific about the form of the noise correlator. We assume the current fluctuations to be spatially uncorrelated as they have their origin in electron-scattering processes. Hence, the correlator $\langle\delta I(z)\delta I(z')\rangle$ has the form [106, 107]

$$\langle\delta I(z, t)\delta I(z', t')\rangle = 4k_{\text{B}}T_{\text{eff}}(z)\sigma A\,\delta(z - z')\delta_c(t - t') .\tag{2.8}$$

Here, k_{B} is the Boltzmann constant. The effective noise temperature is given by [106, 107]

$$T_{\text{eff}}(z) = \int dE f(E, z)[1 - f(E, z)] ,\tag{2.9}$$

where $f(E, z)$ is the energy- and space-dependent non-equilibrium distribution function. A finite voltage across the wire induces a change in the velocity distribution of the electrons and the electrons are thus no longer in thermal equilibrium. Nevertheless, the deviation from an equilibrium distribution is small at room temperature due to the large number of inelastic-scattering processes. The effective temperature T_{eff} accounts for possible non-equilibrium effects such as shot noise. However, contributions of non-equilibrium effects to the noise strongly depend on the length L of the wire compared to the characteristic inelastic scattering lengths. For instance, strong electron-phonon scattering leads to an energy exchange between the lattice and the electrons. The non-equilibrium distribution is "cooled" to an equilibrium distribution at the phonon temperature. Thus, non-equilibrium noise sources, such as shot noise, are strongly suppressed for wires much longer than the electron-phonon scattering length l_{ep} and the noise in the wire is essentially given by the equilibrium Nyquist noise [106, 108, 109]. As the wire lengths used in present experiments are much longer than l_{ep}, we will assume $T_{\text{eff}} \approx 300\text{K}$ in all our calculations. Finally, the function

$$\delta_c(t) = \frac{1}{\pi} \frac{\tau_c}{t^2 + \tau_c^2} \tag{2.10}$$

in Eq. (2.8), is a representation of the delta function. The correlation time τ_c is given by the time scale of the electronic scattering processes.

2.3.2   Equation of motion for the atom cloud

The quantum-dynamical evolution, decay and decoherence of the atom cloud will be described by a density matrix approach. The system is characterized by its density matrix $\rho(\mathbf{x}, \mathbf{x}', t)$, which is here a function of the spatial coordinates $\mathbf{x}$, $\mathbf{x}'$ and the time t. Time evolution of the atomic cloud can be obtained from the von Neumann equation

$$i\hbar \frac{\partial}{\partial t} \rho = [\hat{H}, \rho] . \tag{2.11}$$

The Hamiltonian

$$\hat{H} = \frac{\mathbf{p}^2}{2m} + V_t(\mathbf{r}_\perp) + \delta V(\mathbf{x}, t) , \tag{2.12}$$

describes the time evolution of the trapped-atomic cloud. Here, $V_t(\mathbf{r}_\perp)$ is the confining potential, which will be assumed to be constant along the trap. Writing $\mathbf{r}_\perp$ denotes the coordinate perpendicular to the direction of the current-carrying wire and the waveguide. Finally, a random fluctuation of the potential $\delta V(\mathbf{x}, t)$ arising from the current noise, is included in the Hamiltonian. In order to keep the treatment as general as possible, the problem will be formulated for a system of N parallel quasi-one dimensional magnetic traps generated by a set of M parallel wires on the chip. In general, the number of traps are not required to coincide with the number of wires i.e. $N \neq M$.

For clarity, the same coordinate system as introduced in Sec 2.1.1 (see Fig. 2.1 and Fig. 2.2) will be used in all further calculations. The surface of the atom chip is assumed to lie in the $\hat{x}$-$\hat{z}$ plane and the atoms are trapped in the half space, $y > 0$,

above the chip. All wires on the atom chip, required to form the trapping field, are assumed to be aligned in $\hat{z}$-direction.

The aim of the following discussion is a simplification of the von Neumann equation for the system. To achieve this, the three-dimensional formulation of the equation of motion will be reduced to an effective one-dimensional problem. Returning to Eq. (2.11) and inserting the Hamiltonian Eq. (2.12), the equation of motion in position representation reads

$$
\begin{aligned}
i\hbar\frac{\partial}{\partial t}\quad \rho(\mathbf{x}, \mathbf{x}', t) = & \left[-\frac{\hbar^2}{2m}\left(\frac{d^2}{d\mathbf{x}^2} - \frac{d^2}{d\mathbf{x}'^2}\right) + V_t(\mathbf{r}_\perp) \right. \\
& \left. -V_t(\mathbf{r}'_\perp) + \delta V(\mathbf{x}, t) - \delta V(\mathbf{x}', t) \right]\rho(\mathbf{x}, \mathbf{x}', t) .
\end{aligned}
\tag{2.13}
$$

To derive a quasi-one dimensional expression for Eq. (2.13) we expand the density matrix in eigenmodes of the transverse potential $\chi_n(\mathbf{r}_\perp)$:

$$
\rho(\mathbf{x}, \mathbf{x}', t) = \sum_{n,m} \chi_n^*(\mathbf{r}_\perp)\chi_m(\mathbf{r}'_\perp)\rho_{nm}(z, z', t) .
\tag{2.14}
$$

Here, the channel index n labels the transverse states of the trapping potential. The transverse wavefunctions $\chi_n(\mathbf{r}_\perp)$ are chosen mutually orthogonal and are eigenfunctions of the transverse part of the Hamiltonian. Thus, the transverse wavefunctions are eigenfunctions of Eq. (2.12) in the sense that

$$
\left[-\frac{\hbar^2}{2m}\nabla^2_{\mathbf{r}_\perp} + V_t(\mathbf{r}_\perp) \right] \chi_n(\mathbf{r}_\perp) = E_n\chi_n(\mathbf{r}_\perp) .
\tag{2.15}
$$

In the next step, the decomposition (2.14) in transverse and longitudinal components of the density matrix is inserted in the von Neumann equation, Eq. (2.11). Making use of the orthogonality and the completeness of the transverse states $\chi_n(\mathbf{r}_\perp)$ we obtain a one-dimensional equation for the time evolution of the density matrix

$$
\begin{aligned}
& \left[i\hbar\frac{\partial}{\partial t} + \frac{\hbar^2}{2m}\left(\frac{d^2}{dz^2} - \frac{d^2}{dz'^2}\right) - \Delta E_{lk} \right] \rho_{lk}(z, z', t) \\
& = \sum_n [\delta S_{ln}(z, t)\rho_{nk}(z, z', t) - \delta S_{nk}(z', t)\rho_{ln}(z, z', t)] .
\end{aligned}
\tag{2.16}
$$

Here, the abbreviation $\Delta E_{lk} = E_l - E_k$ was introduced for the difference of the transverse energy levels, and the fluctuations $\delta S_{nk}(z)$ are defined as

$$
\delta S_{nk}(z, t) = \int d\mathbf{r}_\perp \, \chi_n(\mathbf{r}_\perp)\delta V(\mathbf{x}, t)\chi_k^*(\mathbf{r}_\perp) .
\tag{2.17}
$$

The left hand side of the reduced von Neumann equation, Eq. (2.16), describes the evolution of an atom wavefunction in the non-fluctuating trapping potential. In order to keep the notation short, this part of the von Neumann equation will hereafter be abbreviated by $(i\hbar\partial_t - \hat{H}_{lk})$. More interesting are the terms on the right hand side of Eq. (2.16), which contain the influence of the potential fluctuations. The

fluctuations of the confining potential are described by the matrix elements $\delta S_{nk}(z, t)$, which imply transitions between different discrete transverse energy levels induced by the fluctuating potential. In fact, transitions between different transverse levels also influence the longitudinal motion of the atomic cloud. The coupling of the fluctuating potential to the longitudinal motion of the atomic cloud is included in the z dependence of $\delta S_{nk}(z, t)$.

2.3.3 Noise-averaged equation of motion

For the explicit treatment of the stochastic equation of motion, averaging over the fluctuations δS_{nk} is required. It is therefore the goal of this section to derive the equations of motion for the density matrix $\langle \rho \rangle$ averaged over the potential fluctuations [110, 111].

Cumulant expansion

In addition to the averaging, the equation of motion will be simplified by a cumulant expansion to the first non-vanishing order. Instead of directly moving on to the derivation of the equation of motion for the density matrix, a brief recapitulation of the cumulant expansion is provided. Here, only a short derivation of the cumulant-expansion method will be given, following the detailed discussion in [111].

To keep the expressions compact, Eq. (2.16) is rewritten as

$$\left(i\hbar\partial_t - \tilde{H} \right) \rho = \delta\tilde{S}\rho \,, \tag{2.18}$$

where the spatial coordinates $\mathbf{x}$, $\mathbf{x}'$, time t and all indices have been suppressed. The components of the quantities $\tilde{H}$ and $\delta\tilde{S}$ are defined as

$$\tilde{H}_{lkij} = \hat{H}_{lk}\delta_{li}\delta_{kj} \,, \tag{2.19}$$

$$\delta\tilde{S}_{lkij} = \delta S_{li}(z,t)\delta_{kj} - \delta S_{jk}(z',t)\delta_{li} \,. \tag{2.20}$$

The product in Eq. (2.18) is an abbreviation for $\tilde{A}\rho = \sum_{ij} A_{lkij}\rho_{ij}$. It is, however, more convenient to think of Eq. (2.18) as a vector equation instead of a matrix equation. This corresponds to the matrix elements of the density matrix written into a column vector $\boldsymbol{\rho}$. Analogously, all the operators $\hat{H}$, $\delta\tilde{S}$, etc., are rewritten into matrices. Both notations are obviously equivalent and the vector form of the equation of motion will be used later in Sec. 2.4.

Returning to Eq. (2.18), the first step is a transformation into the interaction picture. Following the usual procedure [112, 113], the transformation leads to the time evolution of the density matrix in the interaction-picture representation $\boldsymbol{\rho}_I$ given by

$$\boldsymbol{\rho}_I(t) = \mathcal{T}\left[\exp\left(-\frac{i}{\hbar}\int_0^t dt' \, \delta\tilde{S}(t') \right) \right] \boldsymbol{\rho}_I(0) \,, \tag{2.21}$$

where $\mathcal{T}$ is the time-ordering operator. Next, Eq. (2.21) is averaged over the potential fluctuations. The averaging and the time ordering commute and the expression obtained is

$$\langle \boldsymbol{\rho}_I(t) \rangle = \mathcal{T} \left[\langle \exp\left(-\frac{i}{\hbar} \int_0^t dt' \, \delta\tilde{S}(t') \right) \rangle \right] \langle \boldsymbol{\rho}_I(0) \rangle \,. \tag{2.22}$$

The correlation time of the current fluctuations τ_c is very short compared to the time scale of the atomic motion. Hence, all correlators and cumulants vanish unless the time points, t_1 to t_k, lie within a time domain of τ_c. Assuming moreover, that fluctuations $\delta\tilde{S}$ are small, a cumulant expansion

$$\log\left(\langle \exp\left(\chi \int_0^t dt' \, \delta\tilde{S}(t') \right) \rangle \right) = \sum_{k=0}^{\infty} \int dt_1 \cdots \int dt_k \frac{C_k}{k!} \chi^k \,, \tag{2.23}$$

can be applied. The coefficients

$$C_k = \langle\langle \delta\tilde{S}(t_1) \cdots \delta\tilde{S}(t_k) \rangle\rangle \,, \tag{2.24}$$

are called the cumulants and χ is the small expansion parameter which is in the end taken to $\chi = 1$. Consequently, Eq. (2.22) turns into

$$\langle \boldsymbol{\rho}_I(t) \rangle = \mathcal{T} \left[\exp\left(\sum_{k=0}^{\infty} \left(-\frac{i}{\hbar} \right)^k \int dt_1 \cdots \int dt_k \frac{C_k}{k!} \chi^k \right) \right] \langle \boldsymbol{\rho}_I(0) \rangle \,. \tag{2.25}$$

The contribution of the k-th cumulant is now of the order $\chi^k \tau_c^{k-1} t$ and Eq. (2.25) is an expansion in powers of $\chi\tau_c$. Finally, Eq. (2.25) is approximated to second order, given by

$$\langle \boldsymbol{\rho}_I(t) \rangle \approx \exp\left(-\frac{i}{\hbar} \int_0^t dt_1 \chi \langle \delta\tilde{S}(t_1) \rangle - \frac{1}{\hbar^2} \int_0^t dt_1 \int_0^{t_1} dt_2 \, \chi^2 \langle\langle \delta\tilde{S}(t_1) \delta\tilde{S}(t_2) \rangle\rangle \right) \langle \boldsymbol{\rho}_I(0) \rangle \,. \tag{2.26}$$

Taking χ to 1, the approximated time evolution of the density matrix is the solution of the differential equation

$$i\hbar \partial_t \langle \boldsymbol{\rho}_I(t) \rangle = \langle \delta\tilde{S}(t) \rangle \langle \boldsymbol{\rho}_I(t) \rangle - \frac{i}{\hbar} \int_0^t dt_2 \, \langle\langle \delta\tilde{S}(t) \delta\tilde{S}(t_2) \rangle\rangle \langle \boldsymbol{\rho}_I(t) \rangle \,, \tag{2.27}$$

up to errors of second order. Equation (2.27) is the cumulant approximation for the equation of motion in the interaction-picture representation.

Averaged equation of motion for the density matrix

Let us return to the stochastic equation (2.18) for the density matrix. Averaging over the fluctuating potential, using the cumulant expansion [111], the expression Eq. (2.27) is obtained. Transforming Eq. (2.27) back into the Schrödinger picture and using the matrix notation again one obtains

$$\left(i\hbar \partial_t - \tilde{H} \right) \langle \rho(t) \rangle = \langle \delta\tilde{S}(t) \rangle \langle \rho(t) \rangle - \frac{i}{\hbar} \int_0^t dt' \langle\langle \delta\tilde{S}(t) e^{-\frac{i}{\hbar}\tilde{H}t'} \delta\tilde{S}(t-t') \rangle\rangle e^{\frac{i}{\hbar}\tilde{H}t'} \langle \rho(t) \rangle \,. \tag{2.28}$$

The mean value of the potential fluctuation $\langle \delta V \rangle$ is zero, since the static potential is already included in the Hamiltonian on the left hand side of Eq. (2.28). Hence, the first term on the right hand side of Eq. (2.28) vanishes. The second cumulant corresponds to the variance, and as $\langle \delta \tilde{S}(t) \rangle = 0$, the variance is identical with the correlator $\langle \delta \tilde{S}(t) \delta \tilde{S}(t') \rangle$. The explicit expression for the reduced-potential correlator, $\langle \delta S_{nm}(z,t) \delta S_{ij}(z',t') \rangle$, is derived in Appendix A. The calculation is based on the connection of the current correlator $\langle \delta I(z,t) \delta I(z',t') \rangle$, to the potential correlator, $\langle \delta V(\mathbf{x},t) \delta V(\mathbf{x}',t') \rangle$ as discussed in Sec. 2.3.1. Finally, potential and projected potential fluctuations are connected via Eq. (2.17).

Reinserting the explicit expressions for $\tilde{H}$ and $\delta \tilde{S}$, leads to the desired equation of motion for the density matrix

$$
\begin{aligned}
\left(i\hbar \partial_t - \hat{H}_{lk} \right) \langle \rho_{lk}(z,z',t) \rangle \;=\; & -\frac{i}{\hbar} \sum_{ijmn} \int\limits_0^t d\tau \int\limits_{-\infty}^{\infty} d\tilde{z} \int\limits_{-\infty}^{\infty} d\tilde{z}' K_{ij}(z-\tilde{z}, z'-\tilde{z}', t-\tau) \\
& \times \left[\langle \delta S_{li}(z,t) \delta S_{im}(\tilde{z},\tau) \rangle \delta_{kj}\delta_{jn} \right. \\
& \quad + \langle \delta S_{jk}(z',t) \delta S_{nj}(\tilde{z}',\tau) \rangle \delta_{li}\delta_{im} \\
& \quad - \langle \delta S_{li}(z,t) \delta S_{nj}(\tilde{z}',\tau) \rangle \delta_{im}\delta_{jk} \\
& \quad \left. - \langle \delta S_{jk}(z',t) \delta S_{im}(\tilde{z},\tau) \rangle \delta_{jn}\delta_{li} \right] \langle \rho_{mn}(\tilde{z},\tilde{z}',\tau) \rangle .
\end{aligned}
\tag{2.29}
$$

The kernel $K_{ij}(z-\tilde{z}, z'-\tilde{z}', t)$ is the Fourier transform of

$$
K_{ij}(q,q',t) = \exp\left(-i\frac{\hbar}{2m}\left(q^2 - q'^2 \right) t - \frac{i}{\hbar}\Delta E_{ij} t \right) ,
\tag{2.30}
$$

which can be explicitly evaluated. However, this has no advantage for our further discussion.

Equation (2.29) is the most general form of the stochastic equation of motion. In this form no assumptions have yet been made about the wire configuration which enter via the projected-potential correlator. It is valid for an arbitrary form of the transverse confining potential, thus, in particular, for single- and double-wire traps. Hence, Eq. (2.29) will be the starting point for all further calculations, investigating specific trapping configurations. However, there is still the kernel Eq. (2.30), which requires some further simplification.

Markov approximation

The dominating source of the current noise in the wires is due to the scattering of electrons with phonons, electrons and impurities. These scattering events are correlated on a time scale much shorter than the characteristic time scales of the atomic system. This separation of time scales allows a simplification of the equation of motion (2.29), using a Markov approximation [110, 111].

As a consequence of Eq. (2.8), the correlation function of the fluctuating potential will be of the form

$$
\langle \delta V(\mathbf{x},t) \delta V(\mathbf{x}',t') \rangle = \delta_c(t-t') \langle \delta V(\mathbf{x}) \delta V(\mathbf{x}') \rangle .
\tag{2.31}
$$

Using Eq. (2.17) provides the expression for the projected-potential correlator

$$\langle \delta S_{im}(z,t) \delta S_{nj}(z',t') \rangle = \delta_c(t-t') \langle \delta S_{im}(z) \delta S_{nj}(z') \rangle . \qquad (2.32)$$

Replacing all the correlation functions in the equation of motion (2.29) by the expression (2.32) enables an explicit evaluation of the time integration. The time integration can be performed using the fact, that the averaged density matrix $\langle \rho(\tau) \rangle$ varies slowly on the correlation time scale τ_c. Thus, $\langle \rho(\tau) \rangle$ can be evaluated at time t and taken out of the time integral. Finally, taking τ_c to zero, the Fourier transform of the kernel (2.30) leads to a product of delta functions in the spatial coordinates. Performing the remaining spatial integrations over $\tilde{z}$ and $\tilde{z}'$, Eq. (2.29) reduces to

$$\left(i\hbar\partial_t - \hat{H}_{lk} \right) \langle \rho_{lk}(z,z',t) \rangle = -\frac{i}{2\hbar} \sum_{mn} [\langle \delta S_{ln}(z) \delta S_{nm}(z) \rangle \langle \rho_{mk}(z,z',t) \rangle \quad (2.33)$$
$$+ \quad \langle \delta S_{mk}(z') \delta S_{nm}(z') \rangle \langle \rho_{ln}(z,z',t) \rangle$$
$$- \quad 2 \langle \delta S_{lm}(z) \delta S_{nk}(z') \rangle \langle \rho_{mn}(z,z',t) \rangle] .$$

This formula (2.33) finally allows an explicit calculation of the decoherence rates for the cold atoms in the microchip trap. Only the wire, or the trapping configuration has to be further specified. In general, the trapping potential has N minima, i.e., the channel index n can be written as $n = (\alpha, n_x, n_y)$, $\alpha = 1, ..., N$. In all further considerations, the minima are assumed to be well-separated in $\hat{x}$-$\hat{y}$ direction, such that all matrix elements δS_{ij} with different trap labels α are negligible.

There are three terms on the right hand side of Eq. (2.33), describing the influence of the current fluctuations on the atomic cloud. The projected-potential correlators in the first two terms are spatially auto-correlated. The third term, however, correlates fluctuations at z and z' and is therefore the contribution, which is responsible for the spatial decoherence of the atomic cloud. Having a closer look at Eq. (2.33) allows an identification of the terms involved in intra-waveguide and inter-waveguide processes. Under the assumption of well-separated guiding potentials, the first and second term on the right hand side of Eq. (2.33) depend only on a single trap label. Hence, these terms lead only to transitions within transverse states of the same waveguide. In contrast to the first two terms, the third term may have different trap labels for δS_{lm} as compared to δS_{nk}. Since current noise in one particular wire generates fluctuations of the magnetic field in all trapping wells, there will be a correlation between the fluctuations in different traps. It is, hence, this third term in Eq. (2.33) which describes the correlation between potential fluctuations in different traps.

2.4   Application to special trapping potentials

After the successful derivation of a general formalism to describe the decoherence in a multi-waveguide it is now time to study a few simple applications. Starting with the simplest situation: the single waveguide in Sec. 2.4.1, the dynamics of the noise-averaged density matrix will be discussed using Eq. (2.33). Subsequently, the dynamic in the double waveguide will be discussed. As previously mentioned, this

waveguide configuration is of particular interest. Double waveguides are the key in-gredient for an atom-cloud interferometer as suggested in [76–78]. Decoherence of atom clouds, which are in a coherent superposition of the left and right arm of the interferometer, will be the focus of Sec. 2.4.2.

The brackets denoting the averaging will be suppressed for the remainder of this chapter to keep the notation short. Thus, from now on, the density matrix ρ_{ij} denotes the averaged density matrix $\langle \rho_{ij} \rangle$.

2.4.1   Single-wire configuration

The geometric properties of the single waveguide was previously discussed in Sec. 2.1.1. Forming the minimal setup for a wire atom-chip trap, the single-wire waveguide con-sist only of a single wire and a homogeneous bias field. The schematic setup is shown in Fig. 2.1.

Derivation of the projected-potential correlator

All ingredients required to calculate the dynamics of the system were derived in the previous section. The key equation is the general expression for the averaged equation of motion Eq. (2.33). The remaining exercise concerns the derivation of an explicit expression of Eq. (2.33) for the single-wire trap. Hence, it is the main task of this section to derive the projected-potential correlator, $\langle \delta S_{im}(z) \delta S_{nj}(z') \rangle$, for the single-wire trap geometry. Using Eqs. (2.17), (2.7), (2.8) and the explicit expression for the magnetic field of the single-wire atom-chip trap, Eq. (2.2), leads to

$$\langle \delta S_{im}(z) \delta S_{nj}(z') \rangle = A_{imnj} J(z - z') \ . \tag{2.34}$$

The transition matrix elements are given by

$$
\begin{aligned}
A_{imnj} = \ & k_{\mathrm{B}} T_{\mathrm{eff}} \sigma A \left(\frac{\mu_0 g_F \mu_B}{\pi} \frac{B_{\mathrm{bias}}^{(x)}}{B_{\mathrm{bias}}^{(z)}} \right)^2 \\
& \times \int d\mathbf{r}_\perp \ \chi_i(\mathbf{r}_\perp)(y - y_0)\chi_m^*(\mathbf{r}_\perp) \int d\mathbf{r}'_\perp \ \chi_n(\mathbf{r}'_\perp)(y' - y_0)\chi_j^*(\mathbf{r}'_\perp) \ .
\end{aligned}
\tag{2.35}
$$

This part describes transitions between the different transverse states of the trap. Longitudinal dynamics along the trap is contained in the factor

$$J(z) = \frac{1}{r_0^5} \int\limits_{-\infty}^{\infty} d\tilde{z} \left[1 + \tilde{z}^2 \right]^{-\frac{3}{2}} \left[1 + (z/r_0 - \tilde{z})^2 \right]^{-\frac{3}{2}} \ , \tag{2.36}$$

describing the spatial dependence of the noise correlator along the waveguide. A more detailed derivation of the correlation function is given in Appendix A. The integration in Eq. (2.35) can be done explicitly using harmonic-oscillator states for $\chi_n(\mathbf{r}_\perp)$. Using the harmonic-oscillator states is a good approximation as long as $B_{\mathrm{bias}}^{(z)}$ is of the order of $B_{\mathrm{bias}}^{(x)}$ and the wire to trap distance r_0 is much larger than the transverse size w of

the trapped state. Both requirements are usually well satisfied in experiments. The dashed line in Fig. 2.1 shows the harmonic approximation of the trapping potential. Using the harmonic approximation, the steepness of the trapping potential can be characterized by its trap frequencies. It turns out that the two frequencies coincide

$$\omega = \sqrt{\frac{2\mu_B g_F}{m B_{\text{bias}}^{(z)}} \frac{B_{\text{bias}}^{(x)}}{y_0}} \; , \tag{2.37}$$

i.e., the trap potential can be approximated by an isotropic two-dimensional harmonic oscillator (2D-HO). After the integration over the transverse coordinates, Eq. (2.35) reduces to

$$A_{imnj} = A_0 w^2 \, \delta_{i_x m_x} \tilde{\delta}_{i_y m_y} \delta_{n_x j_x} \tilde{\delta}_{n_y j_y} \; . \tag{2.38}$$

Here,

$$\tilde{\delta}_{i_y m_y} = \sqrt{m_y + 1} \, \delta_{i_y, m_y+1} + \sqrt{m_y} \, \delta_{i_y, m_y-1} \; , \tag{2.39}$$

and the indices n_x, n_y denote the energy levels in $\hat{x}$ and $\hat{y}$ direction of the 2D-HO. The prefactor A_0 is

$$A_0 = \frac{1}{2} k_{\text{B}} T_{\text{eff}} \sigma A \left(\frac{\mu_0 g_F \mu_B}{\pi} \frac{B_{\text{bias}}^{(x)}}{B_{\text{bias}}^{(z)}} \right)^2 \; , \tag{2.40}$$

and $w = \sqrt{\hbar/(m\omega)}$ is the oscillator length of the harmonic potential.

Before moving on to derive the equation of motion for the averaged density matrix, it seems apposite to discuss some consequences of expression (2.38). Inspection of the coefficients A_{imnj} in Eq. (2.38) shows that there is no direct influence on the longitudinal motion of the atom, since the matrix element A_{iijj} vanishes. This result is not unexpected, as the wire is assumed to be strictly one dimensional. Only current fluctuations along the wire are taken into account, which, consequently, give rise to fluctuations in the trapping field solely along the transverse directions of the trapping potential. In fact, only transitions between energy levels of the $\hat{y}$-component of the 2D-HO give a non-vanishing contribution. An explanation can be obtained by examining the change of the trap-minimum position under variation of the current in the wire. Changing the current by δI leaves the trap minimum in $\hat{x}$-direction unchanged at $x_0 = 0$, but shifts the $\hat{y}$-trap minimum by $\delta y_0 = \mu_0 \delta I/(2\pi B_{\text{bias}}^{(x)})$. Note, however, that the non-existence of fluctuations along the $\hat{x}$-direction is a consequence of the very specific choice of the magnetic field direction. The configuration studied here corresponds to the ideal case of the magnetic bias fields being perfectly aligned with the substrate. Having a slight misalignment gives rise to transitions among $\hat{x}$ and $\hat{y}$ states of the 2D-HO. Finally, it is important to note, that even though there is no direct coupling to the motion along the wire there can still be spatial decoherence in $\hat{z}$-direction. The coupling along the wire requires transitions to neighboring transverse energy levels. This will also be apparent from the final result for ρ obtained from Eq. (2.33).

Solution of the equation of motion

Eventually, the expression for the projected-potential correlator, as given by Eqs. (2.34), (2.38) and (2.40), can be inserted into the equation of motion for ρ. This leads to a matrix equation for the averaged density-matrix vector

$$\left[i\hbar\partial_t - \tilde{H}(z,z') \right] \boldsymbol{\rho}(z,z',t) = -i\hbar\tilde{A}(z-z')\boldsymbol{\rho}(z,z',t) \,, \qquad (2.41)$$

where $A(z-z') = \frac{w^2}{\hbar^2} A_0 J(z-z')$. The density-matrix vector is constructed by writing all the matrix elements in a vector

$$\boldsymbol{\rho} = \left(\rho_{0000}, \cdots, \rho_{l_x l_y k_x k_y}, \cdots \right)^T. \qquad (2.42)$$

Instead of discussing the general equation of motion for $\boldsymbol{\rho}$, we will only consider the case, in which the two lowest energy levels of the transverse motion are taken into account. The restriction to the lowest energy levels corresponds to the situation of the atomic cloud being mostly in the ground state of the trap and having negligible population of higher energy levels. This situation is realistic, if the energy spacing of the discrete transverse states is large compared to the kinetic energy. Nevertheless, the result obtained from the two-level model provides a reasonable estimate for the decoherence of an atomic cloud, even if many transverse levels are populated. Equation (2.38) shows that only next-neighbor transitions are allowed. As A_{imnj} is a product of two next-neighbor transitions, there can only be contributions of the next two neighboring energy levels. Higher energy levels contribute only to the decoherence by successive transitions, which are of higher order in A_{imnj} and, hence, are negligible.

Reducing Eq. (2.41) to the two-level subspace leads to a four-dimensional matrix

$$\tilde{A}(\zeta_-) = \begin{pmatrix} A(0) & -A(\zeta_-) & 0 & 0 \\ -A(\zeta_-) & A(0) & 0 & 0 \\ 0 & 0 & A(0) & -A(\zeta_-) \\ 0 & 0 & -A(\zeta_-) & A(0) \end{pmatrix} \,, \qquad (2.43)$$

where $\zeta_- = z - z'$ and the reduced density-matrix vector is defined as:

$$\boldsymbol{\rho} = \left(\rho_{00}, \rho_{11}, \rho_{10}, \rho_{01} \right) \,. \qquad (2.44)$$

The indices of the averaged density matrix ρ_{lk} denote the transverse state $l = (l_x, l_y)$. Here, only the l_y components of the labels are written, as ρ_{lk} can only couple to states with the same $\hat{x}$-state (i.e. as discussed above, only transitions between different $\hat{y}$-states of the 2D-HO are allowed). The $\hat{x}$-label is $l_x = 0$ for all states under consideration.

The equations for the diagonal elements, i.e., ρ_{00}, ρ_{11}, and for the off-diagonal elements, i.e. ρ_{01}, ρ_{10} decouple. However, the decoupling is a consequence of the restriction to the two lowest energy levels and is not found in the general case. Yet, the decoupling allows to find an explicit solution for the time evolution of the diagonal elements. The matrix equation proves to be diagonal for the linear combinations

$\rho^{\pm} \equiv \rho_{00} \pm \rho_{11}$. Introducing the new coordinates $\zeta_- = z - z'$ and $\zeta_+ = \frac{1}{2}(z + z')$, the general solution

$$\rho_k^{\pm}(\zeta_-, \zeta_+, t) = R_k^{\pm}(\zeta_- - \frac{\hbar k}{m} t) e^{ik\zeta_+} e^{-\Gamma_k^{\pm}(\zeta_-,t)t} \,, \tag{2.45}$$

is obtained. The decay function $\Gamma_k^{\pm}$ in Eq. (2.45) is described by

$$\Gamma_k^{\pm}(\zeta_-, t) = A(0) \mp \frac{1}{t} \int\limits_0^t dt' A(\zeta_- - \frac{\hbar k}{m} t') \,. \tag{2.46}$$

The function $R_k^{\pm}$ is fixed by the initial conditions, i.e. by the density matrix at time $t = 0$:

$$R_k^{\pm}(\zeta_-) = \int\limits_{-\infty}^{\infty} d\zeta_+ e^{-ik\zeta_+} \rho^{\pm}(\zeta_-, \zeta_+, t = 0) \,. \tag{2.47}$$

Note, that $\Gamma_k^{\pm}$ in Eq. (2.46) is a function of the spatial variable ζ_- and the wavevector k, and is in general not linear in the time argument t. Adding and subtracting the contributions $\rho^{\pm}$ finally leads to the following expressions for the diagonal elements of the density matrix

$$\rho_{00}(\zeta_-, \zeta_+, t) = \frac{1}{2} \int\limits_{-\infty}^{\infty} \frac{dk}{2\pi} [\rho_k^+(\zeta_-, \zeta_+, t) + \rho_k^-(\zeta_-, \zeta_+, t)] \,. \tag{2.48}$$

The result for ρ_{11} can be obtained from (2.48) by replacing the plus sign between the terms by a minus sign.

To get a feeling for the spatial correlations, it is convenient to trace out the center of mass coordinate ζ_+:

$$\begin{aligned}
\bar{\rho}_{00}(\zeta_-, t) &= \int_{-\infty}^{\infty} d\zeta_+ \, \rho_{00}(\zeta_-, \zeta_+, t) \tag{2.49} \\
&= \frac{1}{2} e^{-[A(0) - A(\zeta_-)]t} \left[\bar{\rho}_{00}(\zeta_-, 0) \left(1 + e^{-2A(\zeta_-)t} \right) + \bar{\rho}_{11}(\zeta_-, 0) \left(1 - e^{-2A(\zeta_-)t} \right) \right] \,.
\end{aligned}$$

Equation (2.49) shows that we can distinguish two decay mechanisms:

Firstly, there is an overall decay of the spatial off-diagonal elements with a rate $\bar{\Gamma}_{\text{dec}}(\zeta_-) = [A(0) - A(\zeta_-)]$. This decay affects the density matrix only for $\zeta_- \neq 0$, thus, suppressing the spatial coherence. The spatial correlation length of the potential fluctuations can be read off Fig. 2.4, showing $\bar{\Gamma}_{\text{dec}}(\zeta_-)$. The value found from Fig. 2.4 gives for the potential fluctuations a correlation length ξ_c of the order of the trap to chip surface distance $\xi_c \approx r_0$. Note, however, that ξ_c is the correlation length of the potential fluctuations and must not be confused with the coherence length describing the distance over which the transport of an atom along the trapping well is coherent. This coherence length is described by the decoherence time and the speed of the moving wavepacket. The correlation length ξ_c characterizes the distance over
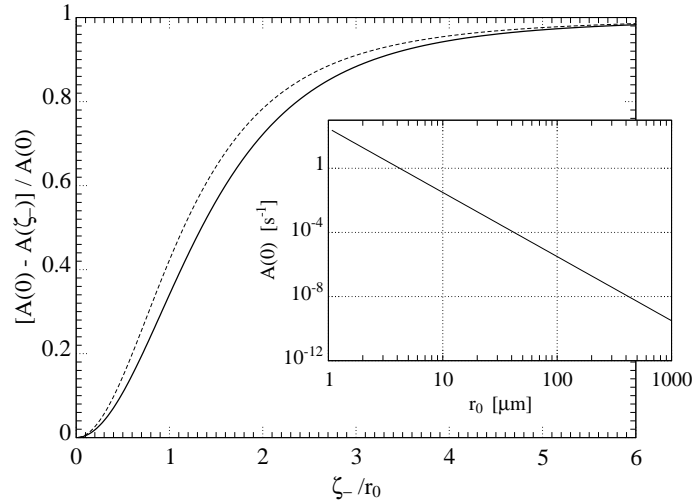
Figure 2.4: Spatial dependence of the decay rate $\bar{\Gamma}_{\mathrm{dec}}(\zeta_-) = A(0) - A(\zeta_-)$ for the diagonal elements $\bar{\rho}_{ii}(\zeta_-, t)$, Eq. (2.49). The wire to trap distance is $r_0 = 100\mu\mathrm{m}$ and the trap frequency is $\omega \approx 2\pi \times 10\mathrm{kHz}$. The dashed line is the approximation Eq. (2.51) for $A(\zeta_-)$. *Inset:* Decay rate $A(0)$ as function of r_0. The parameters chosen in the plots correspond to $^{87}\mathrm{Rb}$ trapped at $T_{\mathrm{eff}} = 300\mathrm{K}$ in a magnetic trap with a gold wire of conductivity $\sigma_{\mathrm{Au}} = 4.54 \cdot 10^7 \Omega^{-1}\mathrm{m}^{-1}$ and a cross section of $A = 2.5\mu\mathrm{m} \times 5\mu\mathrm{m}$. The bias fields are $B_{\mathrm{bias}}^{(x)} = 80\mathrm{G}$ and $B_{\mathrm{bias}}^{(z)} = 2\mathrm{G}$.

which the potential fluctuations are correlated.

Secondly, the factors $(1 \pm e^{-2A(\zeta_-)})$ in front of the density matrix elements, $\bar{\rho}_{ii}$, describes the equilibration of the excited state and the ground state. The equilibration is maximal for the diagonal elements $\bar{\rho}_{ii}(0, t)$, which gives an upper boundary. The equilibration for $\zeta_- = 0$ occurs at a rate $\bar{\Gamma}_{\mathrm{pop}}(0) = 2A(0)$. Here, equilibration means that, due to this mechanism, the probability to be in the ground state, i.e. $\rho_{00}(0, t)$, tends towards $1/2$. Of course, at the same time the probability $\rho_{11}(0, t)$ to be in the excited state approaches $1/2$ at the same rate. Note, that for the spatial off-diagonal matrix elements the equilibration rate depends on ζ_-.

Now, a closer look is taken on the quantity $A(0)$ for realistic trap parameters. Using $J(0) = \frac{3\pi}{8y_0^5}$ and Eq. (2.37), Eq. (2.40) leads to

$$A(0) = \frac{3\pi}{2} k_{\mathrm{B}} T_{\mathrm{eff}} \sigma A \frac{B_{\mathrm{bias}}^{(x)}}{2\hbar\sqrt{m}} \left(\frac{\mu_0}{4\pi}\right)^2 \left(\frac{2\mu_B g_F}{B_{\mathrm{bias}}^{(z)}}\right)^{\frac{3}{2}} \frac{1}{r_0^4} . \tag{2.50}$$

The inset of Fig. 2.4 plots $A(0)$ over r_0 for reasonable trap parameters. Equation (2.50) shows that the decay rate is scaling with the wire to trap distance as $1/r_0^4$, giving a rapid increase of decoherence effects once the atomic cloud is brought close to the wire.

In order to obtain a better feeling for the dynamics, the time evolution of the
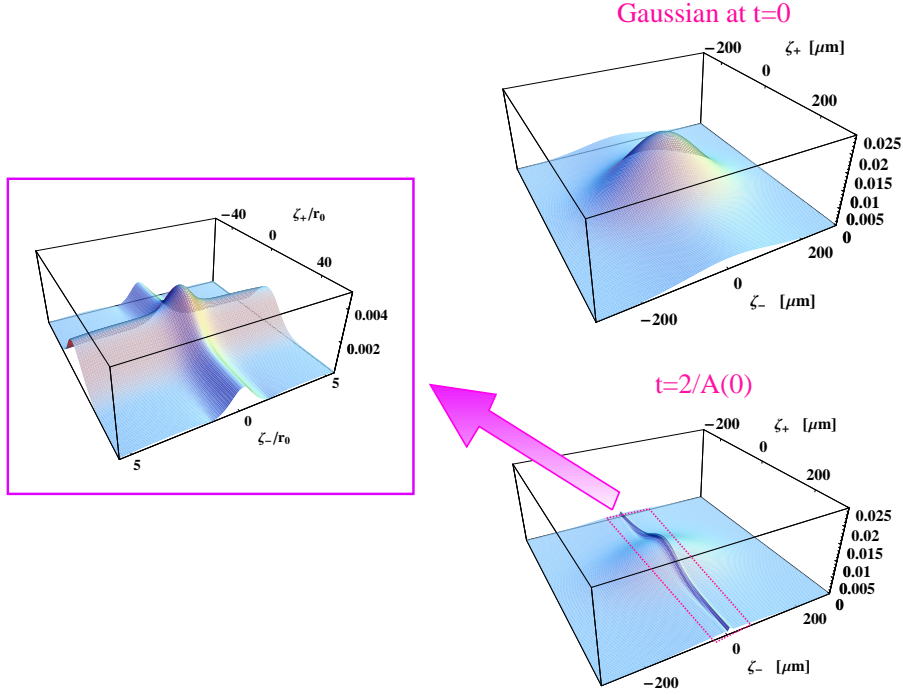
Figure 2.5: *Upper Right:* At $t = 0$ the wavepacket is a Gaussian wavepacket of spatial extent $w_z = 20r_0$. *Lower Right:* Time evolution of $|\rho_{00}(\zeta_-, \zeta_+, t)|$ after $t = 2/A(0)$. The wire-to-trap distance is $r_0 = 5\mu$m and all other parameters correspond to those used in Fig. 2.4. $A(0) \approx 0.5\text{s}^{-1}$ is given by Eq. (2.50). The density matrix shows damped oscillations which become more pronounced as ζ_+ increases. *Left:* Zoom in on the lower right graph showing a detail of the density matrix after a time evolution of $t = 2/A(0)$.

density matrix is studied for an explicit example. Let us suppose, that the system is prepared in a Gaussian wavepacket in the ground state of the transversal potential. Figure 2.5 and Fig. 2.6 show the time evolution of the absolute value of the density-matrix element $|\rho_{00}(\zeta_-, \zeta_+, t)|$ for a Gaussian wavepacket of spatial extent $w_z = 20r_0$ and a wire to trap distance of $r_0 = 5\mu$m. Initially, at time $t = 0$, all elements of the density matrix are zero except of ρ_{00}. The time evolution is calculated for the reduced subspace, using Eq. (2.45) and Eq. (2.48). For the spatial correlation, the approximation

$$A(\zeta_-) \approx 4\frac{A_0}{\hbar^2 r_0^5}\left[\left(\frac{32}{3\pi}\right)^{\frac{2}{3}} + \left(\frac{\zeta_-}{r_0}\right)^2\right]^{-\frac{3}{2}}, \qquad (2.51)$$

is used. The dashed line in Fig. 2.4 shows the approximation compared to the exact curve (solid line). The time evolution of the Gaussian wavepacket shows a strip of $|\zeta_-| < l_c \approx r_0$ in which the density matrix decays much slower. This is a consequence of the ζ_- dependence of the decay rate shown in Fig. 2.4. The spatial correlation length of the wavepacket, hence, can be read off Fig. (2.6) as $l_c \approx r_0$. In addition, a damped oscillation in the relative coordinate ζ_- arises, which becomes more pronounced for larger values of ζ_+. Figure 2.6 shows cuts along the ζ_--direction for

Figure 2.6: Decay of the absolute value $|\rho_{00}(\zeta_-, \zeta_+ = 30r_0, t)|$ and $|\rho_{00}(\zeta_-, \zeta_+ = 0, t)|$ (inset). The wavepacket is a Gaussian of spatial extent $w_z = 20r_0$ at $t = 0$. The wire to trap distance is $r_0 = 5\mu$m. All other parameters are the same as used in Fig. 2.4. $A(0) \approx 0.5\text{s}^{-1}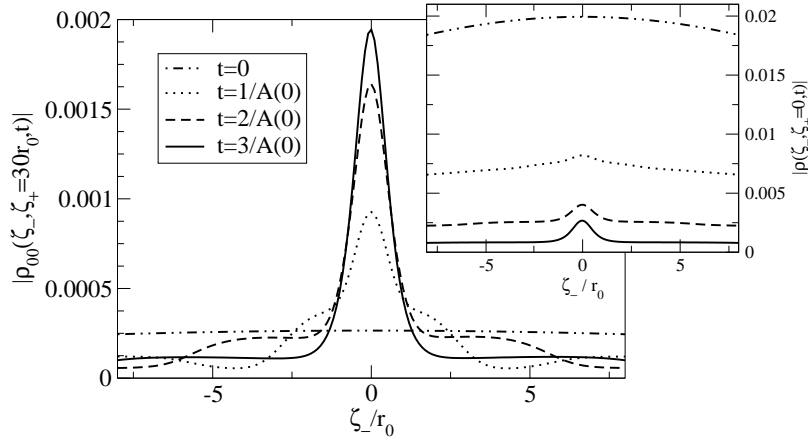$ is given by Eq. (2.50). The dashed line ($t = 2/A(0)$) corresponds to cuts of the left graph of Fig. 2.5 along ζ_- for $\zeta_+ = 30r_0$ (inset $\zeta_+ = 0$). Spatial correlations of the potential fluctuations are restricted to a narrow band around $\zeta_- = 0$. The width of this band is on the order of r_0. The density matrix shows damped oscillations which become more pronounced with increasing ζ_+. The increase of $|\rho_{00}(\zeta_-, \zeta_+ = 30r_0, t)|$ for increasing time t is a consequence of the spreading of the wavepacket.

different values of ζ_+. The origin of the damped oscillations is the k-dependence of the equilibration and decoherence mechanism, which are described by $\Gamma_k^{\pm}$ in Eq. (2.46). To demonstrate the influence of the k-dependent damping the decay rate is assumed to be $\Gamma_k^{\pm} = A(0) \mp [A(\zeta_-) + \beta(\zeta_-, t)k]$. Choosing $\Gamma_k^{\pm}$ linear in k leads to a modulation of the density matrix by a factor proportional to $\cosh(i\alpha_0\beta + \alpha_1)$, describing damped oscillations. The coefficients $\alpha_{0/1}$ are real functions of $\zeta_{\pm}$ and t. The oscillations arise only for non-vanishing β. Decay rates which are k-independent do not show oscillations. The decay described by $\Gamma_k^{\pm}$ in Eq. (2.46) is, however, not linear, but includes higher powers in k. Hence, the simple linear model $\Gamma_k^{\pm} = A(0) \mp [A(\zeta_-) + \beta(\zeta_-, t)k]$ describes the oscillations in Fig. 2.5 and Fig. 2.6 only qualitatively.

2.4.2   Double-wire configuration: interferometer

Having understood the basic features of the decoherence processes in atom-chip traps by studying the single waveguide in the previous chapter, this second example applies the theory to the more interesting case of the double waveguide. Testing for interference effects proved to be an successful experimental method to investigate decoherence properties. It is, hence, not surprising that there are various suggestions to test interference of ultra-cold atomic clouds [76–78]. The necessity of a double waveguide potential is a common feature in all three interferometer suggestions. Thus, the theoretical knowledge of decoherence effects in a double-waveguide potential is a key issue and will be the topic of this section.

The geometrical situation is shown in Fig. 2.2. The setup consists of two parallel wires on the substrate. The current density and the wire distance d are chosen such, that a double waveguide is formed. In this configuration we have two, horizontally spaced, but otherwise identical trap minima. Without restricting the general discussion, the current densities are assumed to be fixed and the distance between the wires is chosen as a variable parameter. Considering the double-waveguide regime, distances $d > 2\bar{y}_0$ are required.

Having defined the setup, we are now able to study the dynamics of the system in the presence of current fluctuations. Starting point of the calculation again is the general expression Eq. (2.33). The calculation is in analogy to the calculation for the single waveguide in Sec. 2.4.1.

Derivation of the potential correlator

Firstly, an explicit expression for the correlation function $\langle \delta S_{im}(z) \delta S_{nj}(z') \rangle$ is required. The derivation of the projected-potential correlator is in analogy to the previous section. After some lengthy calculations the following expression is obtained

$$
\langle \delta S_{im}(z) \delta S_{nj}(z') \rangle = 8 A_0 \frac{x_0^\alpha x_0^\beta}{d^2} \sum_{\gamma = L, R} J_{\alpha\beta}^\gamma(z - z') \tag{2.52}
$$

$$
\times \int d\mathbf{r}_\perp \chi_i(\mathbf{r}_\perp) \left[(y - y_0) - y_0 \frac{(x - x_0^\alpha)}{(x_0^\alpha + \epsilon_\gamma \frac{d}{2})} \right] \chi_m^*(\mathbf{r}_\perp)
$$

$$
\times \int d\mathbf{r}'_\perp \chi_n(\mathbf{r}'_\perp) \left[(y' - y_0) - y_0 \frac{(x' - x_0^\beta)}{(x_0^\beta + \epsilon_\gamma \frac{d}{2})} \right] \chi_j^*(\mathbf{r}'_\perp) .
$$

The spatial correlation $J_{\alpha\beta}^\gamma(z - z')$ in the double waveguide is given by

$$
J_{\alpha\beta}^\gamma(z - z') = \int_{-\infty}^{\infty} d\tilde{z} \left[\left(x_0^\alpha - \epsilon_\gamma \frac{d}{2} \right)^2 + y_0^2 + \tilde{z}^2 \right]^{-\frac{3}{2}} \left[\left(x_0^\beta - \epsilon_\gamma \frac{d}{2} \right)^2 + y_0^2 + (z - z' - \tilde{z})^2 \right]^{-\frac{3}{2}} .
$$

$$
\tag{2.53}
$$

Here, $\alpha \in \{L, R\}$ is the trap label corresponding to $i = (\alpha, i_x, i_y)$ and $m = (\alpha, m_x, my)$, and $\beta \in \{L, R\}$ the trap label corresponding to n and j, of the indices occurring in $\langle \delta S_{im}(z) \delta S_{nj}(z') \rangle$. The wires are located at $x = d_{L/R} = \mp d/2$ and ϵ_γ is defined as $\epsilon_L = -1$, $\epsilon_R = 1$. The result Eq. (2.52) uses the assumption that the extent of the wavefunction w is much smaller than y_0 and much smaller than the trap minimum offset $|x_0^{L/R}|$ from the $\hat{x}$-axis, i.e., $w \ll |x_0^{L/R}|$ and $w \ll y_0$. This approximation breaks down if the wire separation d approaches the critical separation distance $2\bar{y}_0$ at which the two trap minima merge.

In analogy to the preceding section, the transversal wavefunctions χ_n in Eq. (2.52) are approximated by 2D-HO states. However, one has to be careful, as this approximation holds only if the two trapping wells are sufficiently separated such that the

mutual distortion of the magnetic fields are small. If the distance between the two traps becomes close to the critical value $d = 2\bar{y}_0$, a double-well structure arises and the harmonic approximation breaks down. The validity of the approximation is estimated by calculating the distance d_c, at which the local potential maximum, separating the two trapping wells, is of the order of the ground state energy of the isolated single trap. The trap frequency for the double-wire configuration extracted from the harmonic approximation is

$$\omega_d = 2\omega \frac{|x_0|}{d} = 2\omega \frac{\sqrt{d^2/4 - \bar{y}_0^2}}{d} \; , \tag{2.54}$$

where ω is the single-wire trap frequency given in Eq. (2.37). Thus, the ground-state energy $E_0 = \hbar\omega$ of the single-wire trap corresponds to the limit of infinite separation $d = \infty$. This energy E_0 is the maximum value for the ground-state energy $\hbar\omega_d$ of the double-wire trap under variation of d. Hence, E_0 is an upper bound for the ground-state energy of the double well in the case $d > \bar{y}_0$. Using the procedure described above leads to the condition $d > \sqrt{8}\,\bar{y}_0$, restricting the region in which the transversal potential can be approximated as two independent 2D-HOs. The dashed line in the left graph of Fig. 2.2 shows an example for the harmonic approximation of the trapping potential of the double-wire setup.

Performing the integration over the transverse coordinates $\mathbf{r}_\perp$, using 2D-HO states for χ_n, leads to the transition matrix elements

$$\langle \delta S_{im}(z) \delta S_{nj}(z') \rangle = 4A_0 \frac{x_0^\alpha x_0^\beta}{d^2} \sum_\gamma J_{\alpha\beta}^\gamma(z-z') \left[w_y^\alpha \tilde{\delta}_{i_y m_y} + \epsilon_\alpha w_x^\alpha \tilde{\delta}_{i_x m_x} \frac{y_0}{(x_0^\alpha + \epsilon_\gamma \frac{d}{2})} \right]$$
$$\left[w_y^\beta \tilde{\delta}_{n_y j_y} + \epsilon_\beta w_x^\beta \tilde{\delta}_{n_x j_x} \frac{y_0}{(x_0^\beta + \epsilon_\gamma \frac{d}{2})} \right] \; , \tag{2.55}$$

where the functions $\tilde{\delta}_{ij}$ have been defined in Eq. (2.39). In order to simplify the derivation of Eq. (2.55), the current in the left and right wire were chosen to be the same. The derivation of the Eq. (2.52) and subsequently Eq. (2.55) follows the calculations outlined in Appendix A for the general case, using the specific magnetic-field distribution of the double waveguide Eq. (2.3). As the calculation is rather tedious and does not provide additional insight, a detailed discussion of the derivation will be skipped. Instead of going into details of the derivation, the different contributions will be discussed qualitatively. As the system is invariant under mirror imaging at the $\hat{y}$-$\hat{z}$-plane, corresponding to an invariance under the interchange of the left (L) trap and right (R) trap label, only the following three contributions must be distinguished (see Fig. 2.7):

(a) The influence of current fluctuations in the *left wire* on an atom in a state which is localized in the *left arm* of the trapping potential (Fig. 2.7a).

(b) The influence of current fluctuations in the *left wire* on an atom which is in a superposition of *a state localized in the left arm* and *a state localized in the right arm* of the trapping potential (see Fig. 2.7b).
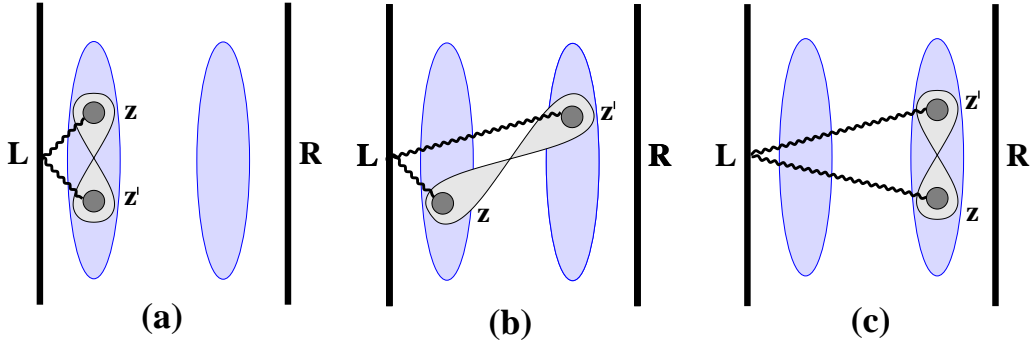
Figure 2.7: Contributions of the noise in the left wire to the decoherence of $\rho_{ij}(z, z', t)$. The figures show only the coupling of one point on the wire to the atomic state. To obtain the total contribution to the decoherence, an integration over all wire elements, coupling to the atomic state, has to be performed.

   (c) The influence of current fluctuations in the *left wire* on an atom in a state which
       is localized in the *right arm* of the trapping potential (Fig. 2.7c).

All other contributions are obtained by symmetry operations. Looking closer at these three cases allows the following classification, referring to the type and strength of the contribution to the decoherence of the atomic cloud.

Case (a): — The current-noise source and the atom wavefunction are on the same side. Contribution (a) is given by the term proportional to J_{LL}^{L} and is the dominating decoherence source in the regime $d > 2\bar{y}_0$. All other contributions (J_{LR}^{L}, J_{RR}^{L} shown in the third and forth column of Table 2.1) are suppressed by orders of $\bar{y}_0/d$.

Case (b): — The contribution in Fig. 2.7b is of particular interest as it describes the cross-correlations between the noise in the left and right trapping well. The contribution (b) is given by terms proportional to J_{RL}^{L} and J_{LR}^{L}. Current fluctuations in one of the wires give rise to magnetic field fluctuations in all the trapping wells. Magnetic field fluctuations are therefore not uncorrelated. These correlations are however suppressed for $\bar{y}_0 \ll d$ as can be seen in Table 2.1.

Case (c): — Contributions of type (c), given by terms proportional to J_{RR}^{L}, are the smallest contributions to the decoherence. They describe the influence of the left wire current noise on the atomic cloud in the more distant right trap. Terms of type (c) are thus negligible for wire distances $d \gg 2\bar{y}_0$ as the magnetic field decreases with $1/r$ and fluctuations in the trapping field are dominated by the nearest noise source i.e. contributions of type (a).

    Finally, it is instructive to compare the result obtained in Eq. (2.55) for the double waveguide with the matrix elements in Eq. (2.38) for the single-wire trap. The comparison reveals the following differences. First of all, transitions in the double-wire trap are no longer restricted to the $\hat{y}$-components of the 2D-HO. This is a direct

	$J_{LL}^{L}(\zeta_-)$	$J_{LR}^{L}(\zeta_-)$	$J_{RR}^{L}(\zeta_-)$
$\zeta_- = 0$	$\frac{1}{\bar{y}_0^5}$	$\frac{2}{\bar{y}_0^2 d^3}$	$\frac{1}{d^5}$
$\zeta_- \ll \bar{y}_0$	$\frac{1}{\bar{y}_0^5}$	$\frac{2}{d^3 \bar{y}_0^2}\left(1 - \frac{3}{2}\frac{\bar{y}_0^2}{d^2}\right)$	$\frac{1}{d^5}$
$\bar{y}_0 \ll \zeta_- \ll d$	$\frac{4}{\bar{y}_0^2 \zeta_-^3}$	$\frac{2}{d^3 \bar{y}_0^2}\left(1 - \frac{3}{2}\frac{\zeta_-^2}{d^2}\right)$	$\frac{1}{d^5}$
$d \ll \zeta_-$	$\frac{4}{\bar{y}_0^2 \zeta_-^3}$	$\frac{2}{\zeta_-^3}\left(\frac{1}{\bar{y}_0^2} + \frac{1}{d^2}\right)$	$\frac{4}{d^2 \zeta_-^3}$

Table 2.1: Estimate of the contributions to the decoherence. The columns for J_{LL}^{L}, J_{LR}^{L}, and J_{RR}^{L} correspond to contributions (a), (b) and (c) of Fig. 2.7, respectively. The $J_{\alpha\beta}^{\gamma}(\zeta_-)$ are given by Eq. (2.53) as a function of $\zeta_- = z - z'$. The approximation assumes $\bar{y}_0 \ll d$.

consequence of the geometry, as the positions of the trap minima are now sensitive to current fluctuations in $\hat{x}$- and $\hat{y}$-direction. This is in contrast to the single-wire trap, where the $\hat{x}$-position of the trap minimum was independent of the current strength in the conductor. Secondly, the prefactor of the transition matrix element in Eq. (2.55) is now a function of the spatial coordinates x_0^{α}, taking the geometric changes of the trap minimum position under variation of the wire separation d into account.

Solution of the equation of motion

Having in mind a spatial interferometer as suggested in Ref. [78], the most interesting quantity is the density-matrix element, describing the coherent superposition of a state in the left arm with a state in the right arm. Figure 2.8 shows the geometry of the interferometer. Before starting with the discussion of the decoherence, a brief description of the basic function of the interferometer device will be provided (see Ref. [78] for a detailed discussion). A wavepacket is initially prepared on the left side in a single waveguide. The wavepacket propagates towards the right and is split into a coherent superposition of a state in the left arm and a state in the right arm. Finally, applying a small offset between the currents in the left and right wire gives rise to a phase shift between the two wavepackets. This phase shift results, after recombination, in a fringe pattern of the longitudinal density. Loss of coherence between the wavepackets in the left and right arm, due to current fluctuations in the conductors, will decrease the visibility of the interference pattern. Consequently, the decay of those components of the density matrix, which are off-diagonal in the trap index, are the most interesting quantities to study.

Keeping the expressions simple, the trap label (L/R) will be suppressed in the
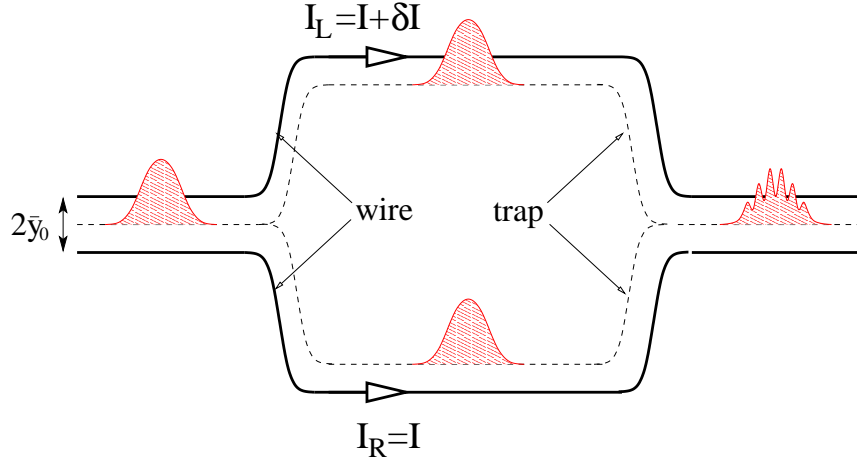
Figure 2.8: Schematic setup of an interferometer for cold atoms, using a double-wire trap. A wavepacket comes in from the left single waveguide which is formed by a double-wire trap with a wire spacing of $d = 2\bar{y}_0$. The wavepacket is split into a coherent superposition of states localized in the left and right arm of the double waveguide. Inducing a potential difference, e.g. by applying a current difference δI between the left and right wire, gives rise to a phase shift. Remerging the wavepackets results into an interference pattern in the atom density. For a more detailed description of atom interferometers of this type see Ref. [78].

following. However, we will bear in mind that the left (right) index of ρ will always denote a state in the left (right) trap. It will be further assumed that the incoming wavepacket is initially split into a symmetric superposition of the left and right arm. In addition, the currents in the left and right wire are chosen to be same. Choosing $I_L = I_R$ does not restrict the validity of the result for the decoherence effects, but keeps the equations simple as the full symmetry of the double-wire geometry is still conserved.

Inserting Eq. (2.55) in Eq. (2.33) leads to a set of equations for the dynamics of the averaged density matrix. Restricting the system again to the ground state and first excited state of the 2D-HO gives a reasonable approximation of the system as was previously argued for the single-wire case. The equation of motion of $\rho(z, z', t)$ leads to a matrix equation in analogy to Eq. (2.41)

$$\left[i\hbar\partial_t - \tilde{H}(z, z') \right] \boldsymbol{\rho}(z, z', t) = -i\hbar\tilde{A}(z - z')\boldsymbol{\rho}(z, z', t) ,$$

but with a density-matrix vector

$$\boldsymbol{\rho} = \left(\rho_{00}^{00}, \rho_{11}^{00}, \rho_{00}^{11}, \rho_{10}^{01}, \rho_{01}^{10} \right) . \tag{2.56}$$

The upper index denotes the $\hat{x}$-state and the lower index the $\hat{y}$-state of the 2D-HO. The left and right pair of indices refer to a state in the left and right well, respectively.
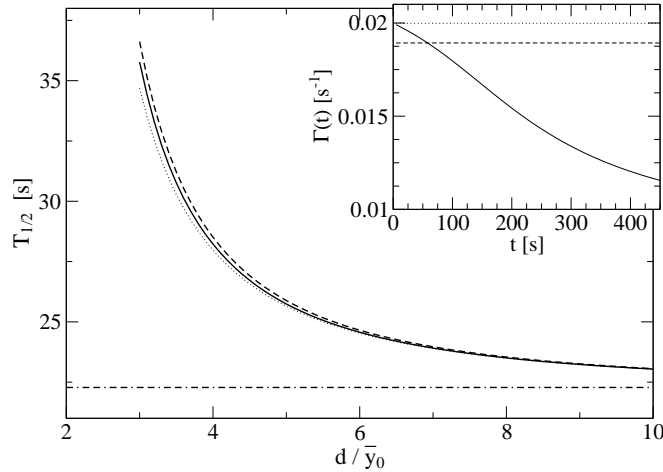
Figure 2.9: Decay time in the double-wire trap. $T_{1/2}$ is defined as the time it takes until $\rho_{00}^{00}(z, z', t)$ has decayed to half of its initial value at $t = 0$. The graph shows its dependence on the wire separation d if all contributions in Eq. (2.57) are taken into account (solid line), if the cross-correlations β_i are neglected (dotted line), and in the limit of $d \gg \bar{y}_0$, Eq. (2.63) (dashed line). The dash-dotted line is the $T_{1/2}$-time using the decay rate Eq. (2.50) for the single-wire configuration. *Inset:* $\Gamma(t) \equiv -\ln(\rho_{00}^{00})/t$ at $d = 3\bar{y}_0$. The trap to chip-surface distance taken for the plot is $\bar{y}_0 = 10\mu$m and all other trap parameters correspond to those used in Fig. 2.4.

The matrix $\tilde{A}$ is

$$
\tilde{A} = \begin{pmatrix}
\sum_{i=1}^{4} \alpha_i & \beta_1 & \beta_2 & \beta_3 & \beta_4 \\
\beta_1 & \alpha_1 + \alpha_3 & 0 & \alpha_6 & \alpha_5 \\
\beta_2 & 0 & \alpha_2 + \alpha_4 & \alpha_5 & \alpha_6 \\
\beta_3 & \alpha_6 & \alpha_5 & \alpha_1 + \alpha_4 & 0 \\
\beta_4 & \alpha_5 & \alpha_6 & 0 & \alpha_2 + \alpha_3
\end{pmatrix}. \tag{2.57}
$$

The explicit coefficients are given in Appendix B. The matrix elements are divided into two classes. Terms labeled by α_i are contributions of the type shown in Fig. 2.7a plus the corresponding term of type Fig. 2.7c. Terms denoted by β_i are cross-correlations as described by contributions shown in Fig. 2.7b. Furthermore, terms abbreviated as α do not depend on the longitudinal coordinate z, z', whereas the cross-correlations β are functions of $(z - z')$.

In order to obtain an explicit number for the strength of the decoherence, a specific example will be studied numerically. We assume, that the extent of the wavepacket w_z along the trapping well is $w_z \ll d$ for the time span of interest. As the cross-correlations β_i vary on a length scale of approximately d, $\beta_i(z - z')$ in Eq. (2.57) can be replaced by the constant $\beta_i(0)$ [5]. Furthermore, let us suppose that at $t = 0$ the density matrix is prepared in a coherent superposition of the ground states of the left

---

[5]Considering the opposite limit $w_z \gg d$, the matrix elements can be approximated as $\beta_i(z-z') \approx \beta_i \delta(z - z')$. The results, compared to those shown in Figure 2.9, are given by $T_{1/2}$-times between the solid and dotted curves in of Fig. 2.9.

and right well. This choice of the initial wavepacket leads to a density matrix vector of the form

$$\boldsymbol{\rho}(t = 0) = \left(\rho_{00}^{00}(t = 0), 0, 0, 0, 0 \right) . \tag{2.58}$$

Solving the equation of motion numerically under the above conditions yields the results shown in Fig. 2.9 The figure shows the time $T_{1/2}$ it takes until $\rho_{00}^{00}(t = 0)$ has decayed to half of its initial amplitude as a function of the wire separation d. Note, that the average currents in the wires were chosen to be constant and the wire separation d is varied. Changing the wire separation is closely connected to the position of the trap minima. The position of the trap minima given by

$$y_0 = \bar{y}_0 \qquad , \tag{2.59}$$

$$x_0^{L/R} = \mp\sqrt{d^2/4 - \bar{y}_0^2} \quad , \tag{2.60}$$

moves horizontally to the surface, leading to a wire to trap distance of

$$r_0 = \frac{d}{\sqrt{2}} \left[1 - \left(1 - 4\frac{y_0^2}{d^2} \right)^{\frac{1}{2}} \right]^{\frac{1}{2}} . \tag{2.61}$$

Let us have a closer look at the results presented in Figure 2.9. The solid line in Fig. 2.9 shows the $T_{1/2}$-time obtained from the solution of Eq. (2.41) and using Eq. (2.57) in the approximation $\beta_i(z - z') \approx \beta_i(0)$ for $w_z \ll d$. Cross-correlation terms β_i play, however, only a minor role for the $T_{1/2}$-time, as can be seen from the dotted line in Fig. 2.9. This dotted line shows the case, where the β_i terms are neglected in Eq. (2.57). The cross-correlation terms, shown in Fig. 2.7b, include contributions describing positive correlations between potential fluctuations, suppressing the decoherence. However, these cross-correlation terms describe also negative correlations between potential fluctuations which enhance the decoherence. Hence, there are two antagonistic effects which reduce the overall contribution to the decoherence. It is thus important to compare the symmetry of the potential fluctuations to the symmetry of the trapping potential. Fluctuations, which lead to the same change in both potential wells, left and right, do not give rise to a net phase difference in the left and right wavefunction. Hence, fluctuations conserving the symmetry do not lead to decoherence between the two waveguides. In contrast, fluctuations yielding large differences in the left- and right-waveguide potential give rise to decoherence. Figure 2.10 shows schematically the potential fluctuations δV induced by a current fluctuation δI in the left wire. The trapping potential posses mirror symmetry with respect to the $\hat{z} - \hat{y}$ plane. Thus, the antisymmetric shifts in horizontal direction conserve the symmetry and lead to positive correlations, reducing the decoherence. The vertical fluctuation of the potential is also antisymmetric, which is in contrast to the strongly non-symmetric potential (see solid line in Fig. 2.2). Hence, the vertical fluctuations give rise to decoherence. The inset of Fig. 2.9 shows the change of the decay rates over time. Taking the full matrix Eq. (2.57) into account (solid line), there is a change of decay rate $\Gamma_{\alpha+\beta}(t)$ towards a slower decay rate for $t \gg \Gamma_{\alpha+\beta}^{-1}(0)$. If the cross-correlations are ignored, the decay rate is constant $\Gamma_\alpha \approx \Gamma_{\alpha+\beta}(0)$. Inspection of $\tilde{A}$, given by Eq. (2.57), shows that neglecting the terms β_i decouples ρ_{00}^{00} from the
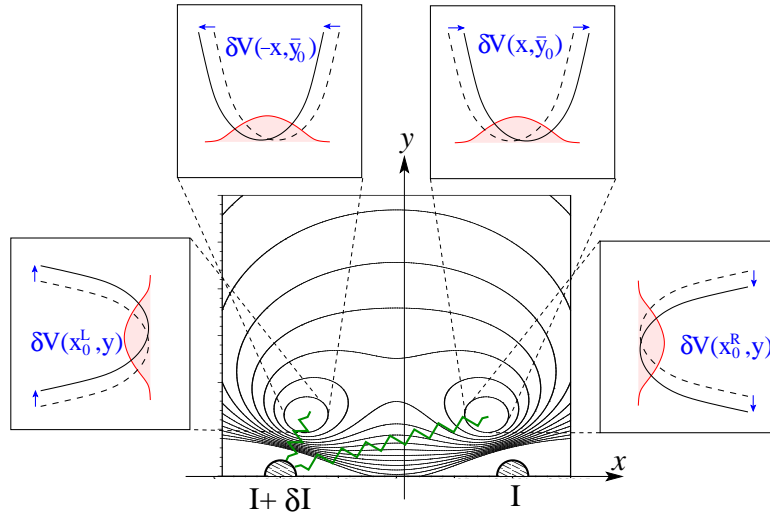
Figure 2.10: Influence of current fluctuations δI in the left wire on the potential of the trapping wells $V(x,y) = -\langle F, m_F | \boldsymbol{\mu} | F, m_F \rangle \mathbf{B}$. The potential fluctuations $\delta V(x, \bar{y}_0) = \delta V(-x, \bar{y}_0)$ are reflection symmetric about the $\hat{y}$-$\hat{z}$-plane for $|x - x_0^{L/R}| \ll \bar{y}_0$. Hence, the fluctuations in $\hat{x}$-direction are conserving the symmetry of the trapping potential. This leads to positive correlations in $\langle \delta S_{im}(z) \delta S_{nj}(z') \rangle$, suppressing the decoherence. The potential fluctuations in $\hat{y}$-direction, $\delta V(x_0^L, y)$, $\delta V(x_0^R, y)$, show negative correlations giving rise to an increase in the decoherence rate.

excited states. This decoupling leads to an exponential decay with a single decay rate.

Finally, decoherence for large distances d between the wires, i.e., $d \gg \bar{y}_0$, is discussed. For $d \gg \bar{y}_0$, it is sufficient to take only the influence of δI_L (δI_R) on the left (right) trap (given by contributions of type Fig. 2.7a) into account. All other contributions are strongly suppressed by orders of $\bar{y}_0/d$ (see Table 2.1). Hence, the matrix Eq. (2.57) decouples ρ_{00}^{00} from the excited states and the remaining equation for ρ_{00}^{00} can be solved analytically. The solution is

$$\rho_{00}^{00}(z, z', t) = e^{-\Gamma t} e^{-\frac{i}{\hbar}\hat{H}t} \rho_{00}^{00}(z, z', 0) \; , \tag{2.62}$$

where $\hat{H}$ is the free Hamiltonian as defined in Section 2.3.2. The decay rate is given as

$$\Gamma = \frac{3\pi}{2\hbar^2} A_0 \frac{|x_0|^2}{d^2} \left[w_y^2 + \frac{\bar{y}_0^2 w_x^2}{(|x_0| + d/2)^2} \right] \frac{1}{r_0^5} \; . \tag{2.63}$$

In the limit $d \gg \bar{y}_0$, Eq. (2.63) reduces to the decay rate obtained for the single-wire configuration, Eq.(2.50), shown by the dash-dotted horizontal line in Fig. 2.9. However, there is no spatial dependence of Γ along the longitudinal direction ($z - z'$) in the case of widely separated trapping wells. Plotting the $T_{1/2}$-time for the approximation given by Eq. (2.62) (dashed line in Fig. 2.9), using the decay rate Eq. (2.63), shows a good agreement of the approximation with the exact solution as soon as d is of the order of several $\bar{y}_0$. Comparing all three graphs of Fig. 2.9 one can conclude, that the increase in $T_{1/2}$ with decreasing separation d is due to geometric

changes of the trap positions. An increase of the wire to trap distance r_0 due to a decrease of d, leads to an increase in the $T_{1/2}$-time as the rate of the dominating decoherence source scales with $1/r_0^4$.

2.5 Summary of Chapter 2

In this chapter, a general method to treat decoherence due to current fluctuations in multi-wire atom-chip traps was developed. Using the density-matrix formalism, an equation of motion Eq. (2.29) was derived, which describes the consequences of current fluctuations on a cold atomic cloud. The model allows the description of decoherence in multiple-wire traps [11,69], as well as more complex guiding systems. This includes multi-waveguide systems required for the implementation of a beam splitter [13] or interference experiments [76–78].

The atom-chip trap was modeled as a multi-channel one-dimensional waveguide, where different channels describe different transverse modes of the waveguide. Assuming one-dimensional wires on the atom chip, we examined the influence of current fluctuations along the wire on the coherence of the atom cloud in the waveguide. New important contributions to the decoherence were found, arising from transitions to neighboring excited states. Decoherence due to the transitions among transverse states become increasingly important as the wire to trap distance decreases.

Based on this model, decoherence effects for two specific trapping configurations were examined. Firstly, the single-wire waveguide was studied and secondly the double-wire waveguide. In both configurations, decoherence of the ground state was discussed, taking processes from transitions to the first excited states into account. The single-wire trap showed for the ground state a decoherence rate Γ which scales with the wire to trap distance r_0 as $1/r_0^4$. The potential fluctuations are correlated over a length scale of r_0. As a consequence, the decoherence rate Γ is a function of the relative coordinate $z - z'$. Using trap parameters based on recent experiments [69] leads to decoherence rates of the order of $\Gamma \approx 0.03\text{s}^{-1}$ for $r_0 = 10\mu\text{m}$. Extending the system to a double-wire waveguide enabled the investigation of decoherence for atoms in a superposition of a state localized in the left arm and a state localized in the right arm of the waveguide. This superposition is the basic ingredient for interference experiments. Approaching the two trapping wells, as required for the splitting and merging of the wavepackets, showed a decrease in the decoherence rate. The decrease arises mostly due to geometrical rearrangements of the trap minima in the system. Cross-correlation effects proved to be of minor importance in our model. An explicit expression could be derived for the decoherence rate, Eq. (2.63), in the limit of wire to trap distances r_0 much smaller than the separation of the two wires d. This decoherence rate approaches the value for the single-wire waveguide, $\Gamma = A(0)$, for a decreasing ratio of r_0/d.

The decay rates extracted in this model are small for distances realized in present experiments [69]. However, with the further improvement expected in microstructure fabrication and trapping techniques [105], the trap-surface distance is expected to

reach soon length scales at which the decoherence from transitions to transverse states may have a considerable influence on trapped atomic clouds.

Chapter 3

Short-range correlations in optical lattices at the Mott-insulator transition

Lattices play a central role in condensed matter physics. The periodic potential gives rise to many effects such as Bloch oscillations or phase transitions. Studying dilute quantum many-body systems such as Bose-Einstein condensates or ultra-cold Fermi gases in optical lattices is thus particularly interesting. In addition to the large number of effects which are present in the world of solid-state crystals, dilute-atom gases in optical lattices offer new physical systems in which many new possibilities open up. Ultra-cold gases in optical lattices allow the investigation of fermions, bosons, fermion-boson mixtures, or spin-polarized gases in a periodic potential. The expected phase landscape of this system is diverse and still an extremely active research field.

The best-known example showing the power of the optical lattices as an experimental system is the demonstration of the superfluid-Mott insulator (SF-MI) quantum phase transition. The essential physics of cold-bosonic atoms in an optical lattice is captured by a bosonic Mott-Hubbard model [19]. The Mott-Hubbard model describes the competition between the hopping of atoms to neighboring lattice sites and the on-site interaction. The Mott-Hubbard model of interacting bosons on a lattice has been used to describe superfluid-Mott insulator transitions in a variety of solid-state systems as, for instance, in Josephson arrays [114–116] (see also references within the review [117]) and granular superconductors [19]. The suggestion to use optical lattices as a tool to investigate the superfluid-Mott insulator transition [23] was quickly followed by a successful experimental demonstration [24]. Experimental realization in optical lattices quickly revived interest in the superfluid-Mott insulator transition. Optical lattices provided a versatile tool to investigate the behavior of the quantum phase transition. In particular, coherence and correlation effects could be studied by examining and understanding the expansion pictures taken in experiments. The expansion patterns of the superfluid state and the expansion picture of the Mott-insulator state look very different. The superfluid state, having long phase coherence over many lattice sites, shows Bragg peaks in the expansion picture. In contrast to the superfluid phase shows the Mott-insulator phase, with very short phase coherence lengths, a dif-

fuse featureless absorption picture. These differences in the expansion patterns allow to characterize the state of the atomic cloud in the optical lattice as one traverses from the superfluid to the Mott-insulator phase.

The topic of this chapter deals with the importance of short-range correlations in the superfluid-Mott insulator transition of a Bose-Einstein condensate trapped in an optical lattice. Based on a Gutzwiller approach, a method will be presented which allows the successive inclusion of inter-lattice site correlations. The advantage of this method is its applicability in the Mott-insulator as well as in the superfluid region. This is of particular importance if the system is not homogeneous but has Mott-insulator and superfluid phases coexisting, as is usually the case in experiments. Applying our perturbative method to analyze the particle-number fluctuations per lattice site shows distinct corrections to the mean-field prediction. The main part of this chapter deals with the corrections to the short-range behavior of the one-particle density matrix. The one-particle density matrix is directly relevant to experimentally observed expansion patterns which are used to characterize the state of the system. Applying the perturbative method to the one-particle density matrix gives rise to short-range correlations in the Mott-insulator region, in contrast to the mean-field result. This result is in agreement with the experimental findings [61], which recently confirmed the theoretical prediction of short-range correlations in the Mott-insulator phase [57–60]. The consequences of the inclusion of short-range correlations to the Gutzwiller ansatz will be discussed for bulk systems and for a harmonic confining potential. Frequent comparison to several other numerical methods will be made to test the applicability of our perturbative approach.

3.1   Introduction

Before going into the detailed discussion, a short introduction to the physical system will be provided. The first subsection briefly describes the basic function of optical lattices. Subsequently, the main features of the superfluid-Mott insulator phase transition will be described. Finally, the section will be concluded with a short description of the expansion patterns which are expected for the Mott-insulator and superfluid state.

3.1.1   Optical lattices

Optical lattices use the forces acting on atoms in laser fields [118,119]. This effect is also known as the AC-Stark effect. Let us consider an atom in its ground state $|g\rangle$ with ground state energy E_g, subject to an electrical field

$$\boldsymbol{\mathcal{E}}(\mathbf{r}, t) = \mathbf{E}(\mathbf{r})e^{i\omega t} + \mathbf{E}^*(\mathbf{r})e^{-i\omega t}\,. \tag{3.1}$$

Assuming that the laser field is changing slowly in space with respect to the size of the atom, the interaction is well described within the dipole approximation

$$\hat{H}_{\text{int}} = -\boldsymbol{d}\boldsymbol{\mathcal{E}}\,, \tag{3.2}$$
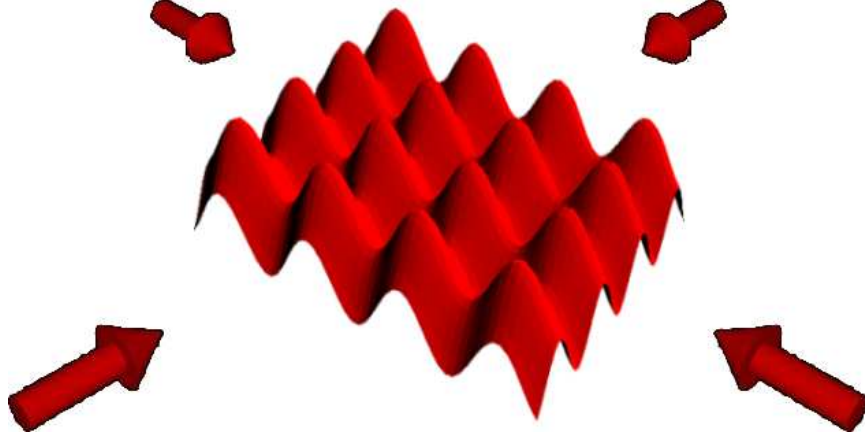
Figure 3.1: Example for the intensity modulation of a two-dimensional optical lattice formed by a set of orthogonal counter-propagating laser beams.

where **d** is the dipole operator of the atom. Performing perturbation theory to second order in the interaction $\hat{H}_{\text{int}}$ leads to the effective potential [119]

$$V_0 = -\frac{1}{2}\alpha\overline{\mathcal{E}^2}\,, \tag{3.3}$$

where the overbar denotes an average in time over one oscillation period and α is the polarizability. Furthermore, we assume that the laser frequency is off-resonant to the transition between the ground state $|g\rangle$ and the excited state, $|e\rangle$, with detuning $\delta = (E_e - E_g)/\hbar - \omega$. The polarizability is derived from perturbation theory to second order [119] as

$$\alpha = \sum_{i\neq g}\frac{2(E_i - E_g)|\langle i|\mathbf{d}\hat{\epsilon}|g\rangle|^2}{(E_i - E_g)^2 - (\hbar\omega)^2}\,, \tag{3.4}$$

where $\hat{\epsilon}$ is the unit-vector along the polarization direction. The main contribution arises from the term $i = e$, as the laser frequency ω is almost resonant with the transition $|g\rangle \to |e\rangle$. Thus, considering only the dominant contribution, the polarizability is approximately given by

$$\alpha \approx \frac{|\langle e|\mathbf{d}\hat{\epsilon}|g\rangle|^2}{E_e - E_g - \hbar\omega}\,. \tag{3.5}$$

All considerations above neglected the finite life time of the ground and excited state due to spontaneous emission. The spontaneous decay can be included in the model using complex eigenenergies of the atomic states, where the imaginary part describes the decay. In this case the polarizability in Eq. 3.3 must be replaced by its real part.

In order to obtain a periodic structure, a set of counter-propagating laser beams is used for the formation of an optical lattice. The standing waves create a periodic modulation of the intensity and hence a periodic effective potential. Choosing the laser beams to be linearly polarized with mutually orthogonal polarization directions leads to an effective potential of the form [24]

$$V(x, y, z) = V_{0,x}\sin^2(k_x x) + V_{0,y}\sin^2(k_y y) + V_{0,z}\sin^2(k_z z)\,. \tag{3.6}$$
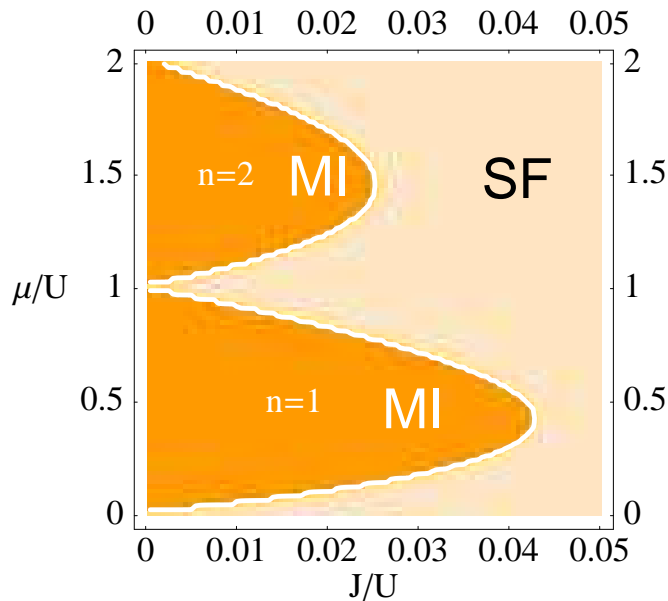
Figure 3.2: Phase diagram for the Mott-Hubbard model for a 2D lattice computed in Gutzwiller approximation. The chemical potential μ varies along the vertical axis and the ratio of hopping to on-site repulsion J/U along the horizontal axis. The dark lobes show the Mott-insulator regions with $n = 1$ and $n = 2$ particles per lattice site (MI) and the bright area is the superfluid phase (SF).

Thus, a perfect one-, two- or three-dimensional lattice potential can be formed by choosing appropriate laser intensities, polarizations and wavevectors k_i. Finally, a Bose-Einstein condensate is loaded into the lattice. Additional harmonic confinement, usually obtained by the shape of the laser beam or a magnetic trap, is required to avoid the unlimited spreading of the condensate and, consequently, the loss of the atoms. An example for the intensity modulation of a two-dimensional optical lattice is sketched in Fig. 3.1.

3.1.2   Mott-insulator transition in optical lattices

The essential physics, describing the dynamics of cold bosonic atoms in an optical lattice is captured by the Mott-Hubbard model [19]

$$\hat{H}_{\mathrm{MH}} = \sum_{i=1}^{M} \frac{U}{2} n_i(n_i - 1) + \sum_{i=1}^{M} (\epsilon_i - \mu)\, n_i - \sum_{\langle i,j \rangle} J_{ij} a_i^\dagger a_j \,. \tag{3.7}$$

Here $a_i^\dagger$ and a_i are the creation and annihilation operators for creating and annihilating a boson on the lattice site i and $n_i = a_i^\dagger a_i$ is the number operator. The first term in Eq. (3.7) describes the repulsive interactions occurring if a lattice site is occupied by n_i bosons. The strength of the repulsion is given by [23]

$$U = \frac{4\pi\hbar^2 a_s}{m} \int d^3\mathbf{x}\, |w(\mathbf{x})|^4, \tag{3.8}$$

where a_s is the scattering length and $w(\mathbf{x})$ are the wavefunctions of the bosons on a lattice site, usually assumed to be Wannier functions. The second term describes the chemical potential which consist of a constant term μ and a spatially varying term ϵ_i. The spatially varying chemical potential is introduced to describe either the trapping potential or disorder effects in the lattice. Finally, the last term describes the inter-site hopping of the bosons. Here, the sum runs only over neighboring lattice sites i, j, which is denoted by $\langle i, j \rangle$. The hopping constant J is given by [23]

$$J_{ij} = \int d^3\mathbf{x}\; w^*(\mathbf{x} - \mathbf{x}_i) \left[-\frac{\hbar^2 \nabla^2}{2m} + V(\mathbf{x}) \right] w(\mathbf{x} - \mathbf{x}_j), \qquad (3.9)$$

where i and j are adjacent sites. In the following discussions, the hopping constant is assumed to be constant i.e. $J_{ij} = J$. A constant hopping parameter is a reasonable approximation to the experiments done with optical lattices.

The dynamics of this model is driven by the interplay of the on-site repulsion U between the bosons and the nearest-neighbor hopping. The system is therefore characterized by the ratio of the hopping to the on-site repulsion J/U. For the remainder of this chapter we will always consider the properties of the ground state of the system.

Two different phases occur in the bosonic Mott-Hubbard model: the superfluid phase (SF) and the Mott-insulator phase (MI). The superfluid phase shows a finite superfluid fraction f_s and a high compressibility κ. In contrast, the Mott-insulator phase has $f_s = 0$ and is incompressible as a consequence of the gap in the excitation spectrum. Let us look at the different phases from the wavefunction point of view. The superfluid state has a finite fraction of the bosons in a superfluid state, described by a delocalized wavefunction. The Mott-insulator phase is characterized by localized bosons and, thus, can be described by a Fock state for each lattice site, in the mean-field picture.

What makes the bosonic Mott-Hubbard model particularly interesting is the phase transition from a superfluid state to a Mott-insulator state for all integer ratios of bosons per lattice site [19]. The phase diagram for the Mott-Hubbard model is shown in Fig. 3.2 for a two-dimensional lattice, computed in Gutzwiller approximation (see Sec. 3.2). For $J/U = 0$, there is always a Mott-insulator phase. Special points are given by the positive integer values of $\mu/U = n$, where the state with n and $n + 1$ bosons per lattice site are degenerate. Increasing J/U from zero to a critical value gives rise to a quantum phase transition from the Mott-insulator phase to the superfluid phase. The phase transitions are in practice only observable for an integer filling i.e. an integer number of bosons per lattice site. In this case, the phase transition occurs along a line, which undergoes the phase transition exactly at the tip of the lobes. Note, that in situations with non-integer filling, there will be no phase transition into a Mott-insulator phase. It will always be favorable for the atomic gas to have the non-integer fraction of bosons in a delocalized superfluid state. In the theoretically considered grand-canonical model, with a fixed chemical potential and a varying number of particles, there occurs a transition into a Mott-Insulator state for all values of μ/U between the degenerate points, as can be seen by the Mott-Lobes in Fig. 3.2.

3.1.3 Experiments

Although being interesting as a theoretical problem by itself, the research on the superfluid-Mott insulator transition in optical lattices had its breakthrough with the experimental demonstration [24] of the phase transition. The experiment comprised a trapped Bose-Einstein condensate in an three-dimensional optical lattice. Varying the laser intensity and, thus, the lattice-potential depth enabled the variation of the parameter J/U. Measurements were done by switching off all traps and letting the cloud expand before an absorption picture was taken. This technique provides a direct measurement of the momentum distribution of the system. Atoms, carrying high momentum are faster than those with low momentum and consequently travel further away from the original trapping position. Hence, atoms at the origin of the absorption picture (defined by the trap position before the expansion) correspond to zero momentum states. Those atoms, which have higher momentum are found further away from the center. The time scale of the expansion must be chosen appropriately such that the original size of the cloud is much smaller than the expanded cloud. This removes any effect on the expansion picture due do the shape of the trapped cloud before the release. Assuming that the cloud is very dilute and expands reasonably fast, the cloud can be considered as non-interacting. Hence, the momentum distribution at the time of the release from the trap is mapped out in the absorption picture.

This technique was also used in [24] to investigate the superfluid-Mott insulator transition in an optical lattice. Optical lattices have, however, an underlying periodic structure. The expansion pictures are intuitively understood if one imagines that every lattice site consists of an independent matter wave. If the system is in a superfluid state, the matter waves in different lattice site all have a fixed phase difference. The expansion picture is, hence, very similar to the interference picture of coherent light scattered from a grating. Bragg peaks appear with a spacing proportional to the inverse lattice constant. In contrast, if the system is in a Mott-insulator state, then the phase is highly fluctuating from lattice site to lattice site. There will be no interference peaks visible in the expansion picture and the momentum distribution will be smooth. The measured Gaussian-like form of the expansion picture is a consequence of the envelope of the single lattice site wavefunctions $w(\mathbf{x})$. The experimental results of [24] for the expansion pictures are shown in Fig. 3.3.

The experiment [24] demonstrated not only that these different interference patterns could be observed, but also demonstrated that a Mott-insulator state was indeed formed. Pushing the state from the Mott-insulator phase back into the superfluid phase and finally taking an absorption picture showed the revival of the interference pattern. The interference pattern revived on a time scale, which is in agreement with the tunneling time between adjacent lattice sites. Hence, simple decoherence of the system into an incoherent state could be ruled out. The importance of the expansion pictures will be discussed in more detail in Sec. 3.4.2. As we will focus in the following on the effect of short-range correlations, another very recent experiment is particularly interesting. This experiment [61] studied short-range correlations in the Mott-insulator phase. Investigation of the interference patterns in the Mott-insulator phase for varying lattice depth confirmed the existence of finite-range correlations as
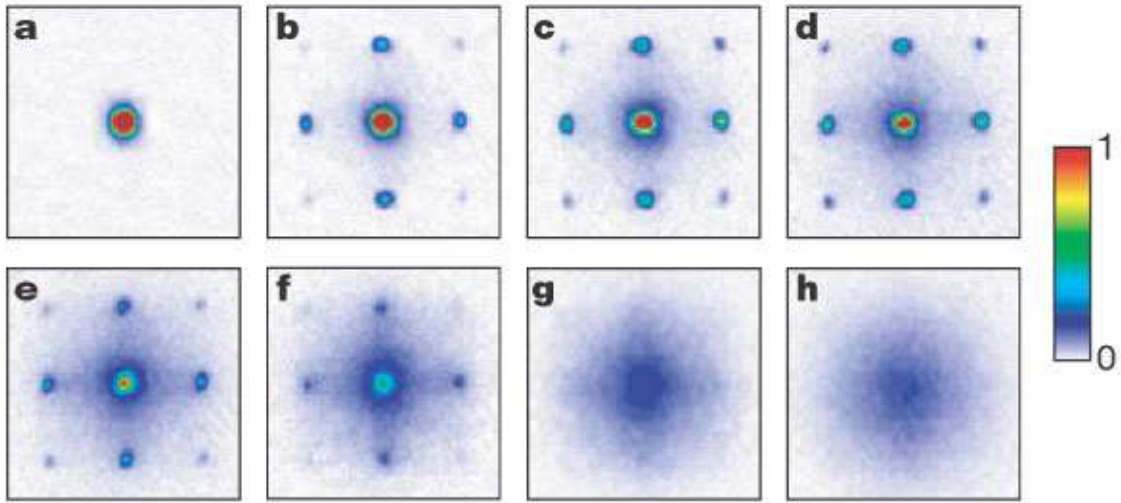
Figure 3.3: Sequence of absorption pictures showing the transition from a superfluid to a Mott-insulator state. The absorption pictures were taken after $15ms$ time of flight. *(a)* $V_0 = 0E_r$; *(b)* $V_0 = 3E_r$; *(c)* $V_0 = 7E_r$; *(d)* $V_0 = 10E_r$; *(e)* $V_0 = 13E_r$; *(f)* $V_0 = 14E_r$; *(g)* $V_0 = 16E_r$; *(h)* $V_0 = 20E_r$. $E_r = \hbar^2 k^2/2m$ is the recoil energy and V_0 defined in Eq. (3.6). Graph taken from [24]

predicted theoretically [57–60]. Finite interference peaks were even visible deep inside the Mott-insulator phase. The importance of short-range correlation will be a main focus in the following sections.

3.2 Gutzwiller ansatz

To date, no analytical solution for the D-dimensional Mott-Hubbard model was found[1] for $D \geq 2$. Nevertheless, there are many successful approximative methods based on strong coupling expansions [124, 125], Bogoliubov theory [126] and mean-field approaches [19, 127]. Moreover, there are many numerical methods to tackle the Mott-Hubbard system. Among the most popular is Density Matrix Renormalization Group (DMRG) [128–130], Quantum Monte Carlo (QMC) [58, 131–139], Exact Diagonalization (ED) [59, 140] and the Gutzwiller [23, 60, 141] method. Recently developed methods like time-dependent DMRG [142] and Time-Evolving Block Decimation (TEBD) [143], allow the computation of the time evolution of the system. Whereas the DMRG, QMC and ED are "quasi-exact" numerical methods, the Gutzwiller approach implies further assumptions about the system. However, there is also an advantage in the Gutzwiller method as it requires the least computational effort and, thus, even large lattices can be treated numerically. As the following sections will focus on a perturbative approach to go beyond the Gutzwiller results, the

---

[1]Exact solutions exist for one-dimensional lattices if occupancies of more than two bosons per lattice site can be neglected [120–123]. In addition, an exact solution of the infinite-range-hopping Bose-Hubbard model [19] can be found.

Gutzwiller method will be discussed in more detail now.

In the Gutzwiller approach, the many-body ground state is approximated by a product of single-lattice-site wavefunctions $|\psi\rangle_i$:

$$|G_0\rangle = \prod_{i=1}^{M} |\psi\rangle_i \,,$$

where the sum runs over all M lattice sites. Rewriting the wavefunction in the number-state basis for each lattice site, $|n\rangle_i$, the Gutzwiller wavefunction reads

$$|G_0\rangle = \prod_{i=1}^{M} \left(\sum_{n=0}^{\infty} f_n^{(i)} |n\rangle_i \right) . \tag{3.10}$$

With this Gutzwiller ansatz for the wavefunction, the ground state of the Mott-Hubbard model, Eq. (3.7), is found, using the variational principle

$$\frac{\delta \langle G_0 | \hat{H}_{\mathrm{MH}} | G_0 \rangle}{\delta f_n^{(i)^*}} = 0 \,. \tag{3.11}$$

We obtain an expression for the coefficients $f_n^{(i)}$

$$\begin{aligned}
\epsilon f_n^{(i)} = {} & \frac{U}{2} n(n-1) f_n^{(i)} - (\mu - \epsilon_i)\, n f_n^{(i)} \\
& - \sum_{\langle i,j \rangle} J_{ij} \left[\sqrt{n}\, \Phi_j f_{n-1}^{(i)} + \sqrt{n+1}\, \Phi_j^* f_{n+1}^{(i)} \right] ,
\end{aligned} \tag{3.12}$$

where ϵ denotes the ground-state energy, and

$$\Phi_i = \sum_n f_n^{(i)^*} f_{n+1}^{(i)} \sqrt{n+1} \,. \tag{3.13}$$

The set of equations (3.12) determine the coefficients $f_n^{(i)}$ of the Gutzwiller ground state, Eq. (3.10). However, the Gutzwiller solution for the Mott-Hubbard Hamiltonian is only an approximation. Using the Gutzwiller ansatz corresponds to a restriction of the variational solutions to the subset of product states. In fact, the Gutzwiller solution can be identified as a mean-field solution for the Mott-Hubbard model [144] with a lattice site dependent mean field $\Psi_i = \langle G_0 | a_i | G_0 \rangle$. Thus, finding the variational wavefunction using the Gutzwiller ansatz corresponds to the ground state of the mean-field version of the Mott-Hubbard Hamiltonian Eq. (3.7)

$$\begin{aligned}
\hat{H}_{\mathrm{MF}} = {} & \sum_{i=1}^{M} \frac{U}{2} n_i (n_i - 1) + \sum_{i=1}^{M} (\epsilon_i - \mu)\, n_i \\
& - J \sum_{\langle i,j \rangle} \left(a_i^\dagger \Psi_j + \Psi_i^* a_j - \Psi_i^* \Psi_j \right) .
\end{aligned} \tag{3.14}$$

Nevertheless, the Gutzwiller solution provides a good approximation in the limit of $J \to 0$ (i.e. far in the Mott-insulator regime) and in the limit of $U \to 0$ (i.e. far in

the superfluid regime). Yet, the ansatz fails in the intermediate regime, where the decay of the inter-lattice site correlations become important. The Gutzwiller ansatz describes the lattice-site correlation only on a mean-field level. Consequently, the lattice-site correlations $\langle a_i^\dagger a_j \rangle$ are replaced by the product of the mean fields $\Psi_i^* \Psi_j$ for $i \neq j$. Considering the special case of a homogenous lattice, where the mean field is lattice site independent $\Psi = \Psi_i$, the Gutzwiller approximation shows no decay of the inter-lattice site correlations. The Gutzwiller results drops directly from the particle number n_i on the i-th lattice site, $\langle a_i^\dagger a_i \rangle = n_i$, down to the constant off-diagonal value $\langle a_i^\dagger a_j \rangle = |\Psi|^2 \neq n_i$ for $i \neq j$. However, inter-lattice site correlations are important for experimentally measurable observables such as expansion patterns. The consequences of the inclusion of short-range correlations to the expansion pictures will be discussed in Sec. 3.4.3. In order to investigate the consequences of the short-range correlations, we will introduce a perturbative approach to improve the inter-lattice site correlations of the Gutzwiller solution.

3.3 Beyond Gutzwiller: A perturbative approach

The aim of this section is the development of a method to improve the Gutzwiller method by including inter-lattice site correlations. Using a perturbative approach, we will be focusing on the short-range correlations and study the consequences of taking these correlations into account. In order to study long-range correlations we would have to calculate the perturbative corrections up to an order comparable to the lattice size. This requires, however, a considerable effort as the number of contributions rise quickly with the order of the perturbation theory.

3.3.1 Perturbative inclusion of short-range correlations

As the Gutzwiller wavefunction presents a good approximation far in the Mott-insulator phase and far in the superfluid phase [57], we will use it as the starting point of the perturbative expansion. Note, that this approach differs from the perturbative treatments known as strong-coupling expansions [124]. In the strong-coupling expansion, the hopping J is usually assumed to be the small parameter for the perturbative expansion. This corresponds to the perturbative expansion in the kinetic energy based on the number-state basis of the unperturbed ground state. Hence, this approach is only suitable for the treatment of the Mott-insulator phase. For a treatment of the superfluid phase a Bogoliubov approach [126] is often used. However, the Bogoliubov method is only applicable in the superfluid regime. The aim of our perturbative expansion is the applicability to both phases: the Mott-insulator as well as the superfluid phase. The applicability of the perturbation theory to both phases is of particular interest, as the trapping potentials used in experiments are combinations of a periodic potential with a harmonic trapping potential. The harmonic trapping potential is required to confine the atoms to a finite region of the optical lattice. However, the combined trap generates an inhomogeneous lattice. Hence, in most cases there are Mott-insulator and superfluid phases coexisting.

First, we re-express the Mott-Hubbard Hamiltonian, Eq. (3.7), by adding and subtracting the mean-field Hamiltonian Eq. (3.14):

$$\hat{H}_{\mathrm{MH}} = \hat{H}_{\mathrm{MF}} + (\hat{H}_{\mathrm{MH}} - \hat{H}_{\mathrm{MF}}) = \hat{H}_{\mathrm{MF}} + V \,, \qquad (3.15)$$

with

$$V = -J \sum_{\langle i,j \rangle} (a_i^\dagger - \Psi_i^*)(a_j - \Psi_j) \,. \qquad (3.16)$$

Hence, we will treat the difference between the mean-field and the full Mott-Hubbard Hamiltonian V as a perturbation to the mean-field Hamiltonian. The unperturbed part is given by $\hat{H}_{\mathrm{MF}}$, which uncouples into a sum over single-lattice-site Hamiltonians (see Eq. (3.14)). Thus, the excitation spectrum of $\hat{H}_{\mathrm{MF}}$, required for the perturbative expansion in V, can be computed for each lattice site separately. The excitations of $\hat{H}_{\mathrm{MF}}$ can be written as product states of single-lattice-site excitations,

$$|G^\alpha\rangle = \prod_{i=1}^{M} |i_{\alpha_i}\rangle \,, \qquad (3.17)$$

with the excitation spectrum as a sum of excitation energies

$$\epsilon^\alpha = \sum_{i=1}^{M} \epsilon^{(i,\alpha_i)} \,. \qquad (3.18)$$

Here, i labels the lattice sites and α_i is the α-th excitation of the i-th lattice site. Finally, $\alpha = (\alpha_1, \cdots, \alpha_M)$ is introduced as an abbreviation for the set of single-lattice-site excitations. Having obtained the excitation spectrum for the unperturbed part of the Hamiltonian $\hat{H}_{\mathrm{MF}}$ numerically, the Gutzwiller wavefunction can be improved by Rayleigh-Schrödinger perturbation theory [113]

$$\langle G^\alpha | G_l \rangle = \frac{\langle G^\alpha | V | G_{l-1} \rangle - \sum_{n=1}^{l-1} \epsilon_n \langle G^\alpha | G_{l-n} \rangle}{\epsilon_0 - \epsilon^\alpha} \,. \qquad (3.19)$$

Here, the states with a Greek superscript, $|G^\alpha\rangle$, denote the unperturbed states, determined from the mean-field Hamiltonian. States with Latin subscripts describe the perturbative corrections. In particular, the state $|G_l\rangle$ denotes the l-th order correction to the wavefunction $|G\rangle = \sum_l |G_l\rangle$. For computational reasons, the basis formed by the unperturbed Hamiltonian is used and all quantities are expanded in this basis. The perturbative corrections, thus, read

$$|G_l\rangle = \sum_\alpha |G^\alpha\rangle \langle G^\alpha | G_l \rangle \,, \qquad (3.20)$$

where the expansion coefficients are given by Eq. (3.19).

The perturbative corrections to any observable A can now be calculated by evaluating the expression $\langle G | A | G \rangle$ to the desired order, using the perturbatively corrected wavefunction $|G\rangle$. In the following sections, all observables will be computed up to second order in perturbation theory. The explicit derivation and a diagrammatic illustration is given in Appendix C.

3.4 Numerical results

Having developed a perturbative tool to improve the Gutzwiller mean-field solution of the Mott-Hubbard model, we will discuss the consequences of the perturbative inclusion of short-range correlations on several observables in the remainder of this chapter. All calculations are done numerically to second order in the perturbation scheme. First, the Gutzwiller ground state is computed using a conjugate-gradient algorithm [145] in combination with an imaginary time propagation routine. The imaginary time propagation step is frequently performed to check if the minima, found by the steepest-descend method, is the real ground state. Finally, knowing the Gutzwiller ground state of the system, the excitation spectrum for every lattice site is computed by exact diagonalization of the the mean-field Hamiltonian Eq. (3.14). Now, perturbation theory to second order is performed, based on the equations derived in Appendix C.

3.4.1 Local observables

Local observables are observables composed of operators which act only on a single lattice site. Hence, they describe local properties. The Gutzwiller mean-field solution provides in most cases already a good approximation to the mean value of local observables. However, there are difficulties in reproducing the correct behavior of fluctuations of local variables, as, for instance, the lattice site-number fluctuations. Perturbation theory gives for local observables no correction in first order. The first non vanishing contribution is the second order. Figure 3.4 shows the results for the order parameter $\Psi_i = \langle a_i \rangle$, the compressibility κ_i and the number fluctuations σ_i. Here, the ratio J/U has been scaled by the dimension, to keep the same mean-field phase-transition point. The solid lines in Fig. 3.4 show the results from perturbation theory, as compared to the Gutzwiller result (shown as the dashed - dotted line). All three quantities show a vanishing perturbative correction both for small and large J/U, as the Gutzwiller wavefunction becomes a good approximation in these regimes (for lattice dimensions $D > 1$). In general, the strongest deviations from the mean-field solution are seen in the one-dimensional case. Moreover, the corrections to the mean-field solutions decrease with increasing dimensionality. This is, however, not surprising as the mean-field solution is exact in infinite dimensions and therefore deviates from the exact solution less and less in higher dimensions.

The inset, Fig. 3.4b, shows the mean value of the order parameter $\Psi_i = \langle a_i \rangle$. The perturbative correction leads to a suppression of the order parameter. However, the suppression is less distinctive in two and three dimensions. This is in agreement with the discussion of the validity of the mean-field solution in the previous paragraph. The critical value for the superfluid Mott-insulator transition remains unmodified $(J/U)_c = 0.086/D$. This is a consequence of using the Gutzwiller mean-field solution as the basis of the perturbation theory. A detailed analysis of the phase boundaries of the Mott-Hubbard model is shown in [124] based on a strong-coupling expansion. The second example for a single-lattice-site observable is the local compressibility for
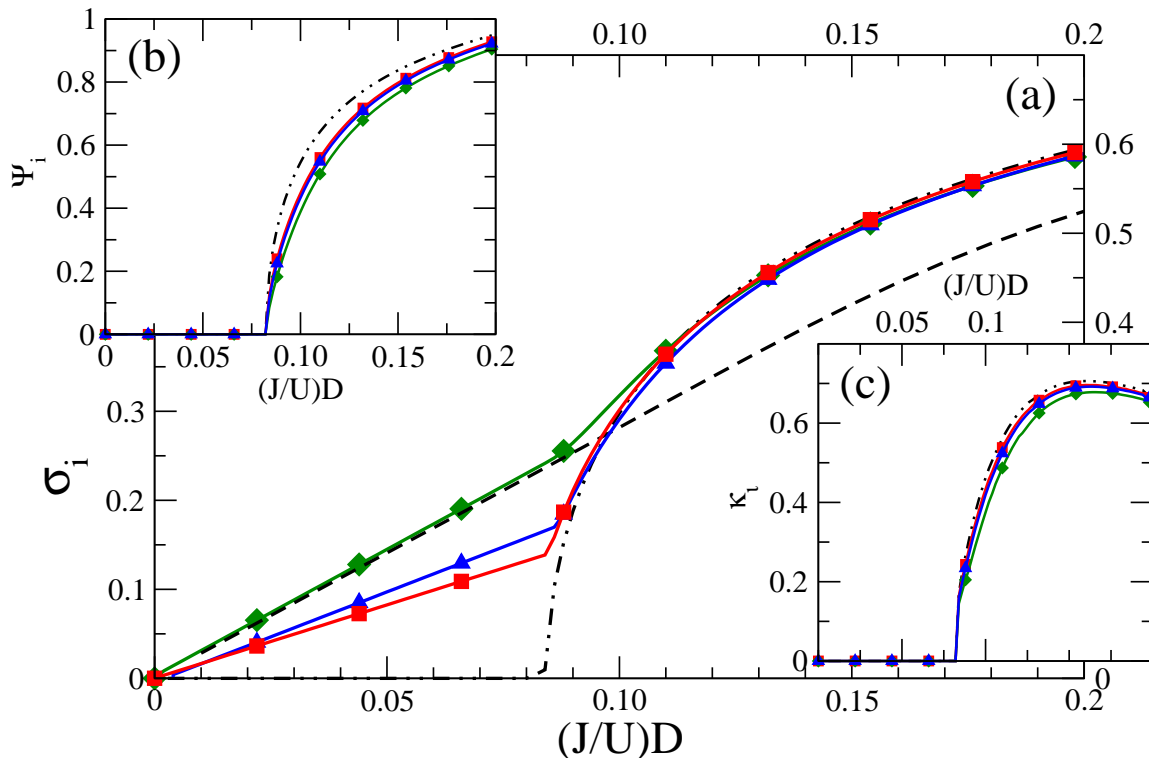
Figure 3.4: Results from perturbation theory for homogeneous lattices in $D = 1$ (diamonds), $D = 2$ (triangles), and $D = 3$ (squares) dimensions. The dashed-dotted lines in Fig. 3.4a-c are the Gutzwiller results. *(a)* Number fluctuations $\sigma_i = \sqrt{\langle n_i^2 \rangle - \langle n_i \rangle^2}$ calculated for a commensurate filling of one boson per lattice site. The dashed line shows the result from the exact diagonalization for 7 lattice sites and $N = 7$ bosons. *(b)* Order parameter $\Psi_i = \langle a_i \rangle$ and *(c)* compressibility κ_i both computed at a fixed chemical potential $\mu/U = 0.5$.

a total number of N bosons in M lattice sites

$$\kappa_i = \frac{M}{N^2} \sum_{i=1}^{M} \frac{\partial \langle n_i \rangle}{\partial \mu} ,$$

depicted in Fig. 3.4c. The results of perturbation theory show a decrease of the compressibility, pointing to an increasing stiffness of the superfluid phase induced by the short-range interaction.

A very different behavior is seen for the number fluctuations

$$\sigma_i = \sqrt{\langle n_i^2 \rangle - \langle n_i \rangle^2} .$$

Unlike the previous examples, the perturbative contributions to the number fluctuations show a large correction in the Mott-insulator region. In contrast to the Gutzwiller result, which predicts zero number fluctuations throughout the whole Mott-insulator phase (see the dashed-dotted line in Fig. 3.4c), the perturbative

approach leads to a non-vanishing contribution. Comparing the perturbative results in one-dimension with an exact diagonalization for seven lattice sites (dashed line in Fig. 3.4c) shows good agreement in the Mott-insulator region. Based on the good agreement of our perturbative result with the exact diagonalization for a large region in the Mott-insulator, we conclude that the number fluctuations are mainly produced by next-neighbor particle-hole fluctuations which are included in the perturbative treatment. Significant deviations from the exact-diagonalization result are seen for higher values of J/U. Again, this misbehavior of the perturbatively-corrected mean-field results can be attributed to the low dimensionality. Additionally, one has to bear in mind that the small parameter, used for the perturbative expansion, corresponds to the deviation of the full Hamiltonian Eq. (3.7) from the mean-field Hamiltonian, Eq. (3.16). This quantity, however, is not expected to be small at the transition point. Thus, this may explain the strong mismatch of the exact-diagonalization and the perturbative results, starting from the mean-field critical value, $(J/U)_c = 0.086$, [23, 124, 127, 144] up to values of the order of the critical values of $(J/U)_c \approx 0.2 \cdots 0.3$ obtained from DMRG [129] and QMC [128, 133] calculations.

3.4.2 The correlation function

The one-particle density matrix, defined as $\rho_{ij} = \langle a_i^\dagger a_j \rangle$, is of particular importance in connection with optical-lattice experiments. The one-particle density matrix, often called correlation function, provides a direct connection to the expansion pictures, which are commonly measured in experiments.

In contrast to the observables discussed above, the correlation function represents a non-local quantity. It describes the correlations between the different lattice sites. Considering the correlation function in Gutzwiller approximation leads to

$$\rho_{ij} = \langle a_i^\dagger a_j \rangle_{\mathrm{GW}} = \langle a_i^\dagger \rangle_{\mathrm{GW}} \langle a_j \rangle_{\mathrm{GW}} = \Psi_i^* \Psi_j \,, \tag{3.21}$$

for $i \neq j$ and to

$$\rho_{ii} = \langle a_i^\dagger a_i \rangle_{\mathrm{GW}} = n_i \,. \tag{3.22}$$

Note, that the average $\langle \cdot \rangle_{\mathrm{GW}}$ is taken with respect to the Gutzwiller wavefunction. Thus the correlation function drops abruptly from $\rho_{ii} = n_i$ for the diagonal elements to its off-diagonal values $\rho_{ij} = \Psi_i^* \Psi_j$. This has particularly distinct consequences for a homogeneous lattice. In this case, the Gutzwiller approximation predicts for any arbitrary two lattice sites, $i \neq j$, the same correlation $\rho_{ij} = \Psi_i^* \Psi_j$, independent of the distance over which the lattice sites are separated. Especially in the Mott-insulator phase, the Gutzwiller result predicts no correlation between lattice sites, as $\Psi_i = 0$. However, finite correlations for the many-body wavefunction are expected even in the Mott-insulator regime [57–59, 61, 97]. Therefore, taking short-range correlations into account improves the shortcomings of the Gutzwiller approximation.

In order to get a feeling for the modifications caused by the inclusion of short-range correlations , comparison to the exact-diagonalization results of a small one-dimensional lattice are made in figure 3.5. Applying perturbation theory to the
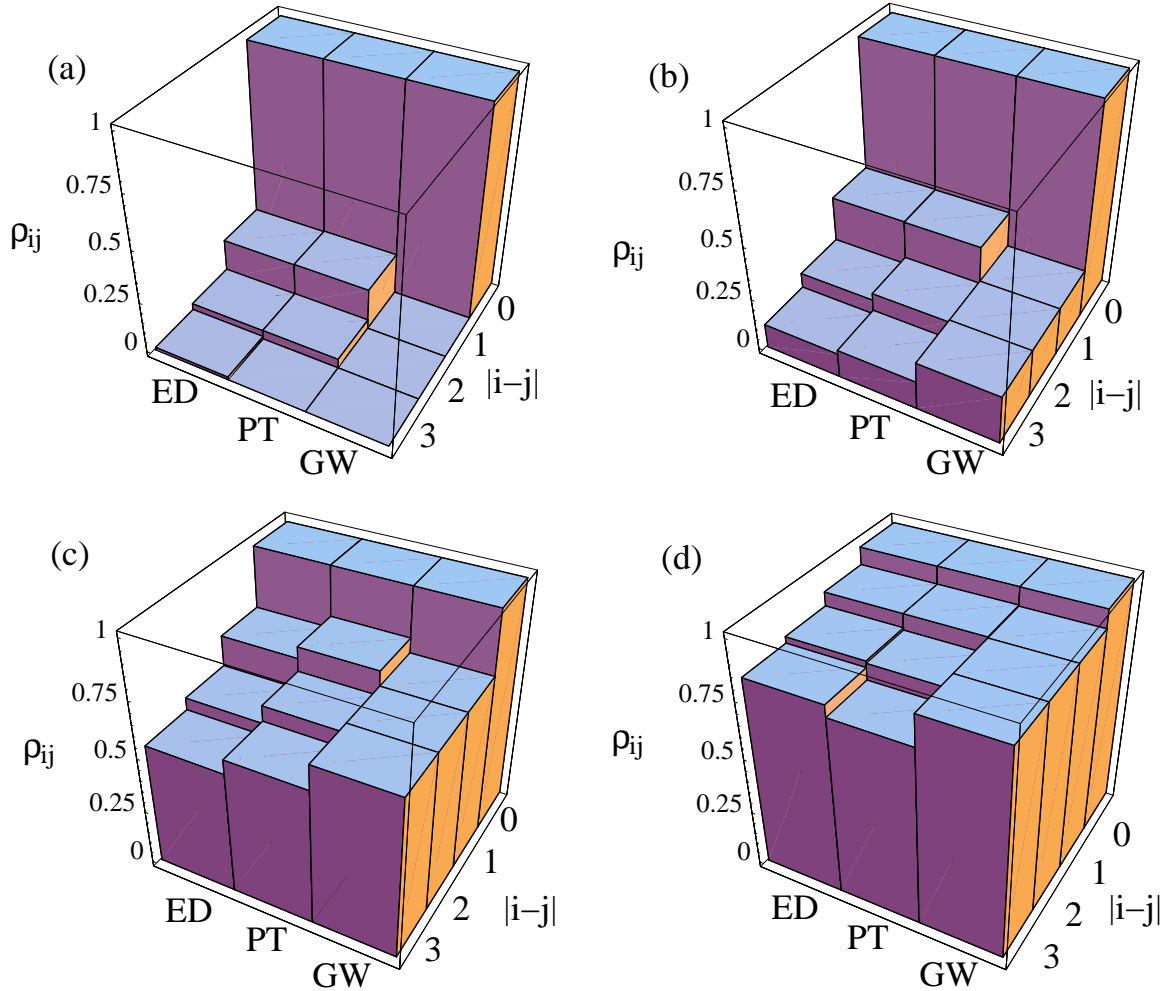
Figure 3.5: Short-range behavior of the one-particle density matrix ρ_{ij} as a function of site distance $|i-j|$. Results for a homogeneous lattice of 7 sites with $N = 7$ bosons have been obtained from exact diagonalization (ED), from second-order perturbation theory (PT), and from the Gutzwiller mean-field ansatz (GW). *(a)* $J/U = 0.05$ (MI regime), *(b)* $J/U = 0.1$, *(c)* $J/U = 0.2$, *(d)* $J/U = 0.5$ (deep SF regime). All calculations use periodic boundary conditions. The mean-field value $(J/U)_c$ for the SF-MI transition in the commensurate case with one boson per lattice site is $(J/U)_c = 0.086$ in 1D (see Fig. 3.4). (The mean-field value differs strongly from $(J/U)_c = 0.277$ derived from QMC calculations [128] or $(J/U)_c = 0.260$ for DMRG calculations [129]).

Gutzwiller wavefunction improves the structureless Gutzwiller correlation function. In Fig. 3.5, we have compared the results of Gutzwiller mean-field theory, with perturbation theory, and with exact diagonalization (ED). The exact diagonalization has been carried out for a small one-dimensional lattice, where it is easily feasible. Although there is no long-range order in the superfluid phase for the one-dimensional case in which the density matrix exhibits a power-law decay towards zero, it is still reasonable to compare the short-range correlations. In fact, we find a nice agreement between the perturbation theory and the exact-diagonalization results, not only for the Mott-insulator region (see Fig. 3.5a), but also for the short-range behavior in the superfluid. This good agreement is a consequence of the slow decay of ρ_{ij} and the negligible corrections from higher-order contributions in small lattices. An example for the superfluid case is shown in Fig. 3.5d. Figure 3.5d for the superfluid case, shows, however, still a considerable difference for $\rho_{i,i+3}$. This is not surprising as we do perturbation theory up to second order. Hence, correlations over a distance of three and more lattice sites are only improved by the global mean-field correction for the infinite lattice (see Eq. (C.11), Eq. (C.12), and Fig. C.2 in Appendix C). We expect better agreement for larger lattice sizes as finite-size effects, arising in small lattices, are still considerable for $M = 7$ sites, used in our exact-diagonalization calculations.

Finally, for intermediate values of J/U, shown in Fig. 3.5b,c, we observe a faster drop in the off-diagonal correlations, such that higher-order contributions in the perturbation theory become more important. In any dimension, the perturbation V is no longer small at the tip of the SF-MI transition lobe (Fig. 3.5c), and the perturbation theory breaks down. Nevertheless, comparing with exact-diagonalization results, Fig. 3.5b shows still good agreement, in contrast to Fig. 3.5c, which shows clear disagreement. Even though the parameter $J/U = 0.2$, chosen for Fig. 3.5c, is close to the SF-MI transition for one-dimensional lattices (as predicted by DMRG [129] and QMC [128, 133] calculations), perturbation theory reproduces the correct slope for the off-diagonal decay and lacks only the wrong offset from the mean field. Thus, even for this case, perturbation theory represents a qualitative improvement on the Gutzwiller result. The results for both approximations, Gutzwiller and perturbation theory, are expected to become better in higher dimensions (with the perturbative corrections diminishing in size).

3.4.3 Corrections to the expansion pictures

The experimental observation of the SF-MI transition [24] relies on the different behavior of the density matrix in the Mott-insulator and superfluid regimes. The experimental visualization is done by means of absorption pictures of the freely expanding atomic cloud. Assuming that the expansion time is long enough and that the gas is dilute enough (such that atom-atom interactions can be neglected during the expansion), the shape of the cloud reflects the initial momentum distribution $\rho(\mathbf{k})$. Under these assumptions, the density matrix is directly connected to the expansion

pictures of the many-body system via a Fourier transform

$$\rho(\mathbf{k}) = |w(\mathbf{k})|^2 \sum_{i,j=1}^{M} \rho_{ij} e^{i\mathbf{k}(\mathbf{r}_i - \mathbf{r}_j)} . \tag{3.23}$$

Here, $w(\mathbf{k})$ denotes the Fourier transform of the Wannier functions $w(\mathbf{r} - \mathbf{r}_i)$, describing the wavefunction of a single lattice site. The presence of the factor $w(\mathbf{k})$ in Eq. (3.23) provides a cutoff at high momenta. Expansion pictures provide therefore a tool, allowing to draw one's conclusions about the state of the many-body system. From Eq. (3.23) we can conclude that a many-body state, having no inter-lattice site correlations, i.e. $\rho_{ij} = \rho \delta_{ij}$, leads to a Fourier transform which is a constant. This situation corresponds to the Gutzwiller prediction for the Mott-insulator. Including short-range correlations will drastically change the flat, homogenous expansion pattern predicted by the Gutzwiller approximation. Considering the case in which even distant lattice sites are strongly correlated leads to the superfluid situation. In the strongly correlated case, ρ_{ij} can be approximated by a constant in Eq. (3.23) and we expect to see Bragg peaks in the expansion pattern.

Based on these ideas, Greiner et al. [24] examined the expansion picture, Fig. 3.3, of a Bose-Einstein condensate in an optical lattice for different values of J/U. Starting with a harmonic trapping potential, Fig. 3.3a shows a sharp single peak, typical for a Bose-Einstein condensate. In the following sequence of absorption pictures, Fig. 3.3b – f, the optical lattice and, thus, the parameter J/U was increased. As a consequence of the increasing optical lattice, the Bragg peaks become more and more pronounced from Fig. 3.3b to Fig. 3.3c. According to the discussion above, the expansion patterns Figs. 3.3b-e show the signatures of a strongly correlated many-body state. Therefore, these expansion patterns were identified in the experiment [24] with a state in the superfluid phase. Finally, with increasing J/U, the expansion patterns show an increasing diffuse background, until in Fig. 3.3h there are no peaks visible anymore. The system has undergone a superfluid-Mott insulator transition and is now in the Mott-insulator phase with a very large ratio of J/U. Hence, Fig. 3.3h shows the expected featureless expansion picture of an uncorrelated many-body state.

A closer look at Fig. 3.3 shows further interesting features. Firstly, the expansion pictures show a Gaussian-like envelope. This is a consequence of the single-lattice-site wavefunction, and is taken into account by the function $w(\mathbf{k})$ in Eq. (3.23). Secondly, the experiment used an additional harmonic trapping potential to confine the Bose-Einstein condensate spatially. Consequently, in most cases of Fig. 3.3 there will be superfluid and Mott-insulator regions coexisting. The coexistence of both phases leads to a diffuse background added to superfluid peaks, hence, giving an possible explanation to the expansion pictures in Fig. 3.3c-f. Thirdly, one has to note that our previous interpretation of the expansion patterns were partly based on the Gutzwiller results. There is no sharp transition from a Bragg-peaked pattern in the superfluid phase to the homogenous expansion pattern of the Mott-insulator phase, as will be shown now by means of the perturbative inclusion of short-range correlations.
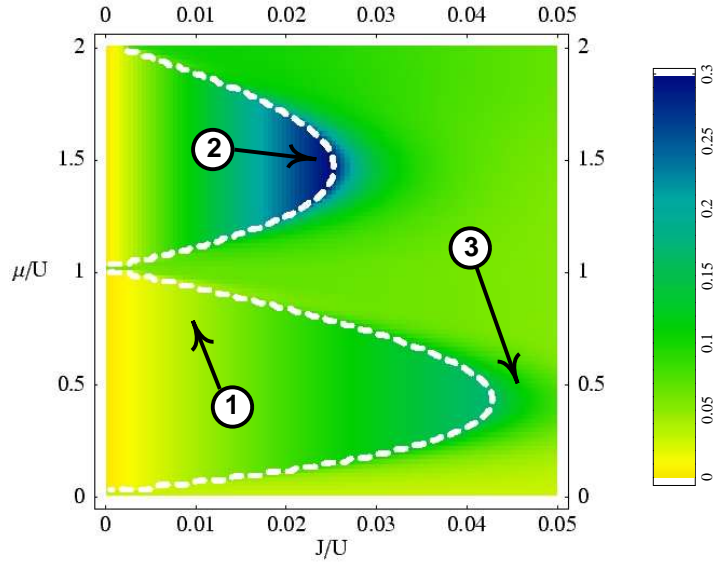
Figure 3.6: The figure shows the correction to $\rho_{i,i+1}$ in second-order perturbation theory as a function of μ/U and J/U. The order parameter $\langle \Psi_i \rangle$ vanishes inside the Mott-insulator lobes. The mean-field phase boundaries are given by the white-dashed line. Arrows in the $(\mu/U, J/U)$ phase diagram indicate the parameters used for the momentum distributions shown in Fig. 3.7. The parameters used are: $\mu/U = 0.75$, $J/U = 0.01$ for (1), $\mu/U = 0.5$, $J/U = 0.044$ for (2), and $\mu/U = 1.5$, $J/U = 0.0225$ for (3).

Bulk situation

Before discussing the full experimental situation, it is instructive to consider the bulk situation first. Thus, we neglect the harmonic confinement and consider the consequences of the perturbative inclusion of short-range correlations for a homogenous optical lattice. The perturbative treatment yields considerable contributions to the correlation function. Figure 3.6 shows an example for the nearest-neighbor correction $\rho_{i,i+1}$ to the correlation function. The most pronounced corrections are seen at the tips of the lobe. These are, however, also the regions where the perturbation series is expected to show large errors, as the expansion parameter is not small anymore.

As a consequence of the corrections to the correlation function, there are also drastic changes in the expansion patterns. A few examples are shown in Fig. 3.7 with their parameters indicated by the arrows in the μ/U-J/U plane in Fig. 3.6. The set of momentum distributions $\rho(\mathbf{k})/|w(\mathbf{k})|^2$ in Fig. 3.7 are computed for a homogeneous two-dimensional lattice. All upper figures are computed using the Gutzwiller approximation. For comparison, the lower graphs show the momentum distributions improved to second order in perturbation theory. These perturbatively improved expansion pictures (lower graphs), show much finer structures than the mean-field results (upper graphs).

The parameters in Fig. 3.7(1) and Fig. 3.7(2) are chosen to lie in the Mott-
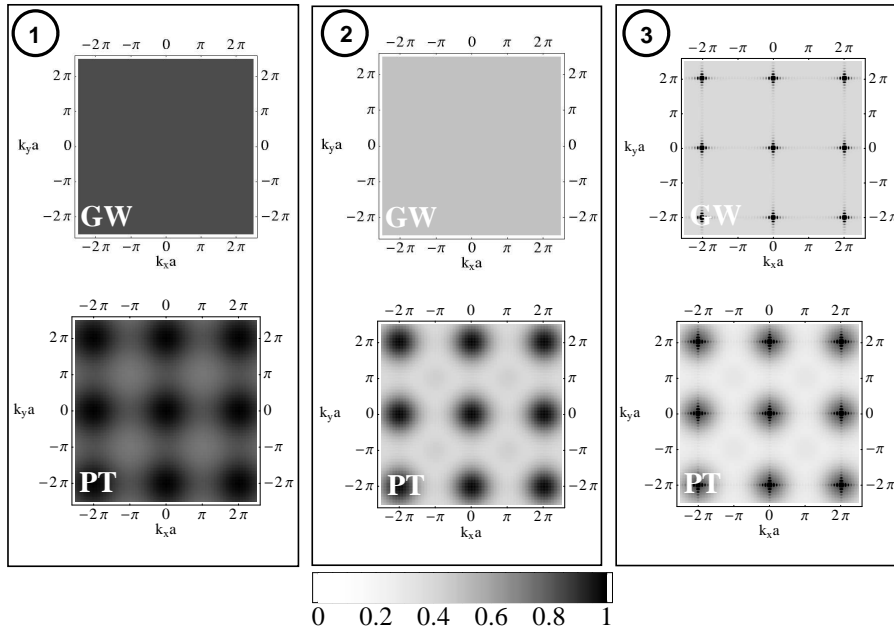
Figure 3.7: Plots (1) – (3) display the momentum distribution without the Wannier form factor, $\rho(\mathbf{k})/|w(\mathbf{k})|^2$, calculated for a 2D lattice with 25×25 lattice sites. The numbers (1) – (3) refer to the parameters in the $(\mu/U, J/U)$ phase diagram as indicated by the arrows in Fig. 3.6. The upper plots are the Gutzwiller mean-field results (GW), and lower plots are calculated using second-order perturbation theory (PT). The parameters used are: $\mu/U = 0.75$, $J/U = 0.01$ for (1), $\mu/U = 1.5$, $J/U = 0.0225$ for (2); and $\mu/U = 0.5$, $J/U = 0.044$ for (3). The gray scales of the plots belonging to the same parameter set are identical. Expansion patterns (1) and (2) are normalized to the peak maximum. The expansion patterns (3) are normalized to 1/20 of the peak maximum.
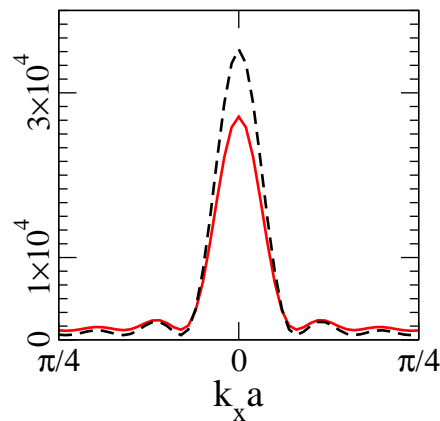
Figure 3.8: Cut through one of the peaks in the upper and lower expansion picture of Fig. 3.7(3). The cut is taken along $k_y a = 0$; dashed line for the Gutzwiller expansion picture (GW in Fig. 3.7(3)) and solid line for the perturbation-theory result (PT in Fig. 3.7(3)).

insulator phase. The previous discussion of perturbative modifications in Sec. 3.4.2 showed quickly decaying correlations with a finite correlation length[2] for the Mott-insulator. Hence, perturbation theory predicts broad peaks in the Mott-insulator regions down to very small values of J/U, Fig. 3.7(1) and Fig. 3.7(2) lower graphs, whereas the Gutzwiller result without perturbation theory shows a structureless flat distribution for the whole Mott-insulator region, Fig. 3.7(1) and Fig. 3.7(2) upper graphs. Naturally, the modifications of $\rho(\mathbf{k})/|w(\mathbf{k})|^2$ are strongest near the phase transition, Figs. 3.7(2). Going towards larger values J/U into the superfluid phase (see Fig. 3.6(3) and Fig. 3.7(3)), perturbation theory gives rise to a suppression of the peaks as shown in Fig. 3.8. This suppression can be larger than 20% of the original peak height and stems from the corrections to the mean field. Additionally, Fig. 3.7(3) shows broad peaks induced by the inclusion of short-range correlations. However, for large lattices, these broad peaks are small compared to the (finite-size broadened) superfluid δ-peaks.

Harmonic confinement

In contrast to what was assumed in the last section, optical lattices used in experiments are not homogeneous. Magnetic or optical trapping potentials are used [24, 146] to confine the atomic gas to a finite volume. The inhomogeneity caused by the trapping potential leads to slowly varying on-site energies, ϵ_i, in the Mott-Hubbard model Eq. (3.7). This slowly varying potential can be interpreted as a spatially varying chemical potential $\mu_{\text{local}} = \mu - \epsilon_i$. Consequently, the lattice is in general not in a pure Mott-insulator or superfluid phase, but shows alternating shells of superfluid and Mott-insulator regions. Examples for different harmonic potentials are shown in the bar graphs of Fig. 3.9. For instance, the bar graph with the box label shows a superfluid region surrounded by a Mott-insulator shell. The diamond-labeled and circle-labeled graphs show the opposite situation i.e. a Mott-insulator surrounded by a superfluid ring. Moreover, the phases need not necessarily be connected but can be fragmented, as shown in the example denoted by a circle in Fig. 3.9. Considering the varying on-site energy as a spatially varying chemical potential gives a qualitative understanding of the shell structures. The spatial variation of the chemical potential corresponds to a path parallel to the μ/U axis in the μ/U-J/U diagram (see the solid lines in the center plot of Fig. 3.9). Starting with the potential minimum in the trap center and then moving away from the center, decreases the effective local chemical potential. Thus, we start at the top of the line and move towards smaller μ/U values. Whenever a MI-SF (SF-MI) phase boundary is hit along the path in the μ/U-J/U diagram, a change from a Mott-insulator to a superfluid shell (superfluid to Mott-insulator shell) appears. Consider, for instance, the particle-number distribution on the right hand side of Fig. 3.9, labeled by a diamond. Starting in the $n = 1$ Mott-insulator lobe, the particle-number distribution shows a plateau with $n = 1$ particles in the trap center. Once the phase boundary is hit we have a transition into the superfluid state, resulting into a superfluid ring in the number distribution. Note, however, that for a harmonic trap, μ/U changes quadratically with the distance to the trap center. This can cause situations as for the number distribution labeled by

---

[2]The correlation function is expected to decay exponentially in the Mott-insulator phase [57].
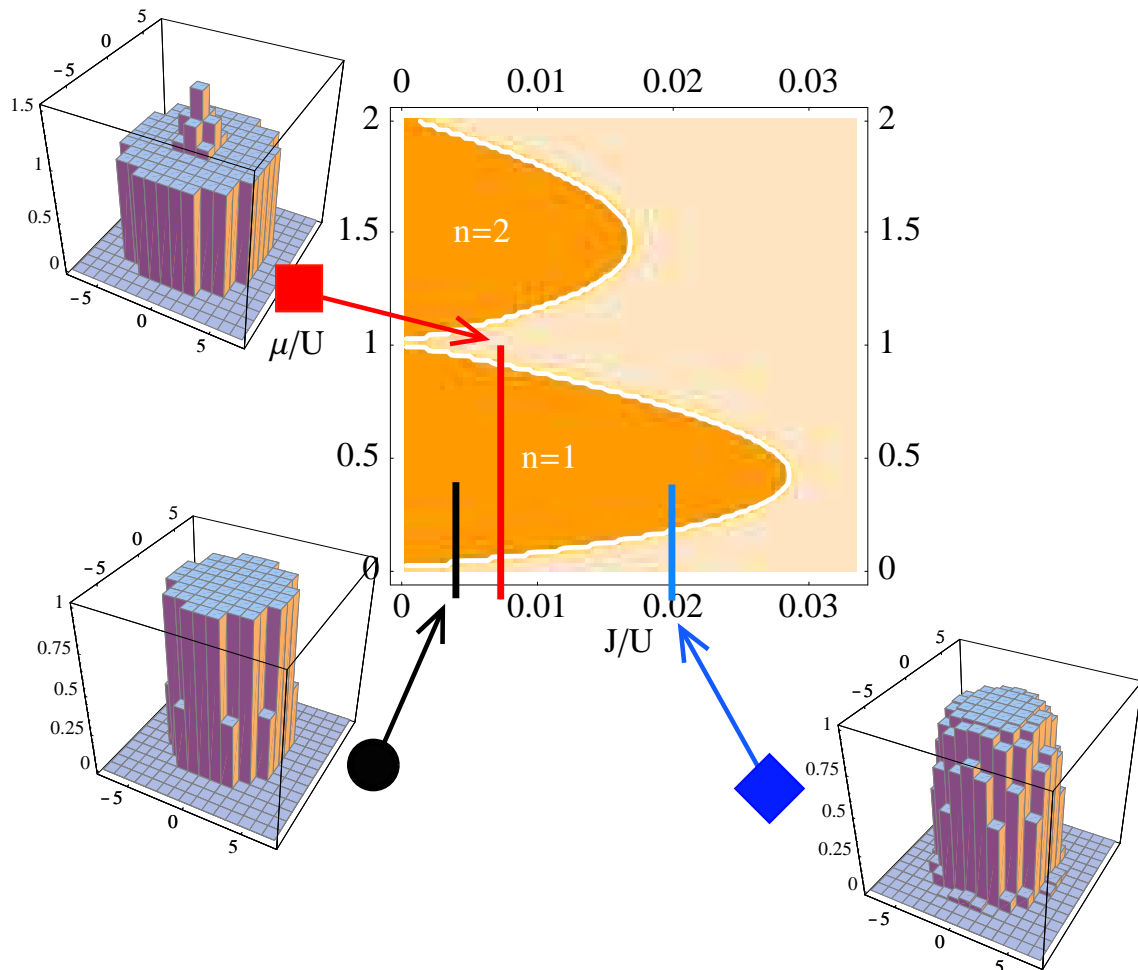
Figure 3.9: *Bar graphs:* Occupation number n_i on a plane through the trap center for a 3D lattice with 15^3 lattice sites. Circle: $\mu/U = 0.4$, $J/U = 0.005$, and $\alpha/U = 0.02$. Square: $\mu/U = 1.5$, $J/U = 0.0075$, and $\alpha/U = 0.03$. Diamond: $\mu/U = 0.4$, $J/U = 0.0075$, and $\alpha/U = 0.02$. *Center graph:* Phase diagram in the μ/U-J/U plane, showing the variation of the chemical potential due to the harmonic confinement.

the box symbol in Fig. 3.9. In the box example, the outer most superfluid shell is missing due to the quadratically fast changing potential and the discretization of the lattice.

The inclusion of short-range correlations gives also rise to considerable modifications in the presence of an inhomogeneous trapping potential. Examples, calculated for a three-dimensional lattice, are shown in Fig. 3.10, where an underlying harmonic potential

$$\epsilon_i = \alpha \sum_{\beta=1}^{3} i_\beta^2, \tag{3.24}$$

was chosen. The three expansion patterns considered in Fig. 3.10 correspond to the three examples of particle-number distributions shown in Fig. 3.9. Calculating the expansion patterns for these situations shows that the perturbative corrections, arising from the short-range correlations, lead to a substantially different behavior in the different cases. For the almost complete Mott-insulator state we obtain a correction to all wavevectors k, with a fast drop at values close to the peak center $k = 0$, which leads to a peak broadening in the expansion picture (see circles in Fig. 3.10). Particularly large changes were found for the case of a superfluid island surrounded by a Mott-insulator phase (squares in Fig. 3.10). Again, corrections arise for all wavevectors, but, in contrast to the almost homogeneous case, the largest increase is now found for $k = 0$, with changes of about 20% of the peak maximum. Finally, the reversed situation, a Mott-insulator island surrounded by a superfluid phase (diamonds in Fig. 3.10) does not show an increase of its maximum peak height but a considerable reduction (over 5% of the peak maximum). This is not surprising, as the majority of the lattice sites are now contributing to the superfluid phase and a peak reduction was also observed for the bulk-superfluid phase.

Comparison with Quantum Monte Carlo calculations

To conclude this section, the Gutzwiller results and perturbatively improved results for the expansion patterns are compared to the Quantum Monte Carlo (QMC) calculation of Kashurnikov et al. [58]. Comparing the different numerical methods with the Quantum Monte Carlo calculations provides information about the shortcomings of the Gutzwiller method. Moreover, insight about the ability to correct these shortcoming using the perturbative expansion is obtained.

The results from the different numerical approaches, computed for a small three-dimensional lattice with harmonic confinement, are shown in Fig. 3.11. The upper graphs always depict the Quantum Monte Carlo results. The lower graphs show the Gutzwiller (dashed-black line) and the perturbatively corrected result (red-solid line). There is in general good qualitative agreement in all cases with high superfluid fraction (compare for example the upper and lower graphs in Fig. 3.11a – c). However, the features of these expansion patterns are already well reproduced using the Gutzwiller mean-field ansatz alone. In particular, the reproduction of the satellite
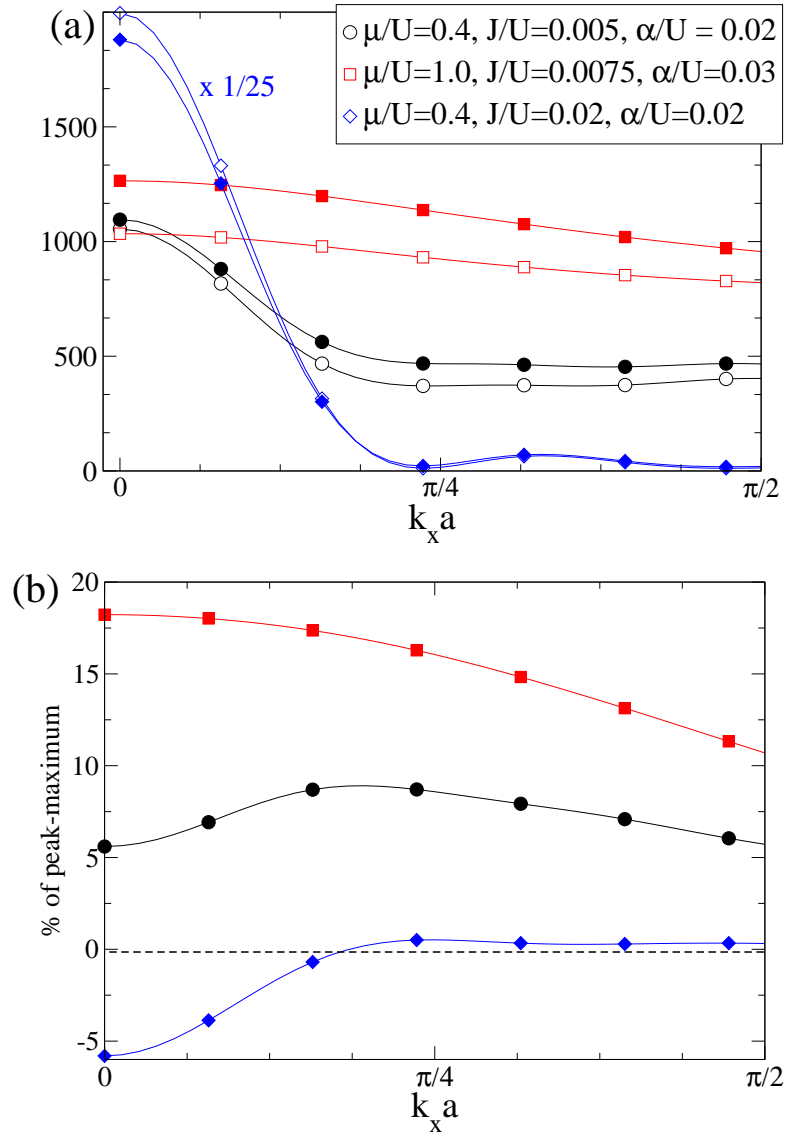
Figure 3.10: Expansion patterns for a 3D lattice with 15^3-sites in the presence of a harmonic potential. *(a)* Momentum distribution without the Wannier form factor, $\rho(\mathbf{k})/|w(\mathbf{k})|^2$, calculated along the k_x direction. Filled symbols are the perturbation-theory results and open symbols are the Gutzwiller results. The graphs for the Mott-insulator surrounded by a superfluid shell (diamonds) are rescaled by a factor $1/25$. The results presented here correspond to the occupation distribution shown in Fig. 3.9 with the corresponding symbols. *(b)* Difference between perturbation-theory and Gutzwiller results.
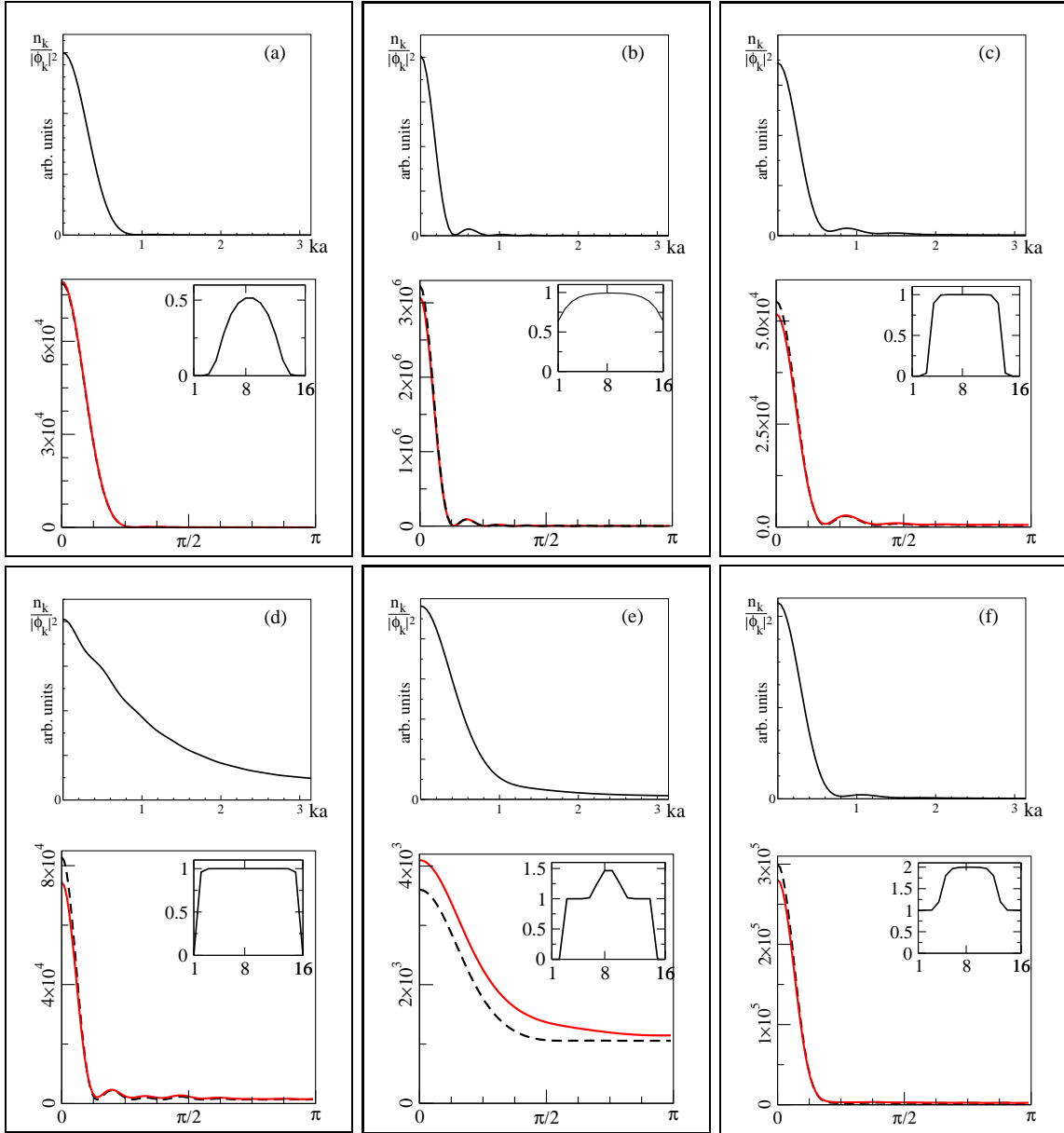
Figure 3.11: Comparing the momentum distribution obtained with different numerical methods (QMC, Gutzwiller, perturbation theory) computed for a 3D optical lattice with an harmonic trapping potential. Each box shows in the upper graph the QMC results, taken from [58] and in the lower graph the Gutzwiller (dashed line) and perturbation-theory (solid line) results. All expansion patterns are cuts along k_x for a system of 16^3 lattice sites. Furthermore, all plots are plotted without the Wannier form factor, $\rho(\mathbf{k})/|w(\mathbf{k})|^2$ (corresponding to $n_k/|\phi_k|^2$ in the notation of [58]). The insets in the boxes of the lower graphs show the occupation number n_i for a cut along the $\hat{x}$-direction. (a) $J/U = 1/24$, $\mu = 0.3775$, $\alpha = 0.00810$. (b) $J/U = 1/32$, $\mu = -0.0383$, $\alpha = 0.00610$. (c) $J/U = 1/80$, $\mu = 0.3125$, $\alpha = 0.01221$. (d) $J/U = 1/80$, $\mu = 0.625$, $\alpha = 0.01288$. (e) $J/U = 1/80$, $\mu = 1$, $\alpha = 0.02505$. (f) $J/U = 1/80$, $\mu = 1.875$, $\alpha = 0.022$. (Note, however, that the Hamiltonian used in [58] differs from Eq. (3.7) and, hence, the parameters used in [58] are converted to the corresponding quantities used in our definitions.)

peak, which was discussed as a signature of the MI-SF shell structure in [58]. Corrections arising from perturbation theory show a suppression of the superfluid peak, as was discussed above. However, there are also considerable discrepancies to the Quantum Monte Carlo results for situations with a large Mott-insulator fraction, even after implementing second-order perturbation theory. In these cases (Fig. 3.11d,e), the influence of the Mott-insulator phase on the expansion picture broadens the peak and leads to a homogeneous background. The discrepancies to the Quantum Monte Carlo approach are clearly visible in Fig. 3.11d. Gutzwiller and perturbation theory show no peak broadening and a satellite peak, in contrast to the Quantum Monte Carlo results. Including the short-range correlations perturbatively corrects the expansion pattern in the correct direction, giving rise to a suppression of the superfluid peak. Considering the expansion pattern with the clearest Mott-insulator features (Fig 3.11e), the correct peak broadening is obtained from Gutzwiller and the perturbative calculation, but a larger ratio of the Mott-insulator background to superfluid peak is visible.

In light of these discrepancies, it is necessary to note that the expansion pattern is highly sensitive to the value of the mean field. Even small deviations can lead to a change in the superfluid-peak height sufficient to mask the flat distribution of the Mott-insulator phase. However, careful checks proved that the observed discrepancy is not due to a lack in accuracy of our numerical calculations. We therefore believe that the discrepancies between Quantum Monte Carlo and the Gutzwiller/perturbation-theory results for situations with a large Mott-insulator fraction can be attributed to the insufficiency of the Gutzwiller approach in describing the long range correlations in this inhomogeneous situation. Situations of the particle-number distribution, as shown in the inset of Fig. 3.9(circle), inherit the special case of an unconnected superfluid phase. This fragmentation of the superfluid phase causes great problems in the Gutzwiller approach. Assuming a local mean field Ψ_i, the correlations of two lattice sites situated in different superfluid fragments are given by $\rho_{ij} = \Psi_i^* \Psi_j$. Thus, the correlation is unaffected by the fact that the two superfluids are unconnected. Even the perturbative correction to the Gutzwiller result can only restore the correct correlation between the superfluid fragments, if the perturbation theory is done to sufficient order i.e higher than the distance between the fragments. The results presented in Fig. 3.11 are done in second-order perturbation theory, and therefore not yet sufficient to give the correct long-range correlation function. In addition, it must be remarked that the lattice, employed in [58], is comparatively small for the given harmonic confinement potential (with no complete shell of empty sites at the perimeter, see insets of Fig. 3.11). Hence, the choice of boundary conditions (periodic in the case of our numerical calculations) may have non-negligible effects on the outer lattice sites.

3.5   Summary of Chapter 3

In conclusion, this chapter showed that short-range correlations play an important role at the Mott-insulator transition in optical lattices. The discussion was based on the description of the optical lattice using the bosonic Mott-Hubbard

model [23]. Introducing a new way to perturbatively include correlations to the mean-field Gutzwiller ansatz allowed the inclusion of short-range correlation. The perturbation theory presented in this chapter is applicable in the Mott-insulator as well as in the superfluid state, in contrast to perturbative approaches using strong-coupling expansions or Bogoliubov theory. Hence, this method is particularly suitable in inhomogeneous situations where superfluid and Mott-insulator phases are coexistent. However, results close to the phase transition must be interpreted with care as the perturbative correction is not small in this region.

Corrections to local quantities, as well as to the correlation function and the expansion patterns were derived. The numerically calculated corrections to the mean-field results used the perturbative method up to second order, thus including correlations between next and next-nearest lattice sites. Modifications to the particle-number fluctuations σ_i, arising from the perturbation theory, gave rise to the expected smooth transition of σ_i at the superfluid-Mott insulator transition. Moreover, comparing the results obtained by perturbation theory to the results for σ_i from exact diagonalization in one-dimensional lattices, showed good agreement for small values of J/U.

Of particular importance are the corrections to the correlation function, and thus to the expansion patterns. Comparing the correlation function obtained from perturbation theory with calculations obtained from exact diagonalization for small one-dimensional lattices showed good agreement. Studying the expansion patterns showed that the inclusion of the short-range correlations to the mean-field ansatz gives rise to distinct modifications. A broad peak can be seen in the perturbation-theory results for the Mott-insulator regime. The peaks remain visible even down to small values of J/U. Comparing perturbation-theory and mean-field expansion patterns obtained for parameters in the superfluid region displayed a considerable suppression of the superfluid peak in the perturbative results. Additionally, on approaching the superfluid-Mott insulator quantum phase transition from the superfluid side, broad peaks underlying the superfluid peaks were found in the perturbation-theory expansion patterns. Including a harmonic confinement potential leads to situations, where superfluid and Mott-insulator regions coexist. Hence, the perturbative corrections to the expansion pattern become more complex. Lattices with different additional harmonic traps were studied. The examples, in which the periodic lattice was combined with a harmonic potential, gave rise to different constellations of superfluid and Mott-insulator regions. As a consequence of the inclusion of short-range correlations, modifications of up to 20% of the peak maximum were found in the expansion patterns .

Finally, the results of the Gutzwiller method and perturbative method were compared with a Quantum Monte Carlo simulation. Expansion pictures for a three-dimensional lattice of 16^3-lattice sites were computed for different harmonic confinement potentials. The comparison to the Quantum Monte Carlo results showed, that for situations with dominating superfluid fraction, the Gutzwiller and perturbation theory results reproduce the expansion pictures quite well. Considerable differences

are seen in the cases, in which the expansion picture is dominated by the Mott-insulator region. The perturbative inclusion corrects the expansion pattern in principle towards the correct direction. However, improving the Gutzwiller results by perturbation theory to second-order was not sufficient to reproduce the Quantum Monte Carlo results.

Chapter 4

Full counting statistics of the BEC-BCS crossover

The final chapter presents an example of the new field of dilute many-body systems accessible in cold atomic gases. Looking at the historical development of the the BEC-BCS crossover research field makes the connection to condensed matter research obvious.

   The crossover from a BEC state of molecules to a BCS state of fermions has raised the interest of physicists for many years. The BCS wavefunction, developed for the description of superconductivity [147], was soon recognized [148,149] also to be applicable for the description of the crossover to a state of Bose-Einstein condensed molecules. The theory was soon extended to non-zero temperatures [150,151]. With the discovery of high-temperature superconductivity, the idea that the BEC-BCS crossover might be relevant for its theoretical description emerged [151–155]. A revival of BEC-BCS crossover physics was launched by the new possibilities offered in experiments with ultra-cold gases of Fermi spin mixtures. Fermions were prepared in an equal number of two different hyperfine spin states and cooled down to a fraction of the Fermi temperature. Applying a magnetic field allows the preperation of the atomic cloud close to a Feshbach resonance. If the interaction between fermions in different spin states is attractive then the gas is expected to form a superfluid BCS state. Tuning the magnetic field over the Feshbach resonance, the Cooper pairs can be transformed into molecules. Fermions which are not bound to molecules are scattering with a positive scattering length on this side of the Feshbach resonance. The great advantage of BEC-BCS crossover experiments in dilute atomic gases is given by the possibility to tune the interaction strength using Feshbach resonances. The first experiments demonstrated the conversion of the Fermi spin mixture into a BEC of molecules [156–159]. Recent experiments have shown a strong indication for the formation of a superfluid BCS state [158,160].

   This Chapter will concentrate on the statistical aspect of the BEC-BCS crossover. The BEC-BCS crossover presents the peculiarity of a transition from bosonic molecules to a state of Cooper-paired Fermions. As a consequence, a drastic change in the particle-number statistics is expected as one changes from the BEC to the BCS side.

71

Hence, measuring the atom-number statistics provides a possibility to gain information about the state of the system. In this chapter, the measurement of atom-number fluctuations in a small subsystem of the dilute atomic cloud is suggested as an experimental approach to investigate the atom-number statistics of atomic clouds. Following this ansatz, number-density correlations are calculated for the BEC-BCS crossover. Statistical properties are obtained using the method of full counting statistics. The very different results obtained for the full counting statistics on the BEC and BCS side of the crossover demonstrate the usage of noise measurement to distinguish these different states of the many-body system. For instance, the order parameter on the BCS side can be extracted from the measurement of the variance at zero temperature. Hence a measurement of the variance provides a way to recognize the formation of the superfluid state.

4.1   The BEC-BCS crossover in ultra-cold fermionic gases

Studying the BEC-BCS crossover regime requires good control over the interaction strength between the particles. Feshbach resonances provide just this control over the inter-atomic interaction strength in dilute atomic clouds. Hence, using Feshbach resonances eventually led to a breakthrough in matter-wave experiments investigating the BEC-BCS crossover. Strong repulsive interactions on one side of the Feshbach resonance and strong attractive interactions on the other side of the resonance allow the formation of a BEC and BCS state, respectively. The aim of this section is to provide a brief overview of the model and the basic mechanism describing ultra-cold atomic Fermi mixtures close to a Feshbach resonance.

4.1.1   Feshbach resonances

A deeper understanding of Feshbach resonances is not necessary for the discussion in the following sections. Hence, we will give only a short introduction to the ideas behind the Feshbach-resonance phenomenon. For the main part of this chapter, the simple treatment of a Feshbach resonance presented here, will be sufficient. A more detailed discussion of the topic is given for example in [36, 161–163].

Feshbach resonances provide a very useful tool to manipulate the interaction strength in atomic gases. The basic principle of the Feshbach resonance relies on the coupling of the two-fermion scattering state to a molecular bound state. Strong coupling is achieved by bringing the scattering state close to resonance with the molecular bound state. A schematic sketch of the potentials as a function of the inter-atomic distance is shown in Fig. 4.1. The molecular bound state presents the so called "closed channel" in contrast to the "open channel" of the two-fermion scattering state. A scattering process between different atoms can generally be described by a set of quantum numbers (e.g. the hyperfine states etc.). Following [36], different sets of quantum numbers will in the following be denoted as a different channels. Scattering between different channels can thus lead to a difference in the Zeeman and
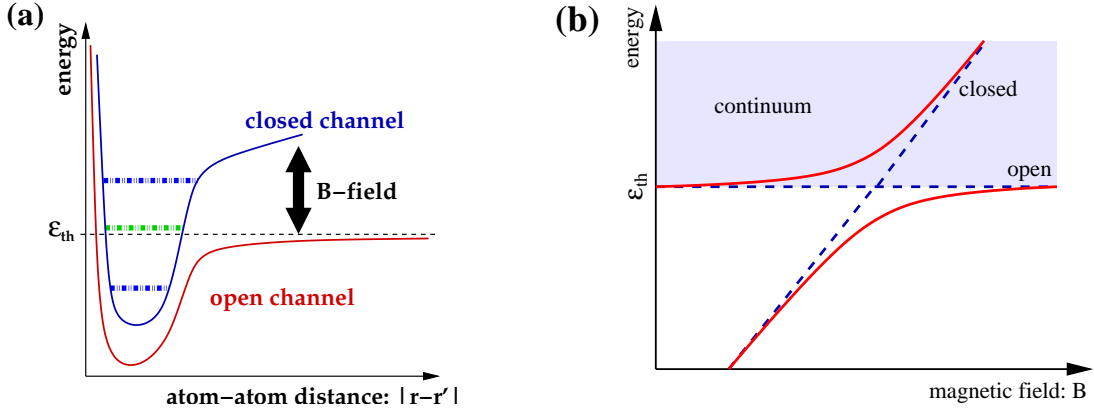
Figure 4.1: *(a):* Sketch of the "open" and "closed" channel potentials involved in a Feshbach resonance. Atoms, incoming in the open channel with energy ϵ_{th} are influenced by the presence of a nearby bound state (closed channel). As the closed and open channel generally are in different Zeeman or hyperfine states, applying an external magnetic field allows to shift the potentials with respect to each other. Hence, the scattering length a can be controlled by the applied external magnetic field **B**. *(b):* Magnetic field dependence of the open and closed channel. The dashed and solid line correspond to the uncoupled and coupled case, respectively.

hyperfine energies of the incoming and outgoing states. Channels which can not be accessed due to energy conservation are called "closed channels".

Let us return to the situation depicted in Fig. 4.1. Here, the incoming scattering channel with threshold energy ϵ_{th} is in the vicinity of a bound state in a closed channel. In order to get an idea of the influence of the close by bound state on the scattering process, it useful to think of a perturbative treatment in the interaction between the open and closed channel. In first order, the closed channel has no impact on the scattering process, as a transition into the bound state is forbidden by energy conservation. However, second-order processes describing the virtual scattering into the closed channel and finally decaying back into the open channel is allowed. Hence, in second-order perturbation theory, the scattering length a can be written as [36]

$$a = a_{\text{bg}} + \frac{m}{4\pi\hbar^2} \sum_{n \in \mathcal{C}} \frac{|\langle \psi_n | \hat{H}_{QP} | \psi_{\text{in}} \rangle|^2}{\epsilon_{\text{th}} - \epsilon_n} , \qquad (4.1)$$

where a_{bg} is the scattering length in absence of the closed channel and the sum runs over all closed states $\mathcal{C}$. The operator $\hat{H}_{QP} = \hat{Q}\hat{H}\hat{P}$ is the Hamiltonian of the system, $\hat{H}$, multiplied by the projection operator projecting on the open states $\hat{P}$ from the right and multiplied by the projector for the closed states $\hat{Q}$ from the left. Summing the projection operators yields the unity operator: $\hat{P} + \hat{Q} = \hat{1}$. Hence, $\hat{H}_{QP}$ describes transitions between the open and the closed channel. Furthermore, $|\psi_{\text{in}}\rangle$ denotes the incoming wavefunction and $|\psi_n\rangle$ the wavefunctions of the bound states in the closed channel. Suppose, that the energy level of one of the bound states in the closed channel, $|\psi_R\rangle$, is very close to the threshold energy of the incoming scattering state

ϵ_{th}. Assuming further that the energy levels of the bound states in the closed channel are well separated, the state $|\psi_R\rangle$ provides the dominating contribution in Eq. (4.1). Consequently, contributions from all other bound states in the closed channel are negligible, reducing Eq. (4.1) to

$$a = a_{\text{bg}} + \frac{m}{4\pi\hbar^2} \frac{|\langle\psi_R|\hat{H}_{QP}|\psi_{\text{in}}\rangle|^2}{\epsilon_{\text{th}} - \epsilon_R} . \tag{4.2}$$

Applying a magnetic field, B, leads to an energy shift of the channel potentials. As different channels denote in general different Zeeman or hyperfine states, the potentials of different channels will have different energy shifts. This results into a relative shift of the closed and open channel potentials, which is controllable by the strength of an external magnetic field. Let B_0 be the magnetic field for which $\epsilon_{\text{th}} = \epsilon_R$. Expanding the channel energies about B_0

$$\epsilon_\alpha(B) = \epsilon_\alpha(B_0) + \mu_\alpha(B - B_0) , \tag{4.3}$$

with $\mu_\alpha = (\partial\epsilon_\alpha/\partial B)|_{B=B_0}$, introduces a magnetic field dependence in the scattering length

$$a(B) = a_{\text{bg}} + \frac{m}{4\pi\hbar^2} \frac{|\langle\psi_R|\hat{H}_{QP}|\psi_{\text{in}}\rangle|^2}{(\mu_{\text{th}} - \mu_R)(B - B_0)} . \tag{4.4}$$

Defining the width of the resonance as

$$\Delta B = \frac{m}{4\pi\hbar^2 a_{\text{bg}}} \frac{|\langle\psi_R|\hat{H}_{QP}|\psi_{\text{in}}\rangle|^2}{\mu_R - \mu_{\text{th}}} , \tag{4.5}$$

yields the common expression [36, 163, 164] for the magnetic field dependence of the scattering length at a Feshbach resonance

$$a = a_{\text{bg}} \left(1 - \frac{\Delta B}{B - B_0}\right) . \tag{4.6}$$

The impact of a Feshbach resonance on the scattering length can now be directly seen from Eq. (4.6). A bound state above the threshold energy of the scattering state, $\epsilon_R > \epsilon_{\text{th}}$, leads to an attraction between the incoming atoms (negative scattering length). If the bound state is below the threshold energy, $\epsilon_R < \epsilon_{\text{th}}$, then the atoms perceive a repulsive interaction (positive scattering length). The scattering length diverges at exact resonance. Experimentally, Feshbach resonances have been observed for bosons, ^{23}Na [165], ^{85}Rb [166–168], ^{87}Rb [169], ^{133}Cs [170], ^{52}Cr [171] as well as for fermionic spin mixtures, ^{6}Li [172], ^{40}K [173].

4.1.2   The single-channel model

The model used in the previous section described the Feshbach resonance in terms of multiple channels. Finally, in Eq. (4.2), the discussion was reduced to the open channel and the nearest closed channel. This two channel approximation was based on the assumption that all other channels have only little influence on the open channel. In a further step, the two-channel model can be reduced to a model with only a single

channel. The influence of the closed channel is approximated by a field dependent interaction. This can in principle be done by using a field dependent scattering length, as for example, Eq. (4.6). A method to optimize the effective interaction for the single-channel model, mimicking the more complicated two-channel model, is described in reference [174]. The detailed form of this effective interaction, however, will be of no importance for the discussion in the following sections. Instead, the validity of the single-channel model is briefly outlined now.

Validity of the single-channel model

In general, single-channel models for the BEC-BCS crossover are expected to provide a good description for broad Feshbach resonances [174–176]. Broad resonances can be described by a single, energy independent parameter: the scattering length a. The partial-wave expansion for conventional scattering theory describes the scattering process in terms of the partial-wave amplitude

$$f_\ell(k) = \frac{1}{k \cot \delta_\ell - ik} \, , \tag{4.7}$$

(see Appendix D for a brief definition and Ref. [112] for details). For finite-range potentials and at low energies only the s-wave contribution is important i.e. $\ell = 0$. Higher angular momenta decrease with $\delta_\ell \sim k^{2\ell+1}$. Following Ref. [112], Eq. (4.7) can be written for low energies i.e small k as

$$f_0(k) = \frac{1}{1/a + Rk^2/2 - ik} \, , \tag{4.8}$$

where the small k expansion of $k \cot \delta_0 \approx 1/a + Rk^2/2$ has been used. The quantity R is known as the effective range of the potential, which is related to the width ΔB of the Feshbach resonance via the relation [177]

$$R = \frac{\hbar^2}{2ma_{\text{bg}}\mu_R \Delta B} \, . \tag{4.9}$$

The wave amplitude $f_0(k)$ is always energy dependent in the close vicinity of the resonance, as $a \to \infty$. The term proportional to $R \sim 1/\Delta B$ can be neglected for $kR \ll 1$. Natural length scales for the wavevector are given by the Fermi wavevector k_F and the inverse scattering length $1/a$. Hence, the approximation $k \cot \delta_0 \approx 1/a$ is reasonable under the conditions $k_F R \ll 1$ and $R/a \ll 1$ [175]. As $R \sim 1/\Delta B$ the resonances can be classified into narrow Feshbach resonances, which have a strong energy dependence, and broad Feshbach resonances, for which the energy dependent $Rk^2/2$ term is negligible. Fortunately, many experiments, investigating the BEC-BCS crossover, use broad Feshbach resonances as found in ^{6}Li [158, 178–181], and ^{40}K [160]. In order to describe narrow Feshbach resonances, multi-channel models are required [163, 182].

There is a fundamental difference between the single-channel and the multi-(two-) channel model. Multi-channel models allow for the coexistence of molecules and fermions. This is often described by a fermion-boson Hamiltonian with an interaction term

$$\hat{V}_{\text{FB}} = \sum_{\mathbf{k},\mathbf{q}} g(\mathbf{k}) \left(b_{\mathbf{q}}^\dagger c_{\mathbf{q}/2-\mathbf{k},\downarrow} c_{\mathbf{q}/2+\mathbf{k},\uparrow} + \text{h.c.} \right) \tag{4.10}$$

transforming bosonic molecules into fermion pairs and vice versa [163,176,182]. Here, the operators $b^\dagger$, b and $c^\dagger$, c describe the boson and fermion creation and annihilation operators, respectively. The wavefunction is therefore a combination of the closed and open channel wavefunctions with a certain mixture $0 \leq z \leq 1$

$$|\psi\rangle = \sqrt{z}|\text{closed}\rangle + \sqrt{1-z}|\text{open}\rangle. \tag{4.11}$$

However, for broad Feshbach resonances, the occupation of the closed channel is quite small [174]. Broad resonances correspond to a strong coupling between the open and closed channels. The strong coupling gives rise to short life times and thus to a low occupation of the closed channel. Consequently, single-channel models provide a good description of the scattering process for broad resonances.

4.1.3 The BCS wavefunction

The system considered in all future discussions is a mixture of fermions in different hyperfine states, which will be denoted with quasi-spin up and down. The fermion gas will be studied in the vicinity of a broad Feshbach resonance. The Feshbach resonance is modeled by a single-channel approach. The use of a single-channel model means that the detailed potential landscape of the scattering process is approximated by an effective potential. This requires that the wavelength of the incoming particle k is much larger than the range of the scattering potential R. The scattering potential is thus replaced by a contact interaction, characterized by a single parameter as, for example, the s-wave scattering length a. The fermionic cloud is characterized by the particle density, which is a function of the Fermi wavevector k_F. The requirement for the effective-potential approximation can then be summarized as $k_F R \ll 1$, and corresponds to the low-energy limit. Combining the two characteristic length scales of the problem, the scattering length a and the Fermi wavevector k_F, leads to the dimensionless quantity $\xi = 1/k_F a$. This dimensionless quantity ξ will be used as a convenient parameter to characterize the crossover from the BEC to BCS side.

The wavefunction of the fermionic spin mixture will be described by a product of up and down fermion singlet states. Following the ideas of [148–150] the fermion spin mixture will be described by a Bardeen-Cooper-Schrieffer (BCS) [147] wavefunction

$$|\Psi_{\text{BCS}}\rangle = \prod_{\mathbf{k}} \left(u_{\mathbf{k}} + v_{\mathbf{k}} c^\dagger_{\mathbf{k}\downarrow} c^\dagger_{-\mathbf{k}\uparrow} \right) |0\rangle. \tag{4.12}$$

The BCS wavefunction is a grand-canonical state of $(\mathbf{k}\uparrow, -\mathbf{k}\downarrow)$ fermion pairs. The functions $u_{\mathbf{k}}$ and $v_{\mathbf{k}}$ are the free parameters of this variational ansatz. They are determined by minimizing the energy of the system, described by the "reduced" Hamiltonian [183]

$$\hat{H} = \sum_{\mathbf{k}\sigma} \xi_{\mathbf{k}} c^\dagger_{\mathbf{k}\sigma} c_{\mathbf{k}\sigma} + \sum_{\mathbf{k}\mathbf{j}} V_{\mathbf{k}\mathbf{j}} c^\dagger_{\mathbf{k}\uparrow} c^\dagger_{-\mathbf{k}\downarrow} c_{-\mathbf{j}\downarrow} c_{\mathbf{j}\uparrow}. \tag{4.13}$$

Here, $\xi_{\mathbf{k}} = \epsilon_{\mathbf{k}} - \mu$ denotes the energy measured with respect to the chemical potential. Using the constraint $|u_{\mathbf{k}}|^2 + |v_{\mathbf{k}}|^2 = 1$ leads to

$$|u_{\mathbf{k}}|^2 = \frac{1}{2}\left(1 + \frac{\xi_{\mathbf{k}}}{E_{\mathbf{k}}}\right), \qquad |v_{\mathbf{k}}|^2 = \frac{1}{2}\left(1 - \frac{\xi_{\mathbf{k}}}{E_{\mathbf{k}}}\right), \tag{4.14}$$

and the self-consistency equation

$$\Delta_{\mathbf{j}} = -\frac{1}{2}\sum_{\mathbf{k}}\frac{\Delta_{\mathbf{k}}}{E_{\mathbf{k}}}V_{\mathbf{jk}}, \tag{4.15}$$

with $E_{\mathbf{k}} = \sqrt{\xi_{\mathbf{k}}^2 + \Delta^2}$. The gap equation (4.15) and the conservation of the total particle number [1]

$$N = \sum_{\mathbf{k},\sigma}|v_{\mathbf{k}}|^2, \tag{4.16}$$

allow a self-consistent determination of the order parameter Δ and the chemical potential μ.

In conventional BCS theory, the interaction is assumed to be isotropic. Consequently, the order parameter is also isotropic. The gap equation can then be rewritten as

$$\Delta = -V\sum_{\mathbf{k}}v_{\mathbf{k}}u_{\mathbf{k}}, \tag{4.17}$$

using Eq. (4.14). Interactions between the up and down fermions are parameterized by the scattering length a in three dimensions and the bound-state energy E_B in two dimensions. The interaction potential in Eq. (4.17) must therefore be rewritten in terms of the parameters characterizing the scattering process. The connection between the effective scattering potential and the interaction potential V of Eq. (4.17) is achieved by a renormalization of the gap equation [152,184]. Based on this renormalized gap equation the self-consistency equations are obtained. Appendix F discusses the self-consistency equations for the two-dimensional, quasi-two dimensional and three-dimensional case. Figure 4.2 shows the results for the order parameter Δ and for the chemical potential μ calculated from the self-consistency equations in three dimensions. All quantities in Figure 4.2 are normalized to Fermi energy ϵ_F. The insets, Fig. 4.2b and Fig. 4.2c, show μ/ϵ_F and Δ/ϵ_F as function of $-(\xi - \xi_0)$, respectively. Here, $\xi = 1/k_F a$ and $\xi_0 \equiv \xi(\mu = 0)$. Let us have a closer look at the behavior of the chemical potential μ and the order parameter Δ as a function of $-(\xi - \xi_0)$. The chemical potential approaches the value $\lim_{\xi\to\infty}\mu = -E_B/2 = -\hbar^2/ma^2$ in the BEC limit. This corresponds to half the molecular binding energy required to dissociate the molecule. In the opposite limit, $\xi \to -\infty$, the chemical potential tends towards the Fermi energy $\mu/\epsilon_F = 1$, which is the expected value known from conventional superconductivity. Finally, in Fig. 4.2c, the order parameter shows an increase in the BEC limit and vanishes exponentially [149] in the BCS limit.

---

[1]Later, a subsystem of the atomic cloud will be considered and the particle number will be replaced by the average particle number.
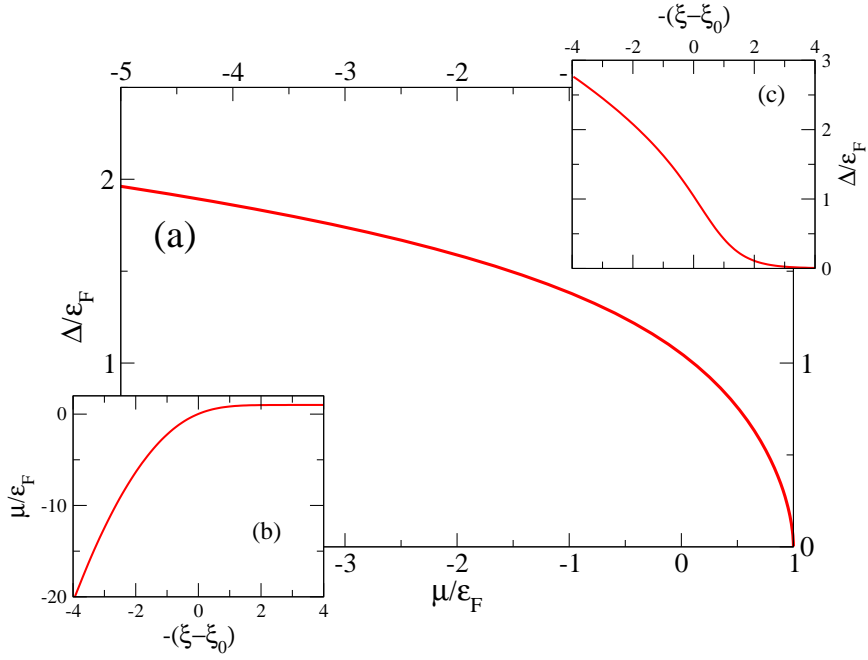
Figure 4.2: Results from the self-consistency equations (4.17) and (4.16) for Δ and μ in 3D. All quantities are normalized with respect to the Fermi energy ϵ_F. (a): Δ/ϵ_F as a function of μ/ϵ_F. (b,c): Figures (b) and (c) show μ/ϵ_F and Δ/ϵ_F plotted over $-(\xi - \xi_0)$, respectively. Here, $\xi = 1/k_F a$ and $\xi_0 \equiv \xi(\mu = 0)$.

The values for Δ and μ, obtained from the self-consistency equations, can be used now to calculate the variational parameters $u_{\mathbf{k}}$ and $v_{\mathbf{k}}$. Figure 4.3 shows the different behavior of $|v_{\mathbf{k}}|^2$ in the BCS ($\mu \approx \epsilon_F$), intermediate ($\mu \approx 0$), and BEC regime ($\mu \ll -\epsilon_F$). The values for $u_{\mathbf{k}}$ and $v_{\mathbf{k}}$ allow a characterization of the state of the system. The parameter $|v_{\mathbf{k}}|^2$ can be interpreted as the probability of the pair $(\mathbf{k} \uparrow, \mathbf{k} \downarrow)$ being occupied, whereas $|u_{\mathbf{k}}|^2$ is the probability that the pair state is unoccupied. The curve for $|v_{\mathbf{k}}|^2$ corresponding to the BCS regime shows a step function broadened by Δ. The curve for the BEC regime shows values of $|v_{\mathbf{k}}|^2$ which are much smaller than the BCS results for $\epsilon < \epsilon_F$. Additionally, $|v_{\mathbf{k}}|^2$ is decaying much slower in the BEC case compared to the BCS case.

Finally, let us have a look at the wavefunction in the BEC limit. In the extreme BEC limit, $\xi \to \infty$, the BCS wavefunction can be rewritten as a coherent state of fermion pairs. Rewriting Eq. (4.12) leads to

$$|\Psi_{\text{BCS}}\rangle = \left(\prod_{\mathbf{k}} u_{\mathbf{k}} \right) \exp \left(\sum_{\mathbf{k}} \frac{v_{\mathbf{k}}}{u_{\mathbf{k}}} c_{\mathbf{k}\downarrow}^{\dagger} c_{-\mathbf{k}\uparrow}^{\dagger} \right) |0\rangle . \qquad (4.18)$$

The product over $u_{\mathbf{k}}$ can be approximated as

$$\prod_{\mathbf{k}} u_{\mathbf{k}} = \exp \left[\sum_{\mathbf{k}} \ln \left(\sqrt{1 - |v_{\mathbf{k}}|^2} \right) \right] \approx \exp \left[-\frac{1}{2} \sum_{\mathbf{k}} |v_{\mathbf{k}}|^2 \right] = e^{-N/4}, \qquad (4.19)$$
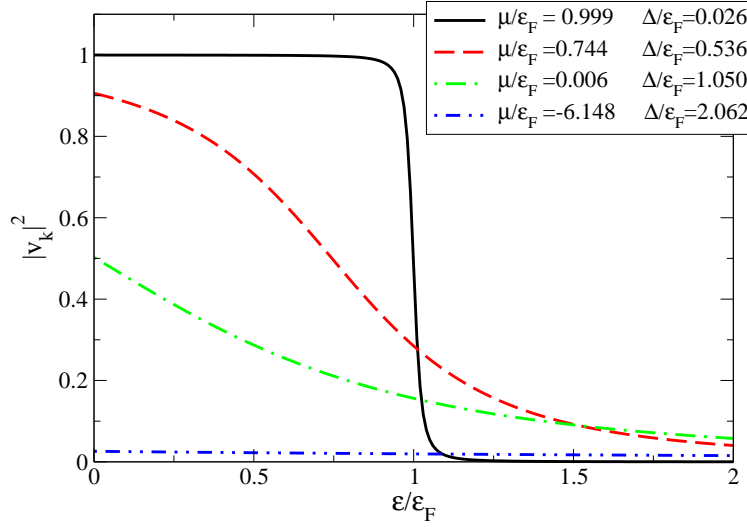
Figure 4.3: The variational parameter $|v_k|^2$ for different values of μ/ϵ_F. The value for Δ corresponding to each μ is obtained from the atom-number conservation. The solid line shows the BCS limit, $\mu/\epsilon_F \approx 1$. The dash-dotted line shows the intermediate regime $\mu/\epsilon_F \approx 0$ and the dash-dot-dot line the BEC limit, $\mu/\epsilon_F \ll -1$.

using the fact, that in the BEC limit $|v_{\mathbf{k}}| \ll 1$, as can be seen from Fig. 4.3. Defining the operator

$$b^\dagger = \sqrt{\frac{2}{N}} \sum_{\mathbf{k}} \frac{v_{\mathbf{k}}}{u_{\mathbf{k}}} c^\dagger_{\mathbf{k}\downarrow} c^\dagger_{-\mathbf{k}\uparrow} \,, \tag{4.20}$$

the BCS wavefunction can be rewritten as a coherent state

$$|\Psi_{\mathrm{BCS}}\rangle = e^{-N/4} \exp\left(\sqrt{\frac{N}{2}} b^\dagger\right)|0\rangle = e^{-N/4} \sum_{\ell=0}^{\infty} \frac{\left(\sqrt{N/2}\right)^\ell}{\sqrt{\ell!}} |\ell\rangle \,. \tag{4.21}$$

The operators $b^\dagger$ and b fulfill in the extreme BEC limit approximately bosonic commutation relations. The commutator can be approximated by

$$[b, b^\dagger] \approx 1 - 8\pi \frac{\hat{N}}{N} (na^3) \,, \tag{4.22}$$

where $\hat{N} = \sum_{\mathbf{k},\sigma} c^\dagger_{\mathbf{k}\sigma} c_{\mathbf{k}\sigma}$ is the number operator and $n = N/V$ is the particle-number density. Assuming, that the inter-particle distance is much larger than the scattering length i.e. $na^3 \ll 1$, one can treat the $b^\dagger$, b as bosonic creation and annihilation operators. The requirement $na^3 \ll 1$ is well satisfied in most experiments with dilute atomic gases. Thus, in the BEC limit, the state can be interpreted as a Bose-Einstein condensate of molecules. In fact, Bose-Einstein condensation of molecules on the BEC side of a Feshbach resonance has been demonstrated in several experiments [156–159].

4.2   Measurement scheme for the particle-number statistics in cold atomic clouds

In this section, we introduce the idea of noise measurements as a source of information. In contrast to the rather bad reputation of noise as a burden which makes the experimental life hard, fluctuations in the measurement observable actually supply a great deal of information about the system. This notion has been successfully applied in quantum optics [185] and in solid state physics [107, 186, 187], for instance, in investigations of current noise in mesoscopic devices.

Recently, the idea to study correlations in the noise of measurements has been carried forward to ultra-cold atomic gases [64, 65, 188]. The authors of Ref. [64] suggest to test the quantum state of the system by measuring correlations in the noise of expansion pictures. Following their suggestions, first successful experiments were performed. Thereby, correlations in the Mott-insulator phase in an optical lattice [63] have been tested. In a different experiment, correlations in the momentum distribution on the attractive side of a Feshbach resonance provided strong indications for a superfluid pair state [62].

We will show in the following sections that measurements of atom-density fluctuations provide a tool to characterize the state in the BEC-BCS crossover region. The characterization of the state of the atomic cloud in the BEC-BCS transition is more difficult as in experiments with Bose-Einstein condensates. Conventional expansion-picture methods proved to be problematic, as the interaction strength changes during the expansion process. This can lead to a reformation of the original state during the expansion. Several approaches to determine the state of a fermionic spin mixture in the BEC-BCS crossover region are under present investigation. Some approaches use light-scattering [189], Bragg spectroscopy [190], or the measurement of collective modes [180, 181, 190–192]. Mapping of preformed Cooper pairs into a molecular Bose-Einstein condensate by rapidly sweeping through the Feshbach resonance provides a strong indication for the existence of a superfluid BCS state [158, 160]. Radio-frequency spectroscopy enabled a direct measurement of the pairing gap [178]. Studying the statistical properties of number-density fluctuations provides a further possibility to extract information about the state in the BEC-BCS crossover region [62, 65]. Measuring the atom-density statistics is particularly interesting since the characteristic form of the state changes drastically from the BEC to BCS side. On the BCS side the system is in a many-body state of fermions. On the BEC side the system forms a molecular Bose-Einstein condensate. Hence, one expects a distinct change in the atom-number statistics along the crossing from the BEC to the BCS side, which allows to characterize the state.

4.2.1   Model and experimental feasibility

In contrast to the measurement of noise correlation of absorption pictures [62–64], we suggest to study the number-density correlations of the dilute atomic cloud directly.
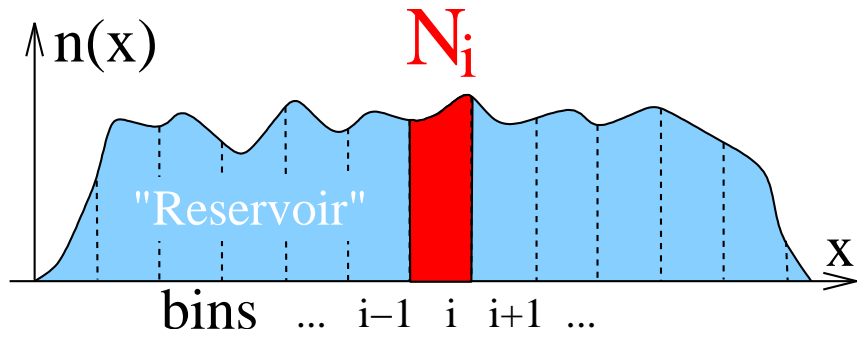
Figure 4.4: Sketch of a typical atomic-number density $n(x)$. The measurement observable is the number of atoms in a bin N_i.

Investigating dilute atomic clouds with the usual measurement of expansion pictures might seriously modify the state during expansion. As the particle density and consequently also the interaction strength changes drastically during expansion of the cloud, it is very likely that the original state of the system will be destroyed. This addresses in particular the superfluid BCS state. Measuring the density distribution of the cloud directly without a free expansion avoids this problem. The disadvantage of a direct density measurement lies in the required resolution as the cloud is not expanded anymore. However, a direct measurement of an atomic cloud has been demonstrated in an recent experiment [179].

We now present a model to substantiate the idea of directly measuring particle-number statistics. Let us assume a fermion spin mixture with particle-number density $n(x)$ as sketched in Fig. 4.4. The atomic cloud is divided into an array of bins. Each bin forms a subsystem of the atomic cloud. The number of particles per bin is given by the atom-number density integrated over the bin volume

$$N_i = \int_{V_i} n(x) \,. \tag{4.23}$$

The number of atoms in a single bin will be fluctuating and the number statistics for such a single bin can be investigated in order to obtain information about the system. The problem can be summarized in the question: What is the probability of finding N particles in the bin? However, there are requirements to the bin size. The bin size must be large enough to sustain a macroscopically large number of atoms. Furthermore, the size of the bin is assumed to inclose only a small subsystem compared to the total number of particles in the full system. The majority of the atoms, surrounding the bin, serve as a particle reservoir. This allows us to treat a single bin as a grand-canonical system. Experiments usually deal with absorption pictures which project the three-dimensional cloud into a two-dimensional column density. As the absorption pictures are commonly taken with a CCD-camera, these pictures are automatically discretized into an array of pixels. Bins are therefore naturally defined by the pixel size (or several pixels, if required to fulfill the above defined requirements for the bin size).

4.3   Short introduction to full counting statistics

The name "Counting Statistics" suggests the simple notion of counting events or particles. Hence, from counting events one obtains the spatial or temporal distribution of a statistical variable. From these data, moments and cumulants can be calculated. Consequently, full counting statistics (FCS) describes a method to obtain all cumulants of the statistic process by computing a single quantity, called the cumulant generating function (CGF). The knowledge of the cumulant generating function provides the possibility to reconstruct the probability distribution. Information about the probability distribution (e.g. poissonian or gaussian process) can often be directly read off the cumulant generating function. In this way, insight about the physical mechanism behind the statistical process (e.g. tunneling or molecule pairing) is obtained directly from the form of the cumulant generating function.

4.3.1   The cumulant generating function

Let us assume a stochastic process with a stochastic variable N. The quantity $\langle N^m \rangle$ defines the moments and $\mu_m = \langle (N - \langle N \rangle)^m \rangle$ the central moments, respectively. Instead of calculating all moments one by one, it is more convenient to obtain the characteristic function

$$e^{-S(\chi)} = \langle e^{iN\chi} \rangle = \sum_{m=0}^{\infty} \frac{i^m \langle N^m \rangle}{m!} \chi^m \,. \qquad (4.24)$$

Taking the r-th derivative of the characteristic function with respect to χ and evaluating the result at $\chi = 0$ gives the r-th moment

$$\langle N^r \rangle = \frac{1}{i^r} \frac{\partial^r}{\partial \chi^r} e^{-S(\chi)} \bigg|_{\chi=0} \,. \qquad (4.25)$$

Writing down the characteristic function explicitly

$$e^{-S(\chi)} = \langle e^{iN\chi} \rangle = \sum_{N} e^{iN\chi} P(N) \,, \qquad (4.26)$$

shows that the characteristic function is the Fourier transform of the probability distribution $P(N)$. The characteristic function exists for any probability distribution even if the moments for this probability distribution do not [185]. The cumulants C_r of a probability distribution are defined by the power-series expansion of the logarithm of the characteristic function

$$S(\chi) = -\log\left(\langle e^{iN\chi} \rangle\right) = -\sum_{r=1}^{\infty} \frac{C_r}{r!} (i\chi)^r \,. \qquad (4.27)$$

Taking the r-th derivative with respect to χ and evaluation of the result at $\chi = 0$ yields the r-th cumulant

$$C_r = \frac{1}{i^r} \frac{\partial^r}{\partial \chi^r} S(\chi) \bigg|_{\chi=0} \,. \qquad (4.28)$$
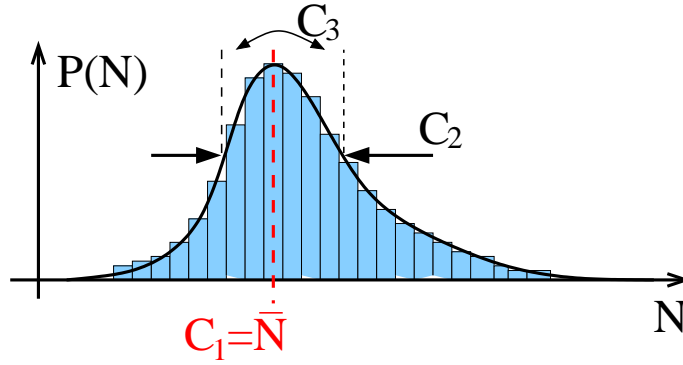
Figure 4.5: Schematic interpretation of the first three cumulants. C_1 corresponds to the mean value of the stochastic variable. The variance, describing the fluctuations about the mean value is given by C_2. Finally, the skewness, $C_3/C_2^{3/2}$, characterizes the deviation of the variance from its symmetric value around the mean value.

The advantage of using cumulants compared to moments lies in their additivity for statistically independent variables. Expressing the first few cumulants by the central moments

$$
\begin{aligned}
C_1 &= \langle N \rangle \equiv \bar{N} = \mu_1 \\
C_2 &= \langle (N - \langle N \rangle)^2 \rangle = \mu_2 \\
C_3 &= \langle (N - \langle N \rangle)^3 \rangle = \mu_3 \\
C_4 &= \mu_4 - 3\mu_2^2 \\
&\cdots
\end{aligned}
$$

shows that the first three cumulants correspond to the first three central moments. The first cumulant, C_1, is therefore the mean value of the distribution, C_2 describes the variance. Finally, $C_3/C_2^{3/2}$ is called the skewness [185] and provides a measure for the asymmetry of the variance with respect to the mean value. Figure 4.5 gives a schematic interpretation of the first three cumulants. Higher cumulants C_r, with $r > 3$, are combinations of the central moments up to μ_r. The interpretation of these higher cumulants is increasingly more difficult. The probability distribution of the stochastic variable can be obtained by a Fourier back-transformation of the characteristic function. In particular, if the stochastic variable is a sum of independent variables $N = \sum_k N_k$, with the cumulant generating function $-S(\chi) = -\sum_k S_k(\chi)$, then

$$
P_k(M) = \int_{-\pi}^{\pi} \frac{d\chi}{2\pi} e^{-S_k(\chi)} e^{-iM\chi} , \tag{4.29}
$$

provides the probability distribution of the k-th stochastic variable[2].

So far only classical statistical variables have been discussed. Let us now consider an operator variable $\hat{N}$. In order to caculate the expection value

$$
\langle f(N) \rangle = \sum_N f(N) P(N) , \tag{4.30}
$$

---

[2]Eq. (4.29) and Eq. (4.26) are derived for discrete stochastic variables.

the probability distribution $P(N)$ for the operator is now used, given by the probability-distribution function

$$P(N) = \text{Tr}\left\{\rho\delta(N - \hat{N})\right\} = \langle\delta(N - \hat{N})\rangle\,. \qquad (4.31)$$

Assuming that the operator $\hat{N}$ takes only discrete eigenvalues N, the expression (4.30) transforms into[3]

$$\sum_N f(N)\langle\delta_{N,\hat{N}}\rangle = \langle\sum_N f(N)\delta_{N,\hat{N}}\rangle = \langle f(\hat{N})\rangle\,. \qquad (4.32)$$

Hence, the extension to the quantum mechanical situation, i.e considering an operator variable, is done by replacing the classical average by an quantum-statistical average.

In conclusion, the main task in obtaining the FCS for an operator variable lies in the computation of its cumulant generating function, Eq. (4.27). In the remainder of this section, explicit calculations of the number-density FCS for free fermions, free bosons and the BCS state will be given as examples. On the one hand the results for these examples will form the basis for further calculations, on the other hand they will be used for comparison with later results.

4.3.2   Full counting statistics of free fermions

The first example discusses the case of non-interacting fermions. The Hamiltonian for spinless fermions is given by

$$\hat{H} = \sum_k \epsilon_k c_k^\dagger c_k\,, \qquad (4.33)$$

with an energy dispersion $\epsilon_k = \hbar^2 k^2/2m$. Following the ideas of Sec. 4.2.1, we are interested in the atom-number fluctuations in a bin of the atom cloud. Thence, the calculation of the cumulant generating function will be done in the grand-canonical ensemble. Choosing the grand-canonical ensemble is justifiable as long as the atom number in the bin N_{bin} is much smaller than the total number of atoms N in the cloud i.e. $1 \ll N_{\text{bin}} \ll N$.

The general expression for the cumulant generating function can be computed in a similar way as the derivation of the grand partition function $Z(\mu)$. The explicit calculation of the characteristic function

$$\langle e^{i\hat{N}\chi}\rangle = \text{Tr}\left\{e^{-\beta(\hat{H}-\mu\hat{N})}e^{i\hat{N}\chi}\right\} = \text{Tr}\left\{e^{-\beta(\hat{H}-(\mu+i\chi/\beta)\hat{N})}\right\} = Z(\mu + i\chi/\beta)\,, \qquad (4.34)$$

leads to the grand partition function with the "complex chemical potential" $\mu + i\chi/\beta$ with $\beta = 1/k_B T$. Explicit calculation of the grand partition function for a gas of

---

[3]Here, we assume, that $f(N)$ can be expanded in a power series.

spinless fermions [37] and using Eq. (4.27) gives the final result for the free-fermion cumulant generating function

$$S(\chi) = -\sum_k \log \left[1 + f_+(e^{i\chi} - 1)\right] , \qquad (4.35)$$

where

$$f_+(\epsilon_k) = \frac{1}{e^{\beta(\epsilon_k - \mu)} + 1} , \qquad (4.36)$$

is the Fermi occupation function. Note, that χ-independent terms have been neglected in Eq. (4.35). However, this is of no consequence as we are only interested in the cumulants, which are obtained from the derivatives with respect to χ. In order to perform the summation over all states in Eq. (4.35), two limiting cases will be discussed: the degenerate and the non-degenerate limit.

The non-degenerate Fermi gas

The non-degenerate Fermi gas corresponds to the high-temperature or classical limit. The non-degenerate limit is applicable if the fugacity is small i.e. $e^{\beta\mu} \ll 1$ [193]. This is the case for high temperatures and a negative chemical potential. The negative sign for the chemical potential is automatically fulfilled at sufficiently high temperatures if the average particle number $\bar{N}$ is kept at a fixed value. Consequently, the Fermi occupation function can be simplified to

$$f_+(\epsilon_k) = \left[e^{\beta(\epsilon_k - \mu)} + 1\right]^{-1} \approx e^{-\beta(\epsilon_k - \mu)} \ll 1 . \qquad (4.37)$$

Using Eq. (4.37), the cumulant generating function in Eq. (4.35) can be approximated by an expansion of the logarithm for small f_+. Truncating the expansion at the first order leads to

$$S(\chi) \approx -(e^{i\chi} - 1) \sum_k f_+ = -\bar{N}(e^{i\chi} - 1) . \qquad (4.38)$$

This is the expected Poissonian statistics for a classical gas with $C_n = \bar{N}$ for all cumulants. It is the approximation done in Eq. (4.37), where all the fermion characteristic is lost. An analogous derivation also applies for the cumulant generating function of the non-degenerate Bose gas. Hence, the same cumulant generating function, Eq. (4.38), is found. This is not surprising, as the classical limit does not distinguish between fermionic and bosonic particles.

The degenerate Fermi gas

Considering the degenerate Fermi gas corresponds to the low-temperature limit, $k_B T \ll \epsilon_F$. Now, the chemical potential is $\mu \approx \epsilon_F > 0$ and the fugacity is large $e^{\beta\mu} \gg 1$. The Fermi occupation function f_+ shows a sharp step at the Fermi energy. This feature can be exploited for the derivation of the cumulant generating function in the degenerate limit as shown in Appendix E.1. The result for the cumulant generating function of the degenerate Fermi gas is finally

$$S(\chi) = -i\bar{N}\tilde{\chi} - (Dk_B T/4\epsilon_F)\bar{N}\tilde{\chi}^2 . \qquad (4.39)$$

Here, $D = 2, 3$ is the dimension of the system and $\tilde{\chi}/2\pi + 1/2 = [\chi/2\pi + 1/2]$, where $[\ldots]$ denotes the fractional part and ensures the 2π-periodicity of the cumulant generating function [194]. From Eq. (4.39), it is obvious that all C_n vanish for $n \geq 3$. Thus the statistics is Gaussian. The first cumulant is the usual average particle number $C_1 = \bar{N}$. More interesting is the variance, $C_2 \sim k_B T/\epsilon_F$ showing, that the particle-number fluctuations are suppressed with decreasing temperature. This is in contrast to the classical case, Eq. (4.38), which gives a temperature independent value for the variance: $C_2 = \bar{N}$.

4.3.3   Full counting statistics of free bosons

The free bosonic cloud is the second example to be discussed. A confining potential is absent and there is no interaction between the bosons. Again, the grand-canonical ensemble is chosen, as we are interested in the atom-number fluctuations in a small subsystem of the atomic cloud. Deriving the cumulant generating function for free bosons is, as in the free fermion case, similar to the derivation of the grand partition function. The cumulant generating function for the free bosonic gas is

$$S(\chi) = \sum_k \log \left[1 - f_-(e^{i\chi} - 1) \right] , \tag{4.40}$$

where

$$f_-(\epsilon_k) = \frac{1}{e^{\beta(\epsilon_k - \mu)} - 1} , \tag{4.41}$$

denotes the Bose occupation function. Further analysis of Eq. (4.40) will again be made for different temperature limits.

The first case is the high-temperature limit, corresponding to the non-degenerate situation discussed in the free fermion gas. The bosonic high-temperature limit can be treated in exactly the same way as in the fermionic case. In particular, the approximation Eq. (4.37) is also used, which makes the loss of the statistical information (bosons or fermions) evident. Hence, the same classical result, Eq. (4.38), is found for the high-temperature limit of the free Bose gas.

The second case, discussing the situation of an ideal Bose-Einstein condensate, is of much greater interest. Particle-number fluctuations in Bose-Einstein condensates have attracted a lot of theoretical interest [195–202]. However, in these articles lies the main interest in the fluctuations of the total number of condensed bosons and not in the particle-number fluctuation in a bin. Hence, a grand-canonical ansatz is no longer applicable. The grand-canonical ansatz predicts anomalous fluctuations $C_2 \sim N^2$. Using the appropriate canonical ansatz shows, nevertheless, anomalously large fluctuations at finite temperatures $C_2 \sim T^2 N^{4/3}$. Anomalous fluctuations of the condensate number are not only found for ideal Bose gases. Theoretical calculations using Bogoliubov theory [197] showed also anomalous fluctuations for weakly interacting Bose gases. Finally, anomalous fluctuations have been proven to be a general feature for Bose-Einstein condensates and, thus, are expected for arbitrary interactions [198, 202]. This is in contrast to the zero-temperature result which shows

normal fluctuations in the ideal Bose gas and in the interacting Bose gas [197, 198]. Returning to the fluctuations of the atom number in a bin, there is no demand for particle-number conservation. In the following, two different approaches are considered to calculate the number fluctuations in the bin. Each of them leads to a different result for the full counting statistics. On the one hand, the result Eq. (4.40) is used, which describes a mixed state of Fock states. On the other hand, the condensate will be described as a coherent state. The coherent state ascribes a phase to the condensate. Using a state with a fixed phase is attractive as it simplifies the description of interference phenomena observed for Bose-Einstein condensates [40–43]. The price to pay for the definite phase of the coherent state is a fluctuating particle number. As we have the experimental setup of Sec. 4.2.1 in mind, we are interested in the atom-number fluctuations in a bin, which is an open system. Thus a non-particle conserving ansatz, as the coherent state, is fully justified to describe the condensate in the bin.

Mixed number state

Bose-Einstein condensation is commonly described as the macroscopic occupation of a quantum state. The transition temperature at which this macroscopic occupation starts is defined as the critical temperature T_C^{BEC}. For simplicity, we assume a fully condensed bosonic cloud. In other words, we assume that all bosons occupy the same level i.e the ground state. This corresponds to the situation of taking the temperature to zero and at the same time taking the chemical potential towards the ground state energy, such that the average particle number $\bar{N} = \sum_k f_-(\epsilon_k)$ is conserved. Considering a fully condensed bosonic gas, particle number conservation leads to $\bar{N} = f_-(\epsilon_{k=0})$. Hence, the cumulant generating function for the mixed number state can be directly derived from Eq. (4.40) by taking only the contribution for $k = 0$ into account

$$S(\chi) = \log\left[1 - \bar{N}(e^{i\chi} - 1)\right] . \tag{4.42}$$

This is a negative binomial distribution[4] [203]. Computing the cumulants from Eq. (4.42) shows an anomalous behavior for the fluctuations, $C_n \sim \bar{N}^n$.

---

[4]The negative binomial distribution gives the probability of $r - 1$ successes and x failures in $r + x - 1$ trials and success on the $(r + x)$-th trial. Hence, the probability distribution is given as

$$P_{r,p}(x) = \left(\begin{array}{c} x + r - 1 \\ r - 1 \end{array}\right) p^r (1 - p)^x , \tag{4.43}$$

where p is the probability for a success. The characteristic function is

$$\langle e^{ix\chi} \rangle = \sum_{x=0}^{\infty} P_{r,p}(x) e^{ix\chi} = \left(\frac{1}{p} - \frac{1-p}{p} e^{i\chi}\right)^{-r} , \tag{4.44}$$

and from this expression the CGF is derived by taking the logarithm

$$S(\chi) = r \log\left(\frac{1}{p} - \frac{1-p}{p} e^{i\chi}\right) . \tag{4.45}$$

Setting $r = 1$ and identifying $p = 1/(\bar{N} + 1)$, Eq. (4.42) is obtained. Letting $r = 1$ means that only the outcome of the last attempt was an success. All previous attempts failed. Hence, the probability distribution in Eq. (4.42) describes the probability of having x failures until the first success.

Coherent state

The second approach to describe an ideal Bose-Einstein condensate is a coherent state

$$|\Psi_{\text{Coh}}\rangle = e^{-\bar{N}/2} \sum_{n=0}^{\infty} \frac{\bar{N}^{n/2}}{n!} (a_0^\dagger)^n |0\rangle \,. \tag{4.46}$$

Here, $a_0^\dagger$ creates a boson in the ground state. The coherent state is a pure state, however, with fluctuations in the particle number. We derive the characteristic function analogous to the previous cases

$$\langle \Psi_{\text{Coh}} | e^{i\hat{N}\chi} | \Psi_{\text{Coh}} \rangle = e^{-\bar{N}} \sum_{n=0}^{\infty} \frac{\left(\bar{N}e^{i\chi}\right)^n}{n!} = \exp\left(\bar{N}(e^{i\chi} - 1)\right). \tag{4.47}$$

Taking the logarithm of the characteristic function leads to the final expression for the cumulant generating function of the coherent state

$$S(\chi) = -\bar{N}(e^{i\chi} - 1) \,. \tag{4.48}$$

Equation (4.48) is the cumulant generating function for a poissonian stochastic process. All cumulants $C_n = \bar{N}$ are the same, as is obvious by taking the derivatives of Eq. (4.48) with respect to χ. The equity of all cumulants is the typical feature of the Poisson distribution.

Finally, it is interesting to compare the results for the mixed number state and coherent state. Inspections of the results for the cumulants shows an immediate contradiction. Whereas the cumulants for the mixed state shows anomalous fluctuations, the particle-number statistics for the coherent state shows normal fluctuations. This dilemma shows how sensitive the outcome of the stochastical properties is to the choice of the condensate state.

4.3.4   Full counting statistics of the BCS state

In the last example, the cumulant generating function for the BCS state will be discussed. Commonly used to describe conventional superconductivity [147], the BCS-wavefunction

$$|\Psi_{\text{BCS}}\rangle = \prod_{\mathbf{k}} \left(u_{\mathbf{k}} + v_{\mathbf{k}} c_{\mathbf{k}\downarrow}^\dagger c_{-\mathbf{k}\uparrow}^\dagger \right) |0\rangle \,, \tag{4.49}$$

is a grand-canonical state and does not conserve the particle number. In order to find the cumulant generating function for the BCS state, we again use Eq. (4.27). Before proceeding, it is worth noticing that the BCS state is a product state of $(\mathbf{k}\downarrow, -\mathbf{k}\uparrow)$-pairs. It is therefore convenient to rewrite the number operator into

$$\hat{N} = \sum_{\mathbf{k}} \hat{n}_{\mathbf{k}\downarrow} + \hat{n}_{\mathbf{k}\uparrow} = \sum_{\mathbf{k}} \hat{n}_{\mathbf{k}\downarrow} + \hat{n}_{-\mathbf{k}\uparrow} \,, \tag{4.50}$$

where $\hat{n}_{\mathbf{k}\sigma} = c^\dagger_{\mathbf{k}\sigma} c_{\mathbf{k}\sigma}$. Using the number operator in this ordering splits the characteristic function into a product

$$
\begin{aligned}
e^{-S(\chi)} &= \langle 0| \prod_{\mathbf{k}} \left[(u^*_{\mathbf{k}} + v^*_{\mathbf{k}} c_{-\mathbf{k}\downarrow} c_{\mathbf{k}\uparrow}) e^{i\hat{n}_{\mathbf{k}\downarrow}\chi} e^{i\hat{n}_{-\mathbf{k}\uparrow}\chi} (u_{\mathbf{k}} + v_{\mathbf{k}} c^\dagger_{\mathbf{k}\downarrow} c^\dagger_{-\mathbf{k}\uparrow}) \right] |0\rangle \\
&= \langle 0| \prod_{\mathbf{k}} \left[(u^*_{\mathbf{k}} + v^*_{\mathbf{k}} c_{-\mathbf{k}\downarrow} c_{\mathbf{k}\uparrow}) \left(1 - \hat{n}_{\mathbf{k}\downarrow} + \hat{n}_{\mathbf{k}\downarrow} e^{i\chi} \right) \right. \\
&\quad \left. \times \left(1 - \hat{n}_{-\mathbf{k}\uparrow} + \hat{n}_{-\mathbf{k}\uparrow} e^{i\chi} \right) (u_{\mathbf{k}} + v_{\mathbf{k}} c^\dagger_{\mathbf{k}\downarrow} c^\dagger_{-\mathbf{k}\uparrow}) \right] |0\rangle \\
&= \langle 0| \prod_{\mathbf{k}} \left\{ (u^*_{\mathbf{k}} + v^*_{\mathbf{k}} c_{-\mathbf{k}\downarrow} c_{\mathbf{k}\uparrow}) \left[(1 - \hat{n}_{\mathbf{k}\downarrow} - \hat{n}_{-\mathbf{k}\uparrow} + \hat{n}_{\mathbf{k}\downarrow} \hat{n}_{-\mathbf{k}\uparrow}) \right. \right. \\
&\quad \left. \left. + e^{i\chi} (\hat{n}_{\mathbf{k}\downarrow} + \hat{n}_{-\mathbf{k}\uparrow} - 2\hat{n}_{\mathbf{k}\downarrow}\hat{n}_{-\mathbf{k}\uparrow}) + e^{2i\chi} \left(\hat{n}_{\mathbf{k}\downarrow}\hat{n}_{-\mathbf{k}\uparrow} \right) \right] (u_{\mathbf{k}} + v_{\mathbf{k}} c^\dagger_{\mathbf{k}\downarrow} c^\dagger_{-\mathbf{k}\uparrow}) \right\} |0\rangle .
\end{aligned}
$$
$$(4.51)$$

The last expression in Eq. (4.51) used the relation

$$
(\hat{n}_{\mathbf{k},\sigma})^\ell = \hat{n}_{\mathbf{k},\sigma} , \tag{4.52}
$$

for all positive integer ℓ, which can be derived from the anti-commutation relation for the fermion operators, $\{c_{\mathbf{k},\sigma}, c^\dagger_{\mathbf{k}',\sigma'}\} = \delta_{\mathbf{kk}'} \delta_{\sigma\sigma'}$, and the Pauli principle: $c^2_{\mathbf{k},\sigma} = \left(c^\dagger_{\mathbf{k},\sigma} \right)^2 = 0$. Now, the right hand side of Eq. (4.51) can be explicitly evaluated using

$$
\langle \Psi_{\mathrm{BCS}} | \hat{n}_{\mathbf{k}\sigma} | \Psi_{\mathrm{BCS}} \rangle = |v_{\mathbf{k}}|^2 , \tag{4.53}
$$

and

$$
\langle \Psi_{\mathrm{BCS}} | \hat{n}_{\mathbf{k}\downarrow} \hat{n}_{-\mathbf{k}\uparrow} | \Psi_{\mathrm{BCS}} \rangle = \langle \Psi_{\mathrm{BCS}} | c^\dagger_{-\mathbf{k}\uparrow} c^\dagger_{\mathbf{k}\downarrow} c_{\mathbf{k}\downarrow} c_{-\mathbf{k}\uparrow} | \Psi_{\mathrm{BCS}} \rangle = |v_{\mathbf{k}}|^2 . \tag{4.54}
$$

Hence, the characteristic function is given by

$$
e^{-S(\chi)} = \prod_{\mathbf{k}} \left(|u_{\mathbf{k}}|^2 + |v_{\mathbf{k}}|^2 e^{2i\chi} \right) . \tag{4.55}
$$

From expression (4.55) one can immediately read off some typical characteristics of the BCS state. Using Eq. (4.29), one can see that the probability to find the $(\mathbf{k} \downarrow, -\mathbf{k} \uparrow)$-pair state empty is proportional $|u_{\mathbf{k}}|^2$. The probability to find the $(\mathbf{k} \downarrow, -\mathbf{k} \uparrow)$-pair state occupied is proportional to $|v_{\mathbf{k}}|^2$. That only pairs are involved can be seen from the factor of two in front of the counting field χ.

Finally, the expression for the cumulant generating function is obtained by taking the logarithm of Eq. (4.55)

$$
S(\chi) = -\sum_{\mathbf{k}} \log \left(|u_{\mathbf{k}}|^2 + |v_{\mathbf{k}}|^2 e^{2i\chi} \right) . \tag{4.56}
$$

The consequences of Eq. (4.56) for the atom-number statistics will be discussed later in connection with the discussion of the particle-number statistics in the BEC-BCS crossover region.

4.4   Number statistics at the BCS-BEC crossover

In the following, the atom-number statistics for a trapped fermionic spin mixture with variable two-body interaction will be investigated. The model, applied for the description of the BCS-BEC crossover, is based on the earlier studies of references [148–150]. This model relies on the versatility of the BCS wavefunction as a variational ansatz not only for weakly interacting fermions, but also for all interactions strengths in the BEC-BCS crossover regime. However, this ansatz is only an approximative description of the BEC-BCS crossover in cold-atom experiments, as was previously pointed out in Sec. 4.1.2. Nevertheless, the use of this model is justified, as mean-field approximations have proven to be very useful for qualitative predictions.

Using the FCS method, introduced in the previous section, the particle-number correlations for a fermion spin mixture at the BEC-BCS crossover will be computed now. Firstly, the two-dimensional case will be discussed, for which an analytical expression is found. The analytical expressions, found for the pure two-dimensional situation, can be mapped onto the quasi-two dimensional problem. The quasi-two dimensional case can be understood as a three-dimensionally trapped atom cloud which is frozen out in one direction. Thus, the system can move only freely in two dimensions and remains in the transversal ground state of the third direction. In order to map the two-dimensional situation on the quasi-two dimensional problem, the chemical potential must be replaced by $\mu_{2D} = \mu - \epsilon_0$, where ϵ_0 is the transversal ground state energy. In addition, the Fermi energy of the pure two-dimensional case, ϵ_F, must be replaced by the Fermi energy measured from the transversal ground state energy $\epsilon_F - \epsilon_0$. Secondly, the three-dimensional situation will be considered. No analytical expression could be found for the three-dimensional case. A numerical study shows, however, that the behavior is similar to that found in the two-dimensional case.

4.4.1   Cumulant generating function for the BEC-BCS crossover

The starting point is the result for the cumulant generating function of the BCS state derived in Sec. 4.3.4. The task to accomplish now is the evaluation of the sum over the momenta. Using the expression Eq. (4.56) and transforming the sum into an integral over the energy leads to

$$S(\chi) = -\int_0^\infty d\epsilon \, N_D(\epsilon) \log\left(1 + |v_{\mathbf{k}}|^2(e^{2i\chi} - 1)\right). \qquad (4.57)$$

The function $N_D(\epsilon)$ denotes the density of states and depends on the dimensionality of the system. For fermions of only one spin type, the density of states in $D = 2$ and $D = 3$ can be expressed as

$$N_D = \frac{m^{D/2}(2\epsilon)^{D/2-1}}{2\pi^{D-1}\hbar^D}, \qquad (4.58)$$

where m denotes the fermion mass. The $\sqrt{\epsilon}$ behavior of the density of states in three dimensions makes the explicit evaluation of the integral difficult. The three-

dimensional case will therefore be treated numerically. In contrast to the three-dimensional situation allows the energy independent density of states in two dimensions an explicit evaluation of the energy integral. However, the two-dimensional (or quasi-two dimensional) case can be used to understand the qualitative behavior of three-dimensional case.

Let us concentrate on the two-dimensional situation. The integral to solve is

$$S(\chi) = -\frac{m}{2\pi\hbar^2} \int_0^\infty d\epsilon \, \log\left(1 + \frac{1}{2}(e^{2i\chi} - 1)\left(1 - \frac{(\epsilon - \mu)}{\sqrt{(\epsilon - \mu)^2 - \Delta^2}}\right)\right). \quad (4.59)$$

Using the trick of taking the derivative and re-integrating, $\int_0^\alpha d\alpha' \frac{\partial}{\partial \alpha'}$, with respect to $\alpha = (e^{2i\chi} - 1)/2$ allows an explicit integration over the energy

$$
\begin{aligned}
S(\chi) &= -\Delta \frac{m}{2\pi\hbar^2} \int_0^\alpha d\alpha' \int_0^{s_0} ds \, \frac{1 + s^2}{1 + (1 + 2\alpha')s^2} \\
&= -\Delta \frac{m}{2\pi\hbar^2} \int_0^\alpha d\alpha' \left[\frac{s_0}{1 + 2\alpha'} + \frac{2\alpha'}{(1 + 2\alpha')^{3/2}} \arctan\left(s_0\sqrt{1 + 2\alpha'}\right)\right].
\end{aligned} \quad (4.60)
$$

Here, the substitution $s = -\frac{\epsilon-\mu}{\Delta} + \sqrt{\frac{(\epsilon-\mu)^2}{\Delta^2} + 1}$ has been made and $s_0 = \frac{\mu}{\Delta} + \sqrt{\frac{\mu^2}{\Delta^2} + 1}$ is the upper limit of the integral. Further integration over α' leads to the final result

$$S(\chi) = -\bar{N}\frac{\Delta}{\epsilon_F}\left[\cos(\chi)\arctan\left(\frac{2\epsilon_F}{\Delta}e^{i\chi}\right) - \arctan\left(\frac{2\epsilon_F}{\Delta}\right)\right] - \frac{\bar{N}}{2}\frac{\mu}{\epsilon_F}\log\left[1 + v_0^2(e^{i2\chi} - 1)\right]. \quad (4.61)$$

Note, that the density of states was expressed in terms of the average particle number $N(\epsilon_F) = D\bar{N}/2\epsilon_F$. The abbreviation $v_0^2 = \left(1 + \mu/\sqrt{\mu^2 + \Delta^2}\right)/2$ denotes the BCS coherence function for $k = 0$.

4.4.2 Atom-number correlations

From the final result for the cumulant generating function, Eq.(4.61), all cumulants can be computed. Figure 4.6 shows the second to seventh cumulant for the quasi-two and three-dimensional case. The curves show the expected smooth crossover from the BEC, or molecular condensate side $\xi \to \infty$, to the BCS, or Cooper-pair side $\xi \to -\infty$. Comparing the dashed-black curves for the quasi-two dimensional case to the solid-red curves of the three-dimensional case in Fig. 4.6 shows a qualitatively similar behavior in both cases. Larger discrepancies are seen, in particular, for higher cumulants. The quasi-two dimensional case shows much more distinct features. The generic effect of the $\sqrt{\epsilon}$ energy dependence of the density of state in three dimensions is a smoothening of the features. The extreme limits, $\xi \to \pm\infty$, show very different behaviors. In these limits, approximations can be made which lead to simplified expressions for the cumulant generating function. The approximative expressions for the cumulant generating function provide a clearer picture about the statistical properties of the state.
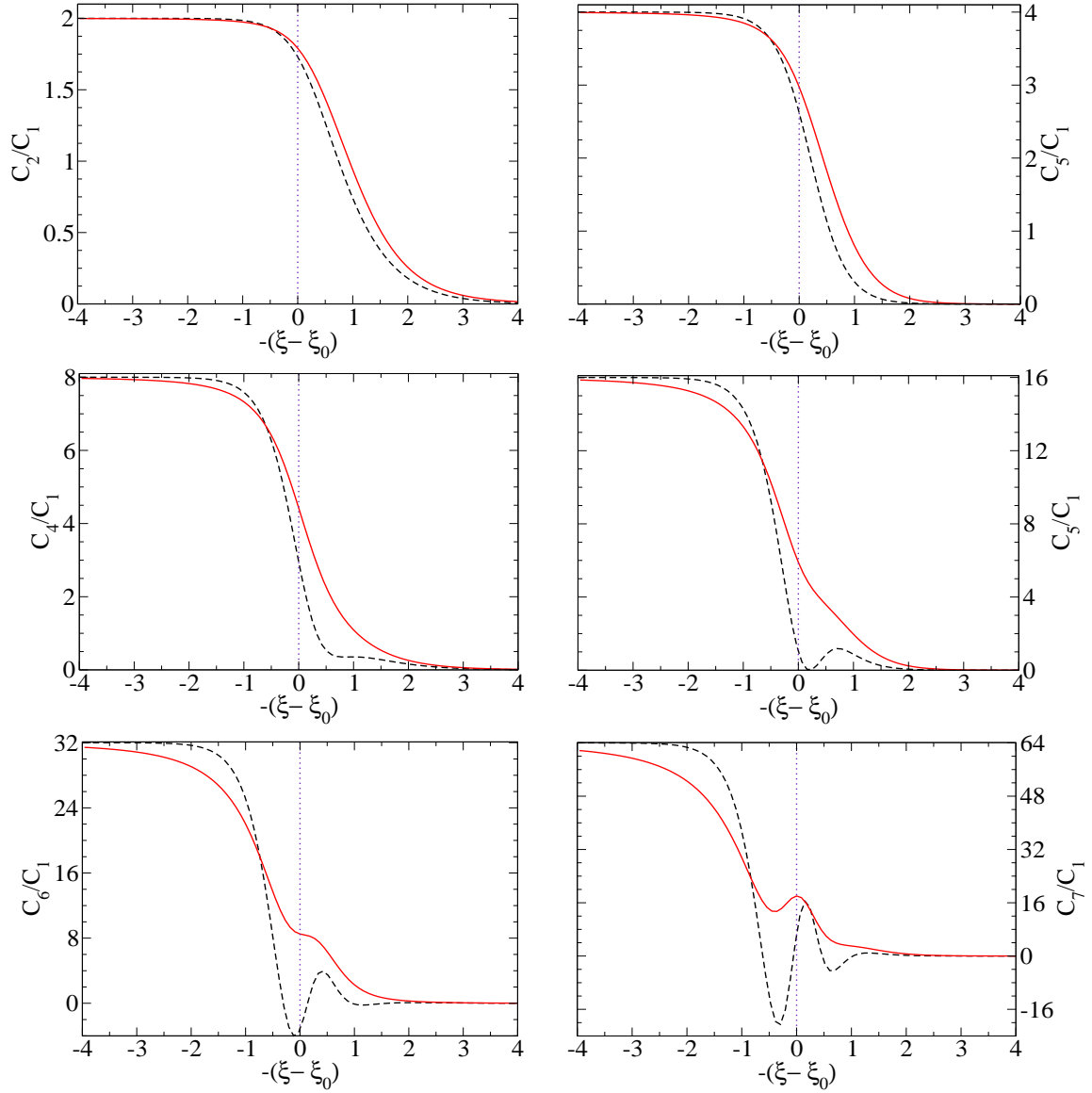
Figure 4.6: Comparing the cumulants C_2 - C_7 computed for the quasi-2D case from Eq. (4.61) (dashed-black line) to the numerically computed 3D results (solid-red line). The cumulants C_n are normalized to $C_1 = \bar{N}$ and plotted over $\xi = 1/k_D a$ where $k_{3D} = k_F = (3\pi^2 n)^{2/3}$ in 3D and $k_{2D} = \pi/\ell_0$ in quasi-2D. Here, ℓ_0 is the inverse of the ground-state size. The quasi-2D results are calculated for a box-potential. The dotted line marks the value $\xi(\mu = 0) \equiv \xi_0$ as a guidance for the eye.

BCS limit

The BCS limit corresponds to the situation known from conventional superconductivity. Interactions between the fermions in different spin states are attractive. Even though there exist no bound state on this side of the Feshbach resonance, a collective many-body state is formed. This collective state is reminiscent of the situation known from superconductivity in solid-state physics. Fermions with opposite momentum and spin are paired, forming so called Cooper pairs. The Cooper pairs are delocalized and overlap mutually to a large extend. In the BCS-BEC crossover picture, the BCS limit corresponds to the situation of a weakly attractive interaction i.e the limit of $\xi \to -\infty$. The chemical potential tends in the BCS limit towards the Fermi energy $\mu \approx \epsilon_F$ and the order parameter vanishes $\Delta \ll \epsilon_F$. Hence, the square root

$$\sqrt{\mu^2 + \Delta^2} \approx \epsilon_F + \frac{1}{2}\frac{\Delta^2}{\epsilon_F}\,, \tag{4.62}$$

can be expanded in terms of $\Delta/\mu \approx \Delta/\epsilon_F \ll 1$. Consequently, v_0^2 in Eq. (4.61) is

$$\lim_{\xi \to -\infty} v_0^2 = \frac{1}{2}\left(1 + \frac{\mu}{\sqrt{\mu^2 + \Delta^2}}\right) \approx 1\,, \tag{4.63}$$

neglecting all terms higher than first order in Δ/ϵ_F. The logarithm in Eq. (4.61) is approximately proportional to the counting field

$$\log\left(1 + |v_0|^2(e^{i2\chi} - 1)\right) \approx i2\chi\,. \tag{4.64}$$

Inserting this expansion in the expression for the cumulant generating function and replacing $\arctan(2\epsilon_F/\Delta) \approx \pi/2$ for $\epsilon_F \gg \Delta$, Eq. (4.61) reduces to

$$S(\chi) = -i\chi\bar{N} - \pi\bar{N}D\frac{\Delta}{4\epsilon_F}(|\cos(\chi)| - 1)\,. \tag{4.65}$$

Note, that the absolute value $|\cos(\chi)|$ is required to conserve the π-periodicity of Eq. (4.61). Equation (4.65) can also be derived directly from Eq. (4.57). The result for the three-dimensional treatment differs from the two-dimensional result only by a prefactor of $3/2$ for the cumulants C_n with $n \geq 2$. This is taken into account in Eq. (4.65) by the factor D, denoting the dimension of the system. Taking the derivative of Eq. (4.65) with respect χ shows that the cumulants can be divided into two classes. On the one hand, the even cumulants approach a universal value $C_{2n} = D\pi\bar{N}\Delta/4\epsilon_F$ as shown in Fig. 4.7. On the other hand, all odd cumulants C_{2n+1} with $n \geq 1$ are vanishing. In fact, plotting the cumulants in a logarithmic scale shows that the decrease is exponential in ξ.

The results for the BCS limit are clearly different from the results of the non-interacting fermion gas in Eq. (4.39). In the superfluid BCS state is the variance constant for zero temperature, $T = 0$. This is in contrast to the linearly vanishing variance for the non-interacting case (see Eq. (4.39)). Thus, an important information which could be obtained from a noise measurement is the order parameter, which can be extracted from a measurement of C_2 in the BCS limit. The order parameter is obtained from the variance as $\Delta/\epsilon_F = 4C_2/\pi\bar{N}D$.
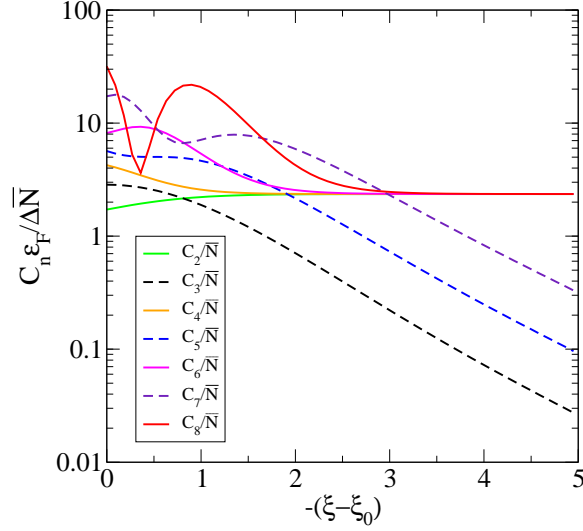
Figure 4.7: Cumulants C_2 to C_8 plotted over $-(\xi - \xi_0)$ for the 3D case in units of $\bar{N}\Delta/\epsilon_F$. Here, $\xi = 1/k_F a$ and $\xi_0 \equiv \xi(\mu = 0)$. All odd cumulants C_{2n+1} for $n \geq 1$ are vanishing in the BCS limit, $\xi \to -\infty$. The even cumulants approach the value $C_{2n} = 3\pi\bar{N}\Delta/4\epsilon_F$.

BEC limit

The repulsive side of the Feshbach resonance is clearly different from the BCS side. The existence of a bound state allows the formation of weakly-bound molecules. Fermions in opposite spin states pair up and form molecules. These molecules show bosonic behavior in the BEC limit, $\xi \to \infty$. The far BEC situation corresponds to a negative chemical potential, $\mu < 0$, and an order parameter which is much smaller than the chemical potential, $|\Delta/\mu| \to 0$. As the BEC limit is approached, the cumulant generating function for the crossover, Eq. (4.61), can be expanded in terms of $\Delta/|\mu|$. Taking the limit $\Delta/|\mu| \to 0$ leads to

$$v_0^2 = \frac{1}{2}\left(1 + \mu/\sqrt{\mu^2 + \Delta^2}\right) \approx \frac{\Delta^2}{4\mu^2}, \tag{4.66}$$

and for the Fermi energy to

$$\epsilon_F = \frac{1}{2}\left(\mu + \sqrt{\mu^2 + \Delta^2}\right) \approx \frac{\Delta^2}{4|\mu|}. \tag{4.67}$$

Using the expansions: $\arctan(x) \approx x$, $\log(1 + x) \approx x$ and $v_0^2 \approx \Delta^2/4\mu^2$ for $\Delta/|\mu| \ll 1$ leads to

$$\begin{aligned}
S(\chi) &\approx -\bar{N}\frac{4|\mu|}{\Delta}\left[\cos(\chi)\frac{\Delta}{2|\mu|}e^{i\chi} - \frac{\Delta}{2|\mu|}\right] + 2\bar{N}\frac{|\mu|^2}{\Delta^2}\frac{\Delta^2}{4|\mu|^2}(e^{i2\chi} - 1) \\
&= -2\bar{N}\left[\frac{1}{2}(e^{i2\chi} + 1) - 1\right] + \frac{\bar{N}}{2}(e^{i2\chi} - 1),
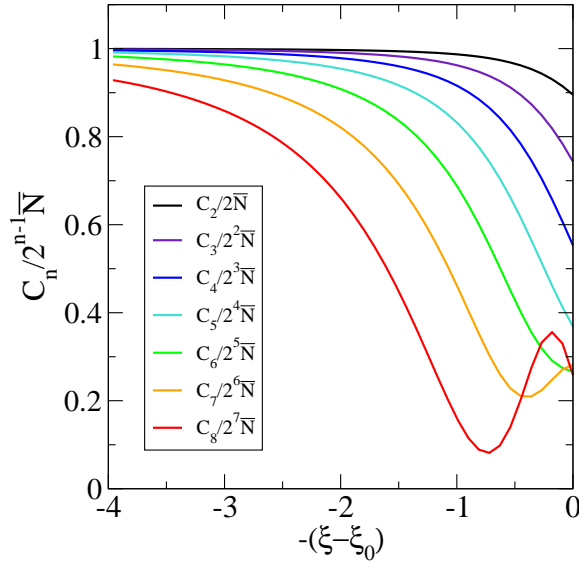\end{aligned} \tag{4.68}$$

Figure 4.8: Cumulants C_2 to C_8 plotted over $-(\xi - \xi_0)$ for the 3D case. Here, $\xi = 1/k_F a$ and $\xi_0 \equiv \xi(\mu = 0)$. All cumulants are normalized to $C_n/2^{n-1}\bar{N}$. In this normalization all cumulants tend towards unity in the BEC limit, $\xi \to \infty$, hence, showing Poisson statistics for fermion pairs (molecules).

which can be further simplified to give the cumulant generating function in the BEC limit

$$S(\chi) = -\frac{\bar{N}}{2}(e^{i2\chi} - 1) \, . \tag{4.69}$$

The result for the cumulant generating function in the BEC limit is a Poisson statistic. This is the expected result for a coherent state of molecules. Furthermore, the coherent state of molecules is reminiscent of the reformulation of the BCS-wavefunction in form of a coherent state of fermion pairs given in Eq. (4.21). There are several distinct features in Eq. (4.69). Firstly, the factor of two in front of the counting field. This is a clear indicator that the fermions have paired up. Secondly, the strongly increasing cumulants $C_n = 2^{n-1}\bar{N}$. Note, however, that Eq. (4.69) describes the cumulant generating function for the atoms and not for the molecules. The fluctuations are therefore strongly increased as only pairs of fermions can be detected. Thirdly, one has to mention, that the same statistics as described by Eq. (4.69) is expected for the atom-number statistics of a classical gas of $N/2$ molecules. The poissonian behavior in the BEC limit is shown in Fig. 4.8, where the cumulants are normalized by the factor $2^{n-1}\bar{N}$. Consequently, all cumulants tend towards unity for $\xi \to \infty$.

4.4.3 Finite-temperature behavior

So far, only the zero-temperature case has been considered. However, experiments are usually not done at zero temperatures. It is therefore desirable to obtain an ex-

pression for the cumulant generating function also for finite temperatures. A detailed discussion of the finite-temperature BEC-BCS crossover, with particular interest in the change of the critical temperature across the transition, is given in Ref. [150,151]. The intention of this section is to give a rough notion of the finite-temperature behavior of the full counting statistics in the different regimes.

Starting point is the zero-temperature BCS theory. The self-consistency equations for the order parameter Δ and the chemical potential μ of Sec. 4.1.3 must be extended to finite temperatures. Following [183], the gap equation is replaced by

$$\Delta_{\mathbf{j}} = -\frac{1}{2} \sum_{\mathbf{k}} \frac{\Delta_{\mathbf{k}}}{E_{\mathbf{k}}} V_{\mathbf{jk}} \tanh\left(\frac{\beta E_{\mathbf{k}}}{2}\right). \tag{4.70}$$

Repeating the renormalization procedure leads to the temperature-dependent gap equation as a function of the scattering parameters. The expression for the three-dimensional situation, with $\xi = 1/k_F a$, is given by

$$\xi = \frac{1}{\pi} \int_0^\infty d\tilde{\epsilon} \, \tilde{\epsilon}^{\frac{1}{2}} \left(\frac{1}{\tilde{\epsilon}} - \frac{\tanh\left(\frac{\tilde{\beta}}{2}\sqrt{(\tilde{\epsilon} - \tilde{\mu})^2 + \tilde{\Delta}^2}\right)}{\sqrt{(\tilde{\epsilon} - \tilde{\mu})^2 + \tilde{\Delta}^2}} \right). \tag{4.71}$$

All quantities denoted with a tilde are normalized to the Fermi energy ϵ_F. The self-consistency equation for the particle-number conservation, Eq. (4.16), becomes

$$N = \sum_{\mathbf{k},\sigma} \left(|v_{\mathbf{k}}|^2 \tanh\left(\frac{\beta E_{\mathbf{k}}}{2}\right) + f_+(\epsilon) \right), \tag{4.72}$$

where $f_+(\epsilon)$ is the fermion occupation function defined in Eq. (4.36).

The temperature-dependent self-consistency equations are, however, not sufficient to compute the cumulant generating function for finite temperatures. The finite-temperature wavefunction will no longer correspond to the zero-temperature BCS wavefunction given in Eq. (4.12). The most difficult part is thus the determination of the state describing the many-body system at finite temperatures. Using a Bogoliubov transformation [204] provides the excitation spectrum on the BCS side and a calculation of the cumulant generating function in the finite-temperature BCS limit is possible. A discussion of this finite-temperature BCS limit is postponed till later. The situation on the BEC side and in the crossover region is more difficult. Nevertheless, knowing the behavior for the free boson and free fermion gas from Sec. 4.3, a qualitative picture of the finite-temperature behavior can be outlined. The qualitative behavior of the variance is sketched in Fig. 4.9. The solid line in the lower part of the graph sketches the temperature behavior on the BCS side. The zero-temperature result gives a finite value for the second cumulant, C_2. The value for the variance of the superfluid state, derived from Eq. (4.65), is proportional to the order parameter, $C_2 = \pi \bar{N} D \Delta / 4\epsilon_F$. The variance calculated for free fermions vanishes linearly with temperature (see Eq. (4.39)). Figure 4.9 shows the variance for a free Fermi gas (dashed-dotted line) as a guide for the eye. The excitations on the BCS side are
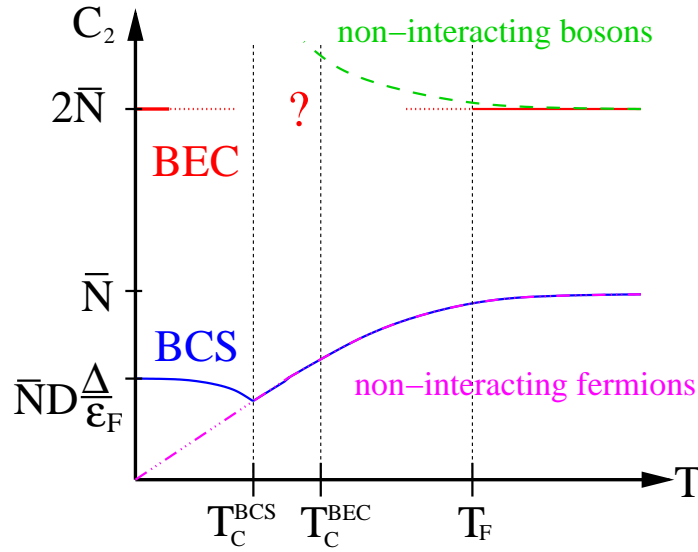
Figure 4.9: Qualitative behavior of the second cumulant C_2 as a function of temperature. Upper curve: BEC limit, lower curve: BCS limit. The dashed (dashed-dotted) lines show the the qualitative behavior in the case of non-interacting bosons (fermions) as derived in Sec. 4.3.2 and Sec. 4.3.3.

fermionic quasiparticles. Increasing the temperature leads to the creation of fermionic quasi particles and, thus, leads to a decrease of the variance on the BCS side. Finally, when the temperature reaches T_C^{BCS} there are no particles left in the superconducting state. Hence, the curve for C_2 in the BCS limit (lower-solid line) merges with the curve for C_2 of the free non-interacting fermion gas (dash-dotted line). The consequence is an increase of the variance for further increasing temperature, until the variance saturates into the value for a classical gas, $C_2 = \bar{N}$, at temperatures far above the Fermi temperature $T \gg T_F$. The results for the variance on the BEC side are very different. The system forms a Bose-Einstein condensate of molecules at zero temperature. Hence, the statistics is Poissonian. Keeping in mind that atoms are detected and not molecules, we can read off the variance from Eq. (4.69) as $C_2 = 2\bar{N}$. Looking at the non-degenerate limit, the variance has to approach the classical limit. Assuming, that the dissociation temperature is much larger then the Fermi temperature, we obtain again the value $C_2 = 2\bar{N}$ for the variance. Note, however, that this time the atom fluctuations have been derived for a classical gas of $\bar{N}/2$ molecules[5]. Comparison to the free non-interacting cloud of molecules leads to the dashed-upper curve. The variance of the non-interacting Bose gas shows a strong increase towards lower temperatures. The fluctuations behave like $C_2 \sim \bar{N}^2$ if zero temperature is approached. The behavior of the variance in the BEC limit for temperatures between $0 < T < T_F$ is more difficult to obtain and is part of future investigation. Finally, if the temperature is above the dissociation temperature, the molecules will dissociate and the variance on the BEC side will drop down to the value $C_2 = \bar{N}$ for a classical

---

[5]The statistics corresponds to Eq. (4.38), however, with $N/2$ particles and double the counting field as we are counting atoms which are always paired as molecules. Thus, the same Poisson statistics as for the coherent state, Eq. (4.69), is obtained in the classical limit.

gas of $\bar{N}$ atoms.

BCS limit

Performing a Bogoliubov transformation provides the energy spectrum of the excitations on the BCS side. The transformation introduces the new quasiparticle creation and annihilation operators $\gamma_{\mathbf{k},0(1)}^{\dagger}$ and $\gamma_{\mathbf{k},0(1)}$. They are connected to the fermion operators $c_{\mathbf{k},\sigma}^{\dagger}$, $c_{\mathbf{k},\sigma}$, via the relations [183]

$$
\begin{aligned}
c_{\mathbf{k}\uparrow} &= u_{\mathbf{k}}^{*}\gamma_{\mathbf{k},0} + v_{\mathbf{k}}\gamma_{\mathbf{k},1}^{\dagger} \quad , \\
c_{-\mathbf{k}\downarrow}^{\dagger} &= -v_{\mathbf{k}}^{*}\gamma_{\mathbf{k},0} + u_{\mathbf{k}}\gamma_{\mathbf{k},1}^{\dagger} \quad ,
\end{aligned} \tag{4.73}
$$

with the parameters $u_{\mathbf{k}}$ and $v_{\mathbf{k}}$ as defined in Eq. (4.14). The unitary Bogoliubov transformation diagonalizes the Hamiltonian. Thus, in the new quasiparticle operators the Hamiltonian reads

$$
\hat{H} = \sum_{\mathbf{k},i\in\{0,1\}} E_{\mathbf{k}}\gamma_{\mathbf{k},i}^{\dagger}\gamma_{\mathbf{k},i} , \tag{4.74}
$$

with the quasiparticle energy spectrum $E_{\mathbf{k}} = \sqrt{(\epsilon_{\mathbf{k}} - \mu)^2 + \Delta^2}$. In order to derive the finite-temperature expression for the cumulant generating function on the BCS side, we have to evaluate the quantity

$$
\langle e^{i\sum_{\mathbf{k}\sigma}\hat{n}_{\mathbf{k}\sigma}\chi}\rangle = \frac{1}{Z}\mathrm{Tr}\left\{e^{-\beta\sum_{\mathbf{k},i}E_{\mathbf{k}}\gamma_{\mathbf{k},i}^{\dagger}\gamma_{\mathbf{k},i}}\,e^{i\sum_{\mathbf{k}\sigma}\hat{n}_{\mathbf{k}\sigma}\chi}\right\} . \tag{4.75}
$$

Note, that the trace is taken over all quasiparticle states. The quantity $\hat{n}_{\mathbf{k},\sigma} = c_{\mathbf{k},\sigma}^{\dagger}c_{\mathbf{k},\sigma}$ is the fermion-number operator. The detailed derivation of the cumulant generating function in the finite-temperature BCS limit is outlined in Appendix E.2. Instead of discussing all the tedious steps, an intuitive interpretation of the finite-temperature result will be given.

Consider an empty pair state ($\mathbf{k}\uparrow, -\mathbf{k}\downarrow$). There are different possibilities to occupy this pair state with quasiparticles or a Cooper pair. Firstly, there could be only one quasiparticle occupying the pair state. Hence, the pair state is blocked for Cooper pairs. Secondly, the pair state can be occupied by two quasiparticles. Thirdly, a Cooper pair can occupy the pair state. The corresponding terms in the cumulant generating function are given by the probability of the occupation times the χ-dependent function ($e^{i\alpha\chi} - 1$). The prefactor in the exponent takes the value $\alpha = 1$ if the state is occupied by a single quasiparticle only and $\alpha = 2$ for the occupation by two quasiparticles or a Cooper pair.

Following this scheme we obtain for the single-quasiparticle occupation a term

$$
2f_{+}(E_{\mathbf{k}})(1 - f_{+}(E_{\mathbf{k}}))(e^{i\chi} - 1) , \tag{4.76}
$$

in the cumulant generating function. Here, $f_{+}(E_{\mathbf{k}})$ is the Fermi occupation function given in Eq. (4.36). The factor $f_{+}(E_{\mathbf{k}})$ is the probability for the occupation with a
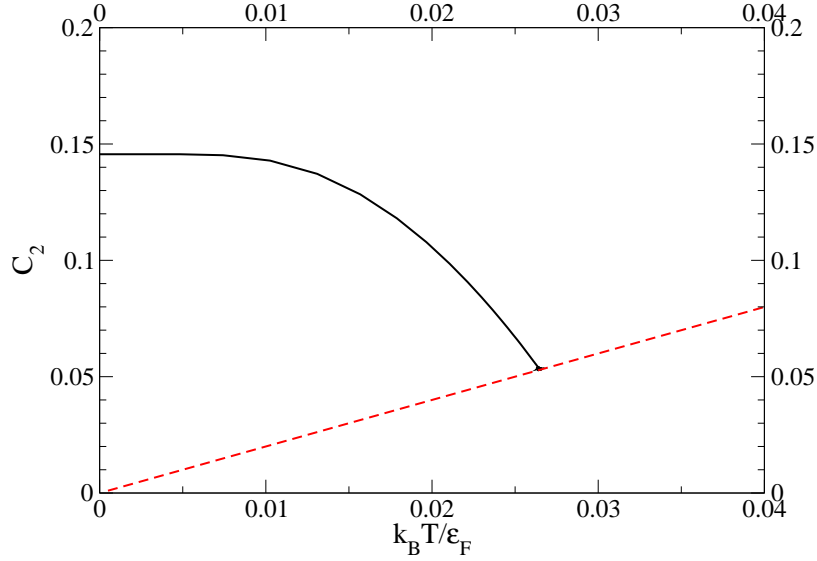
Figure 4.10: Temperature dependence of the variance (second cumulant C_2) in the BCS limit for a 3D cloud and $\xi = 1/k_F a = -2$. The solid line is the result computed from Eq. (4.79) for temperatures $T \leq T_c^{\mathrm{BCS}}$. The dashed line shows the free-fermion case, Eq. (4.35).

quasiparticle and $(1 - f_+(E_\mathbf{k}))$ the probability for an empty state. The factor of two takes the two possibilities to occupy the pair state with a single quasiparticle into account. The term in the cumulant generating function describing the occupation of the pair state by a pair of quasiparticles is given by

$$|u_\mathbf{k}|^2 f_+(E_\mathbf{k})^2 (e^{i2\chi} - 1).$$
(4.77)

The factor $|u_\mathbf{k}|^2$ is the probability that the state is not occupied by a Cooper pair. The last term to the cumulant generating function describes the occupation of the pair state by a Cooper pair

$$|v_\mathbf{k}|^2 (1 - f_+(E_\mathbf{k}))^2 (e^{i2\chi} - 1).$$
(4.78)

Combining all terms, the cumulant generating function is given by

$$S(\chi) = -\sum_k \log \big[\, 1 + 2f_+(E_\mathbf{k})(1 - f_+(E_\mathbf{k}))(e^{i\chi} - 1)$$
$$+ |v_k|^2 (1 - f_+(E_\mathbf{k}))^2 (e^{2i\chi} - 1) + |u_k|^2 f_+(E_\mathbf{k})^2 (e^{2i\chi} - 1) \,\big].$$
(4.79)

The result Eq. (4.79) agrees with the result obtained from the direct calculation of Eq. (4.75). The explicit calculation is shown in Appendix E.2. Figure 4.10 shows the temperature dependence of the variance, C_2, for the three-dimensional case. As the order parameter vanishes for temperatures above T_c^{BCS}, Eq. (4.79) transforms into the cumulant generating function for the free-fermion case, as given in Eq. (4.35). The free-fermion results are shown in Fig. 4.10 by the dashed line.

4.5   Summary of Chapter 4

In conclusion, we propose to measure the atom-number fluctuations in ultra-cold atomic gases to obtain information about the state of system. We suggest to directly measure the atom-number density in a bin, i.e, a subsystem of the trapped cloud. This is in contrast to correlation measurements in expansion pictures [62–64]. The advantage of a direct measurement of the cloud lies in the absence of the expansion. The expansion of the atomic cloud leads to a drastic change in the atom density and, thus, to a drastic change in the inter-atomic interaction which can destroy the initial state as, for example, the superfluid BCS state. A direct measurement avoids the expansion of the cloud. Recent experiments by Bartenstein et al. [180] showed that a direct measurement of the atomic density in trapped atomic clouds is experimentally feasible.

Having this experimental approach in mind, we calculated the full counting statistics for a fermion spin mixture in the BEC-BCS crossover region. Choosing the single-channel ansatz based on the BCS wavefunction [148, 149], we derived an analytical expression for the cumulant generating function in two and quasi-two dimensions. The cumulants for the three-dimensional situation were calculated numerically. Comparing the quasi-two and three-dimensional cases showed that the $\sqrt{\epsilon}$ behavior of the three-dimensional density of states leads to a smoothing of the distinct features obtained for the quasi-two dimensional case. The results in quasi-two, as well as in three dimensions, showed the expected distinct difference between the statistics on the BEC and BCS side. On the BEC side we found Poisson statistics for the atom-number correlations. However, the Poisson statistics corresponds to half the number of particles $\bar{N}/2$. In addition, a prefactor of two is found in front of the counting field. The prefactor of two is not surprising, as this corresponds to the statistics of a coherent state of molecules. The BCS side showed a very different statistical behavior. All odd cumulants, C_{2n+1}, are vanishing for $n \geq 1$. In contrast to the odd cumulants approach all even cumulants a constant value in the BCS limit. The value for the even cumulants, $C_{2n} = D\pi\bar{N}\Delta/4\epsilon_F$, is proportional to the order parameter Δ and the dimension of the system D. Measuring the variance of the atom-number fluctuations allows a determination of the order parameter. Comparing the even cumulants of the superfluid BCS state to the even cumulants of the non-interacting Fermi gas showed another very useful difference. The variance of the free-fermionic gas is vanishing proportional to the temperature, in contrast to the constant value of the BCS state. Hence, measurements of the atom-number statistics can be used as an indicator for the existence of a superfluid BCS state.

Finally, in the last section, a brief discussion of the finite-temperature behavior was given. The results for the zero-temperature BEC-BCS crossover were compared to the results for free non-interacting fermions and free non-interacting bosons. The finite-temperature behavior on the BCS side of the transition was calculated using a Bogoliubov transformation. In future, it would be desirable to get more information about the finite-temperature statistics in the BEC and crossover region.

Appendix

Appendix A

Derivation of the potential-fluctuation correlator

This appendix gives a derivation for the correlation function $\langle \delta S_{im}(z)\delta S_{nj}(z') \rangle$. In fact, it is sufficient to find a general expression of the potential-fluctuation correlator $\langle \delta V(\mathbf{x})\delta V(\mathbf{x}') \rangle$. The derivation of $\langle \delta S_{im}(z)\delta S_{nj}(z') \rangle$ can then be calculated, using Eq. (2.17). Finally, the results for the single-wire trap: Eqs. (2.34 -2.36), and the results for the double-wire trap, Eq. (2.52), Eq. (2.53) can be obtained by specifying the geometries .

In the following, the general expression for the potential-fluctuation correlator $\langle \delta V(\mathbf{x})\delta V(\mathbf{x}') \rangle$ of N parallel traps will be derived. The fluctuations of the trapping potential δV are induced by current noise in the wires, which give rise to a fluctuating field $\delta \mathbf{B}$. The trapping potential δV and the magnetic trapping field $\delta \mathbf{B}$ are linked by Eq. (2.1). Hence, $\langle \delta V(\mathbf{x})\delta V(\mathbf{x}') \rangle$ can be expressed in terms of magnetic-field fluctuations:

$$
\langle \delta V(\mathbf{x})\delta V(\mathbf{x}') \rangle = \sum_{ij} \langle S(\mathbf{x})|\mu_i|S(\mathbf{x}) \rangle
$$
$$
\times \ \langle S(\mathbf{x}')|\mu_j|S(\mathbf{x}') \rangle \langle \delta B_i(\mathbf{x})\delta B_j(\mathbf{x}') \rangle \ . \tag{A.1}
$$

Thus, the first step is to find the expression for $\langle \delta B_i(\mathbf{x})\delta B_j(\mathbf{x}') \rangle$ as a function of the current noise. At first, $\delta \mathbf{A}$ and $\delta \mathbf{B}$ are calculated using

$$
\delta A_i(\mathbf{x}) \quad = \frac{\mu_0}{4\pi} \int d^3\tilde{\mathbf{x}} \frac{\delta j_i(\tilde{\mathbf{x}})}{|\mathbf{x}-\tilde{\mathbf{x}}|} \ , \tag{A.2}
$$
$$
\delta B_i(\mathbf{x}) \quad = \sum_{jk} \epsilon_{ijk} \frac{d}{dx_j} \delta A_k(\mathbf{x}) \ . \tag{A.3}
$$

The current density in the set of one-dimensional wires is

$$
\delta \mathbf{j}(\mathbf{x}) = \sum_{\gamma} \delta I_\gamma(z)\delta(x - d_\gamma)\delta(y)\hat{\mathbf{z}} \ , \tag{A.4}
$$

where d_γ denotes the $\hat{x}$-position of the γ-th wire. The sum over γ reflects the fact, that the total current density $\mathbf{j}$ is a sum of M contributions, arising from the set of M wires. In the next step, Eq. (A.4) is inserted into Eq. (A.2) and combined with

Eq. (A.3) to obtain the expression for the magnetic field, induced by the current in the wire array:

$$\delta\mathbf{B}(\mathbf{x}) = \frac{\mu_0}{4\pi}\sum_\gamma \begin{pmatrix} -y \\ x - d_\gamma \\ 0 \end{pmatrix} \int d\tilde{z}\, \frac{\delta I_\gamma(\tilde{z})}{[(x - d_\gamma)^2 + y^2 + (z - \tilde{z})^2]^{3/2}}\ . \tag{A.5}$$

The correlation function for the current density is now assumed to be of the form

$$\langle \delta I_\alpha(z)\delta I_\beta(z') \rangle = 4 k_{\mathrm{B}} T_{\mathrm{eff}} \sigma A \delta(z - z')\delta_{\alpha\beta}\,, \tag{A.6}$$

for the reasons discussed before in Section 2.3.1. Using Eq. (A.6) in combination with equations (A.1) and (A.5) gives the desired relation for the correlation function of the potential fluctuations

$$\begin{aligned}
\langle \delta V(\mathbf{x})\delta V(\mathbf{x}') \rangle =& 4 k_{\mathrm{B}} T_{\mathrm{eff}} \sigma A \left(\frac{\mu_0}{4\pi}\right)^2 \\
&\times \sum_\gamma \sum_{ij} \langle S(\mathbf{x})|\mu_i|S(\mathbf{x}) \rangle \langle S(\mathbf{x}')|\mu_j|S(\mathbf{x}') \rangle\, Y_{ij}^\gamma(\mathbf{x}, \mathbf{x}') J^\gamma(\mathbf{x}, \mathbf{x}')\,,
\end{aligned} \tag{A.7}$$

where the following abbreviations have been introduced

$$Y^\gamma(\mathbf{x}, \mathbf{x}') = \begin{pmatrix} yy' & -y(x' - d_\gamma) & 0 \\ -(x - d_\gamma)y' & (x - d_\gamma)(x' - d_\gamma) & 0 \\ 0 & 0 & 0 \end{pmatrix}\,, \tag{A.8}$$

$$J^\gamma(\mathbf{x}, \mathbf{x}') = \int_{-\infty}^{\infty} d\tilde{z}\, \left[(x - d_\gamma)^2 + y^2 + (z - \tilde{z})^2\right]^{-\frac{3}{2}} \left[(x' - d_\gamma)^2 + y'^2 + (z' - \tilde{z})^2\right]^{-\frac{3}{2}}\,. \tag{A.9}$$

Equation (A.9) can be further simplified if the transversal positions $x^{(\prime)}$ and $y^{(\prime)}$ are replaced by the position of the trap minimum x_0^α and y_0^α where α is the trap label denoting the trap in which the wavefunction is localized. The replacement of the transversal coordinates by its trap-minima positions is a good approximation as the transversal widths w of the trapped atomic clouds are in general much smaller than the wire to trap distance r_0. We have, thus, reduced J^γ to a function, which now only depends on the difference $\zeta_- = z - z'$:

$$J_{\alpha\beta}^\gamma(\zeta_-) = \int_{-\infty}^{\infty} d\tilde{z}'\, \left[(x_0^\alpha - d_\gamma)^2 + y_0^{\alpha 2} + \tilde{z}'^2\right]^{-\frac{3}{2}} \left[(x_0^\beta - d_\gamma)^2 + y_0^{\beta 2} + (\zeta_- - \tilde{z}')^2\right]^{-\frac{3}{2}}\,, \tag{A.10}$$

where the integration variable was shifted to $\tilde{z}' = \tilde{z} - z$. Applying the formula to the single-wire and double-wire configurations leads to the single-wire result, Eq. (2.36)

$$J(z) = \frac{1}{r_0^5} \int_{-\infty}^{\infty} d\tilde{z}\, \left[1 + \tilde{z}^2\right]^{-\frac{3}{2}} \left[1 + (z/r_0 - \tilde{z})^2\right]^{-\frac{3}{2}}\,,$$

and to the double-wire result, Eq. (2.53)

$$
J_{\alpha\beta}^{\gamma}(z-z') = \int\limits_{-\infty}^{\infty} d\tilde{z} \left[\left(x_0^{\alpha} - \epsilon_{\gamma}\frac{d}{2} \right)^2 + y_0^2 + \tilde{z}^2 \right]^{-\frac{3}{2}} \left[\left(x_0^{\beta} - \epsilon_{\gamma}\frac{d}{2} \right)^2 + y_0^2 + (z - z' - \tilde{z})^2 \right]^{-\frac{3}{2}} ,
$$

respectively.

To obtain $\langle \delta V(\mathbf{x})\delta V(\mathbf{x}')\rangle$ using Eq. (A.7), one still has to calculate the mean value of the atomic-magnetic moment $\langle S(\mathbf{x})|\boldsymbol{\mu}|S(\mathbf{x})\rangle$. Let us assume, that the magnetic moment follows the magnetic trapping field adiabatically, which is reasonable as long as the Larmor precession $\omega_L = \mu_B B/\hbar$ is fast compared to the trap frequency ω. Calculating the spinor $|S(\mathbf{x})\rangle$ for an atom having spin $F = 2$, either by considering the small corrections of the transversal magnetic field to $B_{\text{bias}}^{(z)}$ perturbatively or by calculating the rotation of the spinor as the atomic moment follows the trapping field adiabatically, results in the following expression for the spatial dependence of $|S(\mathbf{x})\rangle$ for small deviations from the trap minimum

$$
|S(\mathbf{x})\rangle = |2, 2\rangle + \frac{B_x(\mathbf{x}) + iB_y(\mathbf{x})}{B_{\text{bias}}^{(z)}}|2, 1\rangle . \tag{A.11}
$$

The spin states are denoted as $|F, m_F\rangle$ and the spin quantization axis is chosen along the $\hat{z}$-axis. Making use of Eq. (A.11) leads to

$$
\langle S(\mathbf{x})|\boldsymbol{\mu}|S(\mathbf{x})\rangle = 2\mu_B g_F \frac{\mathbf{B}(\mathbf{x})}{B_{\text{bias}}^{(z)}} , \tag{A.12}
$$

which is an approximation to the mean value of the magnetic moment to first order in $B_{\perp}/B_{\text{bias}}^{(z)}$. Inserting the expression for the magnetic moment Eq. (A.12) into Eq. (A.7) and inserting the specific magnetic trapping fields for the single-wire trap, Eq. (2.2), or the double-wire trap, Eq. (2.3), the results for $\langle \delta S_{im}(z)\delta S_{nj}(z')\rangle$, given by Eq. (2.35) for the single-wire setup

$$
\langle \delta S_{im}(z)\delta S_{nj}(z')\rangle = \quad J(z - z')k_{\text{B}}T_{\text{eff}}\sigma A \left(\frac{\mu_0 g_F \mu_B}{\pi} \frac{B_{\text{bias}}^{(x)}}{B_{\text{bias}}^{(z)}} \right)^2
$$
$$
\times \int d\mathbf{r}_{\perp} \, \chi_i(\mathbf{r}_{\perp})(y - y_0)\chi_m^*(\mathbf{r}_{\perp}) \int d\mathbf{r}_{\perp}' \, \chi_n(\mathbf{r}_{\perp}')(y' - y_0)\chi_j^*(\mathbf{r}_{\perp}') ,
$$

and by Eq. (2.52) for the double-wire setup

$$
\langle \delta S_{im}(z)\delta S_{nj}(z')\rangle = 8A_0 \frac{x_0^{\alpha} x_0^{\beta}}{d^2} \sum_{\gamma=L,R} J_{\alpha\beta}^{\gamma}(z - z')
$$
$$
\times \int d\mathbf{r}_{\perp}\chi_i(\mathbf{r}_{\perp}) \left[(y - y_0) - y_0\frac{(x - x_0^{\alpha})}{(x_0^{\alpha} + \epsilon_{\gamma}\frac{d}{2})} \right] \chi_m^*(\mathbf{r}_{\perp})
$$
$$
\times \int d\mathbf{r}_{\perp}'\chi_n(\mathbf{r}_{\perp}') \left[(y' - y_0) - y_0\frac{(x' - x_0^{\beta})}{(x_0^{\beta} + \epsilon_{\gamma}\frac{d}{2})} \right] \chi_j^*(\mathbf{r}_{\perp}') ,
$$

are finally obtained.

Appendix B

Matrix elements for the double-wire trap

The matrix $\tilde{A}$ in the equation of motion Eq. (2.41) for the double-wire configuration is given by

$$\tilde{A} = \begin{pmatrix} \sum_{i=1}^{4} \alpha_i & \beta_1 & \beta_2 & \beta_3 & \beta_4 \\ \beta_1 & \alpha_1 + \alpha_3 & 0 & \alpha_6 & \alpha_5 \\ \beta_2 & 0 & \alpha_2 + \alpha_4 & \alpha_5 & \alpha_6 \\ \beta_3 & \alpha_6 & \alpha_5 & \alpha_1 + \alpha_4 & 0 \\ \beta_4 & \alpha_5 & \alpha_6 & 0 & \alpha_2 + \alpha_3 \end{pmatrix} . \tag{B.1}$$

The matrix elements are obtained by inserting Eq.(2.55) into the equation of motion (2.33). This leads to the explicit expressions for the matrix elements of Eq. (2.57) given by

$$\alpha_1 = 4A_0 \frac{\left(w_y^L x_0^L\right)^2}{d^2} \sum_{\gamma \in \{L,R\}} J_{LL}^\gamma(0) \,, \tag{B.2}$$

$$\alpha_2 = 4A_0 \frac{\left(w_x^L x_0^L\right)^2}{d^2} \sum_{\gamma \in \{L,R\}} J_{LL}^\gamma(0) \frac{y_0^2}{\left(x_0^L + \epsilon_\gamma \frac{d}{2}\right)^2} \,, \tag{B.3}$$

$$\alpha_3 = 4A_0 \frac{\left(w_y^R x_0^R\right)^2}{d^2} \sum_{\gamma \in \{L,R\}} J_{RR}^\gamma(0) \,, \tag{B.4}$$

$$\alpha_4 = 4A_0 \frac{\left(w_x^R x_0^R\right)^2}{d^2} \sum_{\gamma \in \{L,R\}} J_{RR}^\gamma(0) \frac{y_0^2}{\left(x_0^R + \epsilon_\gamma \frac{d}{2}\right)^2} \,, \tag{B.5}$$

$$\alpha_5 = -4A_0 \frac{w_x^L w_y^L \left(x_0^L\right)^2}{d^2} \sum_{\gamma \in \{L,R\}} J_{LL}^\gamma(0) \frac{y_0}{x_0^L + \epsilon_\gamma \frac{d}{2}} \,, \tag{B.6}$$

$$\alpha_6 = 4A_0 \frac{w_x^R w_y^R \left(x_0^R\right)^2}{d^2} \sum_{\gamma \in \{L,R\}} J_{RR}^\gamma(0) \frac{y_0}{x_0^R + \epsilon_\gamma \frac{d}{2}} \,, \tag{B.7}$$

$$\tag{B.8}$$

$$\beta_1 \;=\; -4A_0 w_y^L w_y^R x_0^L x_0^R \frac{1}{d^2} \sum_{\gamma\in\{L,R\}} J_{LR}^\gamma(z-z')\,, \tag{B.9}$$

$$\beta_2 \;=\; 4A_0 w_x^L w_x^R x_0^L x_0^R \frac{1}{d^2} \sum_{\gamma\in\{L,R\}} J_{LR}^\gamma(z-z')\frac{y_0^2}{\left(x_0^L+\epsilon_\gamma\frac{d}{2}\right)\left(x_0^R+\epsilon_\gamma\frac{d}{2}\right)}\,, \tag{B.10}$$

$$\beta_3 \;=\; -4A_0 w_x^R w_y^L x_0^L x_0^R \frac{1}{d^2} \sum_{\gamma\in\{L,R\}} J_{LR}^\gamma(z-z')\frac{y_0}{x_0^R+\epsilon_\gamma\frac{d}{2}}\,, \tag{B.11}$$

$$\beta_4 \;=\; 4A_0 w_x^L w_y^R x_0^L x_0^R \frac{1}{d^2} \sum_{\gamma\in\{L,R\}} J_{LR}^\gamma(z-z')\frac{y_0}{x_0^L+\epsilon_\gamma\frac{d}{2}}\,. \tag{B.12}$$

$$\tag{B.13}$$

The ϵ_γ-function is defined as $\epsilon_L = -1$ and $\epsilon_R = 1$

Appendix C

Derivation of perturbative corrections to the matrix elements

We use standard stationary perturbation theory [113] to calculate the corrections to the mean-field results induced by the perturbation

$$V = -\sum_{\langle i,j \rangle} V_{ij} = -\frac{J}{2} \sum_{\langle i,j \rangle} (c_i^\dagger c_j + c_j^\dagger c_i) \,, \tag{C.1}$$

where we introduce the new operators

$$c_i = a_i - \langle a_i \rangle_0 = a_i - \Psi_i \,, \tag{C.2}$$

The expectation value $\langle \cdot \rangle_0$ is taken with respect to the mean-field wavefunction $|G_0\rangle$. Defining the operator for the energy denominator as

$$\frac{1}{\Delta} \equiv \frac{1 - |G_0\rangle\langle G_0|}{\epsilon_0 - H_{\mathrm{MF}}} \,, \tag{C.3}$$

the expectation value of an observable $\langle A \rangle$ including all corrections up to second order is

$$
\begin{aligned}
\langle A \rangle \approx & \langle A \rangle_0 + \langle V \frac{1}{\Delta} A \rangle_0 + \langle A \frac{1}{\Delta} V \rangle_0 \\
& + \langle V \frac{1}{\Delta} V \frac{1}{\Delta} A \rangle_0 + \langle V \frac{1}{\Delta} A \frac{1}{\Delta} V \rangle_0 \\
& + \langle A \frac{1}{\Delta} V \frac{1}{\Delta} V \rangle_0 - \langle V \frac{1}{\Delta^2} V \rangle_0 \langle A \rangle_0 \,.
\end{aligned}
\tag{C.4}
$$

The first line in Eq. (C.4) is the mean-field result $\langle A \rangle_0$, followed by two contributions which are the first-order corrections. Lines two and three in Eq. (C.4) are the second-order corrections to the mean value.

C.1 Density matrix: First-order corrections

As an example we will discuss the corrections to the density matrix $\rho_{ij} = \langle a_i^\dagger a_j \rangle$. The first-order correction to the density matrix is:

$$\langle a_i^\dagger a_j \rangle_1 = \langle c_i^\dagger c_j \rangle_1 + \Psi_i^* \langle c_j \rangle_1 + \langle c_i^\dagger \rangle_1 \Psi_j + \Psi_i^* \Psi_j \,. \tag{C.5}$$
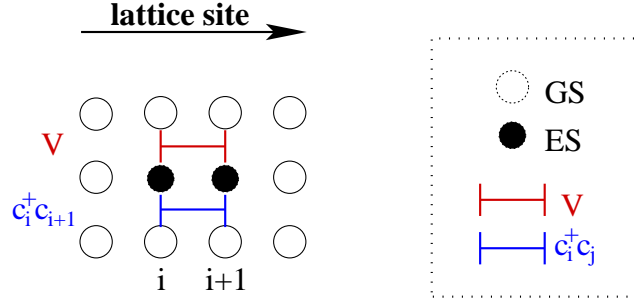
Figure C.1: Schematic diagram illustrating the term $\langle c_i^\dagger c_j \frac{1}{\Delta} V_{ij}\rangle_0$ appearing in the first-order correction $\langle c_i^\dagger c_j\rangle_1$ of the density matrix, where $V_{ij} = \frac{J}{2}(c_i^\dagger c_j + c_j^\dagger c_i)$ is the perturbation connecting sites i and j. The diagram shows the lattice sites in the horizontal direction. The different steps needed to obtain the matrix element are shown vertically. Open circles denote the ground state (GS) of the given lattice site, while filled circles are excited states (ES) of this site, for the mean-field Hamiltonian H_{MF}.

For two different lattice sites $i \neq j$, we find

$$\langle c_i^\dagger c_j \frac{1}{\Delta} c_i\rangle_0 = \langle c_j\rangle_0 \langle c_i^\dagger \frac{1}{\Delta} c_i\rangle_0 = 0 \, , \tag{C.6}$$

since the Gutzwiller ground state is a product state. As a consequence, the contributions $\langle c_i^\dagger\rangle_1$ and $\langle c_j\rangle_1$ vanish. The only remaining contributions to $\langle a_i^\dagger a_j\rangle_1$ stem from

$$\langle c_i^\dagger c_j\rangle_1 = -\langle V_{ij} \frac{1}{\Delta} c_i^\dagger c_j\rangle_0 - \langle c_i^\dagger c_j \frac{1}{\Delta} V_{ij}\rangle_0 \, , \tag{C.7}$$

and $\Psi_i^* \Psi_j$.

To get a better idea of the character of the terms arising in the perturbative expansion, we introduce, in Fig. C.1, a graphical representation (for the example of a 1D-lattice). The graph shows a decomposition of the matrix element, with each row showing the wavefunction at an intermediate step in the evaluation of the matrix element. As we deal with product states

$$|G^\alpha\rangle = \prod_{i=1}^{M} |i_{\alpha_i}\rangle \, , \tag{C.8}$$

we represent the wavefunction by a row of circles, where each circle denotes the state $|i_{\alpha_i}\rangle$ of a particular lattice site i. Open circles in Fig. C.1 denote a lattice site in its ground state (GS), filled circles refer to an excited state (ES) of this particular lattice site, with respect to the local mean-field Hamiltonian. Note that, in general, this can be an arbitrarily highly excited state (although higher contributions are suppressed by the energy denominator, and a cutoff is used in practice). Starting with a row of open circles, denoting the GS, $|G_0\rangle$, each following row corresponds to the state after the action of V or $c_i^\dagger c_j$, as indicated on the left side of the graph. As all matrix elements in Eq. (C.4) can be expressed in terms of a GS expectation value $\langle \cdot \rangle_0$ and
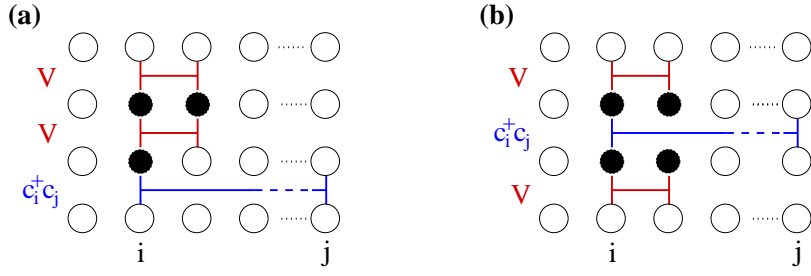
Figure C.2: Diagrammatic representation of the contributions from $\Psi_i^* \langle c_j \rangle_2$ and $\langle c_i^\dagger \rangle_2 \Psi_j$ to the second-order correction of the density matrix. *(a)* Terms representing contributions of the form Eq. (C.11).*(b)* contributions of the form Eq. (C.12). All notations are the same as in Fig. C.1.

a sequence of V and $c_i^\dagger c_j$ operators, the first and last row must always be a line of open circles.

Let us consider for instance the second term in Eq. (C.7)

$$\langle c_i^\dagger c_j \frac{1}{\Delta} V_{ij} \rangle_0 \, . \tag{C.9}$$

Reading the graph in Fig. C.1 from top to bottom corresponds to reading the matrix element from right to left. Starting with the GS, $|G_0\rangle$, the first row consists of open circles. The second row shows the state after the action of the perturbation V. Acting with V_{ij} to the right onto the GS results in a state

$$V_{ij} |G_0\rangle = \sum_{\alpha,\beta} f_{\alpha,\beta} |i_\alpha, j_\beta\rangle \, , \tag{C.10}$$

where i and j are neighboring lattice sites and $|i_\alpha, j_\beta\rangle$ denotes the state with lattice site i (j) in the exited state α (β) and all other sites in their GS. Thus the second row shows the lattice sites i and $i+1$ in an excited state (filled circle), as the perturbation, Eq. (C.1), allows only next neighbor interactions. Finally, the action of $c_i^\dagger c_j$ has to bring the excited states back to the GS, in order to get a non-vanishing contribution. Therefore, in first order PT, only next neighbor corrections to the correlation function arise, as the final row must represent the ground state $\langle G_0|$ again. The graph representing the remaining first term in Eq. (C.7) is obtained by rotating the graph in Fig. C.1 by π.

C.2   Density matrix: Second-order corrections

Rewriting the second-order corrections to the density matrix, $\langle a_i^\dagger a_j \rangle_2$, in terms of the operators $c_i^\dagger$ and c_j gives Eq. (C.5), but with $\langle \cdot \rangle_1$ replaced by $\langle \cdot \rangle_2$. In contrast to the first-order corrections, now the terms proportional to $\langle c_j \rangle_2$ and $\langle c_i^\dagger \rangle_2$ also give non-vanishing contributions. Using Eq. (C.4) we obtain:

$$\langle c_j \rangle_2 \quad = \sum_k' \langle V_{jk} \frac{1}{\Delta} V_{jk} \frac{1}{\Delta} c_j \rangle_0 + \sum_k' \langle c_j \frac{1}{\Delta} V_{jk} \frac{1}{\Delta} V_{jk} \rangle_0 \tag{C.11}$$

$$+ \sum_k' \langle V_{jk} \frac{1}{\Delta} c_j \frac{1}{\Delta} V_{jk} \rangle_0 \, . \tag{C.12}$$
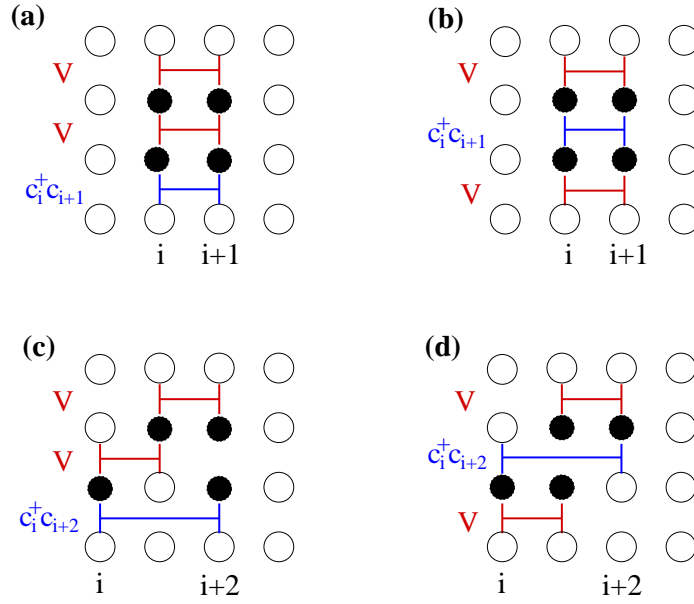
(a)

(b)

(c)

(d)

Figure C.3: Graphs showing second-order corrections arising from $\langle c_i^\dagger c_j \rangle_2$. Diagrams (a) and (b) are coming from direct-neighbor contributions as given by Eq. (C.13) and Eq. (C.14) respectively. Diagrams (c) and (d) are next-nearest-neighbor contributions: (c) corresponds to Eq. (C.16) and Eq. (C.17); (d) corresponds to Eq. (C.18).

Here, the primed sums run over all neighbors k to site j. The corresponding subset of graphs for $\Psi_i^* \langle c_j \rangle_2$ and $\langle c_i^\dagger \rangle_2 \Psi_j$ are given by Fig. C.2a and Fig. C.2b for Eq. (C.11) and Eq. (C.12) respectively. Note that all terms of Eq. (C.11) and Eq. (C.12) give a correction to all matrix elements of the density matrix independent of the distance between the lattice sites. We can understand these contributions as a modification to the mean-field value of the density matrix.

For the second-order contribution, $\langle c_i^\dagger c_j \rangle_2$, we have to distinguish two cases:

(a) Lattice site i and j being direct neighbors. In this case we get

$$\langle c_i^\dagger c_j \rangle_2 = \ \langle V_{ij} \tfrac{1}{\Delta} V_{ij} \tfrac{1}{\Delta} c_i^\dagger c_j \rangle_0 + \langle c_i^\dagger c_j \tfrac{1}{\Delta} V_{ij} \tfrac{1}{\Delta} V_{ij} \rangle_0 \tag{C.13}$$

$$+ \langle V_{ij} \tfrac{1}{\Delta} c_i^\dagger c_j \tfrac{1}{\Delta} V_{ij} \rangle_0 \,. \tag{C.14}$$

Corrections for Eq. (C.13) and Eq. (C.14) are shown in Fig. C.3a and Fig. C.3b, respectively.

(b) Configurations corresponding to two lattice sites $i \neq j$ connected by two suc-

cessive hopping steps via site k. This gives rise to six contributions:

$$\langle c_i^\dagger c_j \rangle_2 = \tag{C.15}$$

$$\sum_{\mathcal{C}} \langle V_{jk} \frac{1}{\Delta} V_{ki} \frac{1}{\Delta} c_i^\dagger c_j \rangle_0 + \sum_{\mathcal{C}} \langle V_{ki} \frac{1}{\Delta} V_{jk} \frac{1}{\Delta} c_i^\dagger c_j \rangle_0 \tag{C.16}$$

$$+ \sum_{\mathcal{C}} \langle c_i^\dagger c_j \frac{1}{\Delta} V_{jk} \frac{1}{\Delta} V_{ki} \rangle_0 + \sum_{\mathcal{C}} \langle c_i^\dagger c_j \frac{1}{\Delta} V_{ki} \frac{1}{\Delta} V_{jk} \rangle_0 \tag{C.17}$$

$$+ \sum_{\mathcal{C}} \langle V_{jk} \frac{1}{\Delta} c_i^\dagger c_j \frac{1}{\Delta} V_{ki} \rangle_0 + \sum_{\mathcal{C}} \langle V_{ki} \frac{1}{\Delta} c_i^\dagger c_j \frac{1}{\Delta} V_{jk} \rangle_0 \,. \tag{C.18}$$

An example for the contributions arising from Eq. (C.16) and Eq. (C.17) is shown in Fig. C.3c. The last term, Eq. (C.18), has the representation shown in Fig. C.3d. Note that for lattices with dimensions $D > 1$, the sites i,j and k need not necessarily form a straight line but can form a chevron.

Appendix D

Scattering Formalism

This Appendix gives a brief summary of the scattering formalism. The following sections are meant as an introduction to the notation used in the main text of this thesis. A detailed discussion of scattering theory is given, for instance, in [112].

D.1 Lippmann-Schwinger Equation

The Hamiltonian of a two-body scattering process is given as

$$(\hat{H}_0 + V)|\Psi\rangle = E|\Psi\rangle \,, \tag{D.1}$$

where V is the scattering potential. For elastic scattering, we have energy conservation i.e. the solution of the scattering problem, $|\Psi\rangle$, has the same energy as the free-incoming wavepacket: $\hat{H}_0|\Phi\rangle = E|\Phi\rangle$. The formal solution of Eq. (D.1) is the Lippmann-Schwinger equation

$$|\Psi\rangle = \frac{1}{E - \hat{H}_0 \pm i\epsilon}V|\Psi\rangle + |\Phi\rangle \,, \tag{D.2}$$

Here, the "+"-sign stands for an outgoing and "−"-sign for an ingoing wave. Using the position basis, we obtain for Eq. (D.2)

$$\langle\mathbf{x}|\Psi\rangle = \langle\mathbf{x}|\Phi\rangle + \int d\mathbf{x}' \,\langle\mathbf{x}|\frac{1}{E - \hat{H}_0 \pm i\epsilon}|\mathbf{x}'\rangle\langle\mathbf{x}'|V|\Psi\rangle \,. \tag{D.3}$$

Defining $k = \sqrt{2mE}/\hbar$ leads to

$$\langle\mathbf{x}|\frac{1}{E - \hat{H}_0 \pm i\epsilon}|\mathbf{x}'\rangle = -\frac{2m}{\hbar^2}\frac{1}{4\pi}\frac{e^{\pm ik|\mathbf{x}-\mathbf{x}'|}}{|\mathbf{x} - \mathbf{x}'|} \,. \tag{D.4}$$

Assuming a plane wave for the incoming wavefunction and assuming that the scattering potential depends only on the position operator $V(\mathbf{x})$, gives

$$\Psi(\mathbf{x}) = \frac{1}{(2\pi\hbar)^{3/2}}e^{i\mathbf{k}\mathbf{x}} - \frac{2m}{\hbar^2}\frac{1}{4\pi}\int d\mathbf{x}' \frac{e^{\pm ik|\mathbf{x}-\mathbf{x}'|}}{|\mathbf{x} - \mathbf{x}'|}V(\mathbf{x}')\Psi(\mathbf{x}') \,. \tag{D.5}$$

Furthermore, we assume that the size of the scatterer is much smaller than the distance to the detector. Defining $|\mathbf{x}| = r$, $|\mathbf{x}'| = r'$ and taking the limit $r \gg r'$, allows us to approximate

$$\frac{e^{\pm ik|\mathbf{x}-\mathbf{x}'|}}{|\mathbf{x}-\mathbf{x}'|} \approx \frac{e^{\pm i(kr+\mathbf{k}'\mathbf{x}')}}{r}, \tag{D.6}$$

in Eq. (D.5). The wavevector $\mathbf{k}'$ with $|\mathbf{k}'| = k$, points in the direction of the outgoing particle. Hence, Eq. (D.6) leads to

$$\Psi(\mathbf{x}) = \frac{1}{(2\pi\hbar)^{3/2}} e^{i\mathbf{k}\mathbf{x}} - \frac{1}{(2\pi\hbar)^{3/2}} \frac{e^{ikr}}{r} \underbrace{\int d\mathbf{x}' \left(\frac{2\pi m^2}{\hbar}\right)^{1/2} e^{-i\mathbf{k}'\mathbf{x}'} V(\mathbf{x}')\Psi(\mathbf{x}')}_{\equiv f(\mathbf{k},\mathbf{k}')}, \tag{D.7}$$

where we restricted ourselves to the outgoing solution.

D.2 Partial Waves

Instead of using the plane-wave basis set we can use the spherical-wave basis set. This is particularly convenient, if the scattering potential has spherical symmetry. In this case, we can expand the scattering amplitude in Legendre polynomials

$$f(\mathbf{k},\mathbf{k}') = \sum_{l=0}^{\infty} (2l+1)f_l(k)P_l(\cos\theta). \tag{D.8}$$

Note, that $f(\mathbf{k},\mathbf{k}') = f(\theta,E)$ due to energy conservation. Expansion of the plane wave into spherical waves leads to

$$e^{i\mathbf{k}\mathbf{x}} = \sum_{l=0}^{\infty}(2l+1)i^l j_l(kr)P_l(\cos\theta) \xrightarrow{\text{large } r} \sum_{l=0}^{\infty}(2l+1)i^l \frac{e^{i(kr-(l\pi/2))} - e^{-i(kr-(l\pi/2))}}{2ikr} P_l(\cos\theta), \tag{D.9}$$

where $j_l(kr)$ is the l-th Bessel function and θ the angle between $\mathbf{k}$ and $\mathbf{x}$. Inserting the expansion of the wave amplitude $f(\theta,E)$, Eq. (D.8), and the expansion of the plane wave, Eq. (D.9), into Eq. (D.7) for the wavefunction, yields

$$\Psi(\mathbf{x}) = \frac{1}{(2\pi\hbar)^{3/2}} \sum_{l=0}^{\infty}(2l+1)\frac{P_l(\cos\theta)}{2ik}\left[(1+2ikf_l(k))\frac{e^{ikr}}{r} - \frac{e^{-i(kr-l\pi)}}{r}\right]. \tag{D.10}$$

The second term in the square brackets is the incoming term and the first term is the outgoing term modified by the factor $1 + 2ikf_l(k)$ due to the scattering process.

Finally, we can make use of the particle-number conservation. In simple words: Any particle going in must come out again. In addition, we have conservation of the angular momentum as a spherically symmetric scattering potential was assumed. Therefore, the incoming and outgoing currents must be the same for every single "l" term, which leads to the condition[1]

$$|(1+2ikf_l(k))| = 1 \quad \Longrightarrow \quad (1+2ikf_l(k)) = e^{i2\delta_l(k)}. \tag{D.11}$$

---

[1]The factor 2 in the phase is convention.

This allows us to rewrite the scattering amplitude as

$$f_l(k) = \frac{e^{i\delta_l} \sin \delta_l}{k} = \frac{1}{k \cot \delta_l - ik} \ . \tag{D.12}$$

In conclusion, we can say, that (in reasonably large distance to the scatterer) the effect of the scatterer results only in a phase shift δ_l for every angular momentum component in the outgoing radial wave.

Appendix E

Cumulant generating functions

E.1 Cumulant generating function of the degenerate Fermi gas

This appendix gives a short derivation of the cumulant generating function for a free fermionic gas in the degenerate limit. The starting point is Eq. (4.35) which is given here once more

$$S(\chi) = -\sum_k \log\left[1 + f_+(e^{i\chi} - 1)\right] . \tag{E.1}$$

The degenerate limit corresponds to the low-temperature case $k_B T \ll \epsilon_F$, for which the Fermi occupation function

$$f_+(\epsilon) = \frac{1}{e^{\beta(\epsilon - \mu)} + 1}$$

shows a sharp step at the Fermi energy $\mu = \epsilon_F$.

The first step is a conversion of the sum in Eq. (E.1) into an integral

$$S(\chi) = -\int_0^\infty d\epsilon\, N(\epsilon) \log\left[1 + f_+(\epsilon)(e^{i\chi} - 1)\right] . \tag{E.2}$$

Here, $N(\epsilon)$ denotes the density of states. The integral is split up into a part for energies smaller than ϵ_F and into a part for energies larger than ϵ_F. After a transformation of variables $\epsilon \to -\eta + \epsilon_F$ and $\epsilon \to \eta' + \epsilon_F$ for $\epsilon < \epsilon_F$ and $\epsilon > \epsilon_F$, respectively, the integral can be rewritten as

$$S(\chi) = -\int_0^{\epsilon_F} d\eta\, N(-\eta + \epsilon_F) \log\left[1 + f_+(-\eta + \epsilon_F)(e^{i\chi} - 1)\right]$$
$$- \int_{\epsilon_F}^\infty d\eta'\, N(\eta' + \epsilon_F) \log\left[1 + f_+(\eta' + \epsilon_F)(e^{i\chi} - 1)\right] . \tag{E.3}$$

Using the equality $f_+(\epsilon_F - \eta) = 1 - f_+(\epsilon_F + \eta)$ and rewriting the logarithm of the

first integral gives

$$S(\chi) = -i\tilde{\chi} \int_0^{\epsilon_F} d\eta \, N(-\eta + \epsilon_F) - \int_0^{\epsilon_F} d\eta \, N(-\eta + \epsilon_F) \log \left[1 + f_+(\epsilon_F + \eta)(e^{-i\chi} - 1)\right]$$
$$- \int_0^\infty d\eta' \, N(\eta' + \epsilon_F) \log \left[1 + f_+(\epsilon_F + \eta')(e^{i\chi} - 1)\right]$$
$$(\text{E.4})$$

where $\tilde{\chi}/2\pi + 1/2 = [\chi/2\pi + 1/2]$, with $[\ldots]$ denoting the fractional part. The first integral corresponds to the average particle number $\bar{N}$. Using the identity

$$f(\chi) - f(0) = \int_0^\chi d\chi' \frac{d}{d\chi'} f(\chi'), \qquad (\text{E.5})$$

and performing the derivative explicitly leads to

$$S(\chi) = -i\tilde{\chi}\bar{N} + i \int_0^\chi d\chi' \int_0^{\epsilon_F} d\eta \frac{N(-\eta + \epsilon_F)e^{-i\chi'}}{f_+(\epsilon_F + \eta)^{-1} + (e^{-i\chi'} - 1)}$$
$$- i \int_0^\chi d\chi' \int_0^\infty d\eta' \frac{N(\eta' + \epsilon_F)e^{i\chi'}}{f_+(\epsilon_F + \eta')^{-1} + (e^{i\chi'} - 1)} \qquad (\text{E.6})$$
$$\approx -i\tilde{\chi}\bar{N} + i \int_0^\chi d\chi' \int_0^\infty d\eta \left[\frac{N(-\eta + \epsilon_F)e^{-i\chi'}}{e^{\beta\eta} + e^{-i\chi'}} - \frac{N(\eta + \epsilon_F)e^{i\chi'}}{e^{\beta\eta} + e^{i\chi'}}\right].$$

Considering the degenerate limit i.e. $k_B T \ll \epsilon_F$, the arguments of the integrals are quickly decaying on a energy scale $\beta^{-1} = k_B T$. Thus, as the density of states is a slowly varying function on this energy scale, $N(\pm\eta + \epsilon_F)$ can be replaced by its value a the Fermi energy $N(\epsilon_F)$. Furthermore, the upper limit of the first integral, ϵ_F, has been taken to infinity, causing no significant change to the value of the integral. Further simplifying the remaining integral leads to

$$S(\chi) = -i\tilde{\chi}\bar{N} + iN(\epsilon_F) \int_0^\chi d\chi' \int_0^{\epsilon_F} d\eta \frac{i \sin \chi'}{\cosh \beta\eta + \cos \chi'}. \qquad (\text{E.7})$$

Finally, the integrals can be explicitly evaluated

$$S(\chi) = -i\tilde{\chi}\bar{N} + N(\epsilon_F) \int_0^\chi d\chi' \frac{2}{\beta} \arctan\left(\tan\left(\chi'/2\right)\right)$$
$$= -i\tilde{\chi}\bar{N} + \frac{1}{2} k_B T N(\epsilon_F) \tilde{\chi}^2, \qquad (\text{E.8})$$

where the 2π-periodicity is again preserved by introducing the quantity $\tilde{\chi}$.

E.2 Cumulant generating function in the BCS limit at finite temperatures

The calculation of the CGF for the finite-temperature BCS limit is based on the quasiparticle spectrum. The transformation between the fermion operators $c_{\mathbf{k},\sigma}^\dagger$, $c_{\mathbf{k},\sigma}$ and the quasiparticle operators $\gamma_{\mathbf{k},i}^\dagger$, $\gamma_{\mathbf{k},i}$ reads [183]

$$c_{\mathbf{k}\uparrow} = u_{\mathbf{k}}^* \gamma_{\mathbf{k},0} + v_{\mathbf{k}} \gamma_{\mathbf{k},1}^\dagger \qquad , \qquad (\text{E.9})$$
$$c_{-\mathbf{k}\downarrow}^\dagger = -v_{\mathbf{k}}^* \gamma_{\mathbf{k},0} + u_{\mathbf{k}} \gamma_{\mathbf{k},1}^\dagger \qquad . \qquad (\text{E.10})$$

The final goal is to find the CGF for the quasiparticle excitations

$$\langle e^{i\sum_{\mathbf{k}\sigma}\hat{n}_{\mathbf{k}\sigma}\chi}\rangle = \frac{1}{Z}\mathrm{Tr}\left\{e^{-\beta\sum_{\mathbf{k},i}E_{\mathbf{k}}\gamma^{\dagger}_{\mathbf{k},i}\gamma_{\mathbf{k},i}}\, e^{i\sum_{\mathbf{k}\sigma}\hat{n}_{\mathbf{k}\sigma}\chi}\right\}. \tag{E.11}$$

Note, that the trace is taken over all quasiparticle states. The quantity $\hat{n}_{\mathbf{k},\sigma} = c^{\dagger}_{\mathbf{k},\sigma}c_{\mathbf{k},\sigma}$ is the fermion-number operator. In the next step, the relation

$$n^{\ell}_{\mathbf{k},\sigma} = n_{\mathbf{k},\sigma}, \tag{E.12}$$

valid for all positive integer ℓ, is used. The relation can be derived from the anti-commutation relation for the fermion operators, $\{c_{\mathbf{k},\sigma}, c^{\dagger}_{\mathbf{k}',\sigma'}\} = \delta_{\mathbf{k}\mathbf{k}'}\delta_{\sigma\sigma'}$, and the Pauli principle: $c^2_{\mathbf{k},\sigma} = {c^{\dagger}_{\mathbf{k},\sigma}}^2 = 0$. Hence, the exponential in Eq. (E.11) can be simplified to give

$$\begin{aligned}e^{i\sum_{\mathbf{k}\sigma}n_{\mathbf{k}\sigma}\chi} &= \prod_{\mathbf{k}\sigma}\sum_{n=0}^{\infty}\frac{(in_{\mathbf{k}\sigma}\chi)^n}{n!} = \prod_{\mathbf{k}\sigma}\left[(1-n_{\mathbf{k}\sigma})+n_{\mathbf{k}\sigma}\sum_{n=0}^{\infty}\frac{i\chi^n}{n!}\right]\\ &= \prod_{\mathbf{k}}\left[(1-n_{\mathbf{k}\uparrow})+n_{\mathbf{k}\uparrow}e^{i\chi}\right]\left[(1-n_{-\mathbf{k}\downarrow})+n_{-\mathbf{k}\downarrow}e^{i\chi}\right].\end{aligned} \tag{E.13}$$

Inserting Eq. (E.13) into Eq. (E.11) leads to

$$\begin{aligned}\langle e^{i\sum_{\mathbf{k}\sigma}\hat{n}_{\mathbf{k}\sigma}\chi}\rangle &= \frac{1}{Z}\mathrm{Tr}\left\{\prod_{\mathbf{k}}e^{-\beta\sum_i E_{\mathbf{k}}\gamma^{\dagger}_{\mathbf{k},i}\gamma_{\mathbf{k},i}}\left[(1-n_{\mathbf{k}\uparrow})+n_{\mathbf{k}\uparrow}e^{i\chi}\right]\left[(1-n_{-\mathbf{k}\downarrow})+n_{-\mathbf{k}\downarrow}e^{i\chi}\right]\right\}\\ &= \frac{1}{Z}\prod_{\mathbf{k}}\sum_{\nu_{\mathbf{k},0},\nu_{\mathbf{k},1}\in\{0,1\}}e^{-\beta E_{\mathbf{k}}(\nu_{\mathbf{k},0}+\nu_{\mathbf{k},1})}\\ &\quad\times\langle\nu_{\mathbf{k},0},\nu_{\mathbf{k},1}|\left[(1-n_{\mathbf{k}\uparrow})+n_{\mathbf{k}\uparrow}e^{i\chi}\right]\left[(1-n_{-\mathbf{k}\downarrow})+n_{-\mathbf{k}\downarrow}e^{i\chi}\right]|\nu_{\mathbf{k},0},\nu_{\mathbf{k},1}\rangle,\end{aligned} \tag{E.14}$$

where $\nu_{\mathbf{k},i}$ are the eigenvalues of the quasiparticle number operator: $\gamma^{\dagger}_{\mathbf{k},i}\gamma_{\mathbf{k},i}$. In order to evaluate the last expression, we have to transform the fermion-number operators $\hat{n}_{\mathbf{k},\sigma}$ with the help of Eqs. (E.9), (E.10), into quasiparticle operators. Transforming the number operator into the new basis yields

$$\begin{aligned}n_{\mathbf{k}\uparrow} = c^{\dagger}_{\mathbf{k}\uparrow}c_{\mathbf{k}\uparrow} &= (u_{\mathbf{k}}\gamma^{\dagger}_{\mathbf{k},0}+v^*_{\mathbf{k}}\gamma_{\mathbf{k},1})(u^*_{\mathbf{k}}\gamma_{\mathbf{k},0}+v_{\mathbf{k}}\gamma^{\dagger}_{\mathbf{k},1})\\ &= |u_{\mathbf{k}}|^2\gamma^{\dagger}_{\mathbf{k},0}\gamma_{\mathbf{k},0}+|v_{\mathbf{k}}|^2\gamma_{\mathbf{k},1}\gamma^{\dagger}_{\mathbf{k},1}+v^*_{\mathbf{k}}u^*_{\mathbf{k}}\gamma_{\mathbf{k},1}\gamma_{\mathbf{k},0}+u_{\mathbf{k}}v_{\mathbf{k}}\gamma^{\dagger}_{\mathbf{k},0}\gamma^{\dagger}_{\mathbf{k},1},\\ n_{\mathbf{k}\downarrow} = c^{\dagger}_{\mathbf{k}\downarrow}c_{\mathbf{k}\downarrow} &= (-v^*_{\mathbf{k}}\gamma_{-\mathbf{k},0}+u_{\mathbf{k}}\gamma^{\dagger}_{-\mathbf{k},1})(-v_{\mathbf{k}}\gamma^{\dagger}_{-\mathbf{k},0}+u^*_{\mathbf{k}}\gamma_{-\mathbf{k},1})\\ &= |v_{\mathbf{k}}|^2\gamma_{-\mathbf{k},0}\gamma^{\dagger}_{-\mathbf{k},0}+|u_{\mathbf{k}}|^2\gamma^{\dagger}_{-\mathbf{k},1}\gamma_{-\mathbf{k},1}-v^*_{\mathbf{k}}u^*_{\mathbf{k}}\gamma_{-\mathbf{k},0}\gamma_{-\mathbf{k},1}-u_{\mathbf{k}}v_{\mathbf{k}}\gamma^{\dagger}_{-\mathbf{k},1}\gamma^{\dagger}_{-\mathbf{k},0},\end{aligned} \tag{E.15}$$

and thus the total number operator is

$$\begin{aligned}\sum_{\mathbf{k},\sigma}n_{\mathbf{k}\sigma} &= \sum_{\mathbf{k}}n_{\mathbf{k}\uparrow}+n_{-\mathbf{k}\downarrow}\\ &= \sum_{\mathbf{k}}\left(2u^*_{\mathbf{k}}v^*_{\mathbf{k}}\gamma_{\mathbf{k},1}\gamma_{\mathbf{k},0}+2u_{\mathbf{k}}v_{\mathbf{k}}\gamma^{\dagger}_{\mathbf{k},0}\gamma^{\dagger}_{\mathbf{k},1}+\sum_{i\in\{0,1\}}\left((|u_{\mathbf{k}}|^2-|v_{\mathbf{k}}|^2)\gamma^{\dagger}_{\mathbf{k},i}\gamma_{\mathbf{k},i}+|v_{\mathbf{k}}|^2\right)\right).\end{aligned} \tag{E.16}$$

Taking the mean value leads to

$$\langle\nu_{\mathbf{k},0}\nu_{\mathbf{k},1}|n_{\mathbf{k}\uparrow}+n_{-\mathbf{k}\downarrow}|\nu_{\mathbf{k},0}\nu_{\mathbf{k},1}\rangle = (|u_{\mathbf{k}}|^2 - |v_{\mathbf{k}}|^2)(\nu_{\mathbf{k},0} + \nu_{\mathbf{k},1}) + 2|v_{\mathbf{k}}|^2\,. \qquad (E.17)$$

Furthermore, the mean value for the product of two number operators must be found. Using again the transformation rule Eq. (E.15) for $\hat{n}_{\mathbf{k},\sigma}$ yields to

$$\begin{aligned}
\langle\nu_{\mathbf{k},0},&\nu_{\mathbf{k},1}|n_{\mathbf{k}\uparrow}n_{-\mathbf{k}\downarrow}|\nu_{\mathbf{k},0},\nu_{\mathbf{k},1}\rangle\\
&= \langle\nu_{\mathbf{k},0},\nu_{\mathbf{k},1}|(|u_{\mathbf{k}}|^2\gamma_{\mathbf{k},0}^\dagger\gamma_{\mathbf{k},0} + |v_{\mathbf{k}}|^2\gamma_{\mathbf{k},1}\gamma_{\mathbf{k},1}^\dagger + v_{\mathbf{k}}^*u_{\mathbf{k}}^*\gamma_{\mathbf{k},1}\gamma_{\mathbf{k},0} + u_{\mathbf{k}}v_{\mathbf{k}}\gamma_{\mathbf{k},0}^\dagger\gamma_{\mathbf{k},1}^\dagger)\\
&\quad\times (|v_{\mathbf{k}}|^2\gamma_{\mathbf{k},0}\gamma_{\mathbf{k},0}^\dagger + |u_{\mathbf{k}}|^2\gamma_{\mathbf{k},1}^\dagger\gamma_{\mathbf{k},1} - v_{\mathbf{k}}^*u_{\mathbf{k}}^*\gamma_{\mathbf{k},0}\gamma_{\mathbf{k},1} - u_{\mathbf{k}}v_{\mathbf{k}}\gamma_{\mathbf{k},1}^\dagger\gamma_{\mathbf{k},0}^\dagger)|\nu_{\mathbf{k},0},\nu_{\mathbf{k},1}\rangle\\
&= \left[|u_{\mathbf{k}}|^2\nu_{\mathbf{k},0} + |v_{\mathbf{k}}|^2(1-\nu_{\mathbf{k},1})\right]\left[|v_{\mathbf{k}}|^2(1-\nu_{\mathbf{k},0}) + |u_{\mathbf{k}}|^2\nu_{\mathbf{k},1}\right]\\
&\quad - |u_{\mathbf{k}}|^2|v_{\mathbf{k}}|^2\langle\nu_{\mathbf{k},0},\nu_{\mathbf{k},1}|\left[-(1-\gamma_{\mathbf{k},1}^\dagger\gamma_{\mathbf{k},1})(1-\gamma_{\mathbf{k},0}^\dagger\gamma_{\mathbf{k},0}) - \gamma_{\mathbf{k},0}^\dagger\gamma_{\mathbf{k},0}\gamma_{\mathbf{k},1}^\dagger\gamma_{\mathbf{k},1}\right]|\nu_{\mathbf{k},0},\nu_{\mathbf{k},1}\rangle,
\end{aligned}$$
$$(E.18)$$

and, thus, to the final result

$$\begin{aligned}
\langle\nu_{\mathbf{k},0},&\nu_{\mathbf{k},1}|n_{\mathbf{k}\uparrow}n_{-\mathbf{k}\downarrow}|\nu_{\mathbf{k},0},\nu_{\mathbf{k},1}\rangle\\
&= \left[|u_{\mathbf{k}}|^2\nu_{\mathbf{k},0} + |v_{\mathbf{k}}|^2(1-\nu_{\mathbf{k},1})\right]\left[|v_{\mathbf{k}}|^2(1-\nu_{\mathbf{k},0}) + |u_{\mathbf{k}}|^2\nu_{\mathbf{k},1}\right]\\
&\quad + |u_{\mathbf{k}}|^2|v_{\mathbf{k}}|^2\left[(1-\nu_{\mathbf{k},1})(1-\nu_{\mathbf{k},0}) + \nu_{\mathbf{k},0}\nu_{\mathbf{k},1}\right].
\end{aligned} \qquad (E.19)$$

Finally, combining Eqs. (E.17), (E.19) into Eq. (E.14) for the CGF gives

$$\begin{aligned}
\langle e^{i\sum_{\mathbf{k}\sigma}\hat{n}_{\mathbf{k}\sigma}\chi}\rangle &= \frac{1}{Z}\prod_{\mathbf{k}}\Big[(1 + 2|v_{\mathbf{k}}|^2(e^{i\chi}-1) + |v_{\mathbf{k}}|^2(|v_{\mathbf{k}}|^2 + |u_{\mathbf{k}}|^2)(e^{i\chi}-1)^2)\\
&\qquad\qquad + 2(1 + (|u_{\mathbf{k}}|^2 + |v_{\mathbf{k}}|^2)(e^{i\chi}-1))e^{-\beta E_{\mathbf{k}}}\\
&\qquad\qquad + (1 + 2|u_{\mathbf{k}}|^2(e^{i\chi}-1) + |u_{\mathbf{k}}|^2(|u_{\mathbf{k}}|^2 + |v_{\mathbf{k}}|^2)(e^{i\chi}-1)^2)e^{-2\beta E_{\mathbf{k}}}\Big]\\
&= \frac{1}{Z}\prod_{\mathbf{k}}\Big[(1 + 2|v_{\mathbf{k}}|^2(e^{i\chi}-1) + |v_{\mathbf{k}}|^2(e^{i\chi}-1)^2)\\
&\qquad\qquad + 2(1 + (e^{i\chi}-1))e^{-\beta E_{\mathbf{k}}}\\
&\qquad\qquad + (1 + 2|u_{\mathbf{k}}|^2(e^{i\chi}-1) + |u_{\mathbf{k}}|^2(e^{i\chi}-1)^2)e^{-2\beta E_{\mathbf{k}}}\Big],
\end{aligned}$$
$$(E.20)$$

where the first line is the result for $(\nu_{\mathbf{k},0},\nu_{\mathbf{k},1}) = (0,0)$, the second line for $(\nu_{\mathbf{k},0},\nu_{\mathbf{k},1}) = (0,1)$ and $(\nu_{\mathbf{k},0},\nu_{\mathbf{k},1}) = (1,0)$, and the third line for $(\nu_{\mathbf{k},0},\nu_{\mathbf{k},1}) = (1,1)$. Grouping the terms by powers of χ, using $(e^{i\chi}-1)^2 = (e^{2i\chi}-1) - 2(e^{i\chi}-1)$ leads to

$$\begin{aligned}
\langle e^{i\sum_{\mathbf{k}\sigma}\hat{n}_{\mathbf{k}\sigma}\chi}\rangle = \frac{1}{Z}\prod_{\mathbf{k}}\Big[&1 + 2e^{-\beta E_{\mathbf{k}}} + e^{-2\beta E_{\mathbf{k}}} + 2e^{-\beta E_{\mathbf{k}}}(e^{i\chi}-1)\\
&+ (|v_{\mathbf{k}}|^2 + |u_{\mathbf{k}}|^2 e^{-2\beta E_{\mathbf{k}}})(e^{2i\chi}-1)\Big].
\end{aligned} \qquad (E.21)$$

Finally, using $Z = 1 + 2e^{-\beta E_{\mathbf{k}}} + e^{-2\beta E_{\mathbf{k}}}$ and $f_+(E_{\mathbf{k}}) = 1/(e^{\beta E_{\mathbf{k}}} + 1)$ we obtain

$$
\begin{aligned}
\langle e^{i \sum_{\mathbf{k}\sigma} \hat{n}_{\mathbf{k}\sigma}\chi} \rangle = \prod_{\mathbf{k}} \{\ & 1 + 2f_+(E_{\mathbf{k}})(1 - f_+(E_{\mathbf{k}}))(e^{i\chi} - 1) \\
& + |v_{\mathbf{k}}|^2 (1 - 2f_+(E_{\mathbf{k}})(1 - f_+(E_{\mathbf{k}})) - f_+(E_{\mathbf{k}})^2)(e^{2i\chi} - 1) \\
& + |u_{\mathbf{k}}|^2 f_+(E_{\mathbf{k}})^2 (e^{2i\chi} - 1)\ \} \\
= \prod_{\mathbf{k}} \{ & 1 + 2f_+(E_{\mathbf{k}})(1 - f_+(E_{\mathbf{k}}))(e^{i\chi} - 1) \\
& + |v_{\mathbf{k}}|^2 (1 - f_+(E_{\mathbf{k}}))^2 (e^{2i\chi} - 1) + |u_{\mathbf{k}}|^2 f_+(E_{\mathbf{k}})^2 (e^{2i\chi} - 1) \} \ .
\end{aligned}
\tag{E.22}
$$

In Eq. (E.22), the relations

$$
f_+(E_{\mathbf{k}})(1 - f_+(E_{\mathbf{k}})) = \frac{e^{-\beta E_{\mathbf{k}}}}{Z} \, , \qquad f_+(E_{\mathbf{k}})^2 = \frac{e^{-2\beta E_{\mathbf{k}}}}{Z} \, ,
\tag{E.23}
$$

and

$$
1 - 2f_+(E_{\mathbf{k}})(1 - f_+(E_{\mathbf{k}})) - f_+(E_{\mathbf{k}})^2 = \frac{1}{Z} \, ,
\tag{E.24}
$$

were used. This leads to the final result for finite-temperature CGF in the BCS limit

$$
\begin{aligned}
S(\chi) = -\sum_{\mathbf{k}} \log [\ & 1 + 2f_+(E_{\mathbf{k}})(1 - f_+(E_{\mathbf{k}}))(e^{i\chi} - 1) \\
& + |v_{\mathbf{k}}|^2 (1 - f_+(E_{\mathbf{k}}))^2 (e^{2i\chi} - 1) + |u_{\mathbf{k}}|^2 f_+(E_{\mathbf{k}})^2 (e^{2i\chi} - 1)\ ] \ .
\end{aligned}
\tag{E.25}
$$

Appendix F

Self-consistency equations

F.1   Self-consistency equations in 2D

The two-dimensional case is particularly interesting, as analytical expressions for the self-consistency equations, Eq. (4.17)

$$\Delta = -V \sum_{\mathbf{k}} v_{\mathbf{k}} u_{\mathbf{k}} \,, \tag{F.1}$$

and Eq. (4.16)

$$\bar{N} = \sum_{\mathbf{k},\sigma} |v_{\mathbf{k}}|^2 \,, \tag{F.2}$$

can be derived. In the first step, the sums in the self-consistency equation are replaced by integrals over the energy. The two-dimensional case has a a constant density of states $N(\epsilon) = m/2\pi\hbar^2$, which will facilitate the calculation of all integrals. Renormalizing the coupling constant V in the gap equation (F.1) and taking the low energy limit leads to [152]

$$\frac{1}{\tau_0(2E)} = \frac{m}{4\pi\hbar^2} \int_0^\infty d\epsilon \left(\frac{1}{\epsilon - E - i\eta} - \frac{1}{\sqrt{(\epsilon - \mu)^2 + \Delta^2}} \right) \,, \tag{F.3}$$

Equation F.3 represents the gap equation in terms of the two-particle s-wave T-matrix, τ_0, in the low-energy limit. In two dimensions, $\tau_0(E)$ is related to the s-wave scattering phase shift δ_0 by

$$\frac{1}{\tau_0(E)} = \frac{m}{4\hbar^2} \left(-\cot\left(\delta_0(E)\right) + i \right) \tag{F.4}$$

where

$$\cot\left(\delta_0(E)\right) = \frac{1}{\pi} \log(E/E_B) + \mathcal{O}(E/\epsilon_R) \tag{F.5}$$

is the low-energy s-wave scattering phase shift [152, 205]. Here, E_B can be identified as the energy of the bound state. The energy ϵ_R is given as $\epsilon_R = \hbar^2/2mR^2$, where we defined the range of attraction of the scattering potential to be R (assuming

$k_F R \ll 1$). Using Eq. (F.4) and Eq. (F.5) in the two-dimensional gap equation (F.3), we obtain

$$
\begin{aligned}
-\log(2E/E_B) + i\pi &= \int_0^\infty d\epsilon \left(\frac{1}{\epsilon - E - i\eta} - \frac{1}{\sqrt{(\epsilon - \mu)^2 + \Delta^2}} \right) \\
&= -\log\left(-2E\right) + \log\left(\sqrt{\mu^2 + \Delta^2} - \mu\right) \\
&= i\pi - \log\left(2E\right) + \log\left(\sqrt{\mu^2 + \Delta^2} - \mu\right).
\end{aligned}
\tag{F.6}
$$

The gap equation gives, thus, a relation between the bound-state energy E_B and the parameters μ and Δ

$$
E_B = \sqrt{\mu^2 + \Delta^2} - \mu.
\tag{F.7}
$$

Equation (F.7) is the first self-consistency equation. The second equation, required in order to determine Δ and μ, is given by the particle-number conservation. The particle-number density can be computed straight forward from Eq. (F.2)

$$
\begin{aligned}
\bar{n} = \frac{2}{V_{2D}} \sum_{\mathbf{k}} |v_{\mathbf{k}}|^2 &= \frac{m}{\pi\hbar^2} \int_0^\infty d\epsilon \, \frac{1}{2} \left(1 - \frac{(\epsilon - \mu)}{\sqrt{(\epsilon - \mu)^2 + \Delta^2}} \right) \\
&= \frac{m}{2\pi\hbar^2} \left(\sqrt{\mu^2 + \Delta^2} + \mu \right).
\end{aligned}
\tag{F.8}
$$

Expressing the average particle-number density in terms of the Fermi energy ϵ_F leads to

$$
\bar{n} = \frac{m}{\pi\hbar^2} \int_0^{\epsilon_F} d\epsilon \quad = \frac{m\epsilon_F}{\pi\hbar^2},
\tag{F.9}
$$

and we finally obtain the second self-consistency equation

$$
2\epsilon_F = \sqrt{\mu^2 + \Delta^2} + \mu.
\tag{F.10}
$$

F.2 Self-consistency equations in 3D

Analogous to the two-dimensional case, we renormalize the gap equation, Eq. (4.17) and take the low-energy limit. This procedure leads to the analog of Eq. (F.3), but with the three-dimensional density of states on the right hand side. The difference to the two-dimensional case, apart from the three-dimensional density of states, enters in the three-dimensional expression for the T-matrix. In the low-energy limit [163] $\tau_0 = 4\pi a \hbar^2/m$, where a is the s-wave scattering length. Following Leggett [149], we write the 3D-gap equation in the form

$$
\xi = \frac{1}{\pi} \int_0^\infty d\tilde{\epsilon} \, \tilde{\epsilon}^{\frac{1}{2}} \left(\frac{1}{\tilde{\epsilon}} - \frac{1}{\sqrt{(\tilde{\epsilon} - \tilde{\mu})^2 + \tilde{\Delta}^2}} \right),
\tag{F.11}
$$

where all quantities with a tilde are normalized to ϵ_F and $\xi = 1/k_F a$. The Fermi energy can be expressed in terms of the particle-number density, $\bar{n}$, using the particle-number conservation

$$
\bar{n} = \frac{(2m)^{3/2}}{2\pi^2\hbar^3} \int_0^\infty d\epsilon \, \sqrt{\epsilon} \, |v_k|^2, \qquad \text{and} \quad k_F = (3\pi^2 n)^{2/3}.
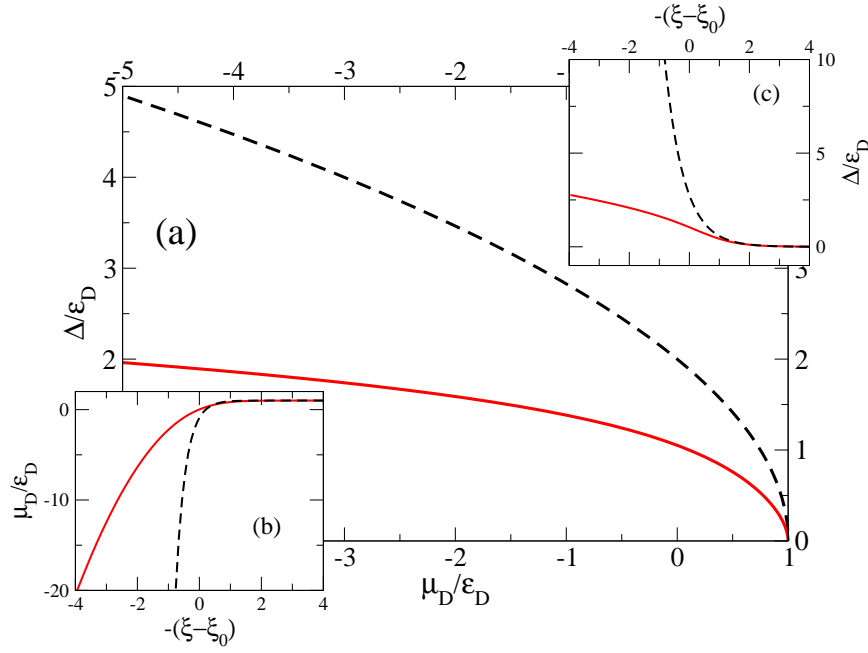\tag{F.12}
$$

Figure F.1: Results from the self-consistency equations (F.11) and (F.13) in 3D (Eq. (F.18) and Eq. (F.21) in quasi-2D) for Δ and μ. The dashed-black line corresponds to the quasi-2D case and the solid-red line corresponds to the 3D case. The quasi-2D results are calculated for a box potential. All quantities are normalized with respect to the energy ϵ_D, where the subscript D denotes the dimension of the system. The energy ϵ_D is the Fermi energy, taken with respect to the transverse ground state $\epsilon_{D=2} = \epsilon_F - \epsilon_0$ in the quasi-2D case and $\epsilon_{D=3} = \epsilon_F$ in the 3D case. *(a):* Δ/ϵ_D as a function of μ_D/ϵ_D. In 3D is $\mu_{D=3} = \mu$. In quasi-2D is μ_D defined with respect to the transverse ground state energy: $\mu_{D=2} = \mu - \epsilon_0$. *(b,c):* Figures (b) and (c) show μ_D/ϵ_F and Δ/ϵ_F plotted over $-(\xi - \xi_0)$, respectively. Here, $\xi = 1/k_D a$ and $\xi_0 \equiv \xi(\mu_D = 0)$. Note that $k_{D=3} = k_F$ in three dimensions. In quasi-two dimensions is $k_{D=2} = \pi/\ell_0$.

Here, k_F is the Fermi wavelength given by $\epsilon_F = \hbar^2 k_F^2/2m$. Thus, the second self-consistency equation in three dimensions, derived from Eq. (F.12), is given by

$$\frac{4}{3} = \int_0^\infty d\tilde{\epsilon} \, \sqrt{\tilde{\epsilon}} \left(1 - \frac{(\tilde{\epsilon} - \mu)}{\sqrt{(\tilde{\epsilon} - \mu)^2 + \tilde{\Delta}^2}} \right) . \tag{F.13}$$

F.3 Self-consistency equations in quasi-2D

The quasi-two dimensional case (quasi-2D) is based on a three-dimensional system, however, the system is frozen out in one direction. This can be achieved in a harmonic trap with very different trapping frequencies: $\omega_z \gg \omega_x = \omega_y$. Alternatively, a box potential with side lengths $\ell_z \ll \ell_x = \ell_y$ can be chosen.

In the following, we will assume a box potential. Again, we consider the gap equation, but this time we go one step back and write the three-dimensional gap equation (F.11) in terms of a sum over the wavevectors k [149]

$$\frac{m}{2\pi\hbar^2 a} = \frac{1}{V} \sum_{k_x,k_y,k_z} \left(\frac{1}{\epsilon_k} - \frac{1}{\sqrt{(\epsilon_k - \mu)^2 + \Delta^2}} \right) . \tag{F.14}$$

Choosing the $\hat{z}$-dimension to be frozen out, the three-dimensional sum reduces to a two-dimensional sum. In contrast to the pure two-dimensional situation, the ground-state energy ϵ_0 has to be taken into account

$$\epsilon_k = \epsilon_0 + \hbar^2(k_x^2 + k_y^2)/2m . \tag{F.15}$$

Hence, rewriting the sum over k_x and k_y into an integral over energy, the gap equation becomes

$$\frac{m}{2\pi\hbar^2 a} = \frac{m}{2\pi\ell_0\hbar^2} \int_{\tilde{\epsilon}_0}^{\infty} d\tilde{\epsilon} \left(\frac{1}{\tilde{\epsilon}} - \frac{1}{\sqrt{(\tilde{\epsilon} - \tilde{\mu})^2 + \tilde{\Delta}^2}} \right) , \tag{F.16}$$

where $\ell_0 = \ell_z$ is the size of the ground state[1]. All quantities with a tilde are normalized to $(\epsilon_F - \epsilon_0)$. On the one hand, studying a quasi-two dimensional system means that the kinetic energy in the quasi-free directions (here $\hat{x}$ and $\hat{y}$) is smaller than the level spacing of the frozen-out direction (here $\hat{z}$). This leads to the restriction $\epsilon_F - \epsilon_0 \ll \epsilon_0$. On the other hand, ϵ_0 is the lower boundary for ϵ_F. In summary, we have the condition $\epsilon_F = \epsilon_0 + \delta$ with $0 \le \delta/\epsilon_0 \ll 1$. Hence, the Fermi wavevector can be approximated for the box potential as [2] $k_F = \sqrt{2m\epsilon_0}/\hbar + k_\delta \approx \sqrt{2m\epsilon_0}/\hbar = \pi/\ell_0$. Here, the ground-state energy for the box potential $\epsilon_0 = \hbar^2\pi^2/2m\ell_z^2$ has been used. Eventually, defining the quantity

$$\xi_{2D} \equiv \frac{1}{\pi a/\ell_0} \approx \frac{1}{k_F a} , \tag{F.17}$$

the quasi-two dimensional gap equation reads

$$\pi\xi_{2D} = \int_{\tilde{\epsilon}_0}^{\infty} d\tilde{\epsilon} \left(\frac{1}{\tilde{\epsilon}} + \frac{1}{\sqrt{(\tilde{\epsilon} - \tilde{\mu})^2 + \tilde{\Delta}^2}} \right) \tag{F.18}$$

$$= -\log(2\tilde{\epsilon}_0) + \log\left((\tilde{\epsilon}_0 - \tilde{\mu}) + \sqrt{(\tilde{\epsilon}_0 - \tilde{\mu})^2 + \tilde{\Delta}^2}\right) .$$

In analogy to the two-dimensional case we find for the number conservation

$$\langle n \rangle = \frac{1}{\ell_0}\frac{m}{\pi\hbar^2} \int_{\epsilon_0}^{\infty} d\epsilon |v_k|^2 = \frac{m}{2\pi\ell_0\hbar^2} \left(\mu - \epsilon_0 + \sqrt{(\epsilon_0 - \mu)^2 + \Delta^2} \right) . \tag{F.19}$$

---

[1]For the harmonic-oscillator potential $\ell_0 = \sqrt{\hbar/m\omega_z}$.

[2]Assuming a harmonic-oscillator trapping potential, the expression for ϵ_F in terms of wavevectors is given by $k_F = \ell_0^{-1} + k_\delta \approx \ell_0^{-1}$, with $\ell_0 = \sqrt{\hbar/m\omega_z}$. This shows that the Fermi wavevector can be approximated to first order by the inverse of the harmonic-oscillator length.

Using the relation between the average number density $\langle n \rangle$ and the Fermi energy

$$\langle n \rangle = \frac{1}{\ell_0}\frac{m}{\pi\hbar^2}\int_{\epsilon_0}^{\epsilon_F} d\epsilon = \frac{1}{\ell_0}\frac{m}{\pi\hbar^2}(\epsilon_F - \epsilon_0) \tag{F.20}$$

leads to the final expression

$$2(\epsilon_F - \epsilon_0) = (\mu - \epsilon_0) + \sqrt{(\epsilon_0 - \mu)^2 + \Delta^2}\,. \tag{F.21}$$

Normalizing all energies to the Fermi energy measured from the ground-state energy, $\epsilon_F - \epsilon_0$, Eq. (F.21) transforms into

$$\tilde{\Delta} = 2\sqrt{1 + (\tilde{\epsilon}_0 - \tilde{\mu})}\,. \tag{F.22}$$

Finally, the order parameter $\tilde{\Delta}$ and the chemical potential $\tilde{\mu}$ can be explicitly expressed as a function of ξ_{2D}

$$(\tilde{\mu} - \tilde{\epsilon}_0) = 1 - \tilde{\epsilon}_0\, e^{\pi\xi_{2D}}\,, \qquad\qquad \tilde{\Delta} = 2\sqrt{\tilde{\epsilon}_0}e^{\pi\xi_{2D}/2}\,. \tag{F.23}$$

The behavior of Δ and μ for the quasi-two dimensional case is shown in Fig. F.1.

Bibliography

[1] S. Chu, Rev. Mod. Phys. **70**, 685 (1998).

[2] C. N. Cohen-Tannoudji, Rev. Mod. Phys. **70**, 707 (1998).

[3] W. D. Phillips, Rev. Mod. Phys. **70**, 721 (1998).

[4] H. F. Hess, Phys. Rev. B **34**, 3476 (1986).

[5] M. Anderson, J. Ensher, M. Matthews, C. Wieman, and E. Cornell, Science **269**, 198 (1995).

[6] K. B. Davis, M.-O. Mewes, M. R. Andrews, N. J. van Druten, D. S. Durfee, D. M. Kurn, and W. Ketterle, Phys. Rev. Lett. **75**, 3969 (1995).

[7] P. Treutlein, P. Hommelhoff, T. Steinmetz, T. W. Hänsch, and J. Reichel, Phys. Rev. Lett. **92**, 203005 (2004).

[8] S. Stringari, Phys. Rev. Lett. **86**, 4725 (2001).

[9] Y.-J.Wang, D. Z. Anderson, V. M. Bright, E. A. Cornell, Q. Diot, T. Kishimoto, M. Prentiss, R. A. Saravanan, S. R. Segal, and S. Wu, Phys. Rev. Lett. **94**, 090405 (2005).

[10] E. A. Hinds and I. A. Hughes, J. Phys. D **32**, R119 (1999).

[11] J. Reichel, Appl. Phys. B **75**, 469 (2002).

[12] R. Folman, P. Krüger, J. Schmiedmayer, J. Denschlag, and C. Henkel, Adv. At. Mol. Opt. Phys. **48**, 263 (2002).

[13] D. Cassettari, B. Hessmo, R. Folman, T. Maier, and J. Schmiedmayer, Phys. Rev. Lett. **85**, 5483 (2000).

[14] J. A. Sauer, M. D. Barret, and M. S. Chapman, Phys. Rev. Lett. **87**, 270401 (2001).

[15] G. Birkl, F. B. J. Buchkremer, R. Dumke, and W. Ertmer, Opt. Commun. **191**, 67 (2001).

[16] T. Calarcro, E. A. Hinds, D. Jaksch, J. Schmiedmayer, J. I. Cirac, and P. Zoller, Phys. Rev. A **61**, 022304 (2000).

[17] P. Horak, B. G. Klappauf, A. Haase, R. Folman, J. Schmiedmayer, P. Domokos, and E. A. Hinds, Phys. Rev. A **67**, 043806 (2003).

[18] P. Horak, J.-Y. Courtois, and G. Grynberg, Phys. Rev. A **58**, 3953 (1998).

[19] M. P. A. Fisher, P. B. Weichman, G. Grinstein, and D. S. Fisher, Phys. Rev. B **40**, 546 (1989).

[20] M. B. Dahan, E. Peik, J. Reichel, Y. Castin, and C. Salomon, Phys. Rev. Lett. **76**, 4508 (1996).

[21] M. Greiner, I. Bloch, O. Mandel, T. W. Hänsch, and T. Esslinger, Phys. Rev. Lett. **87**, 160405 (2001).

[22] M. Köhl, H. Moritz, T. Stöferle, K. Günter, and T. Esslinger, Phys. Rev. Lett. **94**, 080403 (2005).

[23] D. Jaksch, C. Bruder, J. I. Cirac, C. W. Gardiner, and P. Zoller, Phys. Rev. Lett. **81**, 3108 (1998).

[24] M. Greiner, O. Mandel, T. Esslinger, T. W. Hänsch, and I. Bloch, Nature **415**, 39 (2002).

[25] B. Paredes, A. Widera, V. Murg, O. Mandel, S. Fölling, I. Cirac, G. V. Shlyapnikov, T. W. Hänsch, and I. Bloch, Nature **429**, 277 (2004).

[26] H. Moritz, T. Stöferle, M. Köhl, and T. Esslinger, Phys. Rev. Lett. **91**, 250402 (2003).

[27] B. L. Tolra, K. M. O'Hara, J. H. Huckans, W. D. Phillips, S. L. Rolston, and J. V. Porto, Phys. Rev. Lett. **92**, 190401 (2004).

[28] M. Girardeau, J. Math. Phys. **1**, 516 (1960).

[29] E. H. Lieb and W. Liniger, Phys. Rev. **130**, 1605 (1963).

[30] W. Hofstetter, J. I. Cirac, P. Zoller, E. Demler, and M. D. Lukin, Phys. Rev. Lett. **89**, 220407 (2002).

[31] O. Mandel, M. Greiner, A. Widera, T. Rom, T. W. Hänsch, and I. Bloch, Nature **425**, 937 (2003).

[32] A. Widera, O. Mandel, M. Greiner, S. Kreim, T. W. Hänsch, and I. Bloch, Phys. Rev. Lett. **92**, 160406 (2004).

[33] D. Jaksch, H. J. Briegel, J. I. Cirac, C. W. Gardiner, and P. Zoller, Phys. Rev. Lett. **82**, 1975 (1999).

[34] G. K. Brennen, C. M. Caves, P. S. Jessen, and I. H. Deutsch, Phys. Rev. Lett. **82**, 1060 (1999).

[35] H. J. Briegel, T. Calarco, D. Jaksch, J. I. Cirac, and P. Zoller, J. Mod. Opt. **47**, 415 (2000).

[36] C. J. Pethick and H. Smith, *Bose-Einstein Condensation in Dilute Gases* (Cambridge University Press, 2002).

[37] K. Huang, *Statistical Mechanics, 2nd ed.* (John Wiley & Sons, New York, 1987).

[38] F. Dalfovo, S. Giorgini, L. P. Pitaevskii, and S. Stringari, Rev. Mod. Phys. **71**, 463 (1999).

[39] P. E. Sokol, *Bose-Einstein Condensation, edited by A. Griffin, D. W. Snoke, and S. Stringari* (Cambridge University Press, 1995).

[40] M. R. Andrews, C. G. Townsend, H.-J. Miesner, D. S. Durfee, D. M. Kurn, and W. Ketterle, Science **275**, 637 (1997).

[41] B. P. Anderson and M. A. Kasevich, Science **282**, 1686 (1998).

[42] D. S. Hall, M. R. Matthews, C. E. Wieman, and E. A. Cornell, Phys. Rev. Lett. **81**, 1543 (1998).

[43] M. Saba, T. A. Pasquini, C. Sanner, Y. Shin, W. Ketterle, and D. E. Pritchard, Science **307**, 1945 (2005).

[44] J. Denschlag, J. E. Simsarian, D. L. Feder, C. W. Clark, L. A. Collins, J. Cubizolles, L. Deng, E. W. Hagley, K. Helmerson, W. P. Reinhardt, *et al.*, Science **287**, 97 (2000).

[45] L. Khaykovich, F. Schreck, G. Ferrari, T. Bourdel, J. Cubizolles, L. D. Carr, Y. Castin, and C. Salomon, Science **296**, 1290 (2002).

[46] K. W. Madison, F. Chevy, W. Wohlleben, and J. Dalibard, Phys. Rev. Lett. **84**, 806 (2000).

[47] J. R. Abo-Shaeer, C. Raman, J. M. Vogels, and W. Ketterle, Science **292**, 476 (2001).

[48] Q. Chen, J. Stajic, S. Tan, and K. Levin, cond-mat/0404274 (2004).

[49] A. E. Leanhardt, A. P. Chikkatur, D. Kielpinski, Y. Shin, T. L. Gustavson, W. Ketterle, and D. E. Pritchard, Phys. Rev. Lett. **89**, 040401 (2002).

[50] A. E. Leanhardt, Y. Shin, A. P. Chikkatur, D. Kielpinski, W. Ketterle, and D. E. Pritchard, Phys. Rev. Lett. **90**, 100404 (2003).

[51] J. Fortágh, H. Ott, S. Kraft, A. Günther, and C. Zimmermann, Phys. Rev. A **66**, 041604R (2002).

[52] S. Kraft, A. Günther, H. Ott, D. Wharam, C. Zimmermann, and J. Fortágh, J. Phys. B **35**, 469 (2002).

[53] M. P. A. Jones, C. J. Vale, D. Sahagun, B. V. Hall, and E. A. Hinds, Phys. Rev. Lett. **91**, 080401 (2003).

[54] M. P. A. Jones, C. J. Vale, D. Sahagun, B. V. Hall, C. C. Eberlein, B. E. Sauer, K. Furusawa, D. Richardson, and E. A. Hinds, J. Phys. B. **37**, L15 (2004).

[55] C. J. Vale, B. Upcroft, M. J. Davis, N. R. Heckenberg, and H. Rubinsztein-Dunlop, J. Phys. B **37**, 2959 (2004).

[56] M. Greiner, O. Mandel, T. W. Hänsch, and I. Bloch, Nature **419**, 51 (2002).

[57] W. Zwerger, J. Opt. B: Quantum Semiclass. Opt. **5**, S9 (2003).

[58] V. A. Kashurnikov, N. V. Prokof'ev, and B. V. Svistunov, Phys. Rev. A **66**, 031601R (2002).

[59] R. Roth and K. Burnett, Phys. Rev. A **67**, 031602R (2003).

[60] C. Schroll, F. Marquardt, and C. Bruder, Phys. Rev. A **70**, 053609 (2004).

[61] F. Gerbier, A. Widera, S. Fölling, O. Mandel, T. Gericke, , and I. Bloch, cond-mat/0503452 (2005).

[62] M. Greiner, C. A. Regal, J. T. Stewart, and D. S. Jin, Phys. Rev. Lett. **94**, 110401 (2005).

[63] S. Fölling, F. Gerbier, A. Widera, O. Mandel, T. Gericke, and I. Bloch, Nature **434**, 481 (2005).

[64] E. Altman, E. Demler, and M. D. Lukin, Phys. Rev. A **70**, 013603 (2004).

[65] W. Belzig, C. Schroll, and C. Bruder, cond-mat/0412269 (2004).

[66] C. Henkel and S. Pötting, Appl. Phys. B **72**, 73 (2001).

[67] J. Reichel, W. Hänsel, and T. W. Hänsch, Phys. Rev. Lett. **83**, 3398 (1999).

[68] J. Denschlag, D. Cassetari, and J. Schmiedmayer, Phys. Rev. Lett. **82**, 2014 (1998).

[69] R. Folman, P. Krüger, D. Cassettari, B. Hessmo, T. Maier, and J. Schmiedmayer, Phys. Rev. Lett. **84**, 4749 (2000).

[70] D. Müller, D. Z. Anderson, R. J. Grow, P. D. D. Schwindt, and E. A. Cornell, Phys. Rev. Lett. **83**, 5194 (1999).

[71] X. Luo, P. Krüger, K. Brugger, S. Wildermuth, H. Gimpel, M. W. Klein, S. Groth, R. Folman, I. Bar-Joseph, and J. Schmiedmayer, Opt. Lett. **29**, 2145 (2004).

[72] W. Hänsel, J. Reichel, P. Hommelhoff, and T. W. Hänsch, Phys. Rev. Lett. **86**, 608 (2001).

[73] H. Ott, J. Fortagh, G. Schlotterbeck, A. Grossmann, and C. Zimmermann, Phys. Rev. Lett. **87**, 230401 (2001).

[74] W. Hänsel, P. Hommelhoff, T. W. Hänsch, and J. Reichel, Nature **413**, 498 (2001).

[75] S. Schneider, A. Kasper, C. vom Hagen, M. Bartenstein, B. Engeser, T. Schumm, I. Bar-Joseph, R. Folman, L. Feenstra, and J. Schmiedmayer, Phys. Rev. A **67**, 023612 (2003).

[76] W. Hänsel, J. Reichel, P. Hommelhoff, and T. W. Hänsch, Phys. Rev. A **64**, 063607 (2001).

[77] E. A. Hinds, C. J. Vale, and M. G. Boshier, Phys. Rev. Lett. **86**, 1462 (2001).

[78] E. Andersson, T. Calarco, R. Folman, M. Andersson, B. Hessmo, and J. Schmiedmayer, Phys. Rev. Lett. **88**, 100401 (2002).

[79] T. J. Davis, J. Opt. B **1**, 408 (1999).

[80] I. Barb, R. Gerritsma, Y. T. Xing, J. B. Goedkoop, and R. J. C. Spreeuw, physics/0501109 (2005).

[81] C. D. J. Sinclair, J. A. Retter, E. A. Curtis, B. V. Hall, I. L. Garcia, S. Eriksson, B. E. Sauer, and E. A. Hinds, physics/0502073 (2005).

[82] C. D. J. Sinclair, E. A. Curtis, I. L. Garcia, J. A. Retter, B. V. Hall, S. Eriksson, B. E. Sauer, and E. A. Hinds, cond-mat/0503619 (2005).

[83] T. M. Roach, H. Abele, M. G. Boshier, H. L. Grossman, K. P. Zetie, and E. A. Hinds, Phys. Rev. Lett. **75**, 629 (1995).

[84] C. V. Saba, P. A. Barton, M. G. Boshier, I. G. Hughes, P. Rosenbusch, B. E. Sauer, and E. A. Hinds, Phys. Rev. Lett. **82**, 468 (1999).

[85] P. Rosenbusch, B. V. Hall, I. G. Hughes, C. V. Saba, and E. A. Hinds, Appl. Phys. B **70**, 709 (2000).

[86] S. Eriksson, F. Ramirez-Martinez, E. A. Curtis, B. E. Sauer, P. W. Nutter, E. W. Hill, and E. A. Hinds, Appl. Phys. B **79**, 811 (2004).

[87] P. Krüger, X. Luo, M. Klein, K. Brugger, A. Haase, S.Wildermuth, S. Groth, I. Bar-Joseph, R. Folman, and J. Schmiedmayer, Phys. Rev. Lett. **91**, 233201 (2003).

[88] J. Schmiedmayer, Phys. Rev. A **52**, R13 (1995).

[89] J. Fortágh, A. Grossmann, C. Zimmermann, and T. W. Hänsch, Phys. Rev. Lett. **81**, 5310 (1998).

[90] A. Haase, D. Cassettari, B. Hessmo, and J. Schmiedmayer, Phys. Rev. A **64**, 043405 (2001).

[91] D. Pritchard, Phys. Rev. Lett. **51**, 1336 (1983).

[92] E. Andersson, M. T. Fontenelle, and S. Stenholm, Phys. Rev A **59**, 3841 (1999).

[93] J. H. Thywissen, M. Olshanii, G. Zabow, M. Drndić, K. S. Johnson, R. M. Westervelt, and M. Prentiss, Eur. Phys. J. D **7**, 361 (1999).

[94] N. H. Dekker, C. S. Lee, V. Lorent, J. Thywissen, S. P. Smith, M. Drndić, R. M. Westervelt, and M. Prentiss, Phys. Rev. Lett. **84**, 1124 (2000).

[95] Y. Lin, I. Teper, C. Chin, and V. Vuletiċ, Phys. Rev. Lett. **92**, 050404 (2004).

[96] C. Henkel, P. Krüger, R. Folman, and J. Schmiedmayer, Appl. Phys. B **76**, 173 (2003).

[97] C. Schroll, W. Belzig, and C. Bruder, Phys. Rev. A **68**, 043618 (2003).

[98] D. M. Harber, J. M. McGuirk, J. M. Obrecht, and E. A. Cornell, J. Low. Temp. Phys. **133**, 229 (2003).

[99] C. Henkel, S. Pötting, and M. Wilkens, Appl. Phys. B **69**, 379 (1999).

[100] P. K. Rekdal, S. Scheel, P. L. Knight, and E. A. Hinds, Phys. Rev. A **70**, 013811 (2004).

[101] S. Scheel, P. K. Rekdal, P. L. Knight, and E. A. Hinds, quant-ph/0501149 (2005).

[102] D.-W. Wang, M. D. Lukin, and E. Demler, Phys. Rev. Lett. **92**, 076802 (2004).

[103] J. Estève, C. Aussibal, T.Schumm, C. Figl, D. Mailly, I. Bouchoule, C. I. West-brook, and A. Aspect, Phys. Rev. A **70**, 043629 (2004).

[104] C. Henkel and S. A. Gardiner, Phys. Rev. A **69**, 043602 (2004).

[105] S. Groth, P. Krüger, S. Wildermuth, R. Folman, T. Fernholz, D. Mahalu, I. Bar-Joseph, and J. Schmiedmayer, cond-mat/0404141 (2004).

[106] M. J. M. de Jong and C. W. J. Beenakker, *Mesoscopic Electron Transport, NATO ASI Series E, Vol.* **345***, p225, edited by L. L. Sohn, L. P. Kouwenhoven, and G. Schön,* (Kluwer Academic Publishing, Dordrecht, 1997).

[107] Y. M. Blanter and M. Büttiker, Phys. Rep. **336**, 1 (2000).

[108] K. E. Nagaev, Phys. Rev. B **52**, 4740 (1995).

[109] V. I. Kozub and A. M. Rudin, Phys. Rev. B **52**, 7853 (1995).

[110] C. W. Gardiner, *Handbook of Stochastic Methods* (Springer, Berlin, 1998).

[111] N. G. van Kampen, *Stochastic Processes in Physics and Chemistry* (North-Holland, Amsterdam, 1990).

[112] J. J. Sakurai, *Modern Quantum Mechanics* (Addison-Wesley, 1995).

[113] C. Cohen-Tannoudji, B. Diu, and F. Laloë, *Quantum Mechanics* (Hermann, Paris, 1977).

[114] L. J. Geerligs, M. Peters, L. E. M. de Groot, A. Verbruggen, and J. E. Mooij, Phys. Rev. Lett. **63**, 326 (1989).

[115] H. S. van der Zant, F. C. Fritschy, W. J. Elion, L. J. Geerligs, and J. E. Mooij, Phys. Rev. Lett. **69**, 2971 (1992).

[116] A. van Oudenaarden and J. E. Mooij, Phys. Rev. Lett. **76**, 4947 (1996).

[117] R. Fazio and H. van der Zant, Physics Reports **355**, 235 (2001).

[118] C. Cohen-Tannoudji, J. Dupont-Roc, and G. Grynberg, *Atom Photon Interactions* (Wiley-Interscience publication, 1992).

[119] C. J. Pethick and H. Smith, *Bose-Einstein condensation in dilute gases* (Cambridge University Press, 2002).

[120] F. D. M. Haldane, Phys. Lett. **80A**, 281 (1980).

[121] F. D. M. Haldane, Phys. Lett. **81A**, 545 (1981).

[122] T. C. Choy and F. D. M. Haldane, Phys. Lett. **90A**, 83 (1982).

[123] W. Krauth, Phys. Rev. B **44**, 9772 (1991).

[124] J. K. Freericks and H. Monien, Phys. Rev. B **53**, 2691 (1996).

[125] N. Elstner and H. Monien, cond-mat/9905367 (1999).

[126] A. M. Rey, K. Burnett, R. Roth, M. Edwards, C. J. Williams, and C. W. Clark, J. Phys. B **36**, 825 (2003).

[127] D. van Oosten, P. van der Straten, and H. T. C. Stoof, Phys. Rev. A **63**, 053601 (2001).

[128] T. D. Kühner and H. Monien, Phys. Rev. B **58**, R14741 (1998).

[129] S. Rapsch, U. Schollwöck, and W. Zwerger, Europhys. Lett. **46**, 559 (1999).

[130] C. Kollath, U. Schollwöck, J. von Delft, and W. Zwerger, Phys. Rev. A **69**, 031601 (2004).

[131] R. T. Scalettar, G. G. Batrouni, and G. T. Zimanyi, Phys. Rev. Lett. **66**, 3144 (1991).

[132] G. G. Batrouni, R. T. Scalettar, and G. T. Zimanyi, Phys. Rev. Lett. **65**, 1765 (1990).

[133] G. G. Batrouni and R. T. Scalettar, Phys. Rev. B **46**, 9051 (1992).

[134] W. Krauth and N. Trivedi, Europhys. Lett. **14**, 627 (1991).

[135] W. Krauth, N. Trivedi, and D. Ceperley, Phys. Rev. Lett. **67**, 2307 (1991).

[136] J. Kisker and H. Rieger, Phys. Rev. B **55**, R11981 (1996).

[137] G. G. Batrouni, V. Rousseau, R. T. Scalettar, M. Rigol, A. Muramatsu, P. J. H. Denteneer, and M. Troyer, Phys. Rev. Lett. **89**, 117203 (2002).

[138] S. Bergkvist, P. Henelius, and A. Rosengren, Phys. Rev. A **70**, 053601 (2004).

[139] S. Wessel, F. Alet, M. Troyer, and G. G. Batrouni, Phys. Rev. A **70**, 053615 (2004).

[140] R. Roth and K. Burnett, Phys. Rev. A **68**, 023604 (2003).

[141] D. S. Rokhsar and B. G. Kotliar, Phys. Rev. B **44**, 10328 (1991).

[142] C. Kollath, U. Schollwöck, J. von Delft, and W. Zwerger, cond-mat/0411403 (2004).

[143] S. R. Clark and D. Jaksch, Phys. Rev. A **70**, 043612 (2004).

[144] K. Sheshadri, H. R. Krishnamurthy, R. Pit, , and T. V. Ramakrishnan, Europhys. Lett. **22**, 257 (1993).

[145] W. H. Press, S. A. Teukolsky, W. T. Vetterling, and B. P. Flannery, *Numerical Recipies in C, 2nd Ed.* (Cambridge University Press, 1999).

[146] P. Pedri, L. Pitaevskii, and S. Stringari, Phys. Rev. Lett. **87**, 220401 (2001).

[147] J. Bardeen, L. N. Cooper, and J. R. Schrieffer, Phys. Rev. **108**, 1175 (1957).

[148] D. M. Eagles, Phys. Rev. **186**, 456 (1969).

[149] A. J. Leggett, *Modern Trends in the Theory of Condensed Matter* (edited by A. Pedalski and J. Przystawa, Springer, Berlin, 1980).

[150] P. Nozières and S. Schmitt-Rink, J. Low Temp. Phys. **59**, 195 (1985).

[151] M. Randeria, *Bose-Einstein Condensation, p355* (edited by A. Griffin, D. W. Snoke, and S. Stringari, Cambridge University Press, 1995).

[152] M. Randeria, J.-M. Duan, , and L. Y. Shieh, Phys. Rev. B **41**, 327 (1990).

[153] S. Stintzing and W. Zwerger, Phys. Rev. B **56**, 9004 (1997).

[154] Y. J. Uemura, Physica C **194**, 282 (1997).

[155] G. Deutscher, Nature **397**, 410 (1999).

[156] S. Jochim, M. Bartenstein, A. Altmeyer, G. Hendl, S. R. C. Chin, J. H. Denschlag, and R. Grimm, Science **302**, 2101 (2003).

[157] M. Greiner, C. A. Regal, and D. S. Jin, Nature **426**, 537 (2003).

[158] M. W. Zwierlein, C. A. Stan, C. H. Schunck, S. M. F. Paupach, A. J. Kerman, and W. Ketterle, Phys. Rev. Lett. **92**, 120403 (2004).

[159] M. W. Zwierlein, C. A. Stan, C. H. Schunck, S. M. F. Raupach, S. Gupta, Z. Hadzibabic, and W. Ketterle, Phys. Rev. Lett. **91**, 250401 (2003).

[160] C. A. Regal, M. Greiner, and D. S. Jin, Phys. Rev. Lett. **92**, 040403 (2004).

[161] E. Timmermans, P. Tommasini, M. Hussein, and A. Kerman, Phys. Rep. **315**, 199 (1999).

[162] S. J. J. M. F. Kokkelmans, J. N. Milstein, M. L. Chiofalo, R. Walser, and M. J. Holland, Phys. Rev. A, **65**, 053617 (2002).

[163] R. A. Duine and H. T. C. Stoof, Phys. Rep. **396**, 115 (2004).

[164] L. Pitaevskii and S. Stringari, *Bose-Einstein Condensation* (Oxford University Press, 2003).

[165] S. Inouye, M. R. Andrews, J. Stenger, H.-J. Miesner, D. M. Stamper-Kurn, and W. Ketterle, Nature **392**, 151 (1998).

[166] P. Courteille, R. S. Freeland, D. J. Heinzen, F. A. van Abeelen, and B. J. Verhaar, Phys. Rev. Lett. **81**, 69 (1998).

[167] J. L. Roberts, N. R. Claussen, J. P. Burke, C. H. Greene, E. A. Cornell, and C. A. Wieman, Phys. Rev. Lett. **81**, 5109 (1998).

[168] S. L. Cornish, N. R. Claussen, J. L. Roberts, E. A. Cornell, and C. A. Wieman, Phys. Rev. Lett. **85**, 1795 (2000).

[169] T. Volz, S. Dürr, S. Ernst, A. Marte, and G. Rempe, Phys. Rev. A **68**, 010702R (2003).

[170] C. Chin, V. Vuletic, A. J. Kerman, and S. Chu, Phys. Rev. Lett. **85**, 2717 (2000).

[171] J. Werner, A. Griesmaier, S. Hensler, J. Stuhler, T. Pfau, A. Simoni, and E. Tiesinga, cond-mat/0412049 (2004).

[172] K. M. O'Hara, S. L. Hemmer, M. E. Gehm, S. R. Granade, and J. E. Thomas, Science **298**, 2179 (2002).

[173] T. Loftus, C. A. Regal, C. Ticknor, J. L. Bohn, and D. S. Jin, Phys. Rev. Lett. **88**, 173201 (2002).

[174] M. H. Szymanska, K. Goral, T. Köhler, and K. Burnett, cond-mat/050172 (2005).

[175] S. Simonucci, P. Pieri, and G. C. Strinati, Eur. Phys. Lett **69**, 713 (2005).

[176] A. Recati, J. N. Fuchs, and W. Zwerger, Phys. Rev. A **71**, 033630 (2005).

[177] D. S. Petrov, Phys. Rev. Lett. **93**, 143201 (2004).

[178] C. Chin, M. Bartenstein, A. Altmeyer, S. Riedl, S. Jochim, J. H. Denschlag, and R. Grimm, Science **305**, 1128 (2004).

[179] M. Bartenstein, A. Altmeyer, S. Riedl, S. Jochim, C. Chin, J. Hecker-Denschlag, and R. Grimm, Phys. Rev. Lett. **92**, 120401 (2004).

[180] M. Bartenstein, A. Altmeyer, S. Riedl, S. Jochim, C. Chin, J. Hecker-Denschlag, and R. Grimm, Phys. Rev. Lett. **92**, 203201 (2004).

[181] J. Kinast, S. L. Hemmer, M. E. Gehm, A. Turlapov, and J. E. Thomas, Phys. Rev. Lett. **92**, 150402 (2004).

[182] G. M. Falco and H. T. C. Stoof, Phys. Rev. Lett. **92**, 130401 (2004).

[183] M. Tinkham, *Introduction to Superconductivity* (2nd. ed., McGraw-Hill, New-York, 1996).

[184] G. Bruun, Y. Castin, R. Dum, and K. Burnett, Eur. Phys. J. D **7**, 433 (1999).

[185] L. Mandel and E. Wolf, *Optical coherence and quantum optics* (Cambridge University Press, 1995).

[186] W. Belzig, *Advances in Solid State Physics, p.163* (edited by B. Kramer, Springer , Berlin, 2002).

[187] C. W. J. Beenakker and C. Schönenberger, Physics Today **56 (5)**, 37 (2003).

[188] D. Meiser and P. Meystre, Phys. Rev. Lett. **94**, 093001 (2005).

[189] F. Weig and W. Zwerger, Europhys. Lett. **49**, 282 (2000).

[190] H. P. Büchler, P. Zoller, and W. Zwerger, Phys. Rev. Lett. **93**, 080401 (2004).

[191] M. A. Baranov and D. Petrov, Phys. Rev A **62**, 041601R (2000).

[192] S. Stringari, Europhys. Lett **65**, 749 (2004).

[193] L. D. Landau and E. M. Lifshitz, *Course of Theoretical Physics, Vol. 5: Statistical Physics* (Pergamon Press, London, 1958).

[194] L. S. Levitov, H. Lee, and G. B. Lesovik, J. Math. Phys. **37**, 4845 (1996).

[195] H. D. Politzer, Phys. Rev. A **54**, 5048 (1996).

[196] M. Holthaus, E. Kalinowski, and K. Kirsten, Ann. Phys. (N.Y.) **270**, 198 (1998).

[197] S. Giorgini, L. P. Pitaevskii, and S. Stringari, Phys. Rev. Lett. **98**, 5040 (1998).

[198] F. Meier and W. Zwerger, Phys. Rev. A **60**, 5133 (1999).

[199] Z. Idziaszek, M. Gajda, P. Navez, M. Wilkens, and K. Rzążewski, Phys. Rev. Lett. (1999).

[200] V. V. Kocharovsky, V. V. Kocharovsky, and M. O. Scully, Phys. Rev. Lett. **84**, 2306 (2000).

[201] I. Carusotto and Y. Castin, Phys. Rev. Lett. **90**, 030401 (2003).

[202] W. Zwerger, Phys. Rev. Lett. **92**, 027203 (2004).

[203] M. Abramowitz and I. A. Stegun, *Handbook of Mathematical Functions, p927* (Dover Publications, New York, 1968).

[204] N. N. Bogoliubov, Sov. Phys. JETP **7**, 41 (1958).

[205] S. K. Adhikari, Am. J. Phys. **54**, 362 (1986).

Veröffentlichungen:

W. Belzig, C. Schroll, and C. Bruder
Density correlations in ultracold atomic Fermi gases
cond-mat/0412269

C. Schroll, F. Marquardt, and C. Bruder
Perturbative corrections to the Gutzwiller mean-field solution of the Mott-Hubbard model
Phys. Rev. A **70**, 053609 (2004)

C. Schroll, W. Belzig, and C. Bruder
Decoherence of cold atomic gases in magnetic microtraps
Phys. Rev. A **68**, 043618 (2003)

M. Governale, D. Boese, U. Zülicke, and C. Schroll
Filtering spin with tunnel-coupled electron wave guides
Phys. Rev. B **65**, 140403 (2002)

U. Zülicke and C. Schroll
*Interface Conductance of Ballistic Ferromagnetic-Metal-2DEG Hybrid Systems with Rashba Spin-Orbit Coupling (comment to Phys. Rev. Lett. **86**, 1058 (2001))*
Phys. Rev. Lett. **88**, 029701 (2002)